Effects of burrs on a three phase transformer core including local loss, total loss and flux distribution

by

Rafal Mazurek

A thesis submitted to the Cardiff University in candidature

for the degree of Doctor of Philosophy

Cardiff School of Engineering

Cardiff University

Wales, United Kingdom

October 2012

DECLARATION

This work has not previously been accepted in substance for any degree and is not concurrently submitted in candidature for any degree.

Signed ..... (candidate) Date 25/07/2013

STATEMENT 1

This thesis is being submitted in partial fulfilment of the requirements for the degree of PhD.

Signed ..... (candidate) Date 25/07/2013

STATEMENT 2

This thesis is the result of my own independent work/investigation, except where otherwise stated. Other sources are acknowledged by explicit references.

Signed ..... (candidate) Date 25/07/2013

STATEMENT 3

I hereby give consent for my thesis, if accepted, to be available for photocopying and for inter-library loan, and for the title and summary to be made available to outside organisations.

Signed ..... (candidate) Date 25/07/2013

ACKNOWLEDGEMENT

I am truly indebted and thankful to my supervisor Professor A.J. Moses who has patiently endured the process of shaping me into a better researcher through numerous discussions and endless stream of advice. I would like to thank Dr P. Marketos for his extraordinary commitment he has shown boosting my curiosity and experimental skills. I would like to show my gratitude to Dr P.I. Anderson for his invaluable help in the final and most important stages of investigation and writing of this thesis. I am grateful to Dr Thierry Belgrand and Dr Jean-Noel Vincent for their valuable input. I would like to thank Dr E. Melikhov for the time and efforts he spent on many theoretical and practical discussions and for the outstanding moral support.

I am obliged to many of my colleagues at Wolfson Centre for Magnetics for their valuable input in practical and theoretical ideas over the course of this investigation. Big thanks are due to many members of staff at Cardiff University, especially Mr Paul Farrugia and Mr Christopher Dunscombe.

I will always remember the heart warming support of my family and friends who tracked my progress and encouraged me continuously to reach my goals. I would like to show my gratitude to my wife Justyna who stood by me every step of the way with encouragement and support.

ABSTRACT

This thesis examines the effects of burrs on performance of transformer cores through application of artificial burrs, measurements of overall specific total loss and local specific total loss, measurements of flux density redistribution caused by burrs and through development of eddy current loss model incorporating two dimensional eddy current losses and flux density distribution within a conductive sample.

A clamping system was designed for application of artificial burrs in a completely repeatable and reversible manner. Various burr sizes and arrangements were investigated to confirm the effect and show the extent of the effect for different scenarios with the experimental core magnetised in the range of 0.1 T to 1.8 T.

It was observed that for large number of laminations affected by the artificial burrs the overall core losses of the three phase, 350 kVA distribution transformer doubled while the local losses in the vicinity of the burred region reached over 1 kW/kg.

Three eddy current loss models were developed in this investigation. One for a symmetrical case of burrs located on either edge of a stack of laminations, one for a non symmetrical case of burrs located on the edge or within the stack of laminations and finally, one taking into account flux density decay within a conductive material.

A secondary objective of this thesis is a feasibility study of using thin film sensors within a commercial size transformer core. This was achieved by adapting a physical vapour deposition system to accommodate large laminations and depositing thin film needle sensors for flux density measurement and thin film thermocouples for loss measurement inside a stack of the core.

The flux density measurement by thin film needle sensors within the core was successful. Thin film thermocouples did not provide successful results and the development of this part of the work is suggested as future work.

TABLE OF CONTENTS

LIST OF FIGURES

LIST OF TABLES

LIST OF SYMBOLS

B	Flux density	[T]
H	Magnetic field	[A/m]
M	Magnetisation	[A/m]
χ	Susceptibility	[-]
μ	Permeability	[H/m]
$\mathcal{R}$	Reluctance	[H^{-1}]
Φ	Flux	[Wb]
m	Magnetic moment	[Am^2]
E	Electric field	[V/m]
I, i	current	[A]
V,U	Voltage	[V]
f	frequency	[Hz]
R	Resistance	[Ω]
ρ	resistivity	[Ω m]
δ	skin depth	[m]
$\bar{m}$	average number of magnetic moments per atom	[-]
n	number of atoms per unit volume	[-]
e_c	charge of an electron	[C]
v	velocity	[m/s]
r	radius	[m]
T	time	[s]
N	number of conductors carrying current	[-]
dl	line vector corresponding to conductor direction	[m]
F_B	Lorentz force	[N]
q	charge	[C]
s	surface	[-]
A	area	[m^2]
μ_0	permeability of free space	[Hm^{-1}]
μ_r	relative permeability	[-]
μ	permeability	[Hm^{-1}]
μ_m	maximum permeability	[Hm^{-1}]

l	length of a dipole	[m]
χ	susceptibility	[-]
k	number of magnetic moments	[-]
M_0	saturation magnetisation	[A/m]
F_{mm}	magnetomotive force	[A]
d	thickness of an electrical steel sheet	[m]
b	width of electrical steel sheet	[m]
B_{max}	peak flux density	[T]
ω	angular frequency	[rad/s]
e	induced voltage	[V]
E	root mean square (RMS) value of induced voltage e	[V]
P	power loss (various subscripts reflect the sources of loss)	[W]
D	density	[kg m^3]
δ	skin depth	[m]
B_{sat},B_s	saturation value of flux density	[T]
Θ	Curie point	[K]
m_a	active mass	[kg]
l_m	effective magnetic path length	[m]
T	temperature	[K]
c_p	specific heat capacity	[J/K]
K	heat transmission coefficient	[Js/K]
h	burr height	[m]
C	capacity	[F]
N_p, N_s	primary and secondary windings	[-]
H_B	height of short circuited stack portion	[m]
L_B	length of short circuited stack portion	[m]
W_L	width of a stack of laminations	[m]
d_b	thickness of short circuited volume	[m]

Chapter 1. **Introduction**

1.1 GENERAL INTRODUCTION AND AIMS OF THE PROJECT

The demand for energy efficiency is growing in parallel with the demand for more energy. Targets and deadlines were set in the directive 2009/28/EC by the European Parliament to increase the proportion of renewable energy within the European countries to 20% by the year 2020. Each country has been given an individual target to achieve an overall Community's gross final consumption of energy in 2020. For example, the United Kingdom had only 1.3% of energy from renewable sources in gross final consumption of energy in 2005 and the target for 2020 was set to 15% [1]. Achieving these goals requires significant amounts of new infrastructure and the efficiency of new devices influences the investment return, as well as cost of reaching that target. Another important set of rules was agreed in the Kyoto Protocol in 1998 by the United Nations. It sets targets for emissions of greenhouse gases as well as enabling mechanisms to help achieve the targets for countries with too high emissions and to benefit from helping countries with very low emissions [2].

Countries work towards meeting those targets by raising energy efficiency awareness, improving the infrastructure and promoting renewable energy solutions. Increasing the efficiency of the electrical grid means reduced greenhouse gas emission for the same amount of energy consumed. More globally, in 2000, the energy losses of distribution networks around the world was 1279 TWh while efficiency of single countries ranged between 73.3% for India and 96.3% for Finland which still offers scope for improvement across the board [3]. A large part of the electrical grid losses comes from transformers which are often in service for nearly half a century. For

comparison, transmission and distribution losses in United Kingdom totalled 9.4% whilst the Western Europe average was 7.3% of energy production. Typically about a third of the transmission and distribution losses occur in transformers – about 8% -10% of total for transmission and 24 – 32 % for distribution transformers [3], the rest of the losses occurring in the transmission lines and other sources. In general, improvement can be achieved by implementation of new technology or by studying and removing the inefficiencies from current devices. While transformers and electrical motors present opportunities for both types of improvement, this thesis deals only with the latter: analysis of a particular issue that may occur in transformers and electrical motors – electrical short circuits in the cores caused by lamination edge burrs. These defects may increase the transformer losses by a few percent up to 100% or more in some extreme cases [4].

1.1.1 Introduction to transformers and burrs

Transformers are devices consisting of a magnetic core and a set of wires wound around the core in such a way as to use Faradays law of electromagnetic induction to transfer energy between two electrical circuits via a magnetic circuit with no electrical connection between the two circuits. To minimise loss, transformer cores are assembled from thin sheets (around 0.3 mm) of electrical steel [5-7]. Burrs are raised edges of electrical steel sheets which may occur during cutting processes as discussed further in Chapter 5. In some cases those raised edges may create electrical connections between adjacent laminations when they are stacked on top of each other or between two consecutive turns of a strip in a wound core. In case of some electrical machines parts of the stack are short circuited through construction features i.e. iron rods or welds. This in turn may increase the losses in a transformer core previously minimised by using the

thin lamination. Increase in loss by a few percent over the life cycle of a transformer will significantly increase the financial loss but there is also a possibility of an avalanche effect being triggered in which case the steel can even locally melt and the core can be ruined completely [4, 8, 9]. These effects are well known but there is little published work to properly describe and quantify the phenomena.

1.2 OBJECTIVES

The first and main aim of this thesis is the evaluation of the effects of short circuits in transformer cores caused by edge burrs. Total specific core loss and localised loss in the regions affected by burrs as well as flux distribution within the affected limb and within the whole core are investigated. Prediction and confirmation of the experimental findings are investigated by means of eddy current analysis for the case with burrs present in an experimental core of commercial size and rating.

The secondary aim of this project is to develop novel thin film sensors for the measurements of flux density and localised specific loss inside a transformer core.

Chapter 2. **Background on magnetics**

2.1 MAGNETIC MATERIALS

Electrons within materials spin and orbit the atomic nucleus. They have individual magnetic moments which are caused by both the spinning on their own axis and orbiting the nuclei. If aligned together with magnetic moments of other electrons a net magnetic moment in the material is formed Materials where such situation occurs are called magnetic materials. For $\bar{m}$ average magnetic moments per atom and *n* atoms per unit volume of a material, magnetisation M is given by (2.1)

$$\mathrm{M} = \mathrm{n}\bar{\mathrm{m}} \tag{2.1}$$

The magnetic moment magnitude is defined as the product of a current and the area around which that current is flowing. The magnetic moment of a single electron can be calculated in accordance with the classical atomic model where a single charge of $-e_c$ moves with velocity v around an orbit of radius r. The electron moves around the full orbit $2\pi r$ in time $t = 2\pi r/v$. The current associated with this motion can be calculated as

$$\mathrm{I} = -\frac{\mathrm{e_c}}{\mathrm{t}} = -\frac{\mathrm{e_c v}}{2\pi \mathrm{r}} \tag{2.2}$$

and the magnetic moment of a single electron is calculated as

$$\mathrm{m} = \mathrm{IA} = -\frac{\mathrm{e_c v}}{2\pi \mathrm{r}}\pi \mathrm{r}^2 = -\frac{\mathrm{e_c vr}}{2} \tag{2.3}$$

Magnetic materials can be divided into diamagnetic, paramagnetic, ferromagnetic and antiferromagnetic. The difference between them is due to the atomic structure of the

materials, in particular the presence or absence of unpaired electrons. If all the electrons are paired, the magnetic moment in each atom is zero and the material and the net magnetic moment of the material is zero [10]

2.1.1 **Ferromagnetic materials**

This investigation focuses only on electrical steel which is a ferromagnetic material. Ferromagnetic materials have unpaired electrons and therefore have a net magnetic moment greater than zero. When subjected to an external magnetic field they can retain the magnetic properties after the field has been removed. However, even without an external field applied, regions of ferromagnetic material have their magnetic moments aligned in a particular direction due to a coupling of the moments known as the exchange interaction. Such a region with all moments aligned in parallel is called a magnetic domain.

A border between two domains is called a domain wall and is spread between two domains over a region comprising many atoms with spins gradually transitioning from aligned to the collective magnetic moment direction of one domain to aligned to the magnetic moment direction of the other domain. The reason for the spins to gradually change the angle rather than switch instantaneously is minimisation of the exchange energy between each two spins which is proportional to the square of the angle between them. The movement of domain walls through the material gives rise to its magnetic properties.

The alignment direction of each domain is fairly random, but crystallographic structure of the material determines some preferred directions. The most important ferromagnetic materials are alloys of iron, cobalt and nickel [6].

2.1.2 Crystalline structure

Solid substances can be divided into two main categories based on the arrangement of the atoms in their microstructure: amorphous and crystalline materials. Amorphous materials represent random arrangement of atoms and crystalline materials such as electrical steels represent an organised structure with a clear pattern as illustrated in Figure 2.1 where a crystalline structure with a noticeable pattern is visible on the left side and a randomly arranged amorphous structure has formed on the right side. A clear elementary and repeating pattern is marked by a blue circle on the left side while no two patterns are alike in the amorphous material sketch on the right side.

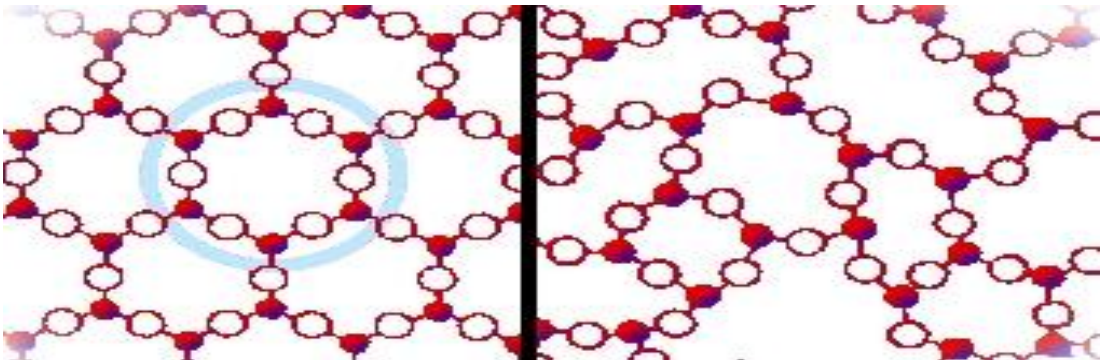

Figure 2.1 Example of crystalline (left) and amorphous (right) structure.

The example in Figure 2.1 is shown in 2D but the same rule applies to 3D shapes and patterns. The crystalline structure of electrical steels will be discussed further in section 3.1 [11].

2.2 MAGNETIC FIELD H AND MAGNETIC FLUX DENSITY B

A magnetic field is produced by moving electrical charges which was first noticed by Ampere and described by

$$NI = \int_{\text{closed path}} \vec{H} \cdot \vec{dl} \qquad \textbf{(2.4)}$$

where: N is the number of conductors each carrying current I; $\vec{H}$ is the magnetic field and $\vec{dl}$ is the line vector corresponding to the conductor direction. For a linear case, this can be written as $NI = HL$.

Magnetic induction is a vector used to calculate the Lorentz force (in the absence of an electrical field) given by

$$\vec{F_B} = q\vec{v} \times \vec{B} \tag{2.5}$$

where: $\vec{F_B}$ is the force acting upon a charge q which is moving at velocity v. The unit of flux density is Tesla (1 T = 1 V s m^{-2} = 1 kg s^{-2} A^{-1}).

Magnetic flux Φ flowing through a surface s is a scalar defined by (2.6)

$$\phi \stackrel{\text{def}}{=} \int_S \vec{B} \cdot \vec{d\mathbf{s}} \tag{2.6}$$

where: s is the surface through which the flux flows and $\vec{B}$ is the flux density. The unit of flux is a Weber (1 Wb = 1 m^2 kg s^{-2} A^{-1}).

For a given surface area A the flux density can be calculated as flux divided by the area $B = \frac{\phi}{A}$.

In free space the relation between the applied field H and the response B is called the permeability of free space $\mu_0 = 4\pi \times 10^{-7}$ [H/m] and is given by

$$\vec{B} = \mu_0 \vec{H} \tag{2.7}$$

The magnetic moment m between the two poles of a dipole of length l and cross-section A is given by $m = \frac{\phi l}{\mu_0}$. Magnetisation M of a material is the measure of magnetic moments m of a material per unit volume V as in $M = m/V$. The magnetisation of a dipole of length l and cross section A is given by $M = m/Al$, hence

$$\overrightarrow{\mathrm{M}} = \frac{\Phi}{\mu_0 A} = \frac{\overrightarrow{\mathrm{B}}}{\mu_0} \tag{2.8}$$

Therefore flux density originating from magnetisation within that material is expressed as

$$\overrightarrow{\mathrm{B}} = \mu_0 \overrightarrow{\mathrm{M}} \tag{2.9}$$

The previous two paragraphs describe magnetic flux density B components from a response to an applied external field and the magnetisation. To consider both components the two vectors are added as in

$$\overrightarrow{\mathrm{B}} = \mu_0(\overrightarrow{\mathrm{H}} + \overrightarrow{\mathrm{M}}) \tag{2.10}$$

2.3 PERMEABILITY, RELATIVE PERMEABILITY AND SUSCEPTIBILITY

Permeability is the ability of a material to sustain a certain value of magnetisation in a given magnetic field and it is expressed as

$$\mu = \frac{\mathrm{B}}{\mathrm{H}} \tag{2.11}$$

Permeability is influenced by various factors such as chemical composition, stress and processing, as well as operating conditions such as magnetising frequency. The permeability of all materials is compared to μ_0 by means of relative permeability μ_r

which is expressed by the ratio of the materials permeability to the permeability of vacuum given by

$$\mu_r = \frac{\mu}{\mu_0} \tag{2.12}$$

The permeability characteristic of electrical steel as a function of the magnetising frequency and peak flux density is illustrated in Figure 2.2. It is desired to use materials at the peak of their permeability characteristic. For example, Steel 4 is best utilised at approximately 1.5 T at 50 Hz magnetising frequency.

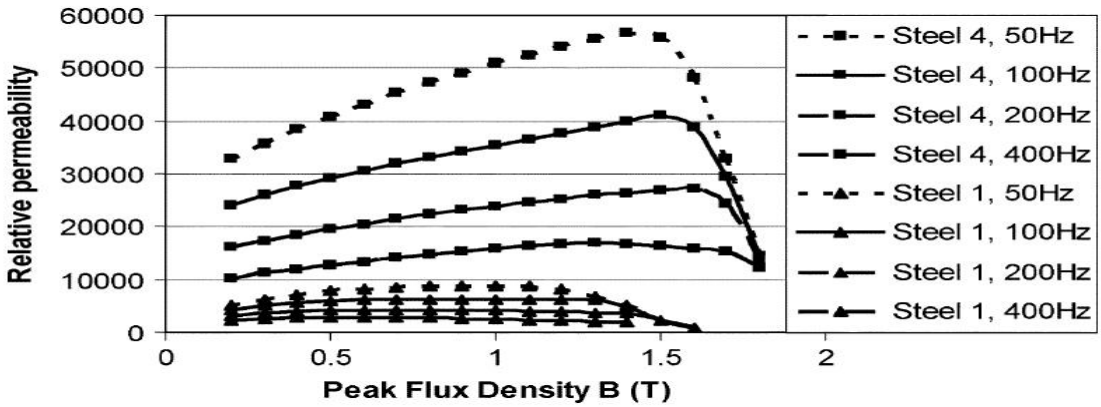

Figure 2.2 Variation of permeability of SiFe of non oriented (Steel 1) and high permeability grain oriented electrical steel with peak flux density for a range of magnetisation frequencies [12].

It is common to compare the permeability of electrical steel for a given applied field value as in $\mathbf{B}_{1000}$ which is the value of peak flux density for an applied field of 1000 A/m [13].

Susceptibility is a measure of the magnetisation of the material in presence of an applied field and is written as

$$\chi = \frac{M}{H} \tag{2.13}$$

Magnetic flux density B and magnetisation M are not linear and therefore permeability and susceptibility are not linear and are often measured as differential values for a given magnetic field value H.

The flux density equation (2.10) can be presented using susceptibility as

$$B = \mu_0(H + \chi H) = \mu_0 H(1 + \chi) \qquad \textbf{(2.14)}$$

2.4 B – H LOOP

The origin of the B-H loop is the work that needs to be done to align the magnetic domains to the direction of the external magnetic field. Movement of domain walls under the influence of an applied magnetic field is impeded by pinning sites which are impurities in the material or inhomogeneous strain caused by dislocations. Work is done to overcome the pinning sites and the loss of energy associated with this work is dissipated in the form of heat. The lag of flux density behind the change of the magnetic field causing it is termed B-H loop and its plot is the most significant single piece of information about a ferromagnetic material [14]. In the presence of an external magnetic field H, the magnetic dipoles of the material align in the direction of that field.

The hysteresis as described above is represented by plotting the change of flux density B with very low frequency, quasi DC, applied field H as shown in Figure 2.3. The curve follows the same path for the same magnetising conditions. When starting the process from a demagnetised state (B=0, H=0), the B-H curve follows a path called the initial magnetisation as shown in Figure 2.3 by the dotted line with flux density increasing from zero up to saturation with the increasing applied field.

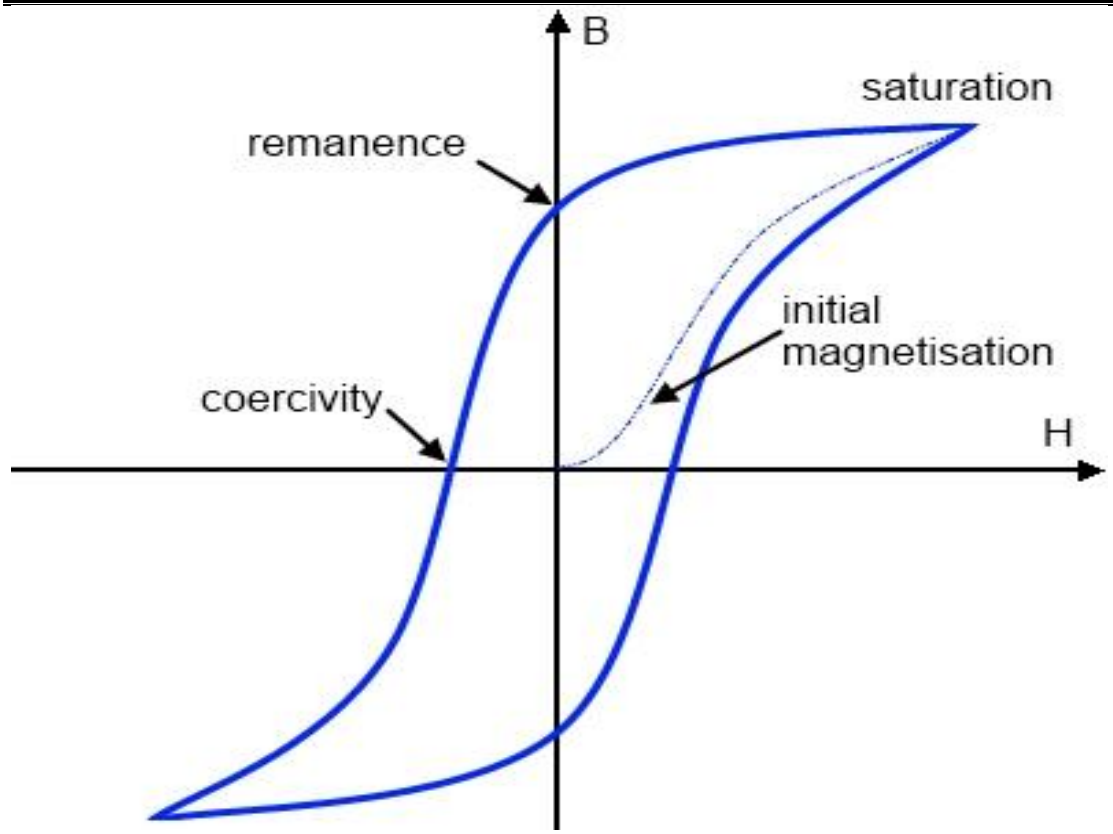

Figure 2.3 Example of a B-H loop of a ferromagnetic material.

The B-H loop can be characterised by three main parameters: saturation, coercivity and remanence. The shape of the loop as well as the three parameters is different for different materials.

2.4.1 **Saturation**

If all the magnetic moments of a ferromagnetic material are aligned in one direction, the material is in a state of saturation magnetisation. For *k* magnetic moments *m* saturation magnetisation M_0 is calculated as $M_0 = km$.

In agreement with (2.10) by increasing the field H, the flux density B rises. However, when saturation magnetisation M_0 is achieved the increase in flux density is due solely to the $\mu_0 H$ component. At this stage susceptibility of the material is zero. This state of saturation is shown in the hysteresis plot in Figure 2.3 [6, 14].

Table 2.1 Saturation magnetisation values of example materials.

Material	Saturation Magnetisation. M_0 [T]
Iron	2.15 [6]
Cobalt	1.78 [6]
Nickel	0.60 [6]
3% Silicon Iron	2.03 [15]

2.4.2 Coercivity, coercive force and remanence

Coercive force is the value of field required to reduce the magnetisation of a magnetised material from any point of magnetisation to zero. Coercivity is the value of field required to bring the flux density of a magnetised material from saturation back to zero which means that coercivity is the maximum value of the coercive force [6, 14]. Ferromagnetic materials with high and low coercivity are called hard and soft magnetic materials respectively. Coercivity higher than 10 000 A/m characterises hard magnetic materials and materials with coercivity below 1000 A/m are considered magnetically soft. Coercivity depends on heat treatment and deformation of the material such as cold working as well as the addition of non magnetic elements such as carbon [6].

Ferromagnets can be magnetised when subjected to magnetic field. However, once the magnetic field is removed, the magnetisation does not disappear. This phenomenon is called remanence. The value of remanence is the amount of flux density remaining in the material after the external magnetic field is removed.

2.5 MMF AND MAGNETIC RELUCTANCE

The magnetomotive force F_{mm} is defined as the product of the magnetising current associated with a magnetic circuit and the number of turns of conductor in that circuit, and is given by

$$F_{mm} = NI \tag{2.15}$$

The magnetic reluctance is the ratio between the magnetomotive force F_{mm} acting on a magnetic circuit and the magnetic flux generated by it as in (2.16).

$$\mathcal{R} = \frac{F_{mm}}{\phi} \tag{2.16}$$

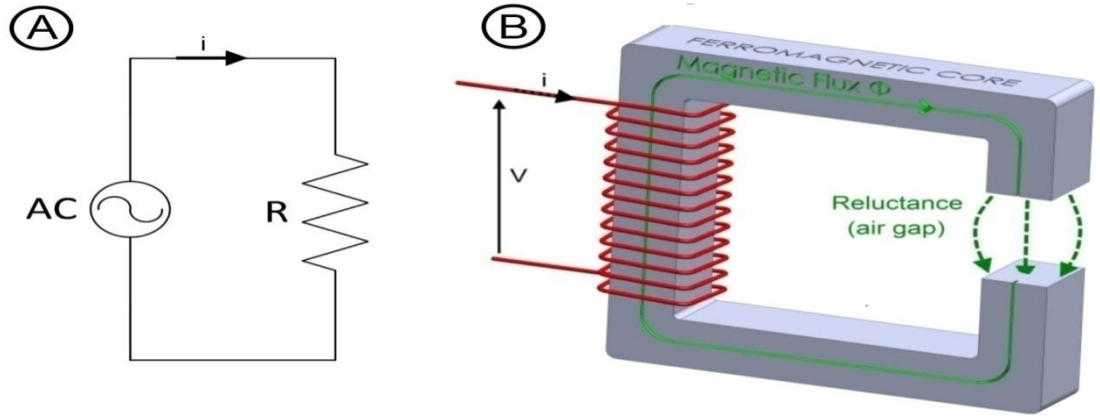

Figure 2.4 Schematic of reluctance in a magnetic circuit.

The relationship between the three values is equivalent to Ohms law in electrical circuits which makes magnetic reluctance, magnetomotive force and magnetic flux the equivalent of resistance, voltage and current respectively. This analogy is visible in Figure 2.4 where magnetic reluctance is pictured as an air gap in the magnetic circuit. However, reluctance applies to every portion of the magnetic circuit. Reluctance is proportional to the length of magnetic path and inversely proportional to the product of the cross section area of the magnetic medium and its permeability and the equation takes the form of (2.19). It can be derived from Ampers circuital law (2.4). For a magnetic circuit of length L and cross-section area A, with N number of turns of wire

wound around it and with current I flowing through this wire, Amperes law can be written as (2.17)

$$\mathrm{HL} = \mathrm{NI} \tag{2.17}$$

Using (2.6) and (2.7) flux density in this magnetic circuit can be calculated as

$$\phi = \mathrm{NI}\frac{\mu_0\mu_r\mathrm{A}}{\mathrm{L}} \tag{2.18}$$

where $\mu_0\mu_r A/L$ is the inverse of the reluctance $\mathcal{R}$ measured in H^{-1} as in

$$\mathcal{R} = \frac{\mathrm{L}}{\mu_0\mu_r\mathrm{A}} \tag{2.19}$$

2.6 FARADAYS LAW OF INDUCTION

Faradays Law: *The voltage induced in an electrical circuit is proportional to the rate of change of magnetic flux flowing through that circuit.*

The definition above can be represented as a change of magnetic flux in time through a coil comprising N turns of wire as

$$\mathrm{V} = -\mathrm{N}\frac{\mathrm{d}\phi}{\mathrm{dt}} \tag{2.20}$$

More specifically, for a cross section area A of the loop the voltage induced is written in terms of flux density as

$$\mathrm{V} = -\mathrm{NA}\frac{\mathrm{dB}}{\mathrm{dt}} \tag{2.21}$$

The minus sign in (2.20) is described in Lenz's law of induction and the meaning is that the polarity of the induced emf opposes the field which has induced it.

2.7 EDDY CURRENTS AND EDDY CURRENT LOSS ANALYSIS

Eddy currents also called “Foucault Currents” were discovered by Foucault in 1855 [16]. They are induced in ferromagnetic materials by reversing the electric field.

The main principle of electrical machines is to use the emf induced in the windings by the magnetic flux flowing through their core according to Faradays Law. However, the core is built of soft magnetic materials which are electrically conductive; hence an emf is induced within the core. This generates eddy currents within the core and these in turn generate i^2R losses where i is the eddy current and R is the resistance of the portion of the core through which that current flows. To minimize this loss, magnetic cores are assembled using thin sheets of silicon steel. The silicon is added to increase its electrical resistivity at the expense of reduced permeability. Electrical insulation provided by the coating on the steel ensures that eddy currents are restricted to flow separately in each lamination as shown in Figure 2.5 [9, 17]. Magnetic flux causing the eddy currents to flow in a solid block core and in a core made of thin laminations is marked with green arrows for both cases. Eddy current paths are marked in both cases by dotted lines with arrows to indicate the direction in which the currents flow.

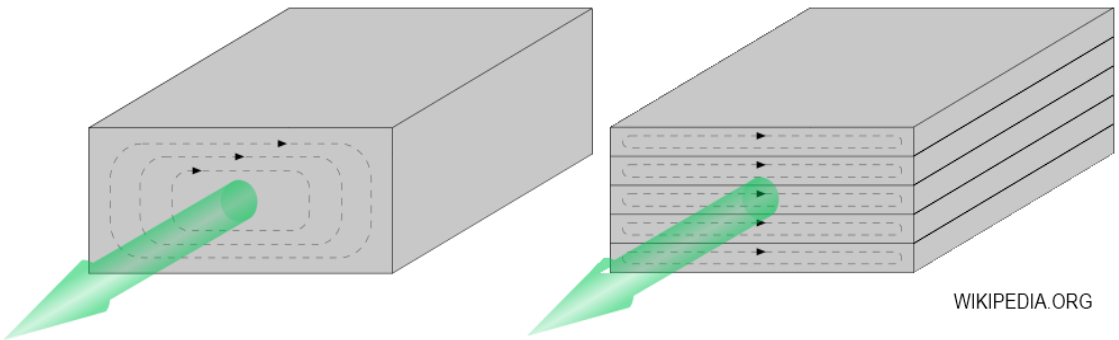

Figure 2.5 Eddy currents in a solid block and a stack of thin laminations.

2.7.1 Classical eddy current loss equations

Derivation of classical expressions for the eddy current loss in thin sheets is carried out making the initial assumption that the sheet is very thin compared to its width [18]. A steel sheet of thickness *d* and width *b* as shown in Figure 2.6 is considered where d<<b. Considering a sinusoidal alternating flux density $B = B_{max} \sin \omega t$ flowing uniformly through the sheet as shown in Figure 2.6 where B is instantaneous flux density at any time t, B_{max} is its peak value and $\omega = 2\pi f$ where *f* is the magnetising frequency.

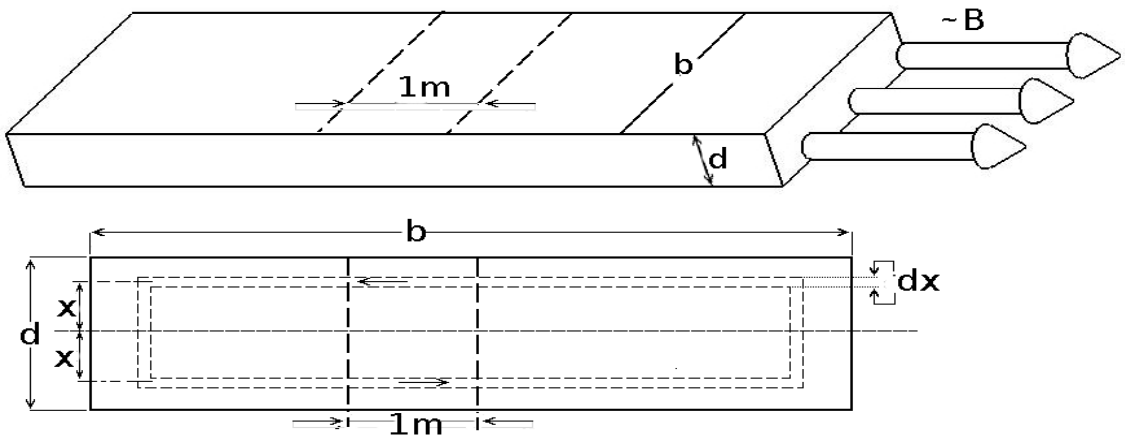

Figure 2.6 Sheet of electrical steel with magnetic flux B flowing through it. (a) plan view of the sheet (b) cross-section of the sheet.

Considering 1 m length of the material 1 m wide, at any instant in time, the flux enclosed by a unit area formed by elemental path of width dx, whose distance from the centre axis is x, is given by

$$\phi = 2x \times 1 \times B = 2xB_{max} \sin \omega t \qquad \textbf{(2.22)}$$

and from Faradays law the induced emf is given by

$$e = \frac{d}{dt}(2xB_{max} \sin \omega t) = 2xB_{max}\omega \cos \omega t = 4x\pi fB_{max} \cos \omega t \qquad \textbf{(2.23)}$$

and the rms value is given by

$$E = \frac{4x\pi f B_{max}}{\sqrt{2}} \quad \textbf{(2.24)}$$

The resistivity of the material ρ is used to calculate the resistance of 1 m length of the steel as in

$$R = \frac{2 \times \rho}{dx \times 1} = \frac{2\rho}{dx} \quad \textbf{(2.25)}$$

The assumption of thickness being negligible as compared to width of the lamination is followed by an assumption that the current flowing perpendicular to the lamination surface is negligible so only the current flowing in parallel to the surface of the sheet is calculated based on Ohms law as

$$i = \frac{E}{R} = \frac{\frac{4x\pi f B_{max}}{\sqrt{2}}}{\frac{2\rho}{dx}} = \frac{2x\pi f B_{max} dx}{\sqrt{2}\rho} \quad \textbf{(2.26)}$$

and the loss due to this eddy current in the path is therefore given by

$$P = i^2 R = \frac{4x^2\pi^2 f^2 B_{max}^2 dx^2}{2\rho^2} \times \frac{2\rho}{dx} = \frac{4x^2\pi^2 f^2 B_{max}^2 dx}{\rho}\,[W] \quad \textbf{(2.27)}$$

Integrating between the limits $x = 0, x = \frac{d}{2}$ gives

$$P_e = \int_{x=0}^{x=\frac{d}{2}} \frac{4x^2\pi^2 f^2 B_{max}^2}{\rho}\,dx \quad \textbf{(2.28)}$$

Hence the loss per cubic metre is given by

$$P_e = \frac{\pi^2 f^2 B_{max}^2 d^2}{6\rho}\left[\frac{W}{m^3}\right] \quad \textbf{(2.29)}$$

and the loss per kilogram is given by

$$P_e = \frac{\pi^2 f^2 B_{max}^2 d^2}{6D\rho}\left[\frac{W}{kg}\right] \quad \textbf{(2.30)}$$

where *D* is the density of the steel. Figure 2.7 shows eddy current loss values at 50 Hz for various conditions calculated using (2.30), B_{max}, is a variable, lamination thickness d is 0.3 mm, 0.6 mm and 0.9 mm, the density of the material is 7650 kg/m^3 [15] and the resistivity ρ is 48×10^{-8} Ω m [15].

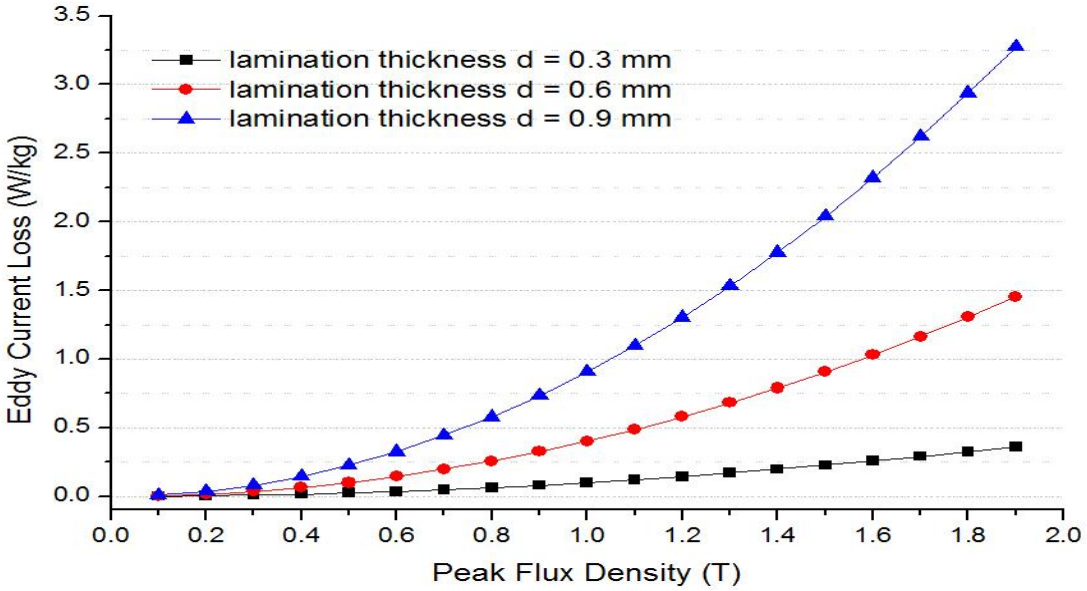

Figure 2.7 Eddy current loss calculated using (2.30) for lamination thicknesses of 0.3 mm, 0.6 mm and 0.9 mm.

2.7.2 Thin lamination design and skin effect

Figure 2.7 illustrates the importance of controlling the thickness of transformer and electrical machine core laminations. However, other factors such as the cost and difficulty in handling due to brittleness and plastic deformations determines the thickness of electrical steel laminations which are typically between 0.18 and 0.5 mm. Another factor considered is the skin effect which is a phenomenon describing a decay of a time dependent magnetic field penetrating an electrically conductive medium such as an electrical steel sheet according to the equation

$$\frac{H}{H_0} = \sqrt{\frac{\cosh 2x\sqrt{\pi f \sigma \mu_0 \mu_r} + \cos 2x\sqrt{\pi f \sigma \mu_0 \mu_r}}{\cosh d\sqrt{\pi f \sigma \mu_0 \mu_r} + \cos d\sqrt{\pi f \sigma \mu_0 \mu_r}}} \quad \textbf{(2.31)}$$

where d is the thickness of the sheet, x is the distance from the middle of the sheet.

It can be characterised by the skin depth δ which is the distance from the surface of the material at which the magnetic field has decayed to 1/e of the value on the surface. This means that the field entering an electrically conductive material is confined within a surface layer of that material. The skin depth is given by

$$\delta = \sqrt{\frac{1}{\pi f \sigma \mu_0 \mu_r}} \quad \textbf{(2.32)}$$

This phenomenon of skin effect is illustrated in Figure 2.8 where flux density within the electrical steel of different thicknesses is calculated using (2.31). This means that if 0.8 mm thick laminations are used at 60 Hz magnetisation, most of the material inside is only magnetised to about 90% of the magnetisation on the surface of it. Due to high cost of electrical steel it is desired to utilise maximum volume of electrical machines and thus use the full potential for energy transfer per kg mass [17].

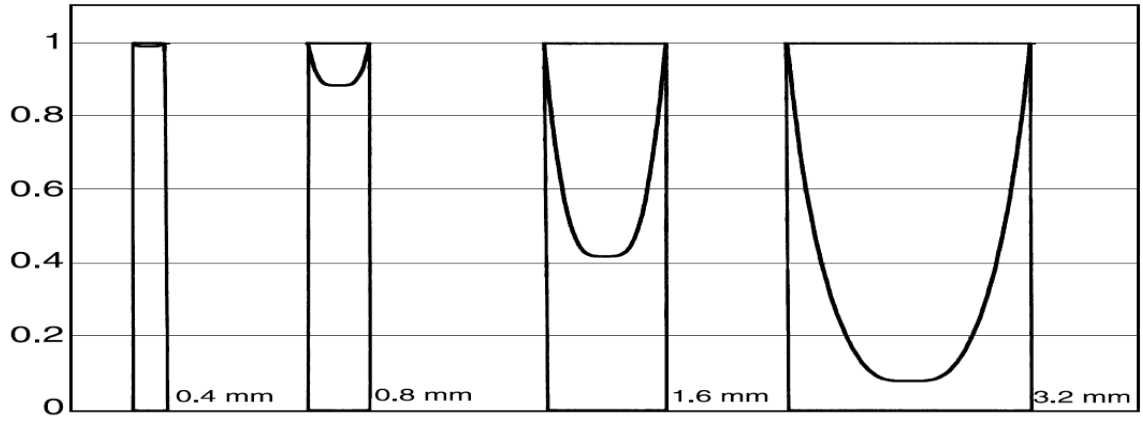

Figure 2.8 Amplitude of flux density within electrical steel sheets of various thicknesses shown as a fraction of the surface value. Calculations made for frequency of 60 Hz and skin depth of 0.5 mm.

Chapter 3. **Electrical steel and electrical machines**

This chapter presents basic information on electrical steel and measurements of electrical steel characteristic relevant to this investigation. Electrical steel is used in electrical machines such as transformers, motors and generators and is produced in such a way as to optimise its magnetic properties such as permeability, eddy currents and hysteresis loss.

3.1 GOSS STRUCTURE

The crystalline structure of electrical steel is classified based on the shape of the smallest crystal unit as shown in Figure 3.1. Iron presents a cubic body centred crystalline structure [11]. In silicon iron some of the atoms of iron are replaced by atoms of silicon. Each atom is represented by a blue sphere in Figure 3.1. In electrical steels the silicon content ranges between 0 to 6.5 %.

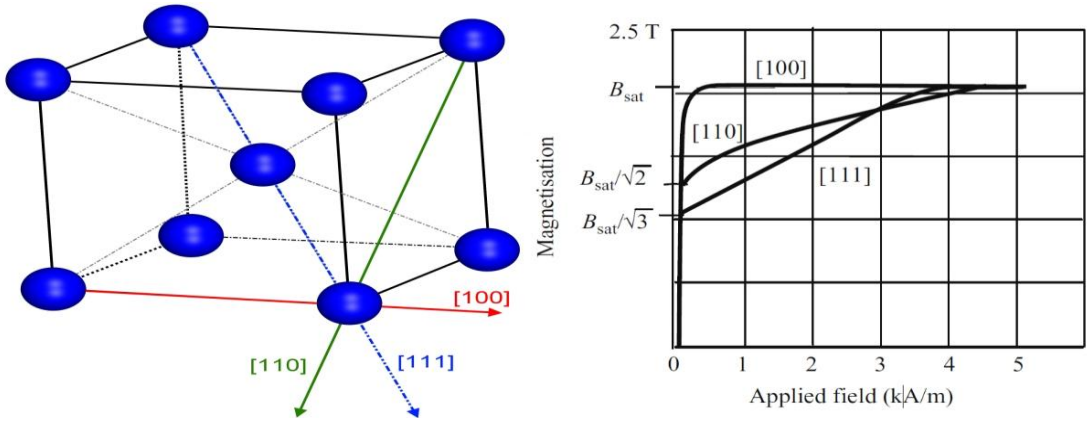

Figure 3.1 Schematic of the crystal structure of electrical steel and magnetisation of the electrical steel in directions: [100] – cube edge, [110] hard cube face diagonal and [111] the hardest to magnetise cube body diagonal [9].

Without any control over the crystallisation of the material, the orientation of each elementary cube is random and the overall magnetic properties of the material are very similar in every direction in the plane of the sheet. Materials representing a random

arrangement of crystal lattice, and therefore similar properties in all directions, are called isotropic. Electrical steel prepared this way and presenting such properties is called non-oriented or non grain-oriented.

Norman Goss (1906-1977) patented in 1934 [19] and published in 1935 [20] his idea for grain oriented electrical steel which presents anisotropic magnetic properties. The production process involves hot and cold rolling of the steel in a controlled atmosphere during heating and cooling. During those processes anisotropy is formed in the material resulting in different magnetic properties in the rolling and transverse directions [8, 9]. Figure 3.2 shows the grain structure as presented by Goss in his patent (A) and as it is commonly available at present (2012) (B).

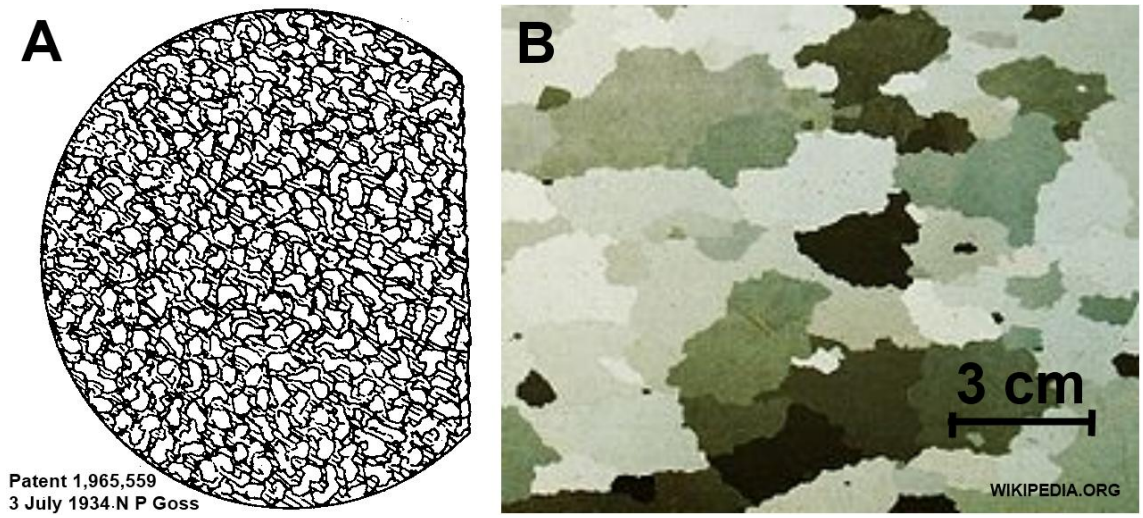

Figure 3.2 Grain structure in electrical steel. A – Presented in 1934 in a patent by GOSS and B – image obtained with removed coating with visible grains [19].

The production process includes many stages each responsible for different parameters of the final product. A schematic of a modern conventional grain oriented (CGO) electrical steel production line with all stages marked and labelled is shown in Figure 3.3.

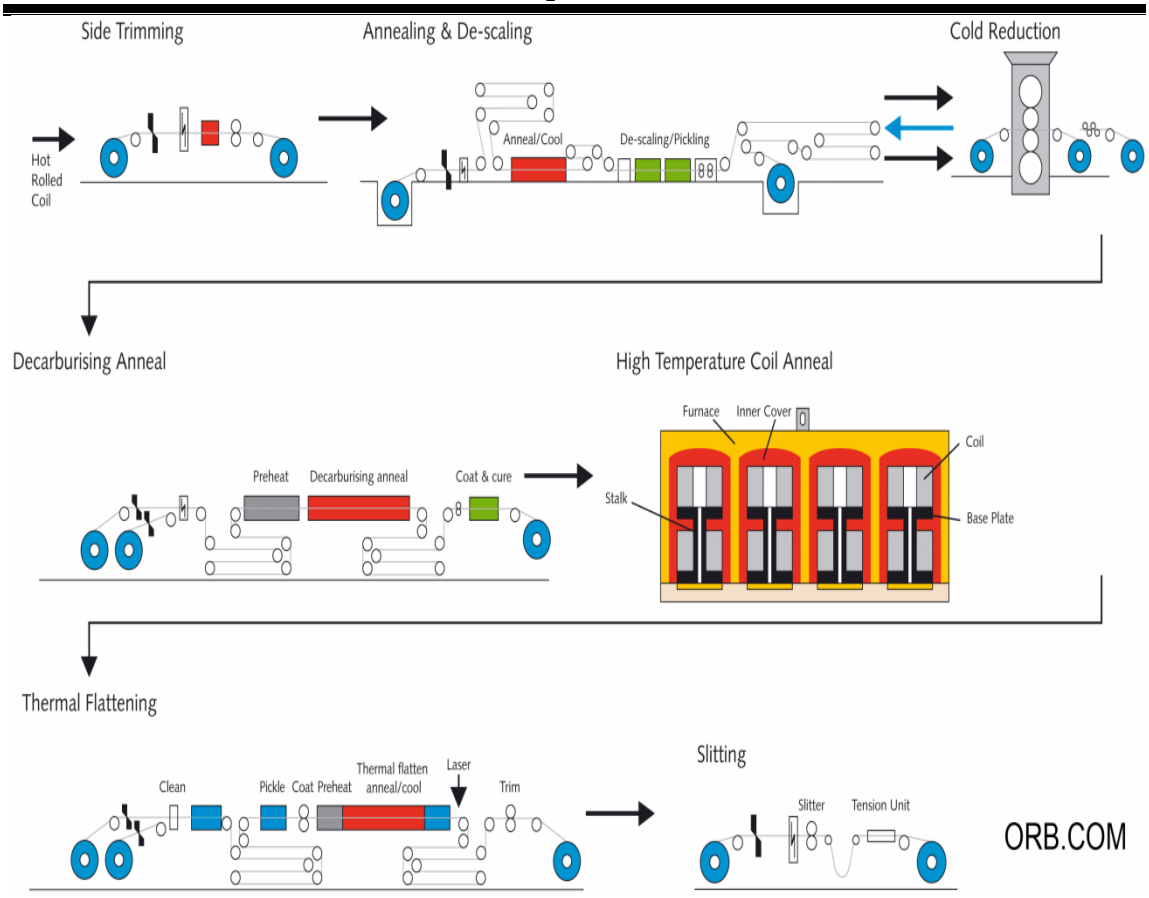

Figure 3.3 Schematic diagram of CGO electrical steel production line.

The hot rolled coil of 1.9 mm thick steel goes through trimming, annealing at 950°C, de-scaling and cleaning processes before it is cold rolled reducing the thickness to 0.6 mm ±0.1 mm after which the steel is annealed again to reduce the stress and dislocations created by first rolling after which it is cold rolled again reducing the thickness further to 0.23 – 0.50 mm. The decarburising anneal which is done in a nitrogen and hydrogen atmosphere at 840°C removes the unwanted carbon which causes aging of the material, causes the grains to re-crystallise and forms a layer of oxide on the surface of the steel. A magnesium oxide coating is applied as an anti-stick layer in the final step before annealing in the furnace in a dry hydrogen atmosphere at temperatures reaching up to 1200°C for four to five days to ensure that the full mass reaches the desired temperatures for a minimum of two hours. During this stage the main grain growth occurs and is inhibited by the manganese sulphide MnS which is

added during the steel making process before hot rolling. The next stage is removing the surplus of magnesium oxides and application of a phosphate coating to either side and annealing at 850°C to flatten the steel [21].

For HI-B electrical steel there is only one cold rolling process and the hot rolled steel contains aluminium nitride in place of MnS as a grain growth inhibitor.

The crystalline structure of Electrical steel as formed through the process described above can be characterised by two main parameters: angle of misalignment of elementary crystals against rolling direction and size of the grains formed in the steel. Initial developments proposed by Goss enabled Armco Steel Corporation to produce material with an average misalignment of 7°. The average grain size within this material was approximately 5 mm. Electrical steel characterized by these parameters is referred to as conventional grain oriented (CGO) steel. Improvement of those two parameters was made by Nippon Steel Corporation and named HI-B for commercial purposes. The misalignment of crystal structure to the rolling direction in HI-B material is 3° and the grain size reaches values up to 30 mm. [8, 22-26].

3.2 LAMINATION COATINGS

Electrical steel laminations are covered with coatings to increase electrical resistance between adjacent laminations as well as to provide resistance to corrosion and improve the properties of the steel. Coatings can be divided into inorganic, organic/inorganic mixtures and fully organic coatings [27]. Organic coatings are used for non oriented steel as they cannot withstand heat treatment. Inorganic coatings have inferior punchability properties but can withstand annealing. Typical coating thickness is 2 μm – 5 μm [15]. The thickness of the coating is significant as it influences the

stacking factor which is the ratio of the magnetic material within the cross sectional area of a core. Example types of coatings used on grain oriented electrical steels are based on: magnesium oxide mixed with colloidal silica forming a forsterite coating (SiO_2 + MgO), aluminium orthophosphate mixed with colloidal silica ($AlPO_4$ + SiO_2), aluminium orthophosphate mixed with colloidal silica and magnesium orthophosphate ($AlPO_4$ + SiO_2 + $MgPO_4$), and aluminium orthophosphate mixed with colloidal silica and chromium trioxide ($AlPO_4$ + SiO_2 + CrO_3) [21].

3.3 SILICON CONTENT (0-6.5% SILICON)

The silicon content in electrical steels has an effect on maximum permeability, saturation flux density, resistivity and Curie point. With rising silicon content, the saturation flux density drops, the Curie point drops and the resistivity rises while the peak permeability has a maximum value at 6.5% silicon content. The saturation flux density, Curie point and resistivity vary with composition only while maximum permeability is also dependent on crystal orientation, heat treatment (strain) and impurities within the material [28]. The variation of the above parameters with silicon content in electrical steel is shown in Figure 3.4 with the values given in CGS units. A balance of those parameters can be found between 0 % and 6.5 %. Typical grain oriented electrical steel contains around 3 % – 3.2% silicon. A higher percentage of silicon increases the brittleness of the material making it prone to be damaged during assembly and handling. The benefit of increased resistivity is the decrease in eddy current losses induced in the steel which narrows the hysteresis loop.

Another reason for adding silicon to electrical steel is to prevent the effects of aging of the material [29]. Other effects are reduction of anisotropy and

magnetostriction of the material. The anisotropy favours the alignment of magnetic moments along certain directions (crystal axes) and can restrict the movement of the moments. Magnetostriction is the change in dimensions of the material under magnetisation and is responsible for the generation of acoustic noise in electrical machine cores. Reduction of the magnetostriction also reduces the stress sensitivity of the material. The density of electrical steel is dependent on the silicon content and ranges from 7600 to 7850 kg/m^3; for 3% grain oriented steel it is 7650 kg/m^3.

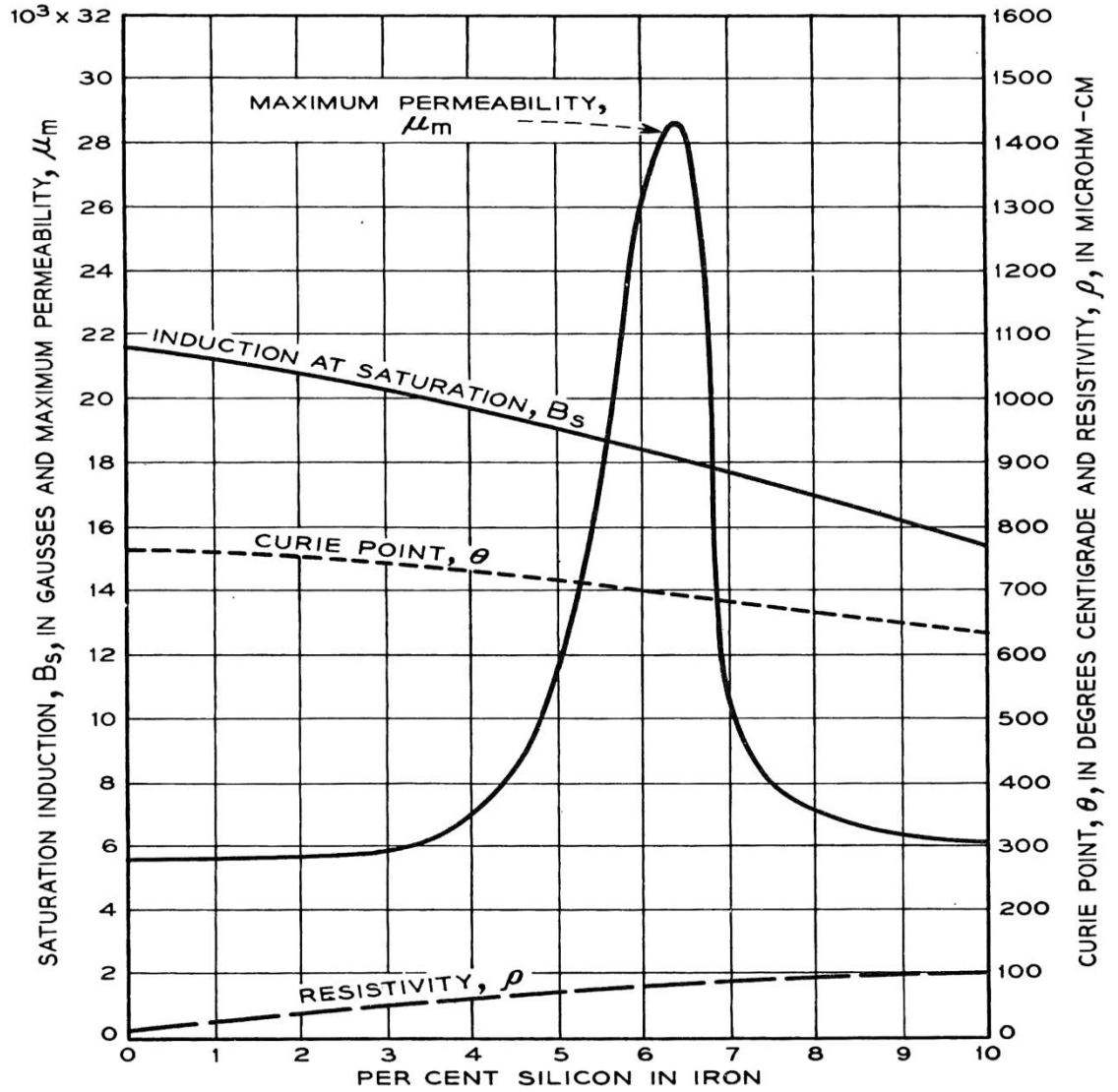

Figure 3.4 Variation of maximum permeability μ_m, saturation flux density B_S, Curie point θ and resistivity ρ with percentage content of silicon in electrical steel in CGS units as presented in [28].

3.4 EPSTEIN FRAME MEASUREMENT

An Epstein Frame or Epstein Square is a measurement setup for measuring magnetic properties of grain oriented and non-oriented electrical steel at frequencies up to 400 Hz. It is described in a British Standard BS EN 604404-2 [30]. A schematic of the measurement rig is shown in Figure 3.5 and it comprises primary and secondary windings arranged in a square and samples of electrical steel forming a core of an unloaded transformer. The strip sizes are 280-320 mm by 30 ±0.2 mm and the corner arrangement of the Epstein Square is a double lap joint as shown in Figure 3.5. A mass applying a force of 1 N can be placed on the corner region as shown in Figure 3.5by the green blocks to ensure the gap between the strips is minimised. BS EN 60404-2 standard sets the dimensions of the Epstein Square at 250 mm measured from the middle axis of laminations in the opposite sides of the square as shown in Figure 3.5. The specimen consists of multiples of four strips with minimum of 4 strips but not less than 240 g of material for strips of 280 mm length. The standard outlines the full procedure for this measurement including air flux compensation, power supply requirements as well as voltage and power measurement with main aspects described below.

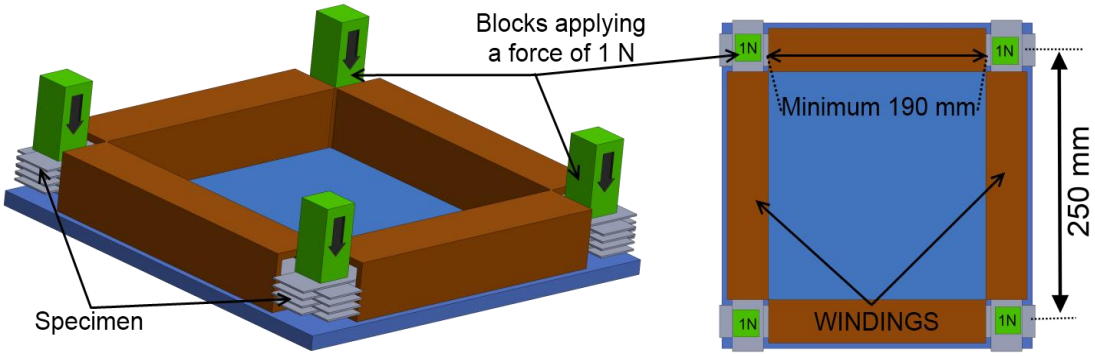

Figure 3.5 Schematic of the 25 cm Epstein Frame measurement rig.

The effective magnetic path length l_m of this arrangement is assumed to be equal to 0.94 m even though it is dependent on factors such as peak value and frequency of magnetisation as well as permeability and anisotropy of the material [12]. The active mass m_a, which is the mass of the material being magnetised in the measurement, is given in kg and calculated as in (3.1) where: l is the length of the specimen (280-320 mm) and m is the mass of the specimen in kg.

$$m_a = \frac{l_m}{4l} m \qquad \textbf{(3.1)}$$

In this project, Epstein frame data was used as reference for localised loss measurements and as basis of eddy current loss modelling. Epstein strips were cut from the same roll of material as the laminations to build the full size core used in the project by the same company who cut and assembled the core. Set of 24 laminations was used for the measurements which were taken at 50 Hz at peak flux density range 0.1 T – 1.9 T. LabView program with a data acquisition card and a power amplifier controlled the magnetising current signal and recorder the results. The process was as follows:

1. Connection of the acquisition card output to the amplifier.
2. Insertion of the Epstein strips into the frame: first into any slot, second into the slot parallel to it, the next two into slots perpendicular to the first two and so on until 24 strips are stacked.
3. Placement of the blocks on top of each corned if the stacked strips.
4. The LabView program controls the amplifier and increases magnetisation by a set interval using the resulting signals as feedback and adjusting the input signal to maintain sinusoidal magnetisation.
5. Results are saved in an excel format into a chosen folder.

3.5 ELECTRICAL MACHINES

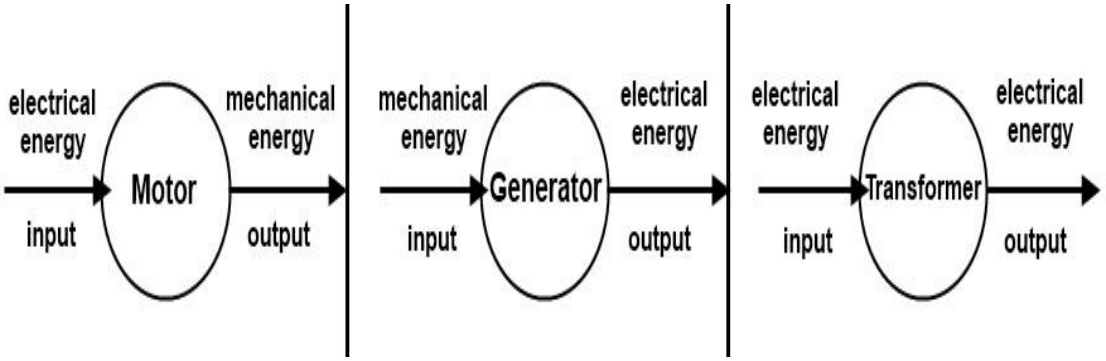

Figure 3.6 Energy conversion diagram of motors, generators and transformers.

An electrical machine is a device which converts electrical energy into mechanical energy (motors), or mechanical energy into electrical energy (generators) or changes the voltage of a current to a different value (transformers). All three types of conversion are illustrated in Figure 3.6.

3.5.1 Transformers

Transformers utilise Faradays law of induction to transport energy between two electric circuits by means of a magnetic circuit. There is no mechanical movement here which allows for high efficiency up to 99% [31]. Transformers consist of primary and secondary windings joined together through a magnetic circuit formed by a magnetic core [5]. Figure 3.7 shows a drawing of a single phase transformer with primary (red) and secondary (blue) windings, a ferromagnetic core (grey) and magnetic flux marked in green. From Faradays law of induction, changing voltage in primary winding generates a changing flux within the magnetic core; that flux flows through the secondary windings generating emf in them.

Efficiency of the transformer is defined as the ratio between the output power and input power as in

$$efficiency = \frac{Output\ Power}{Input\ Power} = \frac{Input\ Power - Loss}{Input\ Power} = 1 - \frac{Loss}{Input\ Power} \quad \textbf{(3.2)}$$

The efficiency of a real transformer, or any other machine for that matter, is therefore always less than 100% due to losses incurred within the transformer.

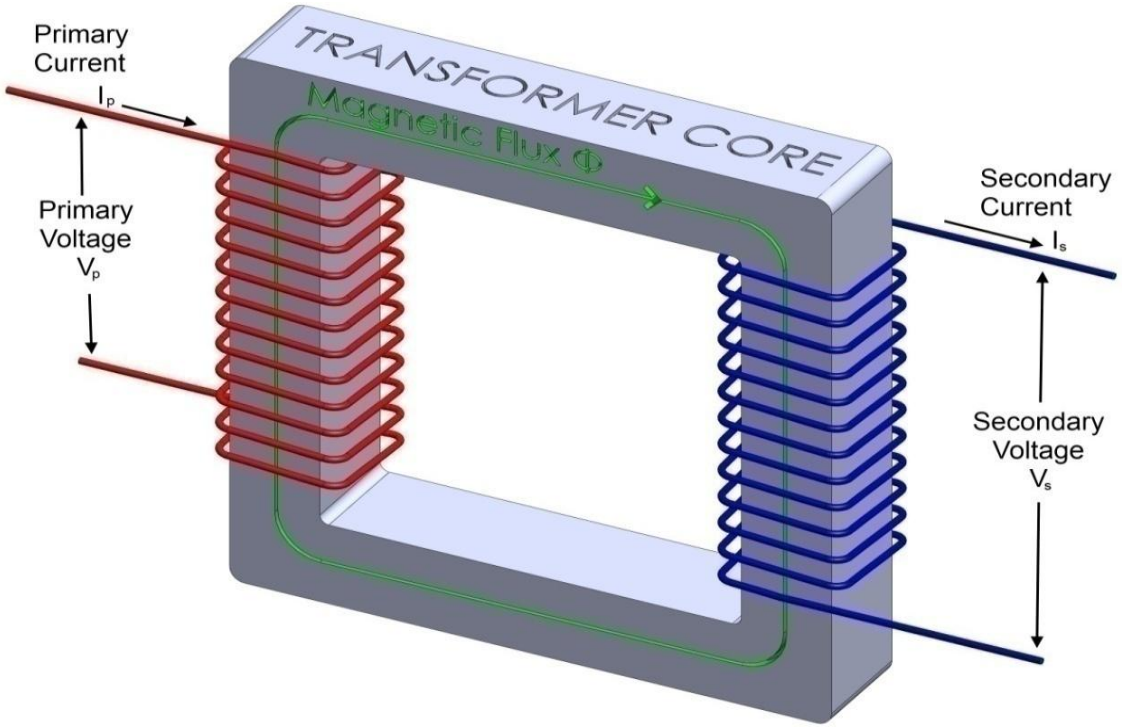

Figure 3.7 Single phase transformer with primary and secondary windings.

Figure 3.8 presents an equivalent circuit of an ideal transformer where it is assumed that input power is equal to output power without any losses. This means that the entire flux generated within the primary windings flows through the magnetic core without any leakage. .

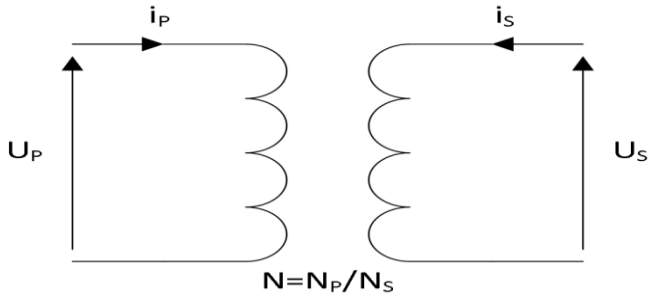

Figure 3.8 Equivalent circuit of a single phase ideal transformer.

The ratio of primary windings N_P and secondary windings N_S fully describes the ideal transformer defining the voltage ratio in the primary and secondary windings as

$$\frac{U_P}{U_S} = N \rightarrow U_P = \frac{N_P}{N_S} U_S \tag{3.3}$$

A real transformer is subject to copper losses associated with the windings. The copper losses dissipated in the form of heat are calculated as the resistance of the windings multiplied by the square value of the current flowing through those windings. The equivalent circuit of a single phase transformer based on an ideal transformer equivalent circuit with copper losses introduced is shown in Figure 3.9.

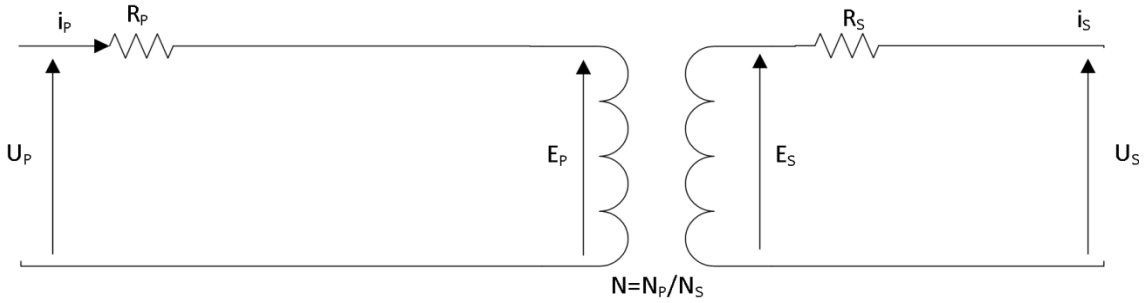

Figure 3.9 Equivalent circuit of a single phase transformer with copper losses added.

Practical transformers are subject to flux leakage which links either the primary winding or the secondary winding but not both windings. Some of the flux flows through the clamping, transformer cover or air which results in a small deviation of the primary and secondary voltage ratio due to the leakage flux not being part of the mutual coupling. Flux leakage can be represented in the equivalent circuit as reactances X_P and X_S of the primary and secondary windings respectively and are connected in series with the input and output of the transformer respectively as shown in Figure 3.10.

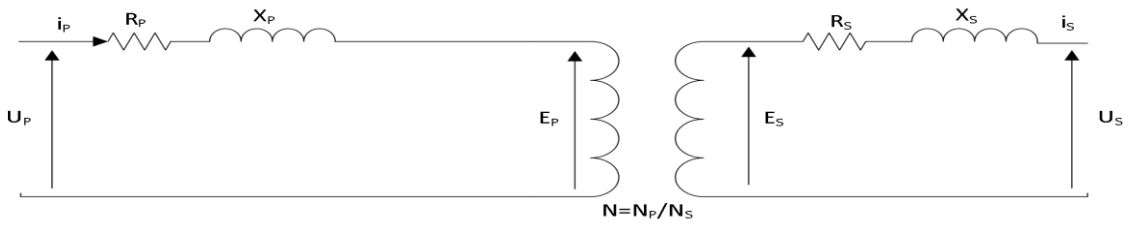

Figure 3.10 Equivalent circuit of a single phase transformer with copper losses R_P and R_S and leakage flux reactances X_P and X_S.

Iron losses comprising mostly hysteresis and eddy current losses can be represented as resistance R_C connected in parallel to the transformer as they are dependent on the square of the core flux density which in turn is proportional to the applied voltage. The iron losses are incorporated in the equivalent circuit as shown in Figure 3.11

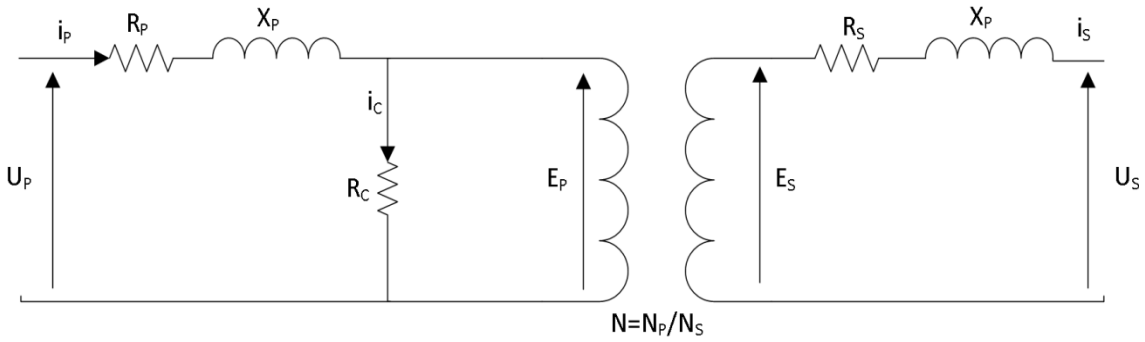

Figure 3.11 Equivalent circuit of a single phase transformer with copper losses R_P, R_S and leakage flux reactances X_P, X_S and iron losses added.

Since permeability is finite a current is required to maintain the core magnetised which is modelled as a magnetising inductance X_M in parallel with the iron losses branch. The representation of all the above phenomena is shown in the equivalent circuit of a non ideal single phase transformer shown in Figure 3.12. Note that the secondary parameters of the transformer have been transferred to primary side utilising simple arithmetic involving the windings ratio N.

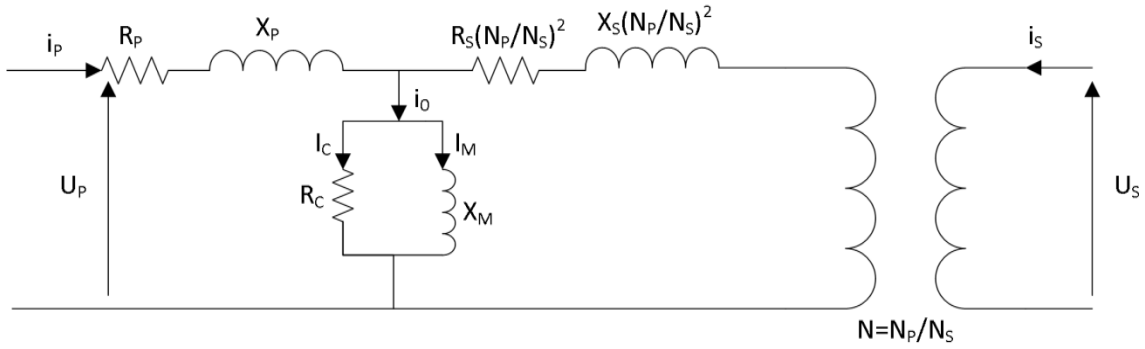

Figure 3.12 Equivalent circuit of single phase transformer based on an ideal transformer with copper losses R_P, R_S and leakage flux reactances X_P, X_S and iron losses and magnetising reactance eadded to the circuit.

Three phase transformers can be made either as a bank of three single phase transformers or a single core transformer with three or five limbs as shown in Figure 3.13.

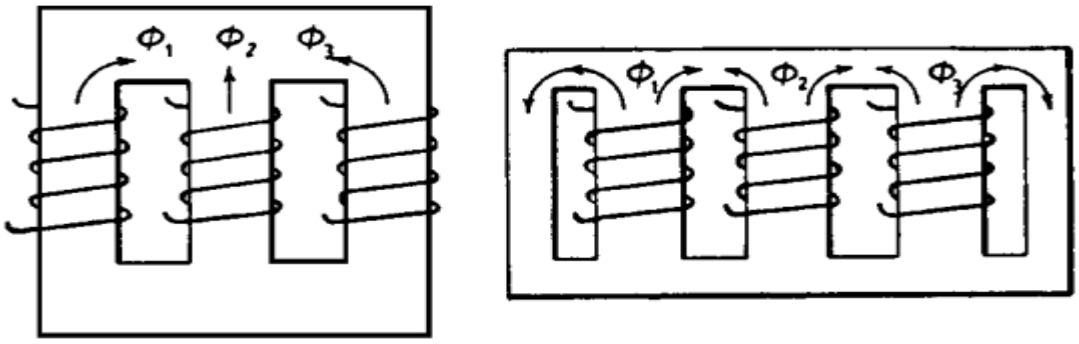

Figure 3.13 Schematic diagrams of a three phase core with three and five limbs.

The primary windings of a three phase transformer can be connected in a star or a delta arrangement. The same can be done for the secondary windings which results in four possible connections: star-star, star-delta, delta-star and delta-delta.

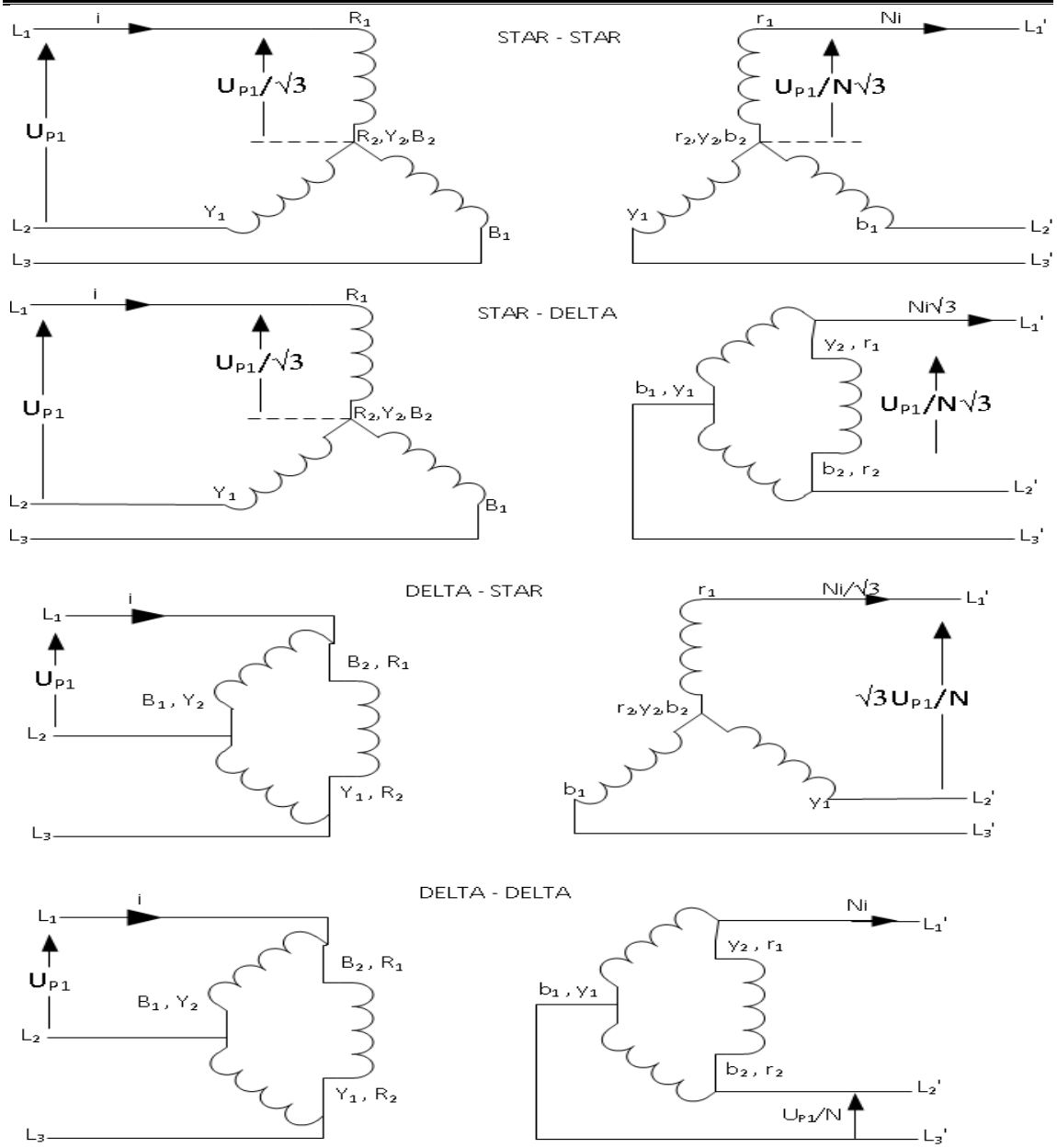

Figure 3.14 Three phase transformer connections. From top: star-star, star-delta, delta-star and delta-delta. For phases R. Y and B, capital letters are used for the primary windings and lowercase letters for the secondary windings.

The measurement of no load loss of the three phase transformer in the project was made using a NORMA D6000 power analyser utilising the three watt meter method, measuring all three currents supplied to the star connected primary windings and all three voltages of the star connected secondary windings. The procedure is described in section 9.3.

The total specific loss of a fully build transformer core is always larger than the nominal total specific loss of the material the core is built of. This is due to the additional losses as described in the non-ideal transformer model as well as to factors such as cut edge and bolt hole stresses affecting the effective permeability, T-joint and corner losses and more similar contributors. The ratio between the total specific loss measured by Epstein frame and the total specific loss of the final product is called a building factor. A typical building factor for a transformer core sized as the one used in this project is 1.1 – 1.4. These additional losses affect transformer cores, generator cores and motor cores in an analogous way.

Transformer cores can be used as air cooled or immersed in a tank with special oil. The purpose of the oil is to transport heat generated within the core and windings to the surroundings as well as to protect from moisture. It is generally a mineral oil with high dielectric strength, low viscosity and high flash point.

Chapter 4. **Sensors**

This chapter focuses on air coils, needle probes and thermocouple sensors needed in this investigation for measuring localised flux density and power loss of the electrical steel. The Rogowski coil described here was not used but is required to explain burr detection techniques in Chapter 5.

The flux density distribution within a transformer core is directly influenced by its design and assembly. Accurate measurement of localised core flux enables core designs to be optimised and any related assembly problems identified and rectified. Also, monitoring the local flux distribution while the core is in use can potentially give warning of developing core faults. Search coils wound from thin gauge wire are traditionally used to make localised measurements of flux density within experimental cores [32, 33]. The thinnest wire which can be practically used is around 20 μm diameter which creates interlaminar air gaps of more than 40 μm between adjacent laminations for a twisted pair. This, as well as the process of drilling holes through the lamination, introduces mechanical stress and local changes to the magnetic properties of the steel, affecting the local flux distribution.

4.1 AIR COIL

A commonly used sensor for measuring magnetic induction is an air coil also called a search coil, pickup coil or magnetic antenna [33]. Faradays Law states that the emf induced in an electrical circuit is proportional to the rate of change of flux through that circuit and is given by

$$\text{emf} = -\text{N}\frac{\text{d}\Phi}{\text{dt}} = -\text{NA}\frac{\text{dB}}{\text{dt}} = -\mu_0\text{NA}\frac{\text{dH}}{\text{dt}} \quad \textbf{(4.1)}$$

where ϕ is magnetic flux, N is the number of turns of coil through which the flux flows, dϕ/dt is the rate of *c*hange of flux, A is the cross sectional area and B is the flux density.

For a flux density given as a series in the form

$$B(t) = \sum_{r=1} a_r \sin(r\omega t + \phi_r) \quad \textbf{(4.2)}$$

B reaches a peak value at time λ

$$B(\lambda) = \hat{B} = \sum_{r=1} a_r \sin(r\omega\lambda + \phi_r) \quad \textbf{(4.3)}$$

At time π/ω, B will be given by

$$B\left(\lambda + \frac{\pi}{\omega}\right) = \sum_{r=1} a_r \sin(r\pi + r\omega t + \phi_r) \quad \textbf{(4.4)}$$

If the flux waveform contains only odd harmonics which means that r is always odd we get

$$B\left(\lambda + \frac{\pi}{\omega}\right) = -B(\lambda) \quad \textbf{(4.5)}$$

Therefore the positive and negative peaks are separated by half a period

$$\frac{dB}{dt} = \sum_{r=1} a_r r\omega \cos(r\omega t + \phi_r) \quad \textbf{(4.6)}$$

dB/dt will have zeroes when $B = \hat{B}$ that is t = λ+nπ/ω

The mean value of dB/dt taken over half a period is

$$\left(\frac{dB}{dt}\right)_{av} = \frac{\omega}{\pi}\int_{\lambda}^{\lambda+\frac{\pi}{\omega}} \sum_{r=1} a_r \cos(r\omega t + \phi_r)$$
$$= \frac{\omega}{\pi}\sum_{r=1} a_r[\sin(r\omega t + \phi_r) - \sin(r\pi + r\omega t + \phi_r)] \quad \textbf{(4.7)}$$

Since r is only odd this reduces to

$$\left(\frac{dB}{dt}\right)_{av} = \frac{2\omega}{\pi}\sum_{r=1} a_r \sin(r\omega t + \phi_r) = \frac{2\omega\hat{B}}{\pi} \quad \textbf{(4.8)}$$

From (4.1) and (4.8) we get

$$V_{av} = NA\left(\frac{dB}{dt}\right)_{av} = NA\frac{2\omega\hat{B}}{\pi} = 4\hat{B}ANF \quad \textbf{(4.9)}$$

For a sinusoidal waveform $\hat{V} = \sqrt{2}V_{rms} = \frac{\pi}{2}V_{ave}$ hence

$$V_{rms} = \frac{\pi}{2\sqrt{2}}V_{ave} = \frac{2\pi}{\sqrt{2}}\hat{B}ANF \approx 4.44\hat{B}ANF \quad \textbf{(4.10)}$$

Equations (4.9) and (4.10) are used for flux density measurements in magnetic materials.

4.2 ROGOWSKI COIL (ROGOWSKI – CHATTOCK COIL)

The Rogowski-Chattock coil is a helical coil, usually wound on a flexible former which can be wrapped around a conductor as it is shown in Figure 4.1. The principle is that the current flowing through the conductor generates a magnetic field around itself and that field is being sensed by the Rogowski coil. The Rogowski coil can be used for

current detection and measurements in which case, the emf induced in the Rogowski coil needs to be integrated in order to show the sensed current waveform [33-36].

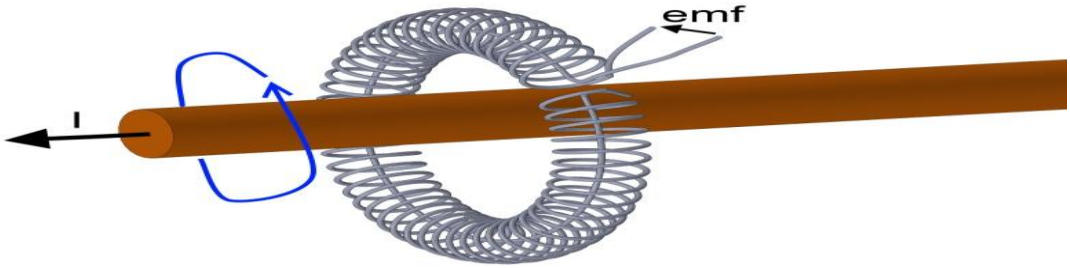

Figure 4.1 Rogowski-Chattock coil wrapped around a conducting wire.

4.3 NEEDLE PROBE TECHNIQUE

The needle probe technique as presented in Figure 4.2, introduced by Werner in 1959 [37], is used to measure local flux density. It is a non destructive method which is a significant advantage over search coils. It allows multiple measurements to be made with no sample preparation. The method is based on forming a half turn air coil as described in section 4.1 using the sample as part of the circuit.. The method is applicable for thin sheets of electrical steel. The voltage measured by the two probes is equal to half of that acquired from a search coil wound across the same width of material as in (4.12) [33, 38]. The schematic of the needle probe technique compared to the search coil is shown in Figure 4.2. The two methods measure flux density over the same width d of the sheet of material of thickness t.

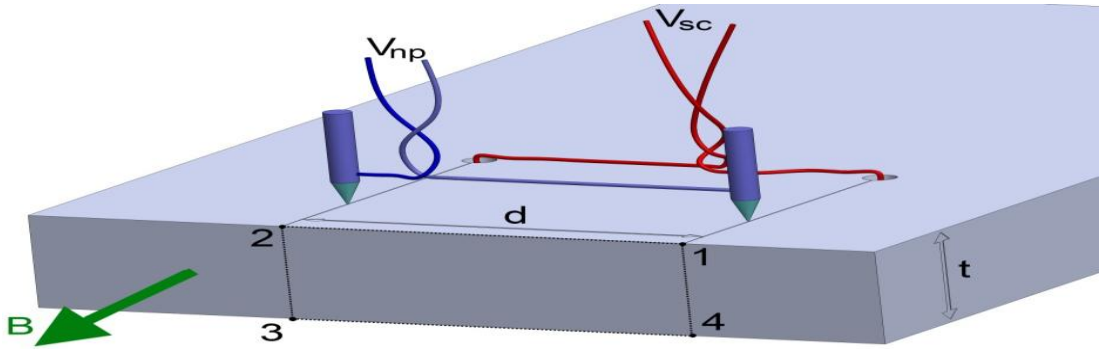

Figure 4.2 Schematic of a non destructive needle probe technique in comparison to a destructive search coil measurement method. Both techniques measure flux density within the material of thickness t across width d.

From Faradays law equation applied to Figure 4.2 where S is the boundary of the surface A enclosed by corners 1, 2, 3 and 4 the voltage induced along S can be written as a sum of four voltages: V_{12}, V_{34} across width d, and V_{23}, V_{41} across thickness t. It can be assumed that $V_{12}=V_{34}$ and $V_{23}=V_{41}$ which leads to (4.11) where the first component is the emf induced in the boundary S due to change in flux and the second component is a voltage due to the vertical component of the electric field.

$$V_{12} = \frac{1}{2}\int_A \frac{\partial B}{\partial t} \cdot dA - V_{14} \tag{4.11}$$

Voltage V_{np} measured by the needle probes also includes emf induced within the circuit above the steel by any flux flowing through the air. However, this can be minimised and comparable to same source of error in threaded search coils. Assuming that thickness of the lamination is small compared to width d, voltage V_{14} can be neglected. Hence the voltage measured by the needle probes is given by (4.12) [33, 38].

$$V \approx \frac{1}{2} td \frac{dB}{dt} \tag{4.12}$$

4.4 TEMPERATURE MEASUREMENTS

In static temperature measurement the temperature of the measured medium is constant while in dynamic measurements the temperature is changing and the temperature reading is subject to a time delay illustrated in Figure 4.3 where the red traces show temperature change in the environment and blue is the measured value. The time delay before the measured value reaches 63 % of the actual value is τ. It is usually accepted that the measured signal matches the actual value after five times the value of τ [39]. This delay plays an important role in the results interpretation in the initial rate of rise of temperature method described in section 4.4.2 below.

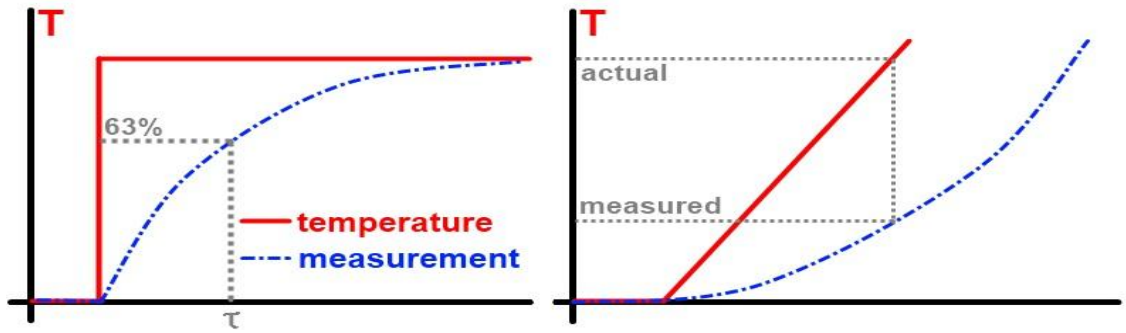

Figure 4.3 Delay in temperature measurement for step and linear change.

There are many temperature measurement devices working on basis of:

- Expansion or contraction of a substance with change in temperature (mercury or alcohol thermometer)
- Thermoelectric voltage (thermocouples)
- Change in electrical resistance of a material with temperature (Resistance Temperature Detectors, thermistors)
- Change in electromagnetic wave properties with temperature (infrared photography, pyrometry) [39]

4.4.1 Thermocouples

The *thermoelectric effect* is a phenomenon in which a temperature difference creates an electric potential or an electric potential creates a temperature difference. The Seebeck effect is a thermoelectric effect in which temperature is converted into current. Seebeck effect was first observed by Seebeck in 1821 and it states that a current will flow within a loop made of two dissimilar materials if there is a temperature difference between the two junctions of the loop [39]. This effect is illustrated in Figure 4.4.

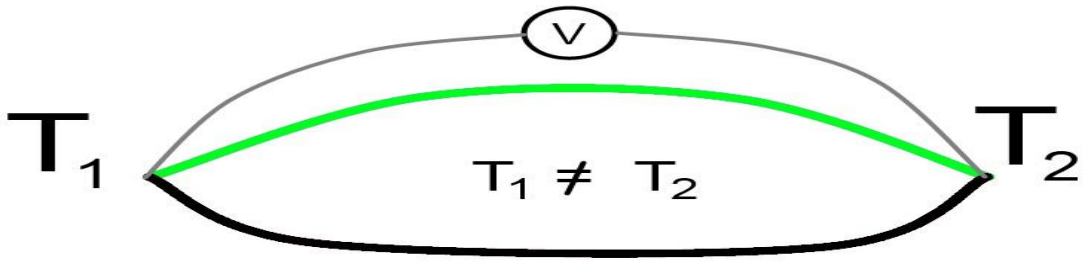

Figure 4.4 Seebeck effect. Two dissimilar wires connected in two junctions at temperatures T_1 and T_2.and voltage V observed between the two junctions.

This phenomenon can be explained on an atomic level. Every conductive material has free conducting electrons that are moving freely across the material. If a material is heated, the electrons gain kinetic energy. If the conductive material is in a form of a long cylinder such as a wire and one end is heated, some of the electrons on the heated end diffuse into the cold end. In this way a gradient of electrons forms within the material which means that an electric potential is created between the hot and cold ends of the material. The electric field created by the two dissimilar concentrations of electrons makes the electrons move back towards the positive charge region – the hot end. The two phenomena – electric field and kinetic energy reach an equilibrium state in which a potential difference between the hot and cold ends of the material is constant. In order to measure this potential, without the problem of creating an identical effect on the leads of the potentiometer, a second conductor with a different electrical conductivity is coupled. The concept is that for two conductors of different conductivity the equilibrium states described above are different and the electrical potentials created on each of them are different as illustrated in Figure 4.5[39, 40].

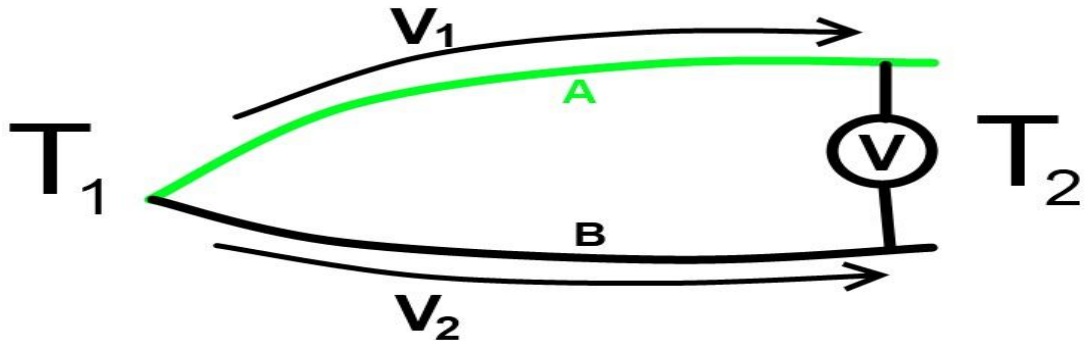

Figure 4.5 Thermoclectric effect in two dissimilar materials.

If the two materials are electrically connected at the end in temperature T_1, the difference between their thermoelectric responses V_1 and V_2 can be measured as V. Thermocouples are classified based on the two types of materials used to form them as shown in Table 4.1 [41].

Table 4.1 Thermocouple types with operation ranges and sensitivity [41]

Type	Materials	Range °C	µV/°C
R	Platinum -13 % rhodium platinum	0 to +1100	~10
S	Platinum -10 % rhodium platinum	0 to 1600	~10
B	Platinum -30 % rhodium platinum	200 to 1700	~10
J	Iron/copper-nickel	-40 to 750	55
T	Copper/copper-nickel	-185 to 300	43
E	Nickel-chromium/copper-nickel	0 to 800	68
K	Nickel-chromium/nickel-aluminium	0 to 1100	41
N	Nickel-chromium-silicon/nickel/silicon	0 to 1100	39

4.4.2 Initial rate of rise of temperature method for local loss measurement.

The initial rate of rise of temperature method is based on the fact that if a matter is generating heat, the initial rate of rise of temperature at a point is directly proportional to the heat generated at that point [42]. The thermal energy generated in an elementary mass which is isolated increases the temperature of that mass. If this mass is not isolated, the dissipation of energy to the surroundings reduces the temperature. However, energy generation within the mass is almost instantaneous while energy dissipation requires some finite time. Therefore, observing the initial temperature increase of the mass one can deduce the energy generated within that mass, as it is directly proportional according to heat exchange equation.

This means that the measurement of temperature at a specific location starting at the moment when heat generation starts and resulting in a temperature curve as shown in Figure 4.6 provides enough information to calculate the rate of heat generation at that point. This method can be used for localised measurements of specific loss in silicon steel [42-46].

In perfect adiabatic conditions, the calculation of power loss at a point is made using (4.13) where c_P is the specific heat capacity of the material, T_0 is the initial temperature at the point of measurement, T is the instantaneous temperature at the point, t is the time when measurement of T takes place and t_0 is the initial time.

$$P = c_P \frac{T - T_0}{t - t_0} \tag{4.13}$$

The specific heat capacity c_P [J/kg K] of any alloy can be calculated using the Kopp-Neumann law presented in (4.14) where N is the number of alloys, C_i and f_i are the specific heat capacity and the mass fraction of i-th component in the alloy. For 3.2% silicon steel $c_P = 461 \left[\frac{J}{kg\,K}\right]$.

$$C_P = \sum_{i=1}^{N} (C_i \cdot f_i) \tag{4.14}$$

In non-perfect adiabatic conditions, some of the heat generated at a point diffuses in time from that point and thus changes the temperature. The rate of heat diffusion can be found by using the cooling curve shown in Figure 4.6 and curve fitting. Equation (4.13) evolves to (4.15) where K is the heat transmission coefficient [47].

$$P = c_P \frac{T - T_0}{t - t_0} + K(T - T_0) \tag{4.15}$$

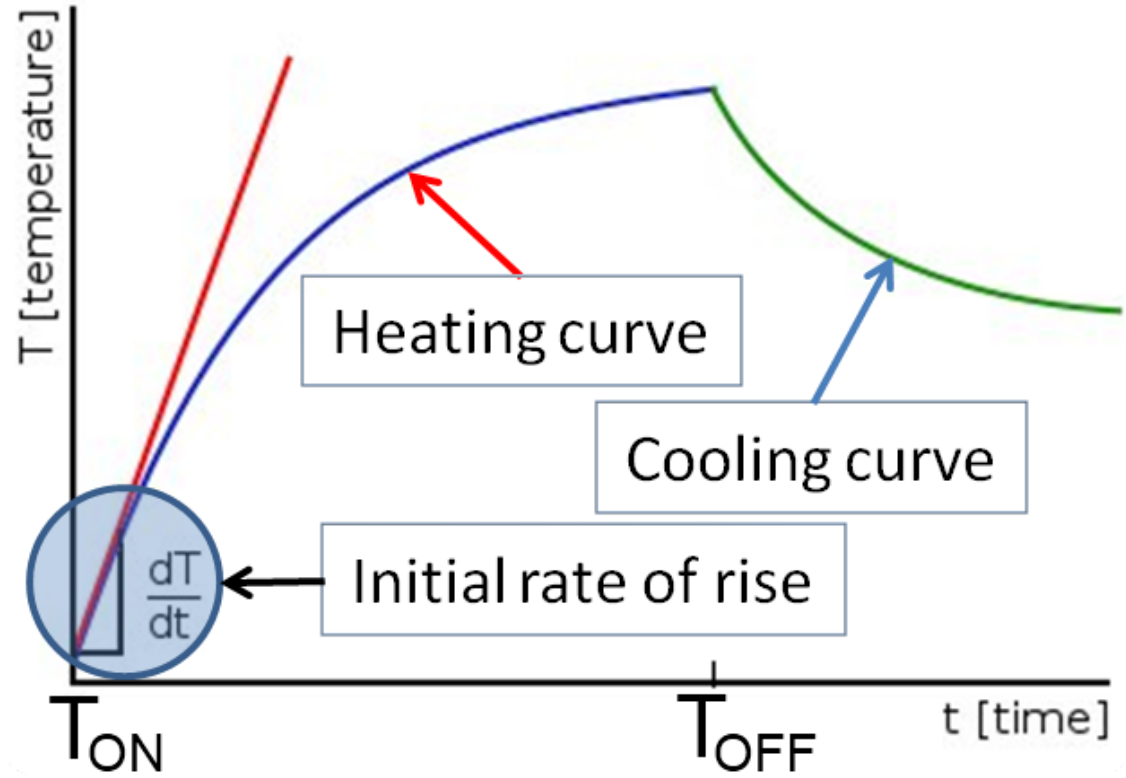

Figure 4.6 Example trace of temperature measured for the initial rate of rise of temperature method with switch on and switch off moments labelled.

4.5 THIN FILM SENSORS FOR MEASUREMENT OF FLUX DENSITY AND LOSS IN ELECTRICAL STEEL

The flux density distribution within a transformer core is directly influenced by its design and assembly. Accurate measurement of localised core flux enables core designs to be optimised and any related assembly problems identified and rectified. Also, monitoring the local flux distribution while the core is in use can potentially give warning of developing core faults. Search coils as described in section 4.1 wound from thin gauge wire are traditionally used to make localised measurements of flux density within experimental cores. The thinnest wire which can be practically used is around 20 μm diameter which creates interlaminar air gaps of more than 40 μm between adjacent laminations in case of a twisted pair wires. Wire connection procedures and bending of

the wires can increase this value above 50 μm [48]. This, as well as the process of drilling holes through the lamination, introduces mechanical stress and local changes to the magnetic properties of the steel, affecting the local flux distribution.

Basak, Rowe and Anayi proposed that thin film techniques such as physical vapour deposition (PVD) can be used for production of flux density sensors and temperature sensors [43-46, 49]. The flux density sensors in their work utilised the same principle as search coils described in section 4.1. Holes were drilled in the lamination, a layer of zinc sulphide (ZnS) was deposited to insulate the drilled holes and aluminium was deposited on both sides of the lamination such as to create thin film conductive loops. The temperature sensors in the form of type K thermocouples were deposited using chromel and alumel deposited in two steps with an overlap forming the junction of the thermocouple. This process of producing thin film search coils required five time consuming depositions each taking several hours. However, multiple sensors can be produced at the same time. The holes drilled in the samples in the process of producing the flux density sensors introduce a significant amount of stress to the laminations [50] contrary to the purpose of using thin films to reduce stress around the sensor. The experimentation was done on a single phase core built of 260 layers of 0.27 laminations 70 mm by 260 mm in size and a stator core of 152 mm outer diameter comprising laminations 0.64 mm thick. They reported the measurements of the core at five peak flux densities between 0.5 T and 1.7 T with the discrepancy between the thin film sensors and equivalent enamelled copper wire search coils ranging between 6.9 % and 13.6 % which is a result acceptable for assessing the usability of these sensors for a particular application. Thin film temperature sensor production was reported as successful; however, there was no report of the results in either of the cores tested within the references quoted here.

Pfutzner presented a proposal for thin film flux density measurement utilising the needle technique as described in section 4.3 [48]. He reports using silicon dioxide SiO_2 as insulation layer before depositing the thin film sensors onto small laminations. On laminations of 1 m in length a manual metal foil plating is reported supplemented by conductive metal paint. The achieved thickness quoted in the paper is an order of 10 μm which is considerably higher than in works of Basak, however, Pfutzner reports further that this thickness was acceptable in his investigation. Thermocouple sensors were reported as not suitable for the purpose of loss measurement. However, no detail is given as to this measurement method. Instead, the author discusses other options of determining the losses such as recalculation of classical eddy current losses from the reading of the needle sensors.

4.6 PHYSICAL VAPOUR DEPOSITION

PVD – Physical Vapor Deposition is a process in which layers of materials are deposited, atom by atom, onto the substrate under vacuum. The layer thicknesses vary from a single atom to one millimetre. Layers can be deposited on top of each other. Various PVD techniques such as thermal evaporation, e-beam evaporation, DC sputtering, DC Magnetron sputtering and RF sputtering are feasible for thin film creation. Thermal evaporation was chosen for this investigation because it could be set up in a laboratory environment and it could be adapted to deposit onto large samples.

4.7 THERMAL EVAPORATION

Thermal evaporation occurs in vacuum which ensures the particles have a long mean free path and hence move mostly in straight lines from the source – crucible to the substrate on which the thin film is created. A typical schematic of a thermal evaporation physical vapour deposition system is shown in Figure 4.7.

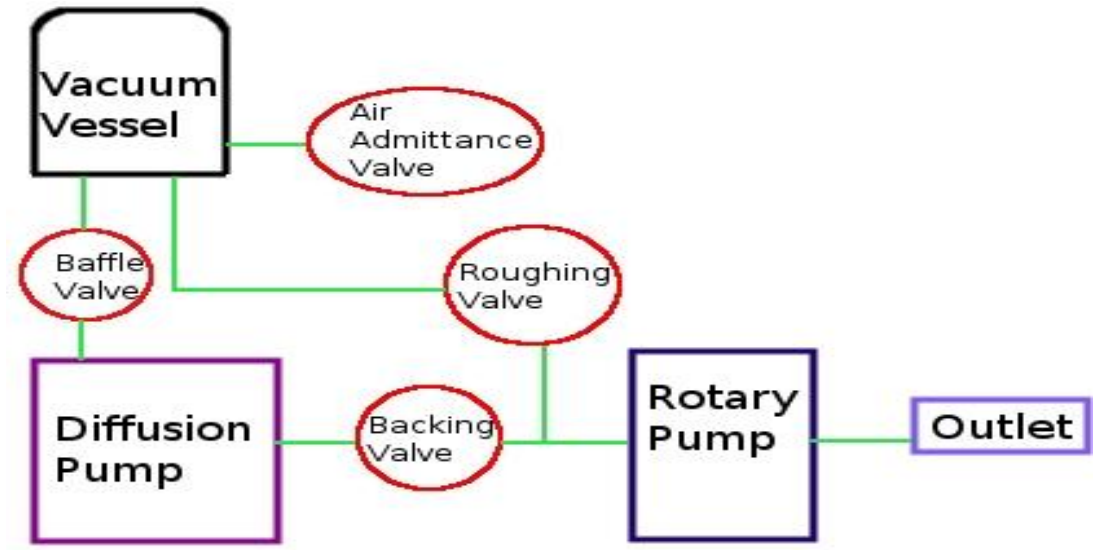

Figure 4.7 Schematic of a two pump Physical Vapor Deposition system.

It is based on two pumps working together to produce a vacuum in the vessel. The basic operation of this system is as follows:

1. The samples and evaporation materials are mounted within the vacuum vessel and the vessel is sealed. The diffusion pump is chilled.
2. With the roughing valve open and all the other valves closed, a small vacuum of about 0.1 Torr is created in the vessel. This process is usually called roughing. It assures that the whole system is brought to the same, initial level of vacuum before the oil pump is turned on.
3. The roughing valve is closed and the backing valve opened and vice versa repeatedly in as many steps as required until the vacuum measured within the whole system is equal or lower than 0.1 Torr and uniform throughout.
4. With equal pressures in the whole system, the roughing valve is shut and the backing valve is opened. The diffusion pump is switched on and allowed to heat up for about 30 – 40 minutes.
5. With a vacuum in the whole system of 0.1 Torr or less, the roughing valve shut and the backing valve open the baffle valve is opened and the vacuum in the vessel starts to build.
6. The evaporation procedure is carried out by passing a high current through the evaporation boat on which the evaporant material is located.
7. A cooling period is necessary before the baffle valve is shut and the air admittance valve is opened to allow the sample to be removed.
8. Any vacuum system should always be kept under vacuum. Hence, after removing the sample from the vessel, the vessel is resealed and the roughing procedure described in steps 2 and 3 above is repeated before closing the system down.

Chapter 5. **Burrs in electrical machine cores**

Burrs are unwanted fragments of material which remain attached to electrical steel strip after machining, cutting or accidental damage. Burrs often occur on the edges of electrical steel laminations that are cut from large strip or sheets into shapes ready for building a specific electrical machine core. An example of a guillotine cutting operation is shown in Figure 5.1 where the electrical steel lamination is placed on a table and a moving blade drops onto the lamination cutting it to the desired size and leaving the usable part on the guillotine table while the cut off drops.

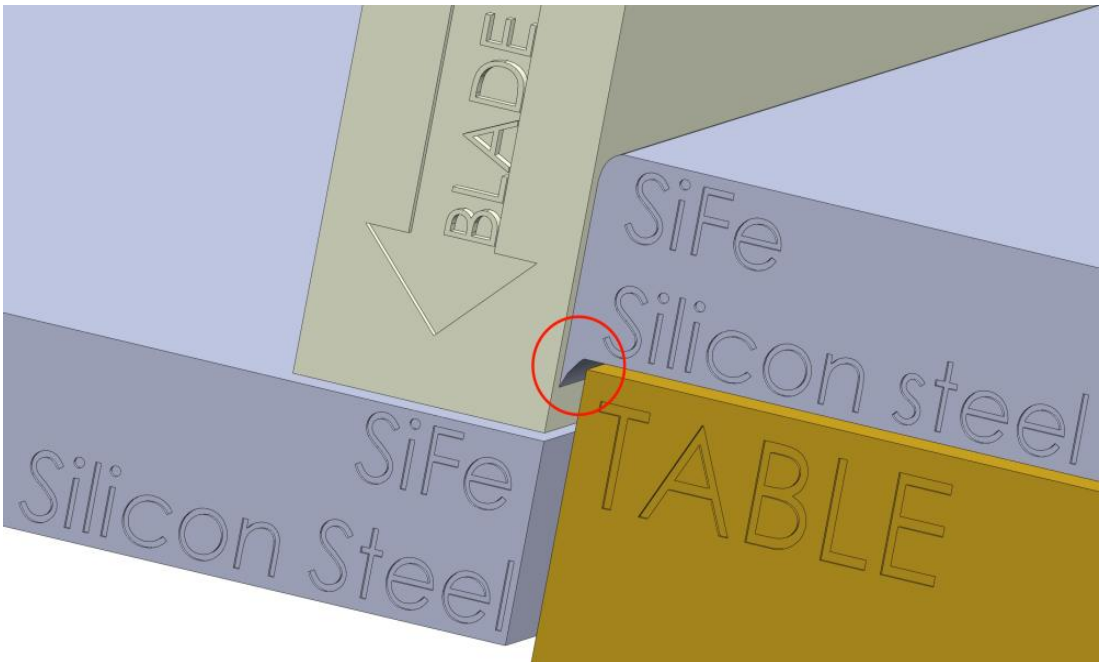

Figure 5.1 Schematic example of how a burr (in red circle) is created on the edge of an electrical steel lamination. (Not to scale).

Burrs usually occur as a sharp curved edge pointing in a direction of the blade movement while cutting the material. Their size depends on the type and wear of the cutting tool as well as on the brittleness of the material being cut and lubricant used for cutting.

5.1 CAUSES OF BURRS AND SHORT CIRCUITS

Burrs in electrical steels are important because they can create short circuits between adjacent laminations which in turn increase core loss. Burrs are not the only cause of short circuits in laminated cores. Coating failure can create large area electrical connections between the surfaces of adjacent laminations, winding failures can cause short circuits between several different locations in the core and accidental damage or foreign objects may create random connections. Various production processes and random causes that could be possibly encountered in electrical machine production industry are listed below.

5.1.1 Shearing operations

All forms of mechanical cutting without the use of melting or burning or without producing any chips are called shearing. Shearing operations can be classified based on the blade shape. Typically shearing operations are used for preparation of materials from 0.025 mm to 20 mm thick [51].

When the blade in a shearing operation is straight the process is simply referred to as shearing. As an example burrs created on grain oriented electrical steel by a newly sharpened blade of a shear guillotine are less than 10 μm in height [52].

Slitting or roll slitting as shown in Figure 5.2 is often used for cutting coils of electrical steel into narrower width coils. The blades are two cylindrical rolls whose circumferences intersect in such a way that one of the rolls rib fits into the other rolls grove. This operation is continuous fast and very economical. The resulting width of the cut coils is very precise.

Figure 5.2 Roll slitting of electrical steel (photo from www.teampacesetter.com).

5.1.1.a Punching

Slitting to final shape is often supplemented by punching holes in the laminations to operate as location guides for use during core assembly or as cooling ducts in the final core assembly. Punching and burrs occurring during the process are illustrated in Figure 5.3. Here the electrical steel lamination (Workpiece) is sandwiched between two plates with a punch dropping through openings in both plates. A hole in the shape of the punch is produced but a burr is likely to occur along the circumference as indicated by red arrows in Figure 5.3.

The burr size produced in a shearing process for a given material varies depending on the machining technique as well as quality and wear of the cutting tools [9]. Figure 5.4 shows how burr size in grain oriented electrical steel can grow with blade wear. Both, height of the burr and the stress zones created by the cutting process increase with the number of times the blade is used. After 2000 cuts the burr is still not visible and harmful magnetic effect disappears after stress relief annealing while after 20000 more

cuts the burr height and stress zone increase dramatically and the harmful influence of the burr remains even after stress relief annealing and deteriorates further after further cuts [9].

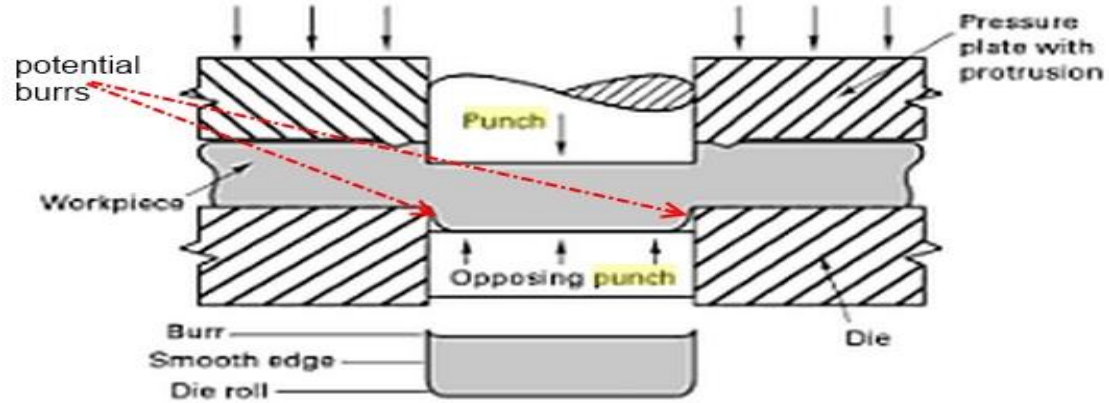

Figure 5.3 Schematic of steel lamination punching with possible location of burrs shown by red arrows [51].

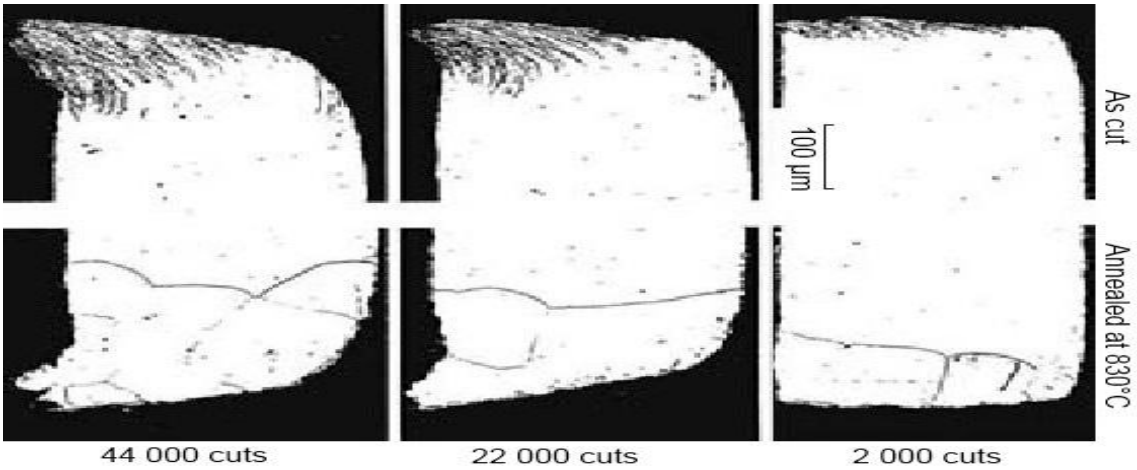

Figure 5.4 Sections through a cut edge of grain oriented electrical steel showing variation of burr height with age of the cutting blade. Burrs as cut are shown in the top row and after annealing at the bottom (Figure taken from [9]).

5.1.2 Electric discharge machining

Electrical discharge machining (EDM) is based on material evaporation occurring during the spark heating of the surface of the electrical steel and it does not produce any burrs; however, it can incur metallurgical change in the steel, it is expensive and very slow compared with most other processes used for cutting electrical steel. EDM uses precisely controlled sparks created between an electrode and the electrical steel so it is classified according to the type of electrode used. When the electrode is a continuous

wire it is called wire erosion. A general schematic diagram of EDM is shown in Figure 5.5 [53]. An electrode and the sample are connected electrically and there is a gap filled with a dielectric between them. A spark is created between the electrode and the portion of the electrical steel when the voltage is high enough to break the insulation of the dielectric.

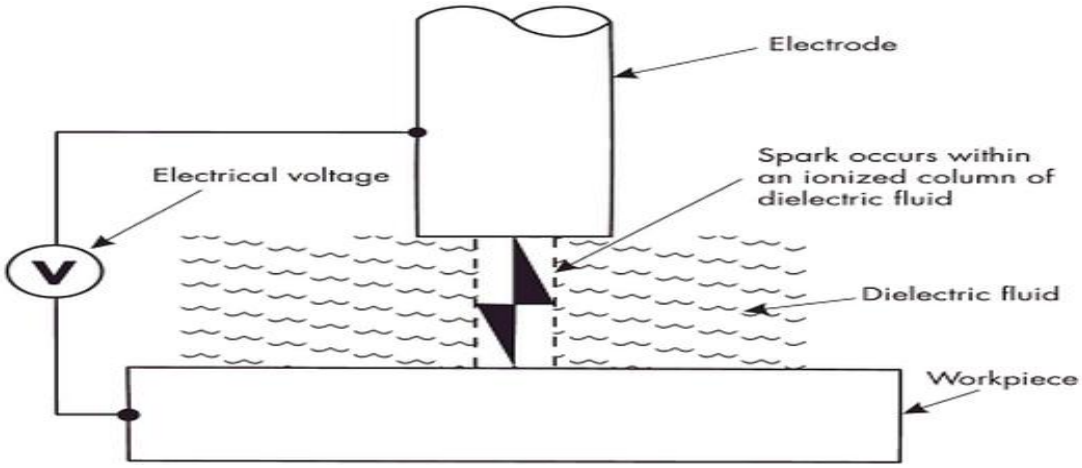

Figure 5.5 Schematic diagram of electric discharge machining (EDM) [53].

In the case of the wire erosion the electrode consists of a continuous wire as shown in Figure 5.6 where the electrical steel sample is fixed and the wire electrode moves along the X Y axis but there are also machines with fixed wire electrode position and moving the sample along X Y axis.

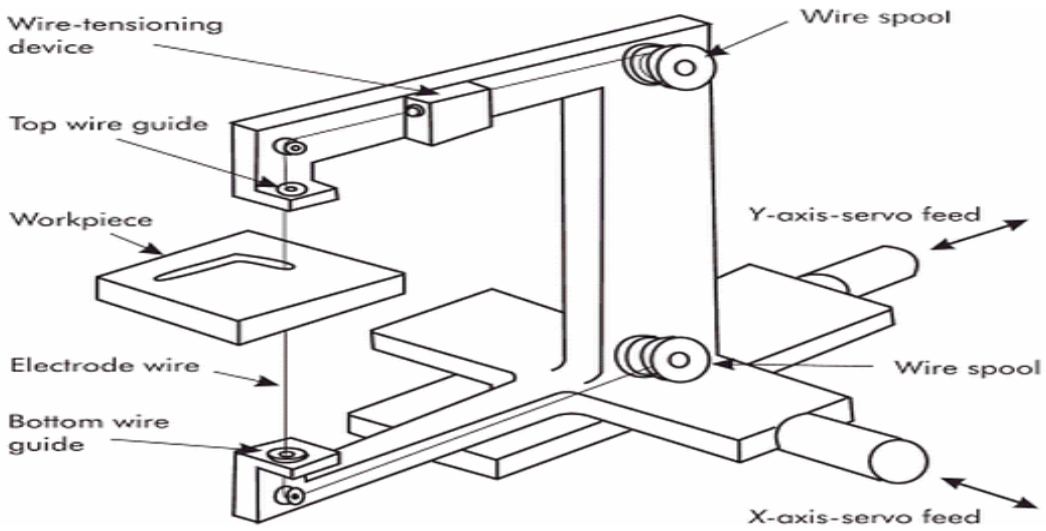

Figure 5.6 Diagram of wire erosion type of electric discharge machining [53].

5.1.3 **Laser cutting**

Laser cutting is one of the methods used to cut electrical steel. It bases on focusing a beam of light heating up the material above the melting point and evaporating it. YAG and CO2 laser cutting methods can be used. They both generate concentrated beams of light. The difference is in the wavelength of the beam used (YAG – 1.064 μm, CO2 – 10.64 μm) which has an effect on reaction of the two types of laser on different materials being cut. Other parameters differing between the two laser cutting techniques include thermal efficiency, heat transfer and minimum and maximum power output. The dimension tolerance of laser cutting is within 10 μm to 25 μm depending on the thickness of the material being cut. Stream of gas can be used to cool down the material just after the laser cuts. It also helps remove any residue from the cut.

5.1.4 **Coating and winding failures**

Damaged coating of electrical steels can cause electrical contact over a large surface area hence eddy currents can occur over a large core volume. Figure 5.7 shows a schematic diagram of a coating insulation failure and eddy currents associated with the short circuited laminations. One small and one large electrical contact are marked by thick red lines. This arrangement of electrical contact between the laminations allows eddy currents to flow between the two laminations within the large short circuited area as well as between the two different short circuited areas.

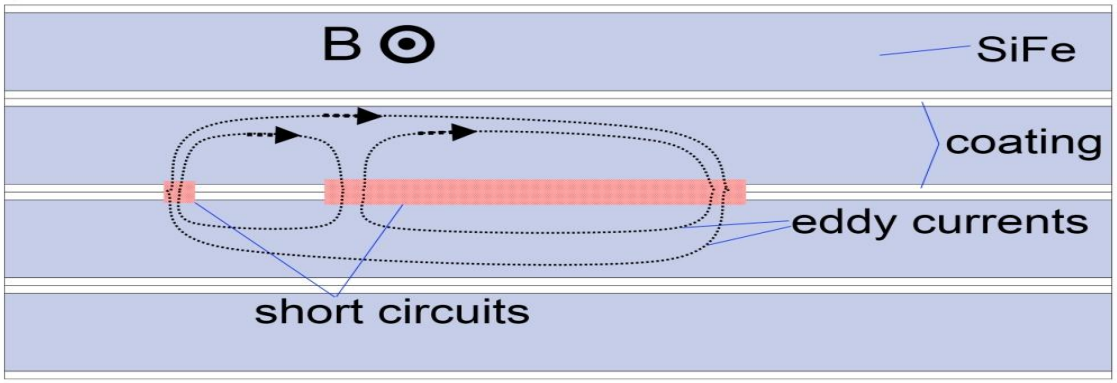

Figure 5.7 Schematic diagram of a coating failure causing additional eddy currents to circulate within the stack of laminations.

Aging or damage of wire insulation in the windings of an electrical machine can cause similar effects to those caused by burrs and coating failures. Figure 5.8 shows a schematic diagram of damaged wire insulation affecting a stack of electrical steel laminations; the wire running vertically on the left, shown in orange, is making an electrical contact with the edges of the electrical steel laminations and thus allowing the flow of eddy currents marked with the dotted arrows. This type of failure involves wire insulation as well as any type of paper or other form separating the windings from the core.

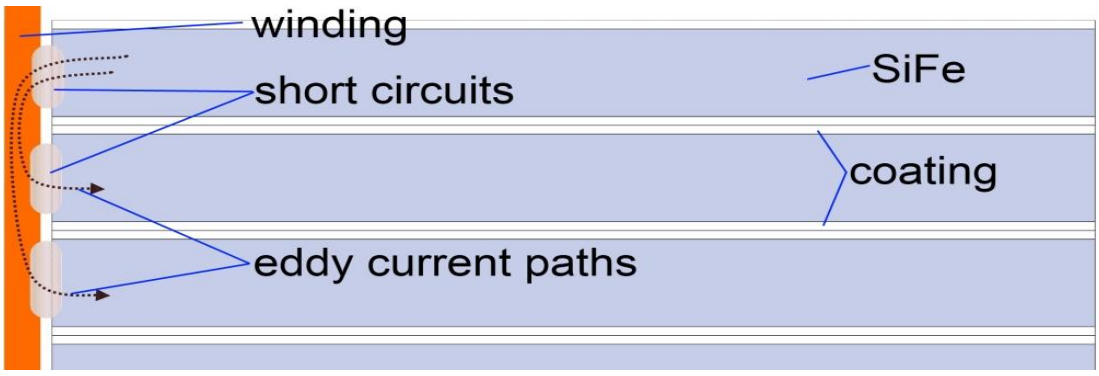

Figure 5.8 Schematic diagram showing damaged winding forming electrical connections between several laminations of electrical steel within a stack.

Accidental damage to the core may also create short circuits in cores of electrical machines. This may include scratches made during core assembly, winding insertion or any other miscellaneous act causing electrical connection between laminations. Such damage might short circuit adjacent laminations.

5.2 PROPERTIES OF BURRS

5.2.1 Burr height

The main parameter of a burr on the edge of an electrical steel sheet is its height which is defined in the British Standard BS EN 10251:1997 [54] as the "Difference between the thickness measured respectively at the cut edge of the sheet and at a distance of 10 mm from this edge". This is illustrated in Figure 5.9 where the burr height h is calculated as the distance h_2 measured at the edge of the lamination minus the sheet thickness h_1 measured 10 mm from the edge of the lamination.

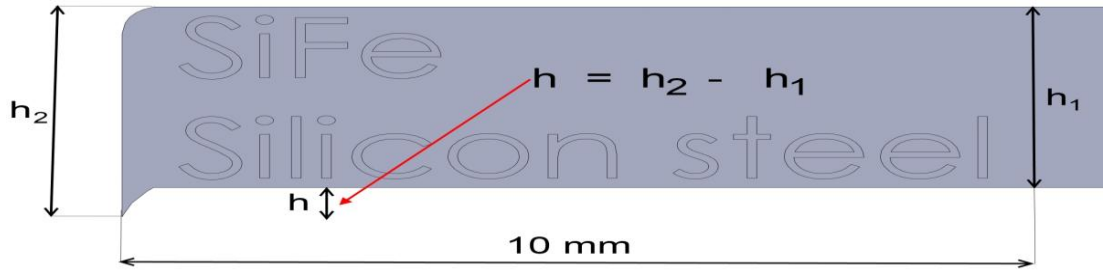

Figure 5.9 Burr height definition as in British Standard BS EN 10251:1997 [54].

Burrs created by cutting the material to the size for final use in electrical machines are not to exceed 0.025 mm in height according to EN 10107:2005 [55].

The procedure for measuring burr height described in British Standard EN 10251:1997 [54] is based on a sample of steel sheet or strip that is ready as required by the product application or specification. The effective length of the material over which the measurement is taken should be 1 m and if the sample under test is less than 1 m in length, several samples need to be measured. A linear measurement device such as a comparator should be used for the measurement.

The required specifications as given by the standard for burr height measurement are listed below and depicted in Figure 5.10:

- resolution of 1 µm
- uncertainty of 2 µm
- axial movement of the sliding anvil is obtained without rotation
- sliding anvil dimensions are 16 mm x 8 mm
- force applied on the anvil is 4 N ±0.2 N

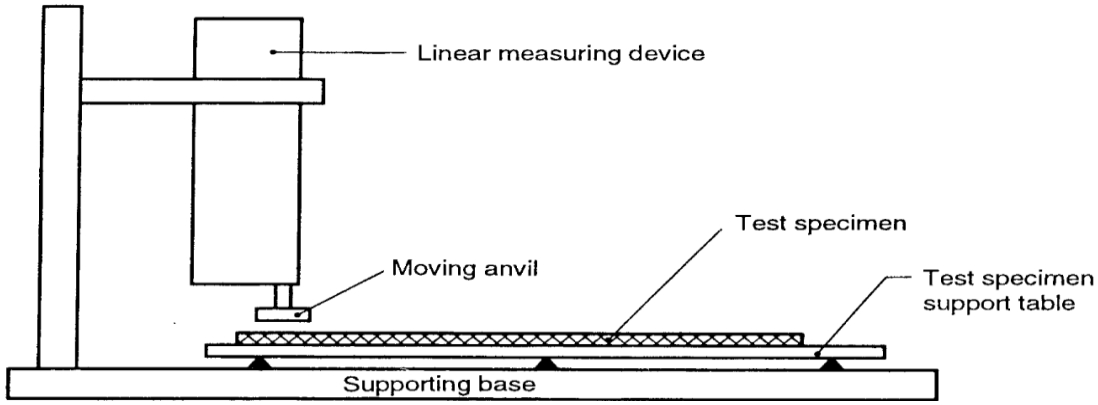

Figure 5.10 Burr height measurement rig as shown in BS EN 10251:1997 [54].

The measurement procedure is illustrated in Figure 5.10. The sample should be placed on a flat support table to which the comparator is fixed in such a way to ensure 90° movement of the anvil in relation to the table surface and to ensure that the surface of the anvil is parallel to the table surface. The parallelism of the table and the anvil can be adjusted by using a three point surface table construction as depicted by the three black triangles. The difference in height of any point of the table's plane must not exceed 2 µm. The measurement of h_1 and h_2 is made at the edge of the sample and 10 mm from the edge of the sample respectively. The measurement is repeated at least every 50 mm along a 1 m length to acquire 20 measurements. The result is given by the average of the 20 measurements as well as by the maximum value obtained in any one measurement.

Although a burr height of 25 µm is allowed by the BS EN 10107:2005 [55] consumers of electrical steel often have higher expectations from the cut steel. The limit set by the standard, which is applicable only to material cut to the width for its final use,

is not strict enough to minimise the risk of faults in electrical machines and core manufacturers set the maximum accepted burr height significantly lower with values reaching below 15 µm [56]. The reason for this strict requirement is that the greater the height of the burr, the greater is the chance for it to break the coating of the adjacent lamination and thus create a short circuit between the two laminations. Electrical steel coatings are 0.5 - 2 µm thick [57] therefore in order to ensure that the burr cannot reach the adjacent lamination burr height should be no more than the thickness of the coating which is impossible to achieve. However, burr height of 5 µm is reasonably achievable [58].

5.2.2 Stress zone at the cut edge

The burr height is not the only important aspect when evaluating the effects of burrs. Apart from the lamination edge deformation made by burr, stress is introduced to the steel up to some distance from the cut edge of the sheet as illustrated in Figure 5.11. This stress degrades the electromagnetic properties of the steel. It affects permeability, losses, flux distribution, B-H loop and magnetostriction [50, 59]. Some of the stress induced changes in magnetic properties can be recovered by stress relief annealing, but it is unlikely to fully restore the magnetic properties of the material to those before cutting [9, 60]. Annealing creates an iron oxide layer on the burrs reducing conductivity and therefore reducing the chance of creating closed eddy current loops [61]. Figure 5.11 shows the deformation zone and the stress zone where plastic stress (burrs) and elastic stress are located respectively. The deformation zone is normally very small, not exceeding 1 mm in depth. The stress zone is reported to reach from 1 mm, to more than 10 mm into the lamination [52, 59, 60, 62].

Figure 5.11 Stress zones introduced by cutting and burr formation [8].

5.3 EFFECTS OF BURRS

The importance of burrs comes from the fact that they introduce a chance of piercing the coating of the electrical steel laminations and in this way create electrical short circuits between adjacent layers which may result in additional eddy currents circulating within the core causing increased losses in the electrical machine. This can lead to localised core heating creating hot spots which can cause the steel to melt or even start an avalanche effect in which melted steel creates more electrical connections and further increment of additional eddy currents circulating within the core and hence further melting of the steel. An example of a large transformer core of 187 MVA rating which failed during the first run resulting in melted steel is described in a report by A.J. Moses [63]. Many more examples are available in rotating machine applications. Figure 5.12 [64] shows a stator core of a 430 MW 496 KVA rated generator with steel melted in several locations and Figure 5.13 [65] shows damage located in one of the teeth of the stator. In each case it is not possible to determine whether the avalanche effect was triggered by short circuits created by burrs, wire or coating failures.

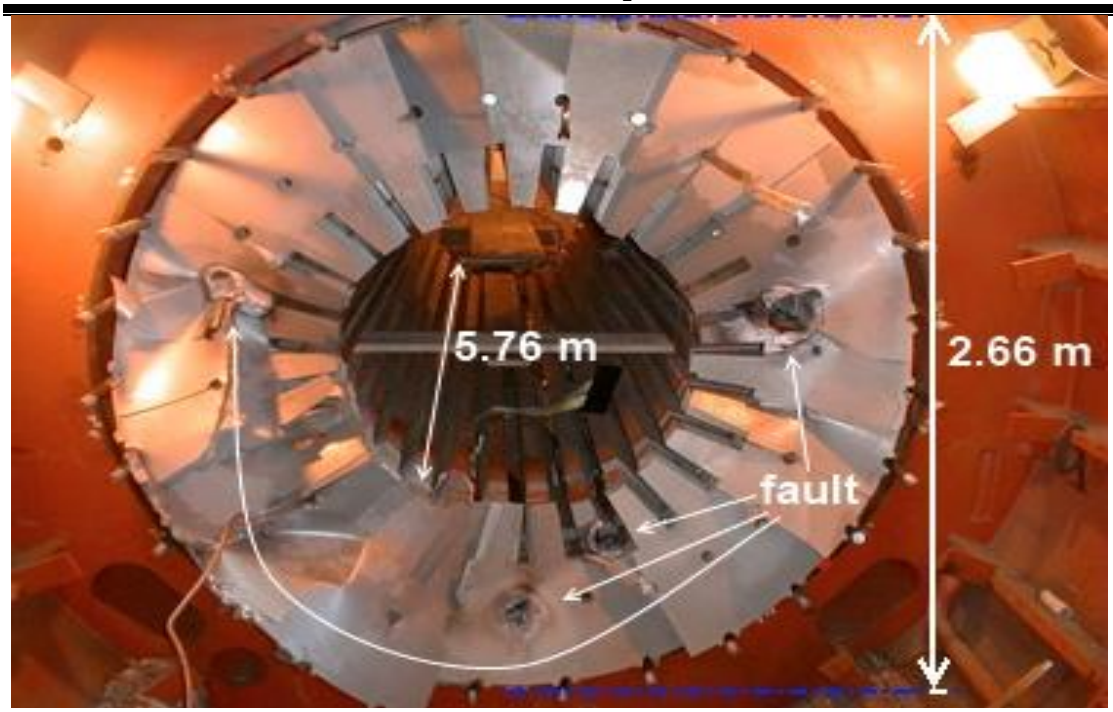

Figure 5.12 Stator core rated at 496 MVA built of 0.46 mm thick laminations. Damage caused by shorted laminations in various locations [64].

Figure 5.13 Stator core damage caused by shorted laminations [65].

An ideal stacked core magnetised longitudinally is shown in Figure 5.14 (a) where the green arrow marks the magnetisation direction and the dotted lines mark the circulating eddy currents. The steel is shown in grey and the coating in white. As can be seen eddy currents circulate separately in each lamination.

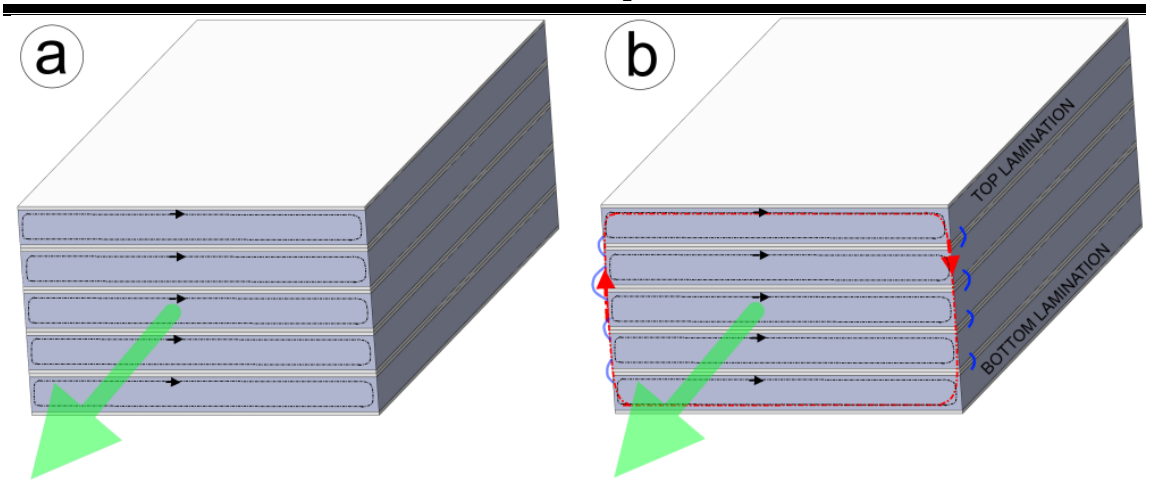

Figure 5.14 A schematic diagram of the eddy currents flowing within a magnetised core with fully insulated laminations.

If burrs are present in the core, they create short circuits between laminations as illustrated in Figure 5.14 (b). Eddy currents flow around a large volume within the core increasing the core losses significantly. The short circuits created by burrs are depicted with blue and light blue connections on the sides of the stack. Eddy currents circulating within individual laminations are shown in black dotted paths. Additional eddy currents, caused by the short circuits are shown in red dotted paths.

There are a few requirements that have to be met for damage such as that shown in Figure 5.12 and Figure 5.13 to occur in an electrical machine core. However, for burrs to have any effect on losses they must be present in more than one location within the cores geometry and they must pierce the coating of adjacent laminations and create electrical contact between the two layers. Furthermore, the electrical connections created by burrs together with the laminations form a loop or multiple loops in a plane including a component perpendicular to flux normally circulating within the core of the machine.

Figure 5.15 shows a stack of laminations of electrical steel which is affected by burrs creating short circuits. All five laminations shown are connected by short circuits

on the left side of the stack, but only the two bottom laminations are short circuited on the right side. The only new eddy current path created in case of the first four laminations is located within the burr itself and is depicted as green dashed loops, however, due to the burr's small size, the effect is negligible. The other two layers of laminations are short circuited on both sides and the new eddy current path created runs through both laminations.

Figure 5.16 shows two cases of burrs present between two adjacent laminations within a stack; case (a) where the burr is too small to pierce through adjacent lamination coating and case (b) where the burr is large enough to pierce the adjacent laminations coating and create an electrical connection between the two laminations.

A simple model of Faradays Law of induction demonstrated on two conductive loops as shown in Figure 5.17 explains how differently arranged loops generate emf or not. Any loop, created by the short circuited laminations, whose plane is perpendicular to the direction of the magnetisation field generates an emf due to the magnetic flux flowing through it; no emf is generated in a loop whose plane is parallel to the magnetising field; The induced emf produces a current in the loop which is an equivalent of the eddy current flow between two laminations affected by burrs on either side of the stack as it is with the two bottom laminations in Figure 5.15. The loop parallel to the magnetisation field shown with red colour in Figure 5.17 does not have any flux flowing through it and thus no emf will be induced and no current will flow in the conductor.

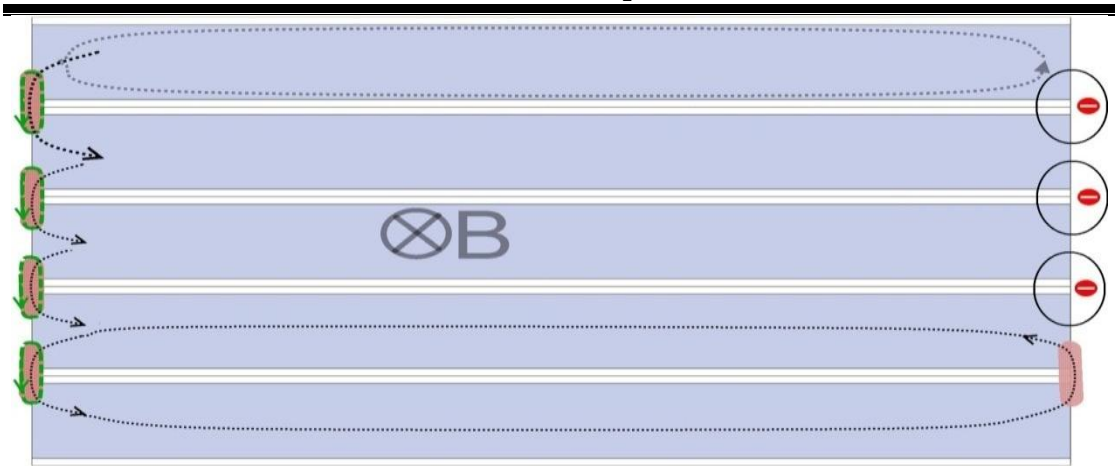

Figure 5.15 Schematic diagram of a stack of laminations with burrs affecting the top four layers only on one side and the last layer on both sides of the stack.

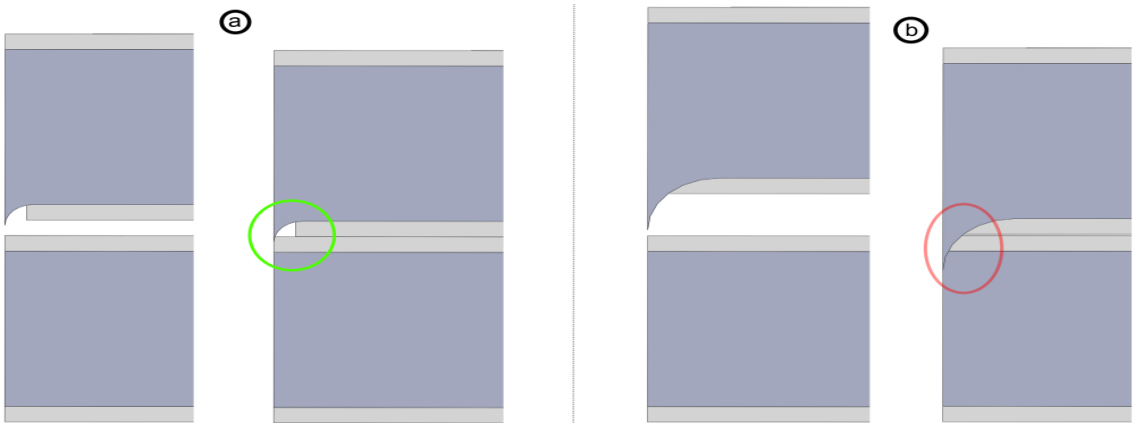

Figure 5.16 Schematic of two sizes of burrs in electrical steel laminations. Case (I) shows a burr not creating an electrical connection between the two layers of laminations. Case (II) shows a burr piercing the coating of the adjacent lamination and creating an electrical connection between the two laminations.

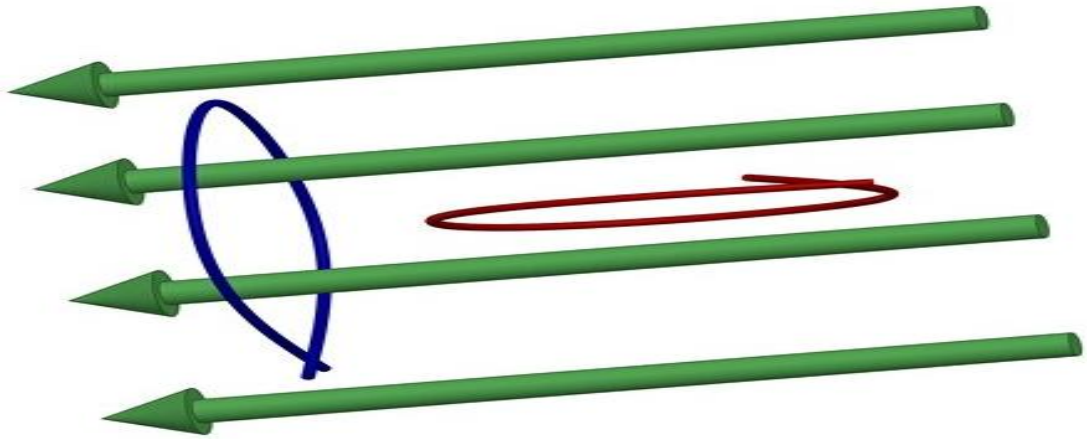

Figure 5.17 Two loops of electrical conductors arranged in parallel (red) and perpendicularly (blue) to the magnetisation direction (transparent green). According to Faradays Law emf will be induced in the blue loop while no emf will be induced in the red loop.

5.4 BURR DETECTION METHODS

Several techniques are used to detect burrs both before and after assembly of a stacked or wound core such as crude and rapid manual detection by touch, burr quality control by burr height measurement, thermal imaging, ring testing, the ELCID technique, flux injection probes and stack capacitance all of which are described below. Pre-assembly methods are used for quality control while post-assembly methods may be used for investigation of faults, underperformance and periodic maintenance checks of machines during their active duty.

Pre-assembly detection of burrs is made as a quality check on the electrical steel sheet production line on a periodic basis or constantly if the process is automated and non-destructive. Manual detection of burrs by touch is an old technique but still used as an ad hoc quality check. It is based on touching the steel lamination with a fingertip and sliding it off the lamination to feel the edge. A cruder version utilises the fingernail to slide off of the edge and detect a click in case a burr is present. It is a very subjective test and does not produce a specific quantitative result; however, it is extremely fast as it obviously does not require any equipment or preparation [66]. Measurement of burr height as described in the British Standard EN 10251:1997 [54] and in section 5.2.1 is performed as a quality check on random samples periodically. The frequency of these control checks depend on quality standards specific for a production line or a factory.

Direct post-assembly detection of burrs is practically impossible unless burrs are large enough to see them with a naked eye. However, in most cases burrs occurring in assembled cores are too small to be detected by visual inspection. The larger burrs, visible by eye, are more likely to be detected in the pre-assembly stages. The presence

of burrs in an assembled machine can be indirectly detected by methods utilising phenomena such as areas of abnormal temperature, power loss or flux density. After detecting a location with abnormal temperature or magnetic properties the source of the problem must be determined. This is because several different conditions separately can cause a similar effect. For example flux density abnormality can be caused by burrs but also by crystal structure defects in the steel or specific design of the lamination such as regions in the corners and T-joints as well as bolt holes where flux tends to move away from rolling direction and locally change the flux density.

5.4.1 Detection of short circuits by the ring flux test

The ring flux test, also called a loop flux test, is a well established method for detecting interlaminar faults within rotating machine stator cores requiring the rotor to be removed. Figure 5.18 shows a schematic diagram of its use on a motor stator core where windings are threaded through the core where interlaminar shorts and eddy currents are illustrated. The concept schematic shows one turn but usually, depending on the power source available, a few turns of a high gauge wire are used with high currents used to magnetise the core; the magnetisation direction is shown in the figure with black arrows. The same or approximately 90% of normal operation magnetisation is used for this test which means that a large power source must be used and caution is required as excessive heat produced during the test could cause further damage to the core. Locally increased losses are produced by the eddy currents circulating within the interlaminar faults which are then detected by infrared equipment [67, 68].

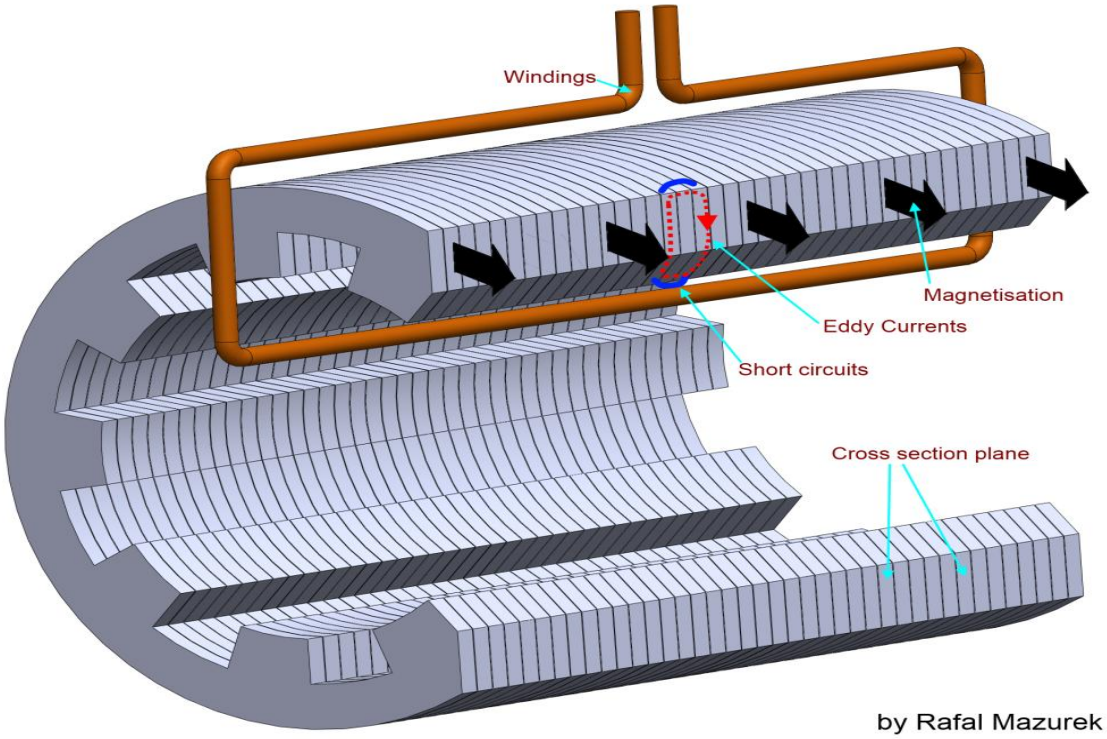

Figure 5.18 Diagram of the ring flux test shown on a stator core.

5.4.2 Detection of short circuits by the EL CID technique

The EL CID method was developed in the early 1980s as an alternative to the ring flux test [67]. In most cases the rotor needs to be removed from the stator. A coil is wound in a similar way as in the ring flux test to excite the core to about 3-4 % of the nominal operating magnetisation level. Fault currents are detected by means of a Chattock coil (see section 4.2 for a definition of a Chattock coil) arranged such as to have its two ends in contact with the motor core under test. The Chattock coil can be carried inside the stator by an automated trolley. EL CID shown schematically in Figure 5.19 requires significantly less man power and working time than the ring flux test [67, 69-74].

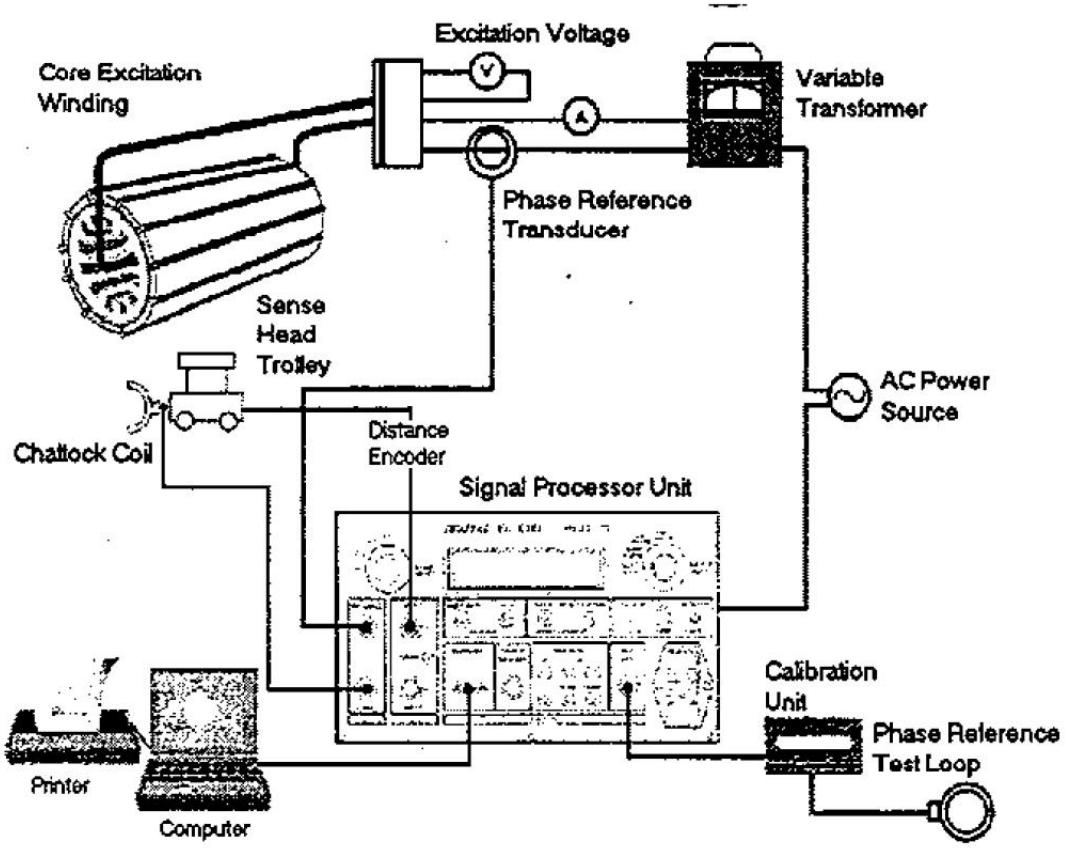

Figure 5.19 Schematic diagram of an EL CID test system.

5.4.3 **Detection of short circuits using stack capacitance**

This idea proposed in 2008 by C. Shulz [75] is based on capacitance measurement in a stack of laminations as shown in Figure 5.20 to determine how many short circuits are present within the stack and a probability calculation to estimate how many pairs of short circuited pairs occur between the same laminations forming a closed electrical circuit between two adjacent laminations. This method does not indicate the location of the fault but it detects the fault between the measurement points. It only shows the overall stack capacitance seen from the contact points and allows for assessment of the number of short circuited laminations between those points [75].

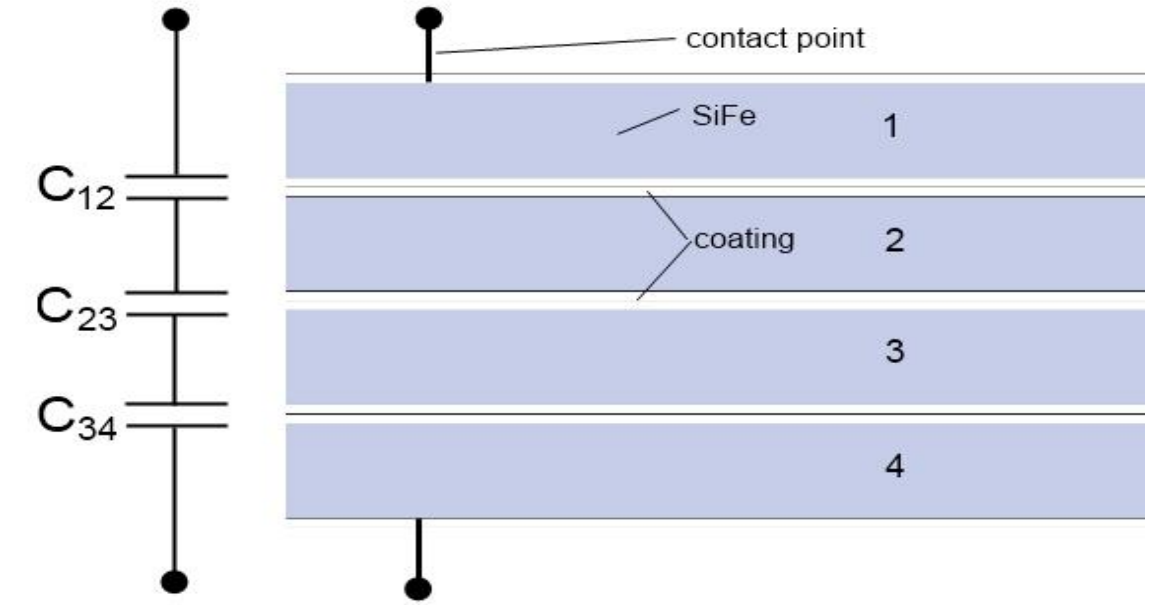

Figure 5.20 Schematic diagram of burr detection method based on stack capacitance measurement. Laminations 1-4 form three capacitors C_{12}, C_{23} and C_{34} contributing to the total stack capacitance seen from the contact points.

5.4.4 Detection of short circuits by flux injection probe

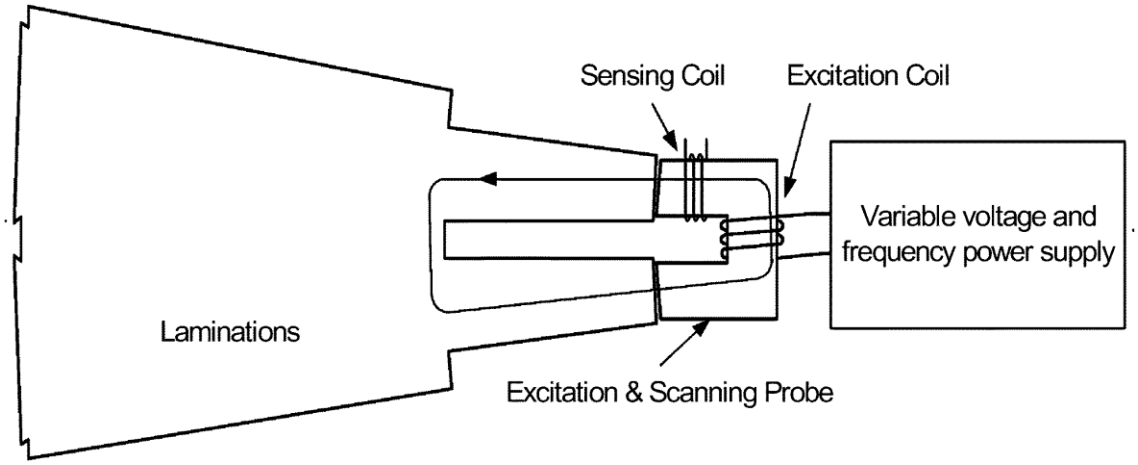

Figure 5.21 Schematic of the flux injection probe.

The flux injection probe is a technique in which a C-shaped yoke forming a magnetic circuit between two adjacent teeth on the stator is used as an excitation and scanning probe as illustrated in Figure 5.21. In this method considerable flux flows through the teeth of the stator which is different to methods using a magnetisation procedure similar to the one shown in Figure 5.18. The method is based on the magnetic circuit loss measurement which is formed by the teeth and the probe. Loss is calculated

over one cycle using the magnetising current, induced voltage and the ratio of the two windings used on the probe as in (5.1) [76].

$$P = \frac{1}{T}\int_{t}^{t+T} \frac{N_e}{N_s} v_s(t) i_e(t) dt \qquad \textbf{(5.1)}$$

where t – time, T – time period, N_e – number of excitation windings, N_s – number of sensing windings, v_s – sensing voltage, i_e – excitation current.

5.4.5 **Burr detection methods summary**

For each application a different method may be most suitable. Detection by finger touch and burr height measurement require access to the edge of the sample and these methods can only be used before the core assembly stage. Access to the inner parts of the stator is also required for ring flux test, ELCID and flux injection methods where rotor is removed from the motor to ensure this access. Basic thermal imaging does not require the core to be disassembled – it can give results based on very limited access to the core, however, only visible surfaces can be tested this way.

The measurement principles vary between the methods from burr detection using touch, through periodic burr height average measurement, surface heat increase measurement for ring test and thermal imaging, measurement of field created by the eddy currents induced and measurement of loss in a core-probe magnetic circuit.

There is also a difference in magnetisation distribution during testing by different methods. The flux ring test and ELCID magnetise the stator using windings threaded through the stator resulting in flux flowing around its circumference and thus not flowing within the teeth of the stator. In the flux injection probe method flux flows

through the two neighbouring teeth which is closer to the working principle of such cores.

Table 5.1 presents some of the advantages and disadvantages of all the burr detection methods described.

Table 5.1 Advantages and disadvantages of various burr detection methods.

Detection method	Advantages	Drawbacks
Finger touch	• Fast (ad hoc) • No preparation • Cheap	• not quantitative • not applicable to finished cores
Height measurement	• standardised measurement • quantitative	• selected samples only • not applicable to finished cores
Thermal imaging	• All magnetisation levels • No preparation required	• limited to visible surfaces
Ring flux test	• Well known procedure • Burr location is detected	• Near rated level of magnetisation may cause further damage • Heavy high gauge wires need to be threaded • Takes a long time • Flux does not flow within teeth of the stator
ELCID	• Low magnetisation • Does not take a long time • Burr location is detected	• Flux does not flow within teeth of the stator
Stack capacitance measurement	• Cheap • Easy to set up • Fast measurement • No magnetisation required	• Burr location is not detected • Statistical analysis is required
Flux injection probe	• Focus of measurement is in the teeth of the stator similar to stator operation • Flux flows through the teeth of the stator	• Magnetisation of a limited volume around the tooth of the stator

5.5 PREVIOUS INVESTIGATIONS OF THE EFFECT OF ARTIFICIAL BURRS

Previously, conducting paint was used to form artificial short circuits between laminations; however, under magnetisation conditions vibrations caused the paint to break. This approach was briefly tested in this project using silver in Methyl Isobutyl Ketone – conductive glue, and using silver paint but both compounds were breaking under vibrations as it was reported by Aimoniotis [77].

Another method investigated by Aimoniotis was drilling of 0.3 mm holes "close to the edge of the stack of laminations and inserting a steel pin" [77]. This is illustrated in Figure 5.22. However, this method is destructive and it introduces point short circuits while in real life burrs tend to form elongated shapes on the edge of the electrical steel. A further drawback is that the burrs created using drilling are located not on the edge but at least a few millimetres into the stack which does not represent the real issue.

The increase in the overall specific total loss of a machine core containing burrs can range from small unnoticeable percentages below 1% up to values reaching 100% and higher in severe cases as demonstrated in the example experimental results shown in Figure 5.23 [77]. The numbers in the data set labels represent burr placement locations as depicted in Figure 5.24. The method of short circuiting the laminations is bolts slotted in holes drilled through the laminations of the stack; This means that results labelled "1,2,3,6 and 7" in Figure 5.23 were obtained for the case where short circuiting rods were inserted into slots marked in Figure 5.24 by numbers 1, 2, 3, 6 and 7. The higher the number of artificial short circuits inserted in the core, the higher is the additional loss increase. The increase in specific total loss reaches approximately 80% for the case with most short circuits introduced in the core.

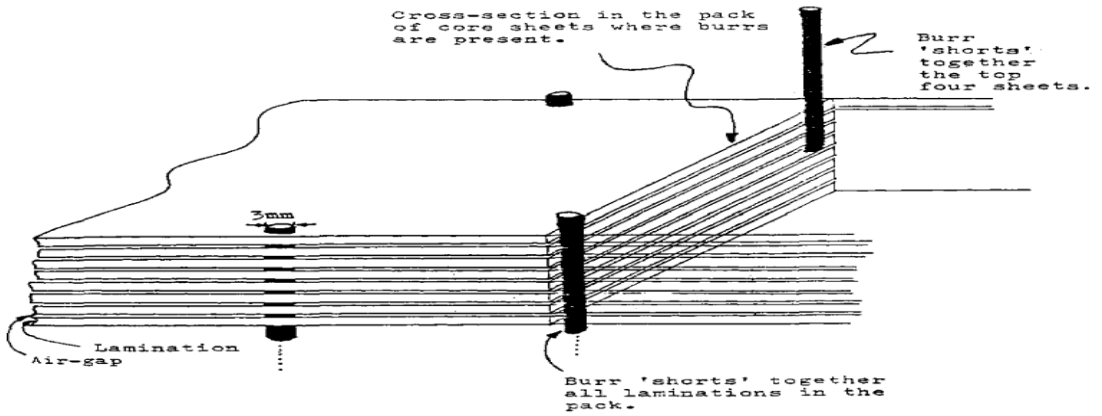

Figure 5.22 Method of producing artificial burrs by drilling holes and inserting steel rods as presented in [77].

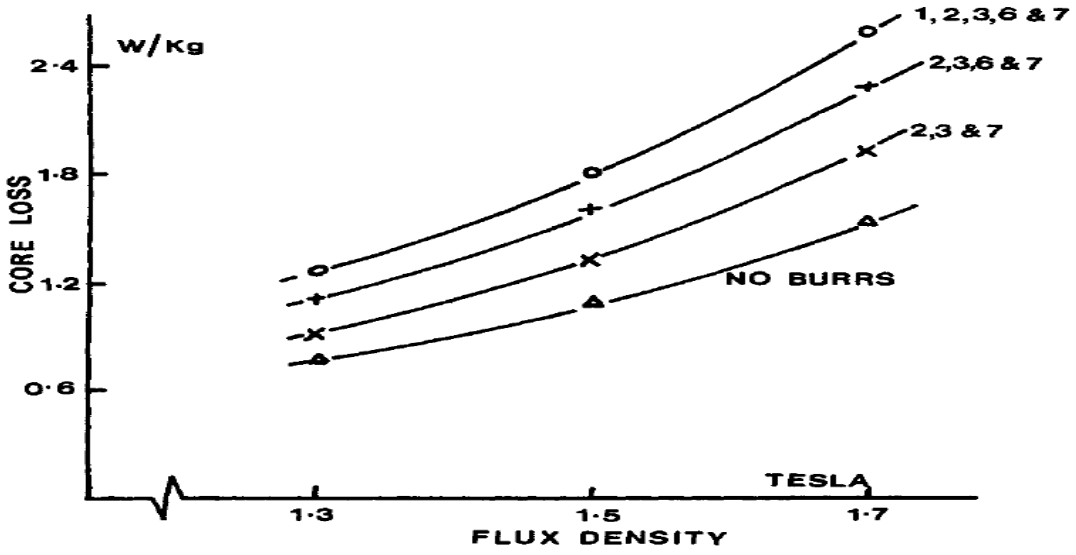

Figure 5.23 Variation of specific total loss with flux density for various burr configurations [77].

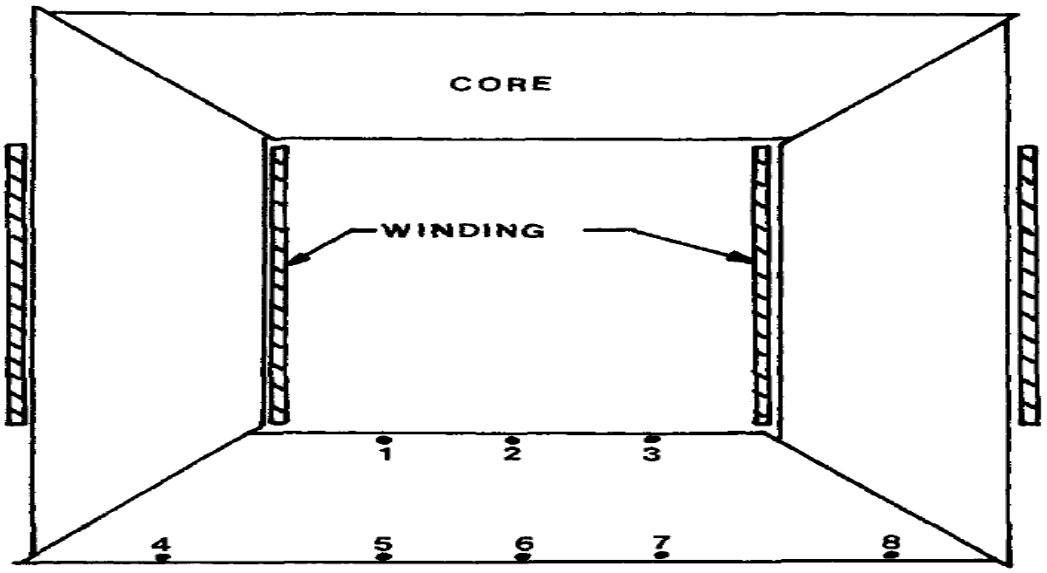

Figure 5.24 Artificial burr placement in the geometry of a single phase transformer core used in [77]. Holes were drilled through the entire stack of laminations at locations 1-8 allowing insertion of conductive bolts in them and thus creating interlaminar short circuits.

Chapter 6. **Thin film sensors production**

6.1 DESIGN AND MODIFICATIONS OF THE VACUUM SYSTEM SETUP

Figure 6.1 shows the Edwards E12E4 vacuum coating unit used for all thermal evaporation procedures in this investigation. A modification was made to enable the use of this unit for production of thin films on large samples. The system presented in Figure 6.1 can be used only for strips up to approximately 30 cm in length which was not sufficient for this investigation where it was necessary to deposit sensors onto laminations 0.8 m long. Cutting the laminations into sections that would fit the chamber shown in Figure 6.1 was considered but cutting would change the flux density distribution when the lamination was placed into a transformer core. Three designs of larger systems were made taking into account the speed of vacuum building for a given volume as well as cost of material and production.

Figure 6.1 Edwards E12E4 Physical Vapour Deposition system used to build a customised system for this investigation.

A perfect vacuum chamber could be made by machining a single solid block of aluminium or stainless steel into a single piece chamber or make a solid piece of glass

as it is the case for the bell jar shown in Figure 6.1. But a large metal vessel required view ports as well as access ports to enable mounting samples and evaporants in the chamber as well as maintain visual control during deposition.

The first design of a custom vacuum chamber is shown in Figure 6.2. It is aimed at minimising the volume of the chamber in order to reduce the vacuum building times. The view ports are located at the top and at the front of the chamber. However, the access to mount and prepare the sample within the chamber is restricted. Also, the flat shape of the design requires the walls of the chamber to be thick in order to withstand the pressure difference of $(1 - 1.33*10^{-8})$ bar between the outside and the inside of the chamber; hence this design was rejected.

The design shown in Figure 6.3 was developed after discussions with manufacturing technicians to include appropriate welding techniques, as shown in Figure 6.4, to avoid creating trapped volumes of air and virtual leaks – trapped volumes of gas with a low conductance pass to the inside of the chamber. For this reason a design approach was developed to allow for full penetration, single pass welds all made on the vacuum side of the vessel [78, 79]. This required sufficient access for the welder to reach all joining surfaces.

Factors such as maximum weight and size without compromising the structure of the adapted system and its functionality were considered when reaching the final design shown in Figure 6.5. It features entry points at the two ends of the large horizontal tube and viewports at the top of the base cylinder closure and at the front side of the horizontal tube.

A crane was used to lift this chamber (mass approximately 200 kg) onto the vacuum pumping system. Using the setup shown in Figure 6.6 the system could be assembled and operated by one person. The supporting chains holding the chamber were set up to take most of its weight off the base of the vacuum system.

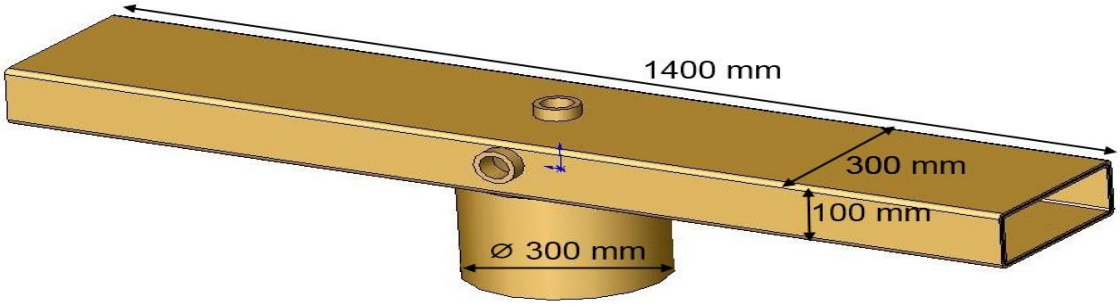

Figure 6.2 First design proposed for the custom evaporation chamber aimed at minimum chamber volume and minimum material.

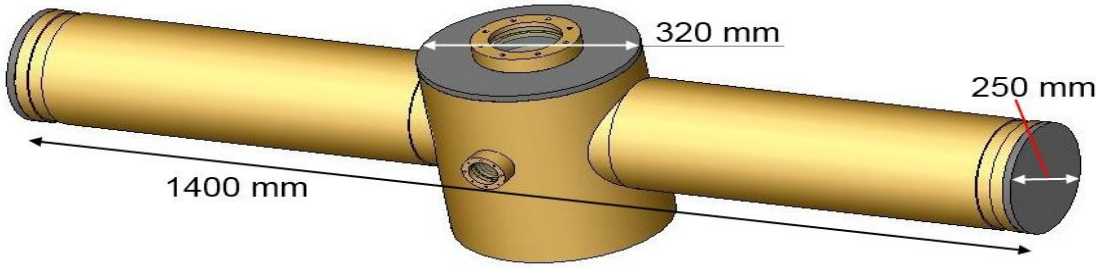

Figure 6.3 Second design proposed for the custom evaporation chamber; aimed to minimise the production requirements.

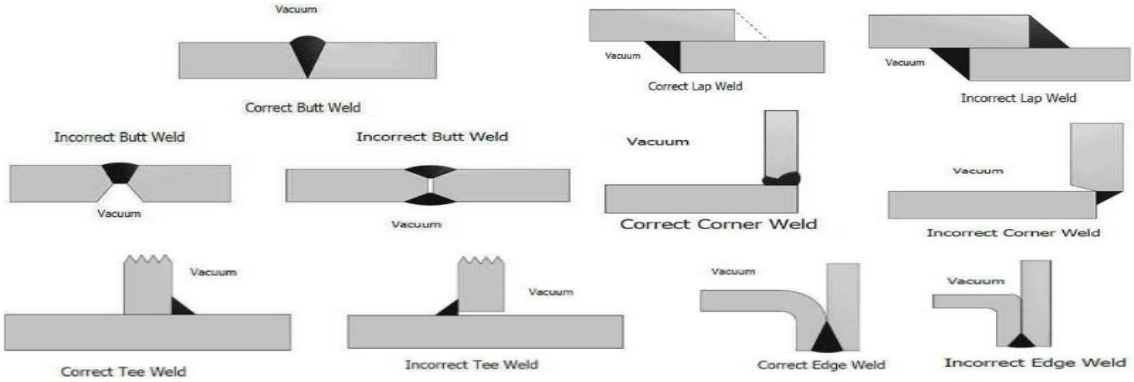

Figure 6.4 Guide to welding vacuum vessel components without creating air pockets or virtual leaks. Good practice is contrasted with bad practice to point out the important factors.

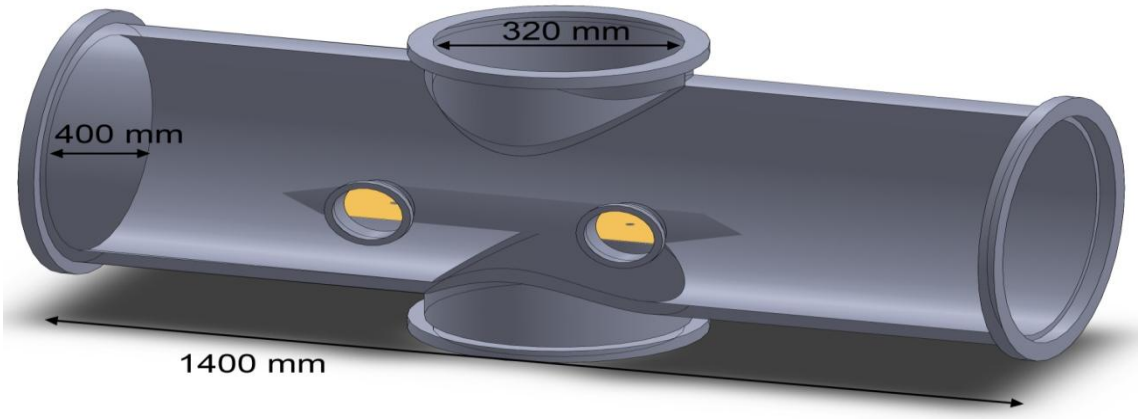

Figure 6.5 Final design of the custom evaporation chamber built to accommodate large samples of electrical steel to evaporate onto.

Figure 6.6 Large evaporation chamber hoisted by a crane on top of the Physical Vapour Deposition system.

6.1 MASKS DESIGNED FOR THIN FILM SENSORS

The performance of a mask depends on factors such as contact between the mask and the sample surface, thickness of the mask, edge effects and mask alignment on the surface. Machined plates of materials able to withstand high temperatures without outgasing and causing contamination can be used [80]. Several methods were tested to assess their suitability for this investigation:

6.1.1 Aluminium foil as a PVD mask

Aluminium foil (15µm thickness) cut outs were successfully used for prototyping masks for thin film sensors as shown in Figure 6.7. The masks made this way are fragile and could normally only be used once but they were quick and simple to prepare when the mask shape was not complicated. The mask needs to be attached to the sample and fully supported during deposition; otherwise it tends to bend away from the sample causing changing the shape and thickness of the deposited paths.

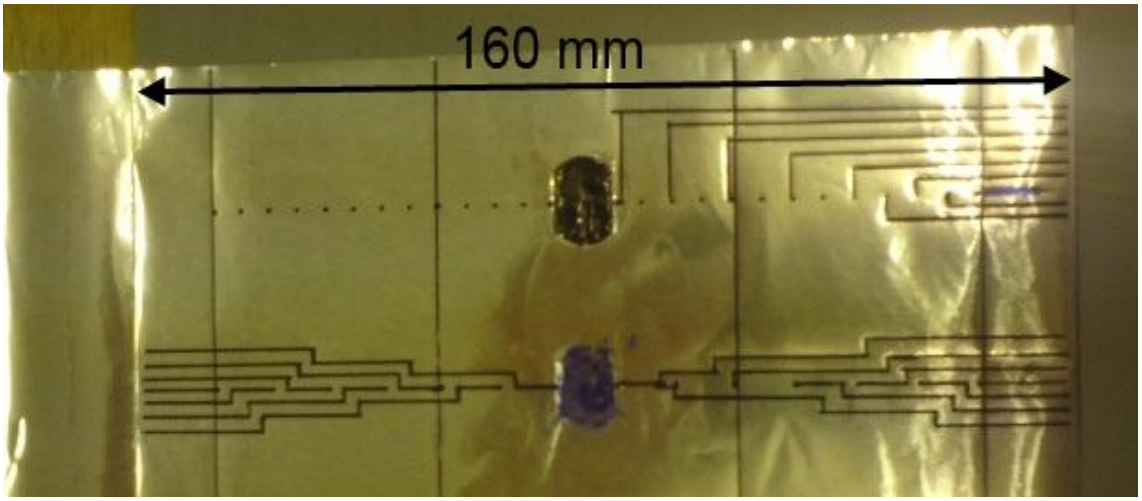

Figure 6.7 Physical Vapour Deposition mask prototype made using kitchen foil.

6.1.2 **Photolithography as a PVD mask on electrical steel**

Two laminations of grain oriented electrical steel of size 30 mm by 15 mm were cleaned with isopropanol and acetone and photoresist was applied to their surfaces. A spinning table was used to help spread the photoresist evenly. Positive and negative photolithography techniques [80] were used to produce thin film shapes shown in Figure 6.8. The technique allowed successful creation of conductive paths on the small samples described above but the photoresist could not be applied evenly to 80 cm long strips A standard spinning table can be used for round samples only and not larger than 30 cm in diameter [81]. The samples shown in Figure 6.8 are two halves of a 30 mm by 30 mm square sample with deposition of around 300 nm thickness.

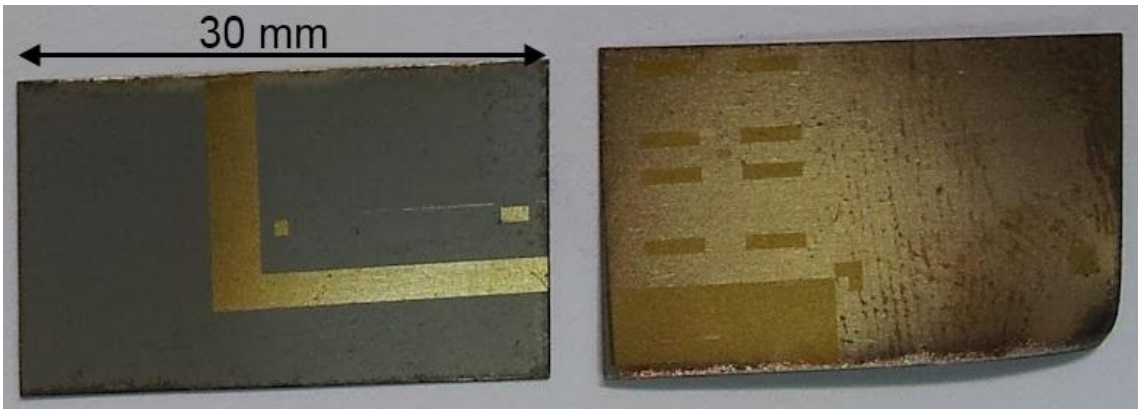

Figure 6.8 Photolithography used for creating thin film deposition on silicon steel using physical vapour deposition. Positive and negative photolithography techniques are shown.

6.1.3 **Adhesive metallic foil used as a PVD mask**

An attempt was made to make masks simply using copper foil glued to the surface of a lamination of electrical steel. The masks created in this way were only suitable for single use but the possibility of the mask bending away from the sample was resolved. However, after deposition of copper onto the lamination, the thin film tended to peel off from the lamination with the copper foil mask while removing it. Hence further evaluation of the method was abandoned.

6.1.4 **Machined aluminium plates and sheets as PVD masks**

The mask shown in Figure 6.9 was made from a 4 mm thick aluminium plate for creating five electrically conductive paths which form a set of needle probes for flux density measurement on laminations of electrical steel. To ensure a clear path between the evaporation source and the lamination, the cross-section of the cut out patterns in the mask is such as to maintain a wide angle access through the machined plate to the surface of the electrical steel lamination.

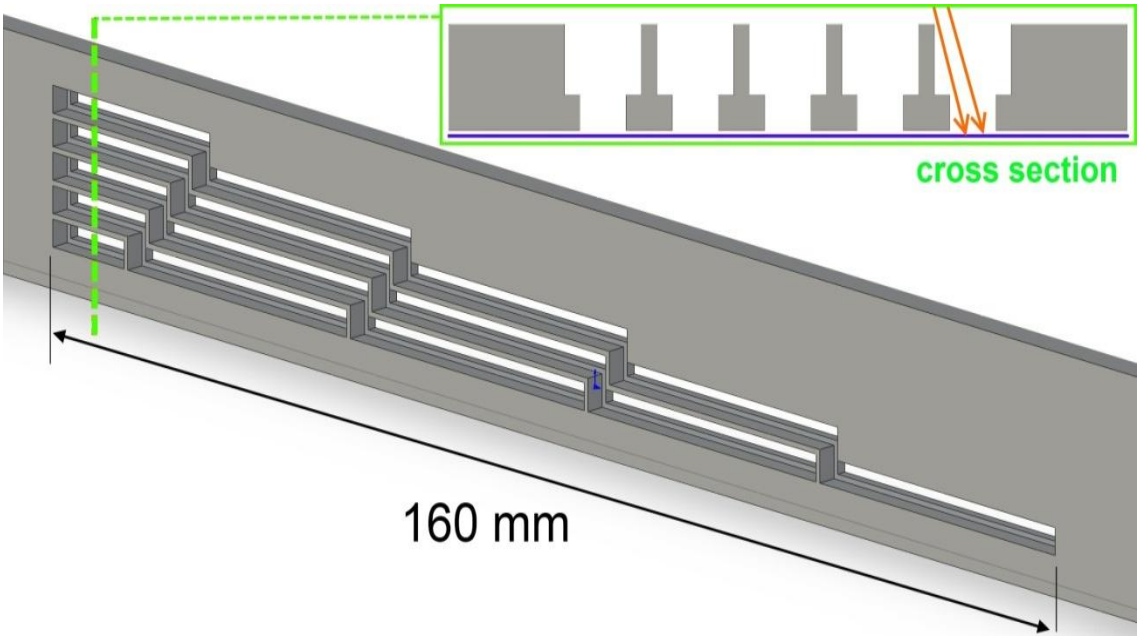

Figure 6.9 Design of a mask for a set of thin film needle probes made out of aluminium plate.

Another design, shown in Figure 6.10 was made using a 2 mm aluminium sheet. The advantage of a thinner sheet is the ability to produce finer shapes of sensors. Flatness of the sheet was assured by sandwiching it between two wooden boards during machining. The pattern was machined out to form a mask for making two sets of two dimensional needle probes for flux density measurements. The deposited line width is 2 mm with 3 mm circles at the locations where the deposited tracks coincide with connection points to the lamination bare metal.

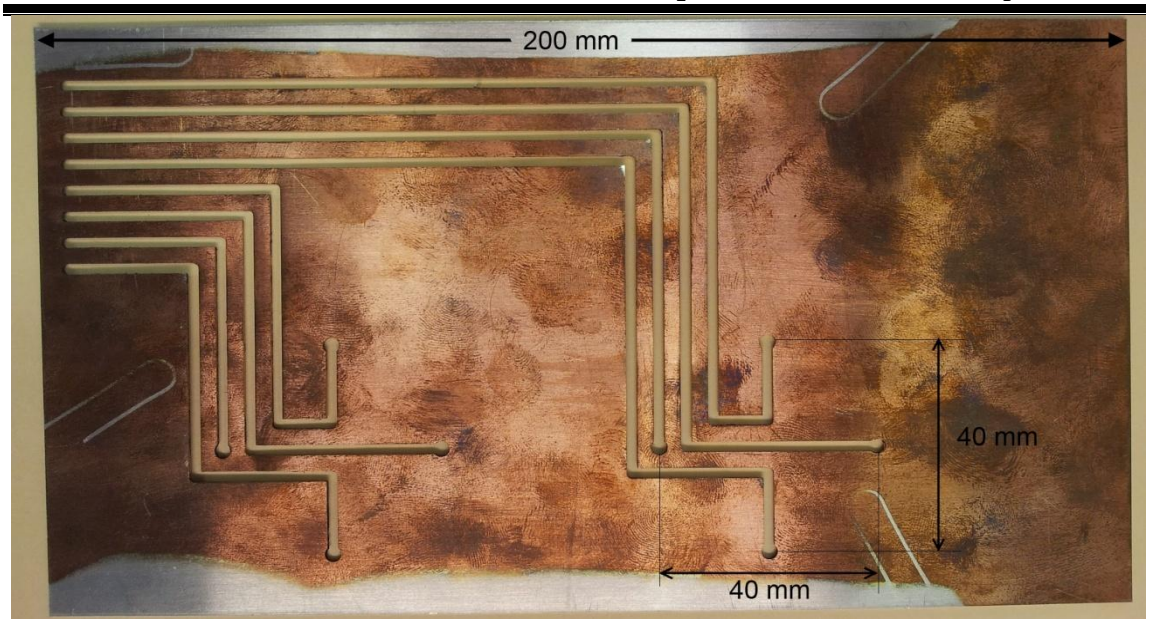

Figure 6.10 Second design of a mask for a set of thin film needle probes.

6.2 DEPOSITED FILMS THICKNESS AND MEASUREMENT OF IT

The expected thickness range of the deposited sensors is less than a few microns. For the application here the most important parameter is the total electrical resistance of the formed sensor rather than the uniformity and precision of the film thickness or width. An expected resistance per meter length of the deposited copper path of 2 mm width and 1 μm thickness is given as

$$R_{1m} = \frac{\rho l}{A} = \frac{16.78 \times 10^{-9} \times 1}{2.00 \times 10^{-3} \times 1.00 \times 10^{-6}} = 8.39[\mathrm{Ohm}] \qquad \textbf{(6.1)}$$

where ρ is resistivity of copper, l is a 1 meter length of the deposited path and A is the cross-sectional area of the deposited path.

6.2.1 Thickness measurement

An experimental approach was used for thickness assessment of sets of deposited thin films. A microscope glass slide was attached to the sample next to the mask so that the same thickness of material was deposited onto the glass slide and the lamination. A

scalpel was used to make a scratch on the glass slide coating and a profilometer was used to plot the profile of the coated surface across that scratch. A sketch of an example plot is shown in Figure 6.11 with the scratch width and the deposition thickness labelled. The difference between the scratched and unscratched region is the resulting thickness.

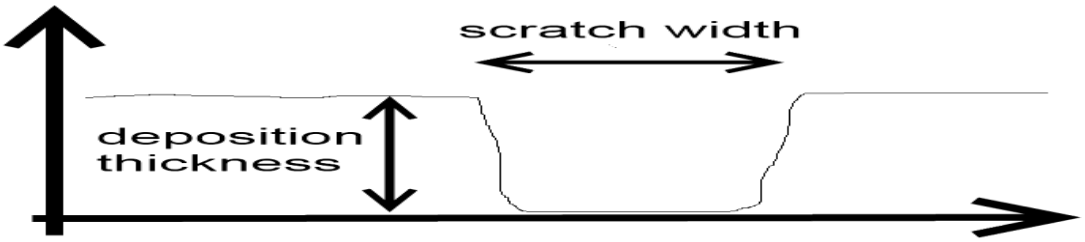

Figure 6.11 Sketch of a surface profile with a scratch made on the deposited layer. Deposition thickness is measured as a displacement of the tip sliding close to the surface in respect to the reference value.

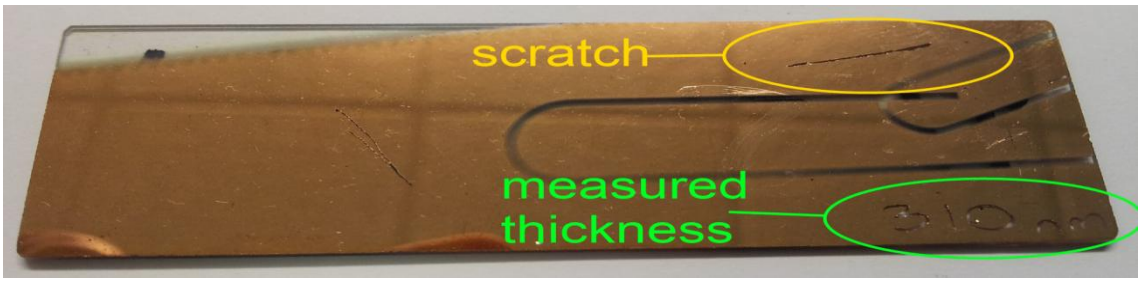

Figure 6.12 Glass slide used for determining the thickness of the deposited film by means of a profilometer. The measured thickness for this example was 310 nm.

One of the slides used during the experiments is shown in Figure 6.12. The 10 mm long horizontal scratch is visible in the upper right corner. The thickness of this particular deposition was measured to be 310 nm.

6.3 EVAPORATION ONTO ELECTRICAL STEEL LAMINATION

Before deposition, laminations are cleaned with isopropanol and then acetone to remove any surface dirt or oil. If oil is still present, deposited films peel off. If pieces of dirt remain during deposition, they tend to break off with a part of thin film and create an open circuit in the sensor or significantly reduce its resistance.

The commercial coating on the surface of grain oriented electrical steel is porous [48], the concept of which is shown in Figure 6.13 (a), and does not provide sufficient insulation for thin film deposited onto the lamination as shown in Figure 6.13 (b) where the deposited conductive material is in direct contact with the steel through the pores in the coating.

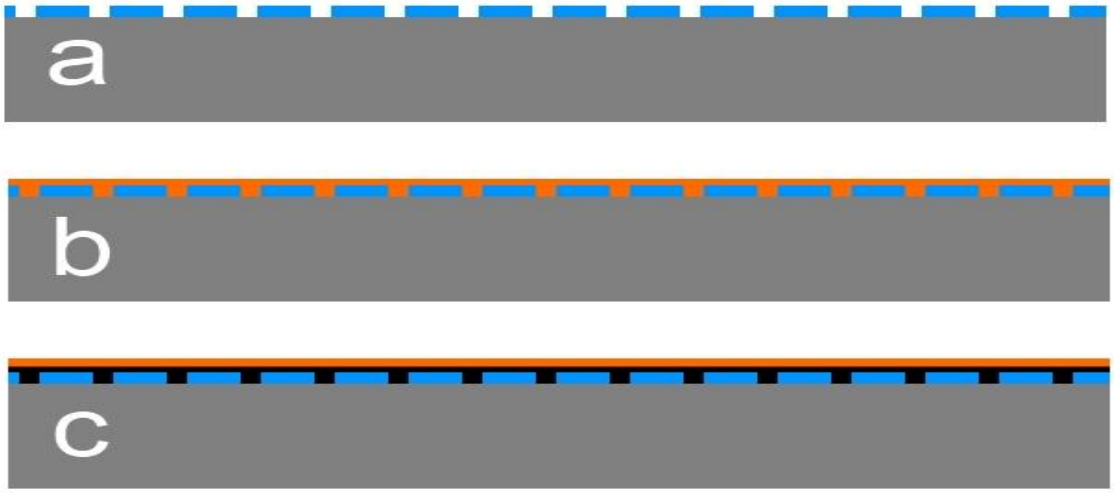

Figure 6.13 Schematic showing an electrical steel lamination with: (a) – porous coating only; (b) – material deposited directly on the coating resulting in direct contact of the deposited material with the steel; (c) – the porous coating covered by an insulation layer before a conductive layer of sensors is deposited.

An additional insulation layer is necessary to fill in these pores and ensure insulation between the steel and the deposited film as shown schematically in Figure 6.13 (c). Silicon dioxide (SiO_2) is frequently used to create the additional insulation layer [48]. However, SiO_2 is deposited using e-beam evaporation equipment which was not available. The approach shown in Figure 6.14 was found to achieve an insulating layer. Silicon monoxide (SiO) particles, in the form of granules in a basket crucible, were evaporated thermally and allowed to oxidise in contact with air forming SiO_2. A lamination with a brown silicon monoxide layer deposited on the coating is shown in Figure 6.15. Estimated thickness of the insulation SiO_2 coating was 0.5 µm.

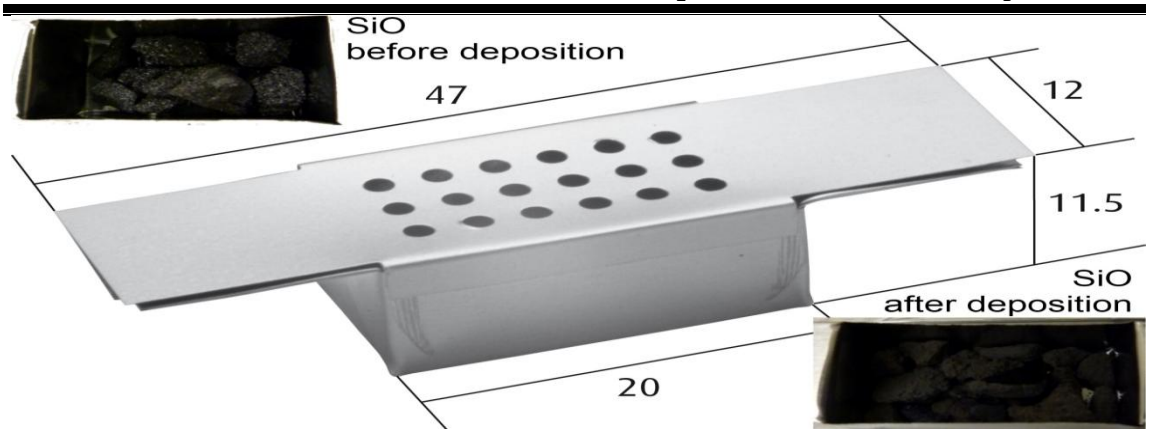

Figure 6.14 Silicon monoxide particles in form of granules and a basket crucible used for creating an insulation layer on an electrical steel lamination.

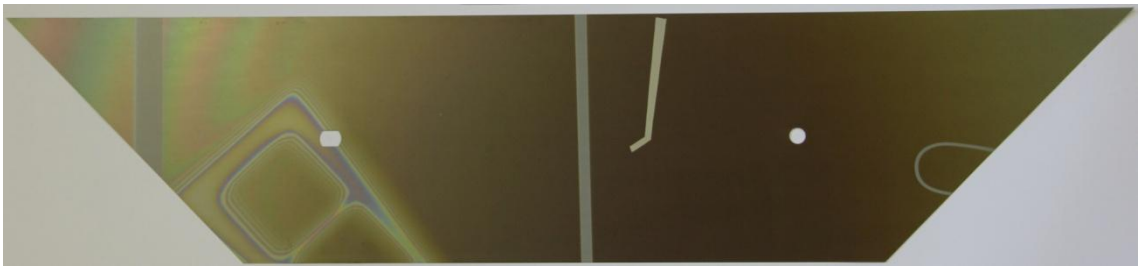

Figure 6.15 Silicon monoxide (SiO) layer (brown colour) deposited on an electrical steel lamination as insulation and base for the next deposition stages.

Silicon monoxide forms a layer which has better adhesive properties for deposition of the sensors than the surface of the silicon steel coating. This improves the durability of the sensor layer.

Production of each sensor set on an electrical steel lamination followed a specific sequence:

1. Cleaning the lamination
2. Deposition of SiO_2
3. Application/placement of the mask
4. Using a small gauge drill bit removing SiO_2 and lamination coating in contact points
5. Deposition of Cu
6. Connection of wires to deposited sensors
7. Application of layer of clear lacquer or other protective layer (optional).

6.4 SENSORS MADE USING THE PVD PROCESS

Initially, needle sensors and thermocouples were produced on Epstein strips of grain oriented electrical steel using a standard vacuum system with a glass bell jar. Needle probes as shown in Figure 6.16, and thermocouples, as shown in Figure 6.20, were made. Conductive silver paint applied directly onto the deposited sensors was used to connect the leads.

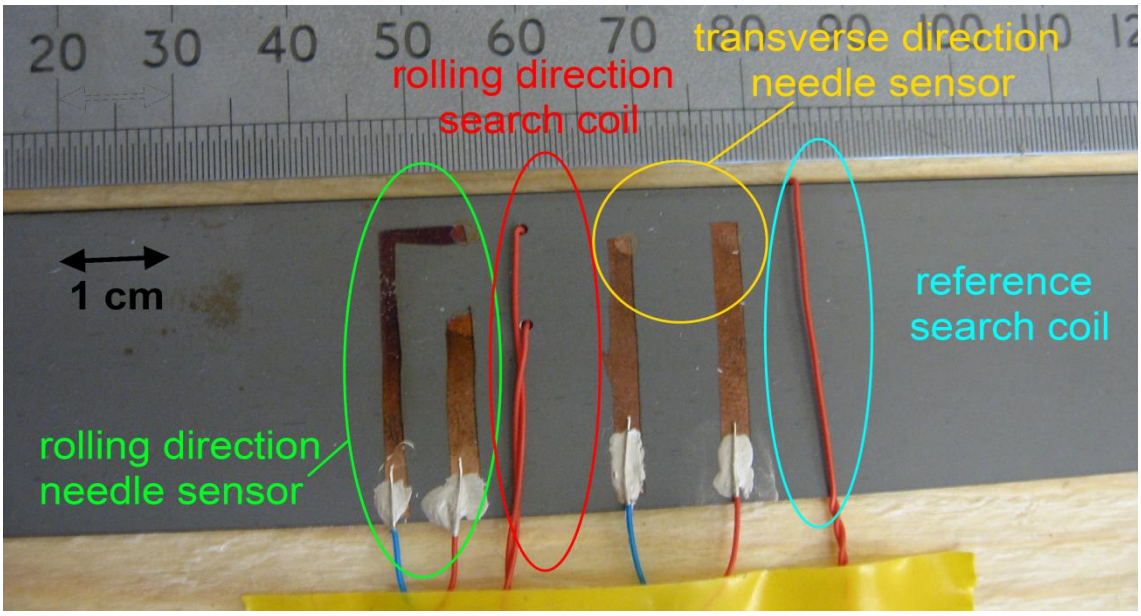

Figure 6.16 Needle probe flux density sensors deposited on an Epstein strip sample of electrical steel. In order from the left: a rolling direction needle type sensor, rolling direction search coil, transverse direction needle type sensor and a reference search coil wound around the whole strip.

The sensors shown in Figure 6.16 were designed for measurements of components of flux in the rolling direction (left sensor) and transverse direction (right sensor), where rolling direction is along the length of this sample (horizontal).

Development of the design of needle probe thin film sensors progressed through many ideas driven by the required sensor parameters such as direction of the flux density measured as well as by the mask making method techniques available to use. Figure 6.17 shows a lamination with five different designs of sensors made using various masking techniques such as heat resistant paper, adhesive copper foil,

aluminium foil and a mix of the individual methods. The aluminium foil proven to be most reliable for prototyping. The other methods either contaminated the deposited layers or destroyed it during removal of the mask.

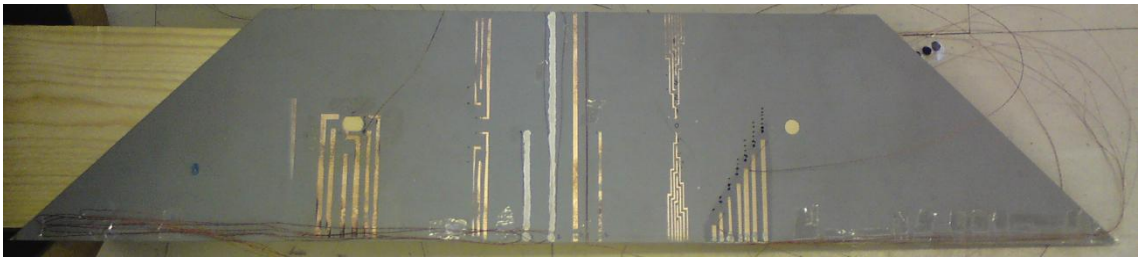

Figure 6.17 Five designs of thin film needle probes made using various masking techniques such as heat resistant paper, aluminium foil and adhesive copper foil.

An example set of thin film needle probes for flux density measurement across the width of a 160 mm wide lamination is shown in Figure 6.18. A more complex geometry of two sets of two dimensional flux density sensors shown in Figure 6.19 was made using the mask shown in Figure 6.10.

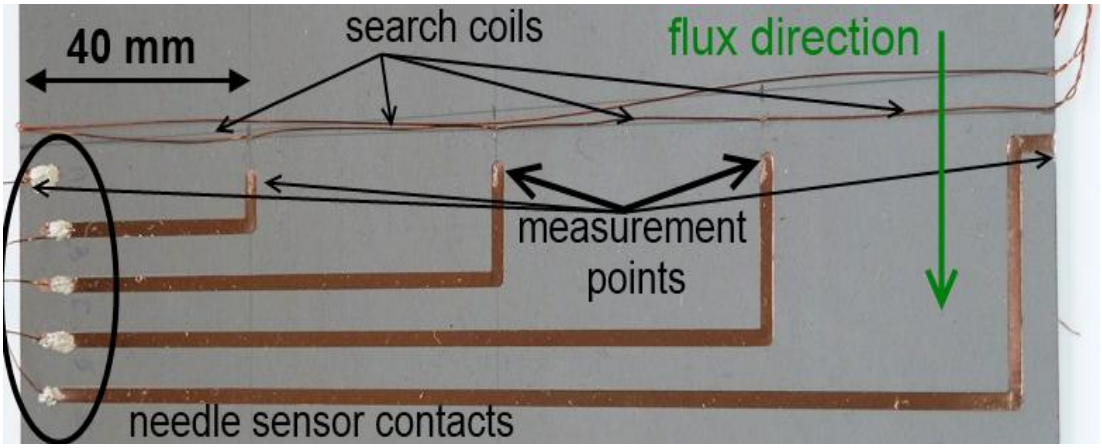

Figure 6.18 Set of needle probes for flux density measurements. Each of the five contacts can be used with any other one to measure flux density over various cross sectional areas.

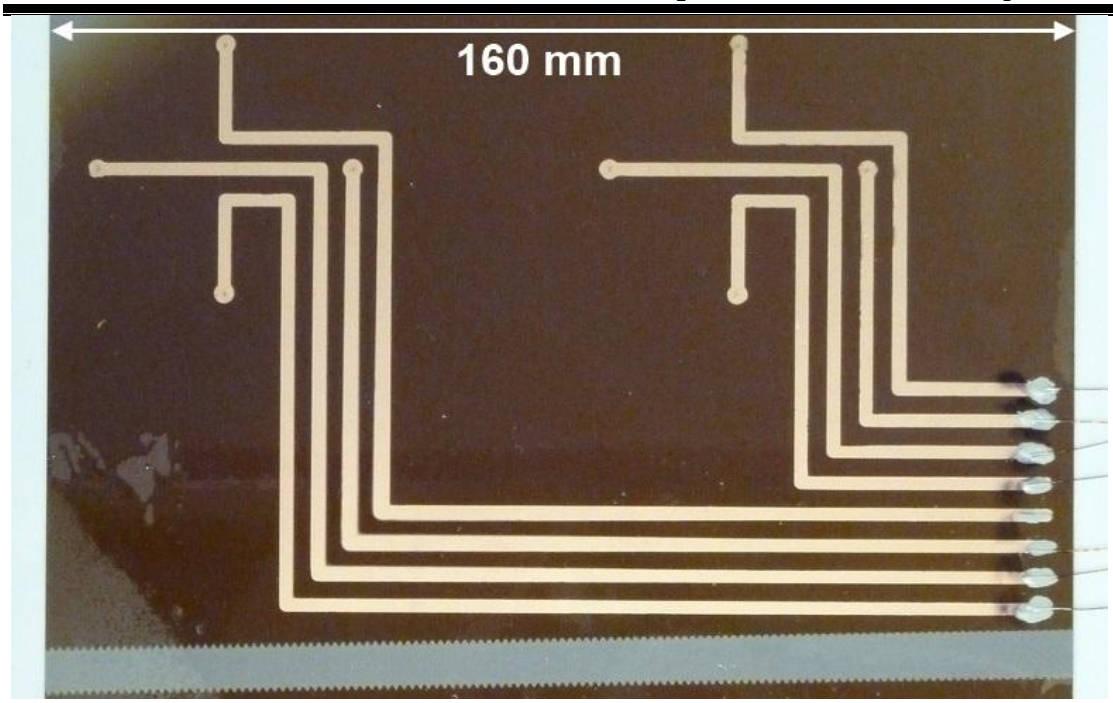

Figure 6.19 Two sets of two dimensional flux density needle probe sensors.

Type K thermocouples deposited on grain oriented electrical steel samples as shown in Figure 6.20 were tested in a setup with an ice-bath, to measure room temperature, boiling water temperature and human body (finger touch) temperature. The schematic of the measurement setup is shown in Figure 6.21. The thin film thermocouple was submerged in boiling water, touched by a finger and placed in a cardboard box for measurement of room temperature. Side by side with the thin film thermocouple, an electronic commercial thermometer with rated accuracy of 0.1°C was used to measure the same temperatures. The results obtained from the thin film thermocouple were accurate with less than 1°C error. However, in the early stage of the project, the thin film thermocouples did not work while the samples were magnetised. This was due to the fact that at this stage the SiO_2 insulation layer was not yet used and numerous unwanted contact points with the steel were present.

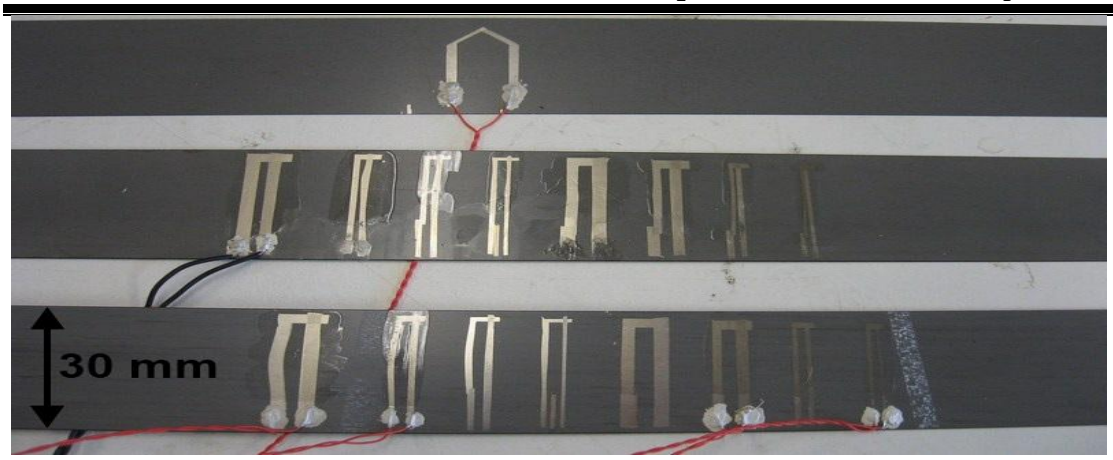

Figure 6.20 Thermocouples type K created using physical vapour deposition technique on Epstein strips of grain oriented electrical steel.

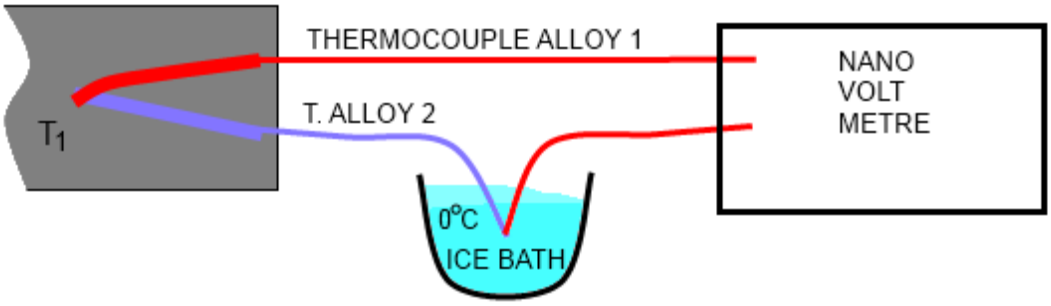

Figure 6.21 Schematic diagram of the experimental setup used to test the thin film thermocouples. Two thermocouple junctions are connected in an opposite series which results in a measurement of the temperature difference between the two junctions.

In conclusion of this chapter, the methodology used for production of sensors used in the results of this thesis was the 4 mm thick aluminium plate, with the improvement of the 2 mm aluminium sheet to follow in suggested future work. The thin film thermocouple production method was correct, however, due to technical issues and time restrains the experimental work using them was not finished and it is suggested as future work.

Chapter 7. **Modelling eddy current losses in the presence of burrs**

The classical approach to eddy current loss, as described in section 2.7, assumes that the thickness of the material is negligible compared to its width and therefore neglects any eddy current components flowing perpendicular to the sheet surface. This is acceptable for lamination thicknesses of 0.3 mm at 50 Hz magnetisation but if many laminations in a stacked core are affected by short circuits, the assumption is not valid.

7.1 ANALYSIS OF EDDY CURRENT LOSS IN A STACK OF LAMINATIONS AFFECTED BY SHORT CIRCUITS

7.1.1 Symmetrical short circuits

Work presented in this section was the published in an IEEE journal paper [4]

A schematic diagram of a situation where short circuits meeting all the requirements to cause an effect on power loss of a core as described in section 5.3 is shown in Figure 7.1(b) where the short circuit area is marked in red and additional eddy currents flowing through the stack of laminations are shown in blue. The short circuit embrace the stack of height H_B and width W_L. The thickness of the short circuited volume is d_b.

The eddy current loss is derived here for the case of the burred stack of laminations shown in Figure 7.1(b) in which burrs located on each side of the stack

create short circuits at the edges of the stack and of the same dimensions on both sides and equal to d_B.

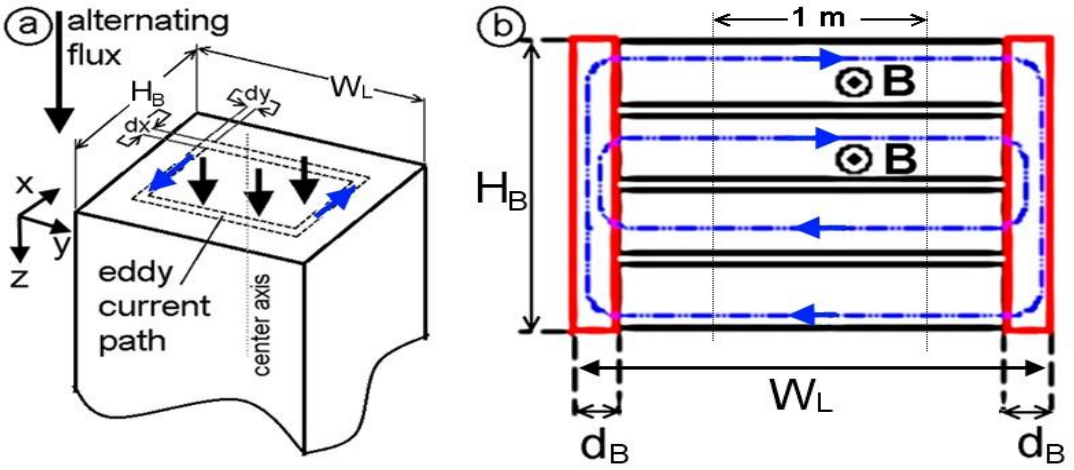

Figure 7.1 Sketch of eddy current model in a solid block (a) and eddy current paths flowing through a stack of laminations affected by symmetrically positioned short circuits (b).

The eddy current losses in the solid block shown in Figure 7.1(a) are calculated first. As opposed to the derivation of the eddy current loss in a thin sheet as shown in section 2.7.1, this derivation takes into account the fact that the material width is comparable in size to its thickness. At this point it is assumed that the flux distribution is uniform within the block. It is also assumed that electrical contact of the shortcircuited area is perfect resulting in the whole area having resistivity identical to that of the electrical steel laminations. Another assumption made simultaneously is that the eddy current paths are constrained within a simple geometrical shape based on the short circuited area dimensions. It will be later discussed that this is not true as the currents flow through a much wider region showing a fringing effect.

The flux density within the whole block given by

$$B = B_{max} \sin \omega t \tag{7.1}$$

alternates in the direction shown in Figure 7.1(a).

Considering 1 m axial length and 1 m width of the rectangular block – the x component of eddy current loss is calculated. In the case of the elemental eddy current paths of width dx flowing at distance *x* from the centre of the conducting block and whose depth is dx, the flux enclosed is, at any instant, given by

$$\phi = 2xB_{max} \sin \omega t. \tag{7.2}$$

The instantaneous EMF induced in that portion of the path is given by

$$e_x = \frac{d\phi}{dt} = 2xB_{max}\omega \cos \omega t \tag{7.3}$$

and its RMS value is given by

$$E_x = \frac{4\pi f x B_{max}}{\sqrt{2}} \tag{7.4}$$

The resistance of this portion of the path is

$$R_x = \frac{2\rho}{dx}, \tag{7.5}$$

the eddy current is calculated as

$$i_x = \frac{E_x}{R_x} \tag{7.6}$$

and the eddy current loss in this path per unit length and per unit width is equal to

$$\mathrm{P_{ex}} = \frac{4\pi^2 \mathrm{f}^2 \mathrm{x}^2 \mathrm{B}_{\mathrm{max}}^2 \mathrm{dx}}{\rho} \tag{7.7}$$

To calculate the loss in the 1 m axial length and 1 m width of the stack, the integration limits $x = \frac{H_B}{2}; x = 0$ cover the volume from the centre of the stack to either sides of the height H_B as in

$$P_{ex} = \int_{x=0}^{x=\frac{H_B}{2}} \frac{4\pi^2 f^2 B_{max}^2}{\rho} x^2 dx \tag{7.8}$$

And the loss per kilogram is

$$P_{ex} = \frac{\pi^2 f^2 B_{max}^2 H_B^2}{6\rho D} \tag{7.9}$$

The derivation for the x component is therefore similar to that for a thin sheet described in section 2.7.1. To determine the P_y component of eddy current loss, the initial steps are similar to those in the derivation of P_x but the integration boundaries in (7.8) change in order to take into account only the region in which eddy currents flow. Hence, the integral takes the form

$$P_{ey} = \int_{y=\frac{W_L}{2}-d_B}^{y=\frac{W_L}{2}} \frac{4\pi^2 f^2 B_{max}^2}{\rho} y^2 dy \tag{7.10}$$

and the loss per metre length and width for a symmetrical case is therefore given by

$$P_{ey} = \frac{4\pi^2 f^2 B_{max}^2}{\rho} \frac{1}{3}\left(\left(\frac{W_L}{2}\right)^3 - \left(\frac{W_L}{2} - d_B\right)^3\right)$$

$$P_{ey} = \frac{\pi^2 f^2 B_{max}^2}{6\rho}((W_L)^3 + (d_B - W_L)^3) \tag{7.11}$$

The loss per cubic meter is given by

$$P_{ey} = \frac{\pi^2 f^2 B_{max}^2}{6\rho}((W_L)^3 + (d_B - W_L)^3)\frac{1}{2d_B} \quad \textbf{(7.12)}$$

and the loss per kilogram within the burr is

$$P_{ey} = \frac{\pi^2 f^2 B_{max}^2}{6\rho}((W_L)^3 + (d_B - W_L)^3)\frac{1}{2d_B}\frac{1}{D} \quad \textbf{(7.13)}$$

The *y* component of eddy current loss is only present within the burr itself as shown in Figure 7.1(b) by red rectangles enclosed by height of a burr H_B, and thickness of the burr d_B. Hence, the integration boundaries for the *y* component of eddy current loss change in order to take into account only the region affected by burrs.

The combined per kilogram loss in y direction and x direction can only be calculated taking proportional values of each component by weight. Therefore the total eddy current loss within a stack of laminations affected by burrs is calculated as

$$P_{exy} = P_{ex} + \frac{\text{mass}(P_{ey})}{mass(P_{ex})}P_{ey} \quad \textbf{(7.14)}$$

7.1.2 **Non symmetrical short circuits**

A schematic diagram of a stack of electrical steel laminations affected by non symmetrical short circuits is shown in Figure 7.2. This is to model not only edge burrs but also short circuits within pin-guide holes and lamination coating failures which can occur at some depth into the stack and do not have to be of symmetrical dimensions. The regions of thickness d_{B1} and d_{B2} affected by short circuits are at distances d_{w1} and d_{w2} from the edge of the stack; this is to represent short circuits created by coating

failures or at bolts inserted into bolt holes. It should be noted that $y_1 \neq y_2$, $d_{w1} \neq d_{w2}$ and $d_{B1} \neq d_{B2}$; because defects and faults are random.

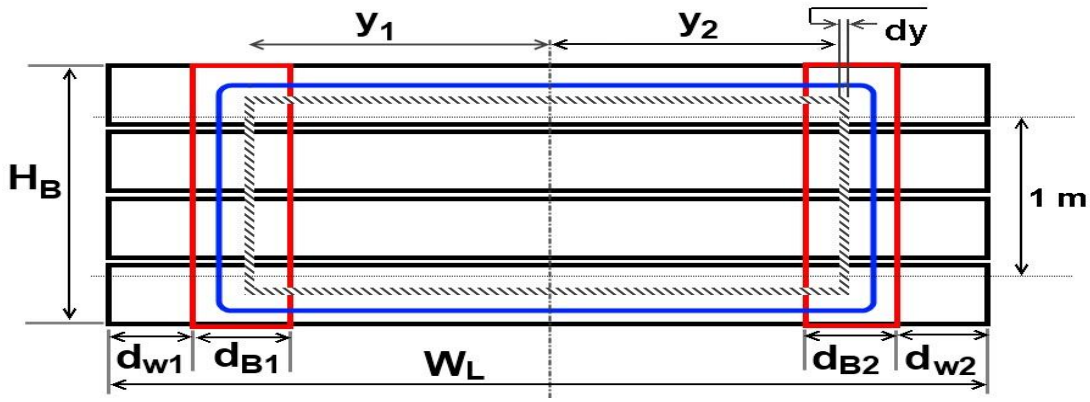

Figure 7.2 Eddy current paths flowing through a stack of laminations affected by symmetrically positioned short circuits.

Similar analysis as for the symmetrical case was undertaken. However, flux calculated within the non-symmetrical model is split into halves marked by the centre axis in Figure 7.2. The x component of eddy current loss remains the same as in (7.9).

The y component of eddy current loss is calculated considering 1 m axial length and 1 m height of the stack of laminations shown in Figure 7.2. In the case of the elemental eddy current path of width dy flowing at distance y_1 from the centre of the stack and whose depth is dy, the flux at any instant enclosed by dy and the centre axis of the stack is, at any instant, given by

$$\phi_1 = y_1 \times 1 \times B_{max} \sin \omega t \tag{7.15}$$

The EMF induced in that portion of the path is given by

$$e_{y_1} = \frac{d\phi}{dt} = y_1 B_{max} \omega \cos \omega t \tag{7.16}$$

and its RMS value is given by

$$E_{y_1} = \frac{2\pi f y_1 B_{max}}{\sqrt{2}} \quad \textbf{(7.17)}$$

The resistance of this portion of the path is

$$R_{y_1} = \frac{\rho}{dy} \quad \textbf{(7.18)}$$

the eddy current is calculated as

$$i_{y_1} = \frac{E_{y_1}}{R_{y_1}} \quad \textbf{(7.19)}$$

and the eddy current loss in this path per unit length and per unit height is equal to

$$\mathrm{P_{ey_1}} = \frac{2\pi^2 \mathrm{f}^2 \mathrm{B}_{\mathrm{max}}^2}{\rho} \mathrm{y}_1^2 \mathrm{dy} \quad \textbf{(7.20)}$$

The integration boundaries for P_{y1} reflect the portion of the stack where the eddy currents flow in y direction. Substituting $W_{L1} = \frac{W_L}{2} - d_{w_1} - d_{B_1}$ and $W_{L2} = \frac{W_L}{2} - d_{w_1}$ the integration takes the form

$$\mathrm{P_{ey_1}} = \int_{\mathrm{W_{L1}}}^{\mathrm{W_{L2}}} \frac{2\pi^2 \mathrm{f}^2 \mathrm{B}_{\mathrm{max}}^2}{\rho} \mathrm{y}_1^2 \mathrm{dy} \quad \textbf{(7.21)}$$

and the loss per metre length and width for a non-symmetrical case is given by

$$\mathrm{P_{ey_1}} = \frac{2\pi^2 \mathrm{f}^2 \mathrm{B}_{\mathrm{max}}^2}{\rho} \frac{1}{3} \left(\left(\frac{\mathrm{W_L}}{2} - \mathrm{d_{w_1}} \right)^3 - \left(\frac{\mathrm{W_L}}{2} - \mathrm{d_{w_1}} - \mathrm{d_{B_1}} \right)^3 \right) \quad \textbf{(7.22)}$$

The loss per cubic meter is given by

$$P_{ey_1} = \frac{2\pi^2 f^2 B_{max}^2}{\rho}\frac{1}{3}\left(\left(\frac{W_L}{2} - d_{w_1}\right)^3 - \left(\frac{W_L}{2} - d_{w_1} - d_{B_1}\right)^3\right)\frac{1}{d_{B_1}} \quad \textbf{(7.23)}$$

The loss per kilogram is given by

$$P_{ey_1} = \frac{2\pi^2 f^2 B_{max}^2}{\rho}\frac{1}{3}\left(\left(\frac{W_L}{2} - d_{w_1}\right)^3 - \left(\frac{W_L}{2} - d_{w_1} - d_{B_1}\right)^3\right)\frac{1}{d_{B_1}}\frac{1}{D}$$

$$P_{ey_1} = \frac{\pi^2 f^2 B_{max}^2}{12D\rho d_{B1}}\left(\left(2d_{B_1} + 2d_{w_1} - W_L\right)^3 + \left(W_L - 2d_{w_1}\right)^3\right) \quad \textbf{(7.24)}$$

The eddy current loss within the other half of the stack is calculated in the same manner arriving at a loss per kilogram given by

$$P_{ey_2} = \frac{2\pi^2 f^2 B_{max}^2}{\rho}\frac{1}{3}\left(\left(\frac{W_L}{2} - d_{w_2}\right)^3 - \left(\frac{W_L}{2} - d_{w_2} - d_{B_2}\right)^3\right)\frac{1}{d_{B_2}}\frac{1}{D}$$

$$P_{ey_2} = \frac{\pi^2 f^2 B_{max}^2}{12D\rho d_{B_2}}\left(\left(2d_{B_2} + 2d_{w_2} - W_L\right)^3 + \left(W_L - 2d_{w_2}\right)^3\right) \quad \textbf{(7.25)}$$

When short circuits on both sides of the stack are identical and located symmetrically to the centre axis, $y_1 = y_2$, $d_{w1} = d_{w2}$ and $d_{B1} = d_{B2}$ and the sum of (7.24) and (7.25) is the same as for the y component in the symmetrical case (7.13).

The combined total eddy current loss per kilogram within the region affected by non symmetrically arranged short circuits can be calculated taking proportional values of each component by weight.

$$P_{exy} = \frac{\text{mass}(P_{ex})}{mass(total\ affected)}P_{ex} + \frac{\text{mass}(P_{ey1})}{mass(total\ affected)}P_{ey_1} + \frac{\text{mass}(P_{ey2})}{mass(total\ affected)}P_{ey_2} \quad \textbf{(7.26)}$$

It will be discussed later that the affected mass (or volume) is not a simple geometrical shape enclosed by the burrs and therefore it is difficult to predict the ratios proposed in this calculation. However, a simplified calculation based on a geometrical shape enclosed within the boundaries of the burrs can be used.

7.1.3 **Eddy current model considering non uniform B**

The flux density within a lamination is affected by the eddy currents and can be significantly decreased towards the middle of the lamination as shown in Figure 2.8 in Chapter 2.

An equation for flux density within a single lamination is derived in Appendix 1. The equation given by Russel in 1904 [82], Bozorth in 1951 [83] and applied by Hamzehbahmani in 2012 [84] applied to the model shown in Figure 7.2 is given by

$$\mathrm{B(x,t)} = \mathrm{B_{max}} \sqrt{\frac{cosh\ 2\mathrm{x}\sqrt{\pi \mathrm{f}\sigma\mu_0\mu_\mathrm{r}} + cos\ 2\mathrm{x}\sqrt{\pi \mathrm{f}\sigma\mu_0\mu_\mathrm{r}}}{cosh\ \mathrm{H_B}\sqrt{\pi \mathrm{f}\sigma\mu_0\mu_\mathrm{r}} + cos\ \mathrm{H_B}\sqrt{\pi \mathrm{f}\sigma\mu_0\mu_\mathrm{r}}}} cos\ (\omega \mathrm{t} - \gamma) \qquad \textbf{(7.27)}$$

where H_B is the thickness of the short circuited stack, x is the distance from the centre of the lamination (or stack of short circuited laminations), B_0 is the flux density at the surface of the lamination, σ is the conductivity of the material and γ is a phase difference between flux density on the surface and flux density inside of the lamination and is a function of x given by (7.28) and is a function of x which means that there is a phase lag in flux density between the surface and any point within the thickness of the sheet.

$$\gamma = arctan\left(\frac{\mathrm{k}}{\mathrm{h}}\right)$$

$$= \frac{-2\mathrm{A}\ sinh\left[\sqrt{\pi \mathrm{f}\sigma\mu_0\mu_\mathrm{r}}\mathrm{x}\right] sin\left[\sqrt{\pi \mathrm{f}\sigma\mu_0\mu_\mathrm{r}}\mathrm{x}\right] + 2\mathrm{B}\ cosh\left[\sqrt{\pi \mathrm{f}\sigma\mu_0\mu_\mathrm{r}}\mathrm{x}\right] cos\left[\sqrt{\pi \mathrm{f}\sigma\mu_0\mu_\mathrm{r}}\mathrm{x}\right]}{\mathrm{A2}\ cosh\left[\sqrt{\pi \mathrm{f}\sigma\mu_0\mu_\mathrm{r}}\mathrm{x}\right] cos\left[\sqrt{\pi \mathrm{f}\sigma\mu_0\mu_\mathrm{r}}\mathrm{x}\right] + 2\mathrm{B}\ sinh\left[\sqrt{\pi \mathrm{f}\sigma\mu_0\mu_\mathrm{r}}\mathrm{x}\right] sin\left[\sqrt{\pi \mathrm{f}\sigma\mu_0\mu_\mathrm{r}}\mathrm{x}\right]} \qquad \textbf{(7.28)}$$

Where A and B are both functions of material thickness and derived in APPENDIX I. Let the flux density within the stack shown in Figure 7.2 be as calculated in (7.27). Considering 1 m axial length and 1 m height of the block of the stack of laminations, in

case of elemental eddy current paths of width dx flowing at distance x from the centre of the conducting block and whose depth is dx, the flux enclosed in 1 m width of the path at any instant is given by

$$\phi = 2xB_{max}\sqrt{\frac{cosh\left(2x\sqrt{\pi f\sigma\mu_0\mu_r}\right)+cos\left(2x\sqrt{\pi f\sigma\mu_0\mu_r}\right)}{cosh\left(H_B\sqrt{\pi f\sigma\mu_0\mu_r}\right)+cos\left(H_B\sqrt{\pi f\sigma\mu_0\mu_r}\right)}}\,cos\,(\omega t-\gamma) \quad \textbf{(7.29)}$$

And the EMF induced in that portion of the path is given by

$$e_x = \frac{d\phi}{dt} = 2B_{max}x\omega\sqrt{\frac{cosh\left(2x\sqrt{\pi f\sigma\mu_0\mu_r}\right)+cos\left(2x\sqrt{\pi f\sigma\mu_0\mu_r}\right)}{cosh\left(H_B\sqrt{\pi f\sigma\mu_0\mu_r}\right)+cos\left(H_B\sqrt{\pi f\sigma\mu_0\mu_r}\right)}}\,Sin[\gamma - t\omega] \quad \textbf{(7.30)}$$

The RMS value is calculated as in

$$E_x = 2\sqrt{2}B_{max}f\pi x\sqrt{\frac{cosh\left(2x\sqrt{\pi f\sigma\mu_0\mu_r}\right)+cos\left(2x\sqrt{\pi f\sigma\mu_0\mu_r}\right)}{cosh\left(H_B\sqrt{\pi f\sigma\mu_0\mu_r}\right)+cos\left(H_B\sqrt{\pi f\sigma\mu_0\mu_r}\right)}} \quad \textbf{(7.31)}$$

The resistance of the portion of the path is $R_x = \frac{2\rho}{dx} = \frac{2}{\sigma dx}$, the eddy current is calculated according to ohms law as $i_x = \frac{E_x}{R_x}$ and the eddy current loss in this path per unit length and per unit width is equal to $i_x^2 R_x$ as in

$$P_{ex} = \left(\sqrt{2}B_{max}f\pi\sigma x\sqrt{\frac{cosh\left(2x\sqrt{\pi f\sigma\mu_0\mu_r}\right)+cos\left(2x\sqrt{\pi f\sigma\mu_0\mu_r}\right)}{cosh\left(H_B\sqrt{\pi f\sigma\mu_0\mu_r}\right)+cos\left(H_B\sqrt{\pi f\sigma\mu_0\mu_r}\right)}}dx\right)^2\frac{2}{\sigma dx}$$

$$P_{ex} = 4\pi^2B_{max}^2f^2\sigma\frac{\left(cosh\left(2x\sqrt{\pi f\sigma\mu_0\mu_r}\right)+cos\left(2x\sqrt{\pi f\sigma\mu_0\mu_r}\right)\right)}{\left(cosh\left(H_B\sqrt{\pi f\sigma\mu_0\mu_r}\right)+cos\left(H_B\sqrt{\pi f\sigma\mu_0\mu_r}\right)\right)}x^2dx \quad \textbf{(7.32)}$$

Integrating between the centre of the stack to the top and bottom of the stack gives

$$P_{ex} = \int_{x=0}^{x=\frac{H_B}{2}} 4\pi^2 B_{max}^2 f^2 \sigma \frac{\left(cosh\, 2x\sqrt{\pi f\sigma\mu_0\mu_r} + cos\, 2x\sqrt{\pi f\sigma\mu_0\mu_r}\right)}{\left(cosh\, H_B\sqrt{\pi f\sigma\mu_0\mu_r} + cos\, H_B\sqrt{\pi f\sigma\mu_0\mu_r}\right)} x^2 dx \quad \textbf{(7.33)}$$

Substituting $p = f\sigma\mu_0\mu_r$ this gives loss per one square meter

$$\begin{aligned} P_{ex} = {} & \frac{f^2 B_{max}^2 \sigma\sqrt{\pi}}{2p^{3/2}\left(Cos\left[\sqrt{p\pi}H_B\right] + Cosh\left[\sqrt{p\pi}H_B\right]\right)} \\ & \times \left(2\sqrt{p\pi}H_B Cos\left[\sqrt{p\pi}H_B\right] - 2\sqrt{p\pi}H_B Cosh\left[\sqrt{p\pi}H_B\right]\right. \\ & + (-2 + p\pi H_B^2) Sin\left[\sqrt{p\pi}H_B\right] \\ & \left. + (2 + p\pi H_B^2) Sinh\left[\sqrt{p\pi}H_B\right]\right) \end{aligned} \quad \textbf{(7.34)}$$

The loss per kilogram is therefore

$$\begin{aligned} P_{ex} = {} & \frac{1}{H_B}\frac{1}{D}\frac{f^2 B_{max}^2 \sigma\sqrt{\pi}}{2p^{3/2}\left(Cos\left[\sqrt{p\pi}H_B\right] + Cosh\left[\sqrt{p\pi}H_B\right]\right)} \\ & \times \left(2\sqrt{p\pi}H_B Cos\left[\sqrt{p\pi}H_B\right] - 2\sqrt{p\pi}H_B Cosh\left[\sqrt{p\pi}H_B\right]\right. \\ & + (-2 + p\pi H_B^2) Sin\left[\sqrt{p\pi}H_B\right] \\ & \left. + (2 + p\pi H_B^2) Sinh\left[\sqrt{p\pi}H_B\right]\right) \end{aligned} \quad \textbf{(7.35)}$$

For a symmetrical case, where $d_{w_1} = d_{w_2}$ and $d_{B_1} = d_{B_2}$ the same algorithm as for the x component can be used to derive eddy current loss component in the y direction but the integration is from $\left(\frac{W_L}{2} - d_{w_1} - d_{B_1}\right)$ to $\left(\frac{W_L}{2} - d_{w_1}\right)$ so is given by

$$\begin{aligned} P_{ey} = {} & \int_{\frac{W_L}{2}-d_{w_1}-d_{B_1}}^{\frac{W_L}{2}-d_{w_1}} 4\pi^2 B_{max}^2 f^2 \sigma \\ & \times \frac{\left(cosh\, 2y\sqrt{\pi f\sigma\mu_0\mu_r} + cos\, 2y\sqrt{\pi f\sigma\mu_0\mu_r}\right)}{\left(cosh\, W_L\sqrt{\pi f\sigma\mu_0\mu_r} + cos\, W_L\sqrt{\pi f\sigma\mu_0\mu_r}\right)} y^2 dy \end{aligned} \quad \textbf{(7.36)}$$

Substitutions $\left(\frac{W_L}{2} - d_{w_1} - d_{B_1}\right) = W_{L1}$ and $\left(\frac{W_L}{2} - d_{w_1}\right) = W_{L2}$ and $p = f\sigma\mu_0\mu_r$ are made to give the simplified expression

$$\begin{aligned} P_{ey} = &-\frac{f^2\sqrt{\pi}\sigma B_{max}^2}{p^{\frac{3}{2}}\left(cos\left[H_B\sqrt{p\pi}\right] + cosh\left[H_B\sqrt{p\pi}\right]\right)} \times \\ &\times \left(-sin\left[2\sqrt{p\pi}W_{L1}\right] + sin\left[2\sqrt{p\pi}W_{L2}\right] + sinh\left[2\sqrt{p\pi}W_{L1}\right]\right. \\ &- sinh\left[2\sqrt{p\pi}W_{L2}\right] \\ &+ 2\sqrt{p\pi}\left(cos\,2\sqrt{p\pi}W_{L1} - cosh\left[2\sqrt{p\pi}W_{L1}\right]\right)W_{L1} \\ &+ 2p\pi\left(sin\left[2\sqrt{p\pi}W_{L1}\right] + sinh\left[2\sqrt{p\pi}W_{L1}\right]\right)W_{L1}^2 \\ &- 2\sqrt{p\pi}\left(cos\left[2\sqrt{p\pi}W_{L2}\right] - cosh\left[2\sqrt{p\pi}W_{L2}\right]\right)W_{L2} \\ &\left.- 2p\pi\left(sin\left[2\sqrt{p\pi}W_{L2}\right] + sinh\left[2\sqrt{p\pi}W_{L2}\right]\right)W_{L2}^2\right) \end{aligned} \quad \textbf{(7.37)}$$

which results in the loss per kilogram given by

$$\begin{aligned} P_{ey} = &-\frac{1}{2d_{B_1}}\frac{1}{D}\frac{f^2\sqrt{\pi}\sigma B_{max}^2}{p^{\frac{3}{2}}\left(cos\left[H_B\sqrt{p\pi}\right] + cosh\left[H_B\sqrt{p\pi}\right]\right)} \times \\ &\times \left(-sin\left[2\sqrt{p\pi}W_{L1}\right] + sin\left[2\sqrt{p\pi}W_{L2}\right] + sinh\left[2\sqrt{p\pi}W_{L1}\right]\right. \\ &- sinh\left[2\sqrt{p\pi}W_{L2}\right] \\ &+ 2\sqrt{p\pi}\left(cos\,2\sqrt{p\pi}W_{L1} - cosh\left[2\sqrt{p\pi}W_{L1}\right]\right)W_{L1} \\ &+ 2p\pi\left(sin\left[2\sqrt{p\pi}W_{L1}\right] + sinh\left[2\sqrt{p\pi}W_{L1}\right]\right)W_{L1}^2 \\ &- 2\sqrt{p\pi}\left(cos\left[2\sqrt{p\pi}W_{L2}\right] - cosh\left[2\sqrt{p\pi}W_{L2}\right]\right)W_{L2} \\ &\left.- 2p\pi\left(sin\left[2\sqrt{p\pi}W_{L2}\right] + sinh\left[2\sqrt{p\pi}W_{L2}\right]\right)W_{L2}^2\right) \end{aligned} \quad \textbf{(7.38)}$$

The equations (7.35) and in (7.38) can be used to calculate the total eddy current taking proportional mass of P_{ex} and P_{ey} by weight.

Chapter 8. **Artificial burrs application**

8.1 CHOOSING THE CONDUCTIVE MATERIAL FOR ARTIFICIAL BURR APPLICATION

Before choosing the final approach, several methods for creating artificial burrs were investigated including welding, conductive paint, drilling holes with bolts, aligned wires, metal wool and copper foil.

Welding as shown in Figure 8.1 is destructive and does not offer precision so short circuiting a planned number of laminations or area is difficult. Preliminary experiment made on a toroidal sample showed promising results, however it was impossible to separate the effects caused by pure electrical connections created by the weld and the effects on the property of the material and its coating caused by the welding itself.

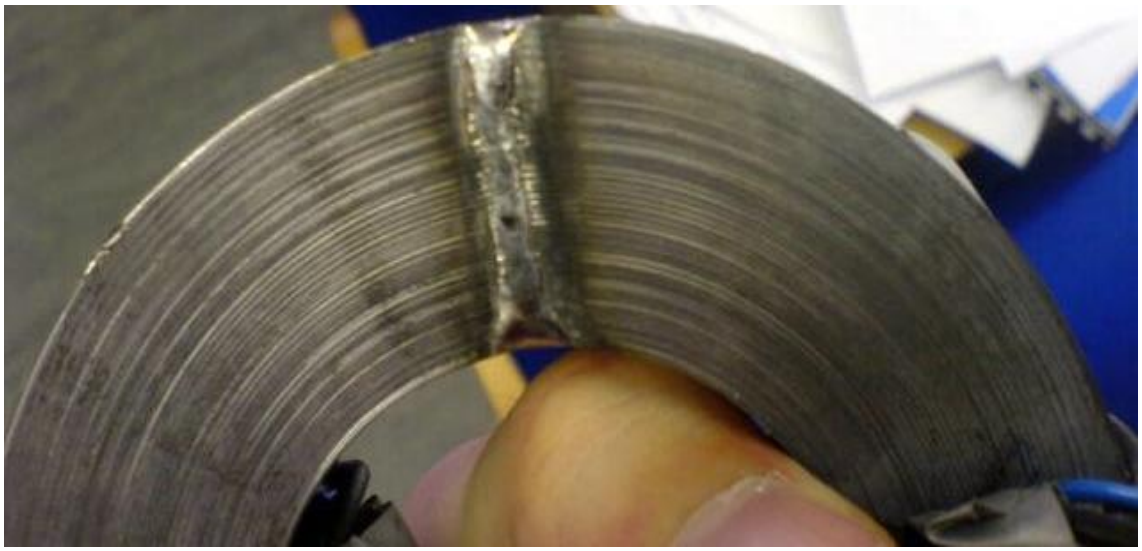

Figure 8.1 Welding as an example of artificial burr application.

Conductive paint as shown in Figure 8.2, as described in previous work [77], did not maintain contact under magnetisation conditions and therefore was discarded as unreliable.

Figure 8.2 Conductive paint as an example of artificial burr application.

Drilling holes and inserting bolts into them as shown in Figure 8.3 was investigated to provide an improvement in stability and repeatability. However, the bolts suffered wear with each insertion and the results were not repeatable across the range of measurements which were made in an Epstein frame at flux densities 0.1 to 1.9 T for 50 Hz. Figure 8.4 shows the results of three consecutive measurements of specific total power loss measured with bolts used as the artificial burrs. From these results it is clear that the effect of increased power loss reduces with each application.

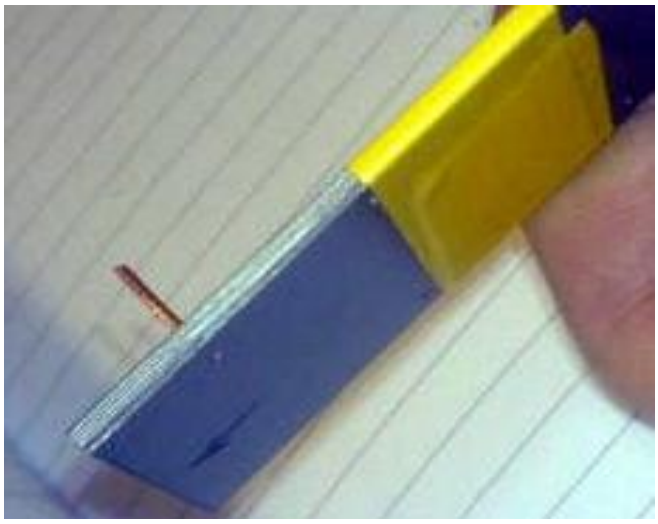

Figure 8.3 Bolts 1 mm diameter inserted into holes drilled in Epstein strips as artificial burr application.

Wires aligned together glued to a plastic frame as shown in Figure 8.5 were pressed against the sides of the toroidal core as shown in Figure 8.1. However, they again wore down quickly and the measurements were not repeatable.

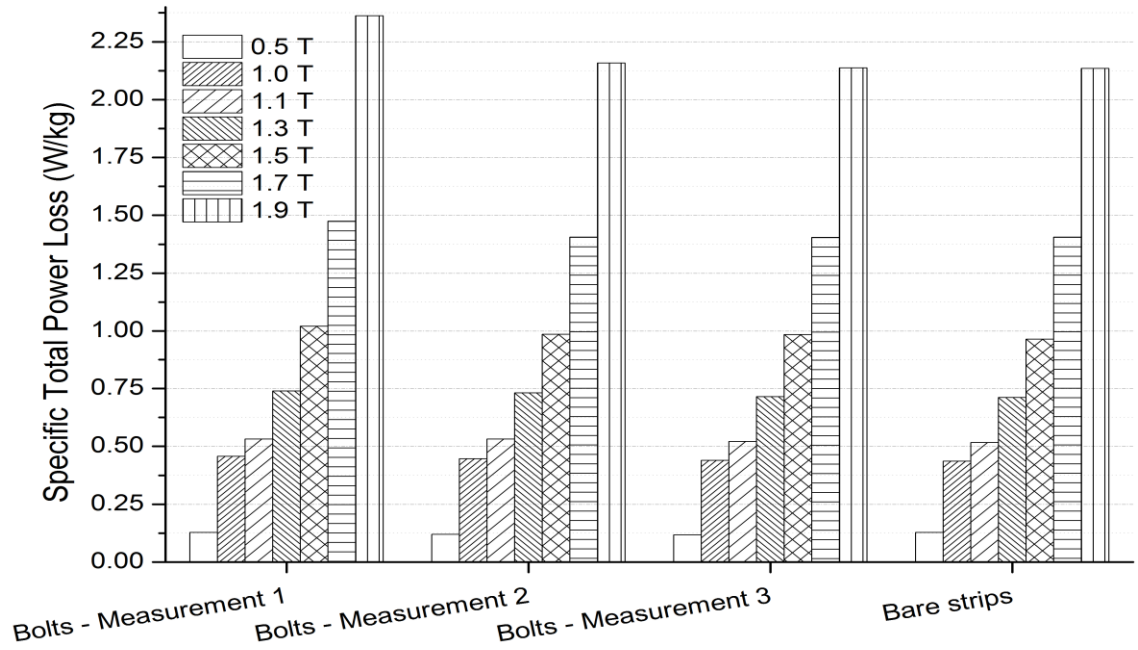

Figure 8.4 Specific total power loss measurements with use of copper wire bolts inserted in holes drilled in Epstein strips as artificial burrs. Three consecutive measurements show that the effect reduces which suggests wearing of the bolts used.

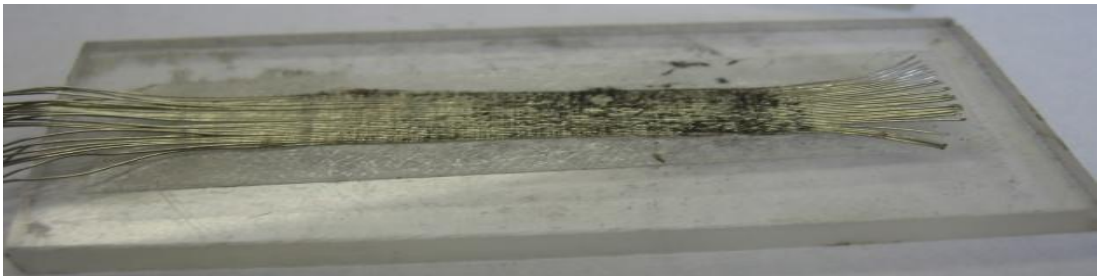

Figure 8.5 Aligned wires as an example of artificial burr application. The wires aligned together were pressed

Wire wool as shown in Figure 8.6 (left) was tested in the same way as the aligned wires as a material which would not deform; however, it also gave unrepeatable results.

Copper foil of approximately 8 micron thickness as shown in Figure 8.6 (right) pressed against the edges of the core limbs by means of a clamping device has shown good repeatability with reliable contact of the artificial burr to the electrical steel.

Figure 8.6 Wire wool (left) and copper foil (right) as an example of artificial burr application.

8.1 CLAMPING AS MEANS TO ENSURE REPEATABILITY

In initial experiments, to ensure a good contact of the artificial burr materials with the side of the sample stacks of laminations, toroidal samples and Epstein square, off the shelf clamping devices were used such as a G-clamp as illustrated in Figure 8.7. It lacked control of the pressure applied and therefore had to be replaced.

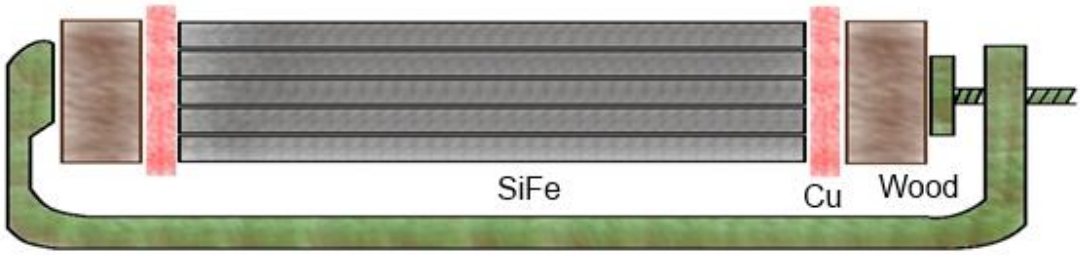

Figure 8.7 Clamping arrangement of the artificial burrs on small samples and stacks.

A clamping device shown in Figure 8.8 was designed to fit the experimental core described in section 9.1. It consists of two steel plates secured by four bolts enabling a known pressure to be applied to the copper foil on both sides of a stack of laminations. Wooden blocks were used as insulation between the steel clamps and the lamination edges as illustrated in Figure 8.8. The effect of the clamps without artificial burrs applied on the total specific power loss of the core was negligible as shown in Figure 8.9.

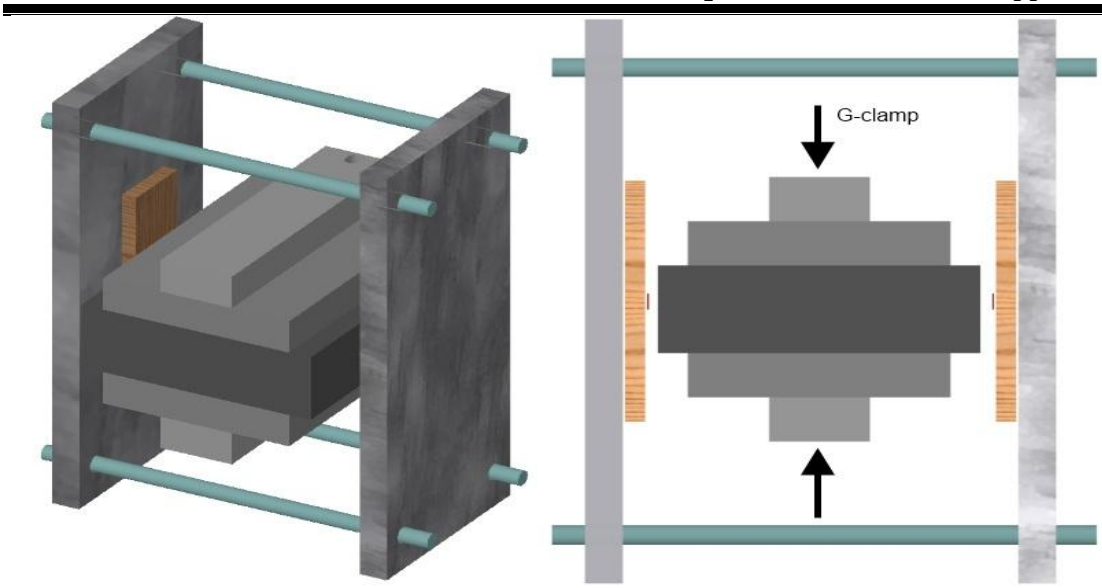

Figure 8.8 Clamping device designed for application of artificial burrs to the sides of a stack of laminations. Three-dimensional view (left) and cross sectional view (right).

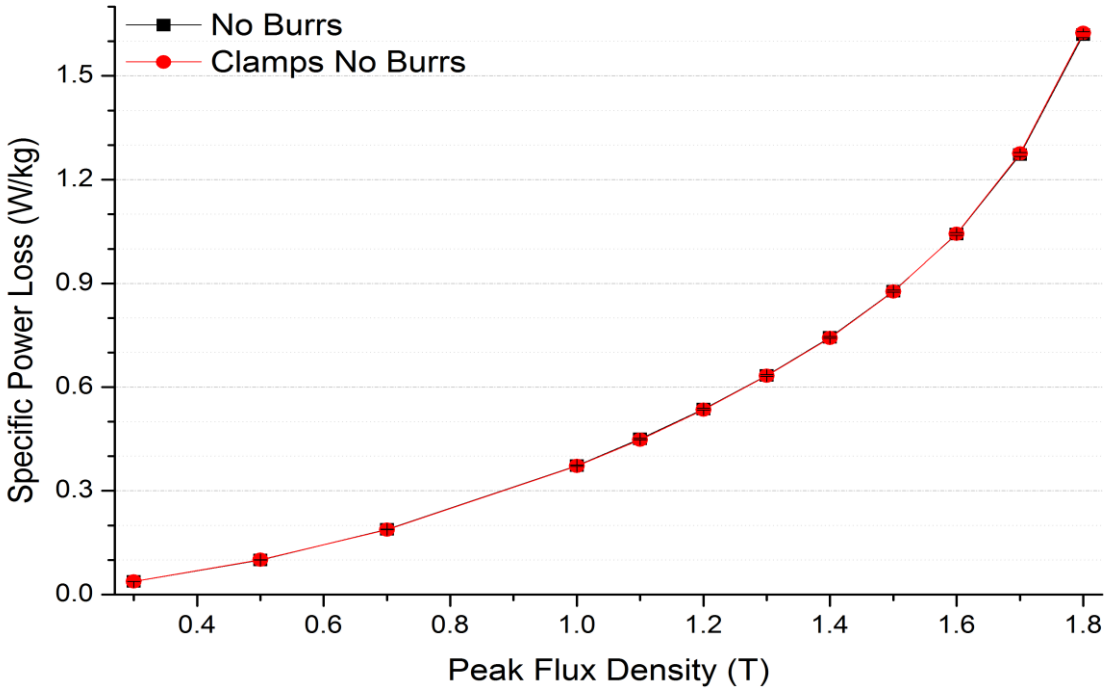

Figure 8.9 Effect of the clamping device on the total specific core losses of the three phase transformer.

The procedure was to stick the conductive foil using an adhesive onto the wooden blocks located on both sides of the stack and gradually tighten each of the four bolts in turns to ensure even pressure distribution. Torque value of 20 Nm on each bolt was chosen as a value ensuring repeatable experimental results. An additional G-clamp holding the core laminations from top to bottom as illustrated in Figure 8.8 was applied

in the experiments to prevent the stack of laminations from bending in an arc under the pressure from the main clamping device.

A detailed sketch of the components of a single artificial burr application is shown in Figure 8.10. The edge of the limb of the experimental transformer is shown on the left. Right next to the edge is the conductive material used to create electrical contacts between laminations. An insulation block of wood ensures insulation between the core and the steel plate of the clamping device.

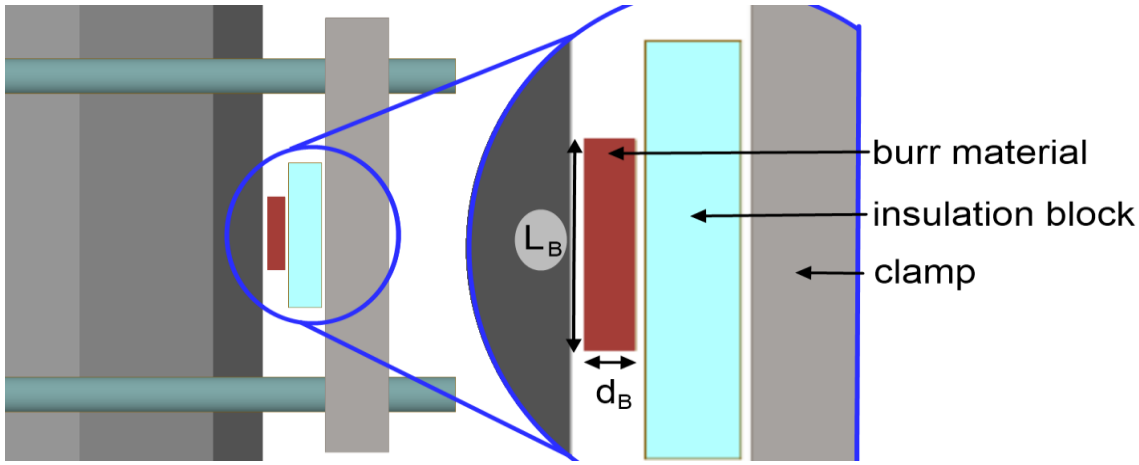

Figure 8.10 Artificial burr setup zoomed in - top view.

The clamping device allows applying burrs of various sizes to the experimental core. A schematic of the application location is shown in Figure 8.11. A burr of height H_B and length L_B is applied here to stack C of one of the transformer core limbs.

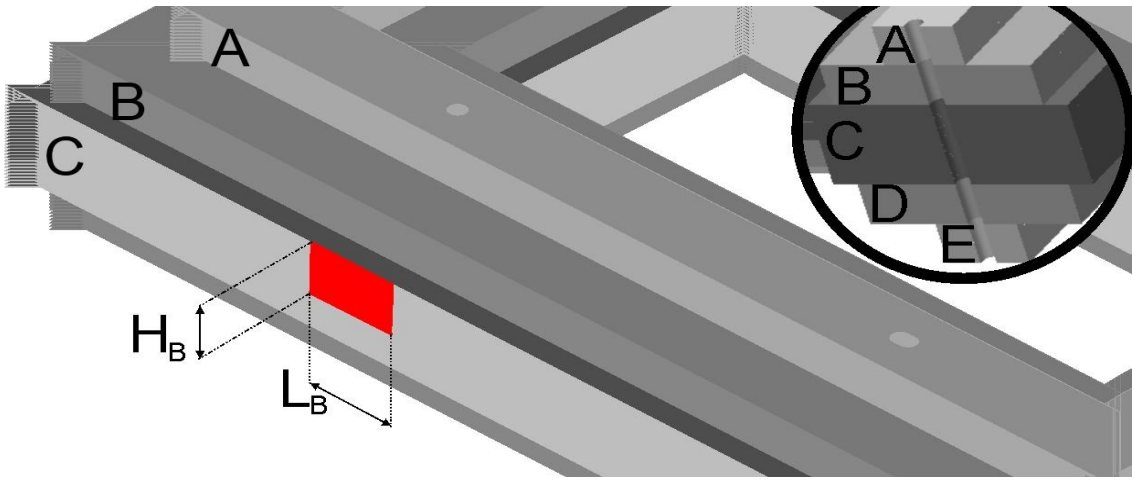

Figure 8.11 Artificial burr placement and dimension labels.

The clamping device allows for application of artificial burrs in several different configurations on the core layout. The possible short circuit placement is shown in Figure 8.12. Two clamping devices can be placed on the same limb allowing application of the short circuits not opposite each other but in a shifted configuration.

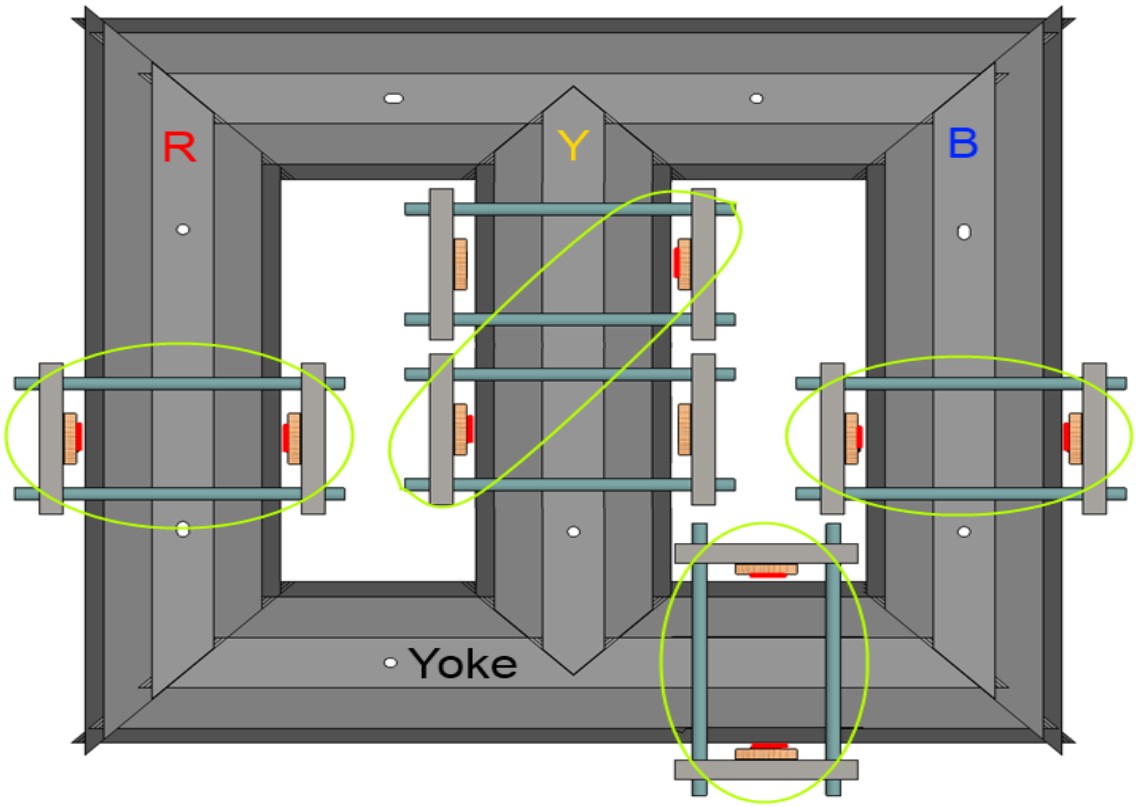

Figure 8.12 Sketch of example artificial burr clamping placement configurations: opposite burr placement on limbs R,.B, opposite burr placement on the yoke and shifted burr placement on limb Y

Two sets of clamping devices as shown in Figure 8.8 were produced; they were used for all experiments with artificial burrs applied to the experimental core in this project.

8.2 OTHER IDEAS FOR ARTIFICIAL BURRS APPLICATION

A device for introducing artificial burrs inside pin guide holes of the experimental core was designed as shown in Figure 8.13. The device consists of a threaded bolt of 6 mm diameter inserted into a steel pipe 8 mm in outer diameter which is inserted into a

copper pipe of 10 mm in outer diameter. The principle is to insert the device into the pin guide hole which is 10 mm in diameter and tighten the screws on the threaded bolt. The profile on the ends of the steel bar transfers the pressure from the direction along the threaded bolt to the direction perpendicular to it. Although the working principle of the design was discussed with mechanical engineers and assessed correct, due to the scale of the device it was not functioning well enough to ensure identical and uniform pressure applied with each use. Likely the reason for this was that the inner steel tubing was not rigid enough.

Other ideas which for various reasons were not pursued in this investigation include filling the pin guide hole with conductive paste and inserting and pressurising an expandable tube.

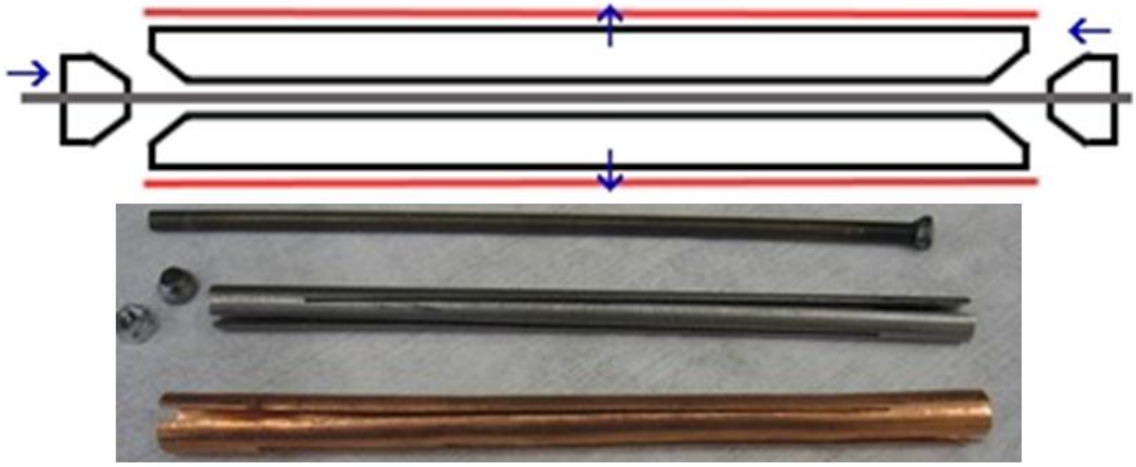

Figure 8.13 Schematic and a picture of the device designed for application of pressure to artificial burrs inserted into the pin guide holes of the experimental core.

Chapter 9. **Transformer core, sensor laminations and measurement methods**

9.1 TRANSFORMER CORE IN THE PROJECT

A three phase, 388 kg, 350 kVA, multi step-lap, power transformer core as shown in Figure 9.1 assembled from 0.3 mm thick laminations of high permeability grain oriented 3% SiFe (HGO) with nominal loss of 0.97 W/kg at 1.7 T, 50 Hz was used for all experiments in this investigation involving an assembled core. The cross section of this core with five packets of three different widths is shown in Figure 9.2. The seven step-lap configuration shown in Figure 9.3 was used. Holes and slots used as guides during assembly of the core are shown in Figure 9.4. The core is clamped with wooden clamps across the two yokes with a torque of 20 Nm on the bolts. At the beginning of the project the core was inspected visually in search of any defects and visible burrs. No defects were found.

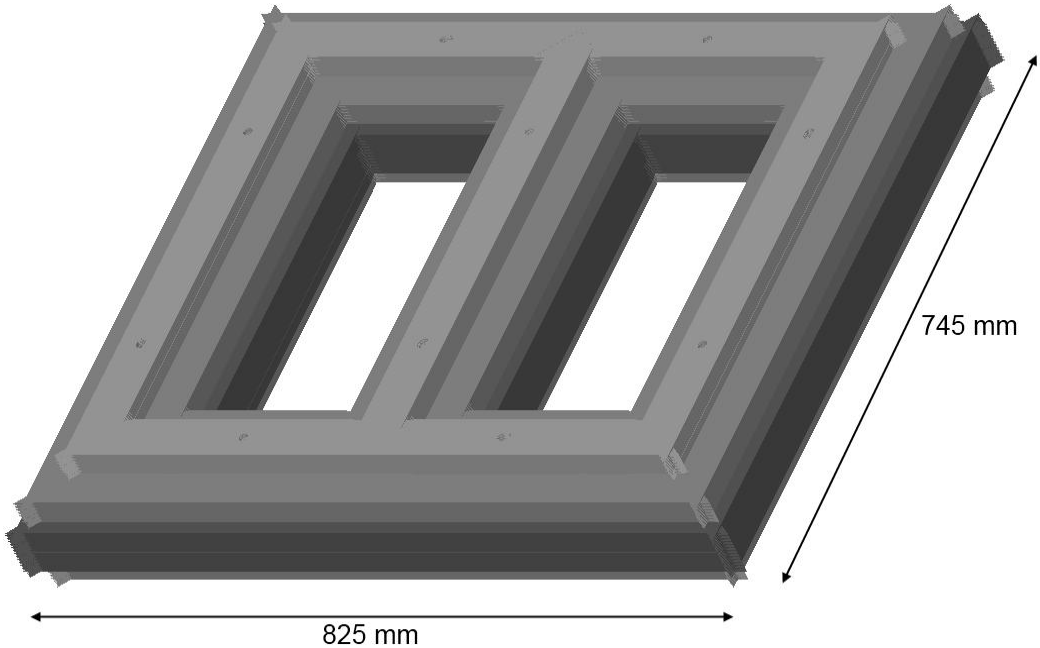

Figure 9.1 Surface view of the three phase 388 kg, 350 kVA, multistep-lap, transformer core used in investigation of effect of artificial burrs.

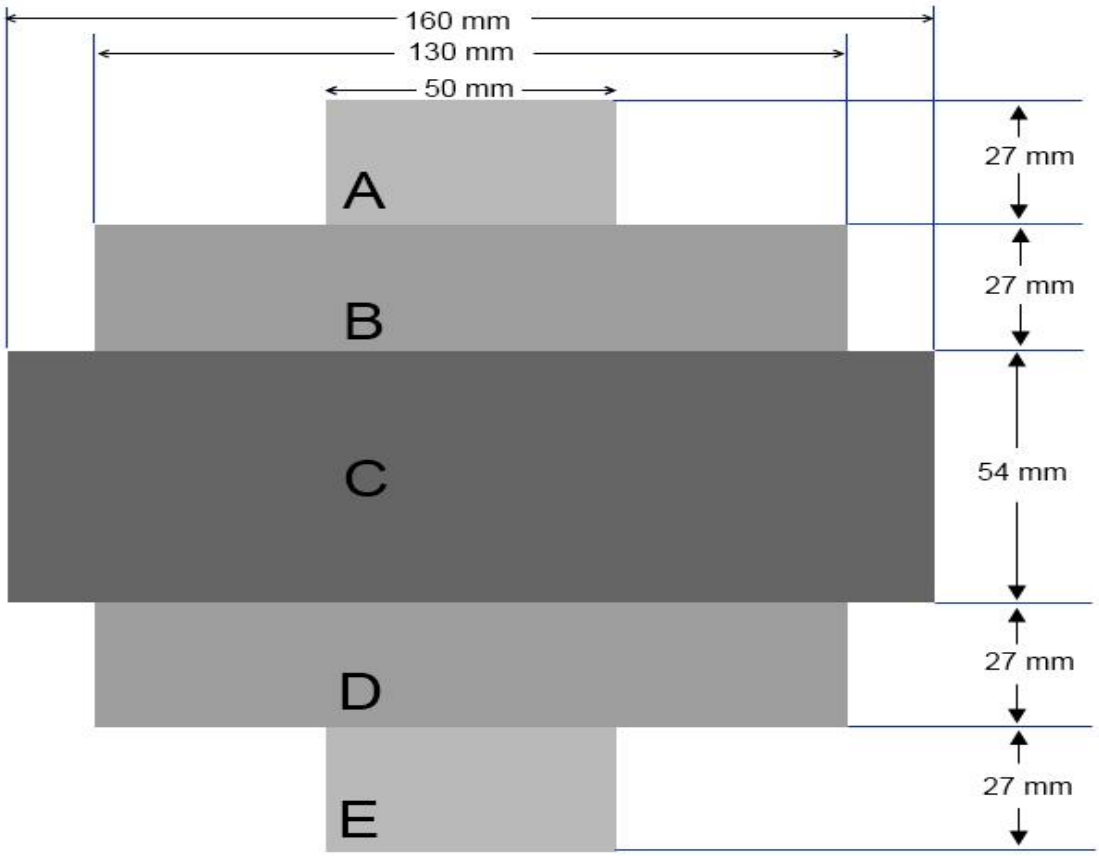

Figure 9.2 Cross section view of a limb of the experimental core with dimensions and stacks A-E labelled.

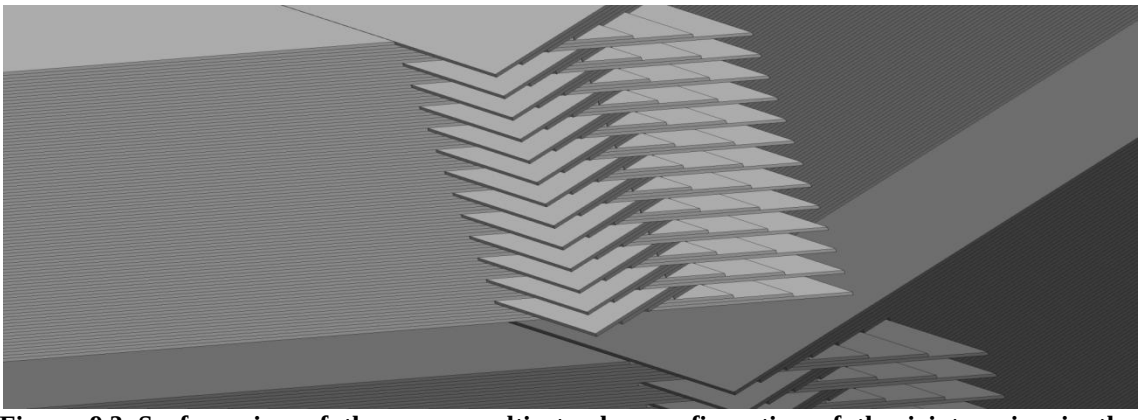

Figure 9.3 Surface view of the seven multi step-lap configuration of the joint region in the transformer core. Seven steps are used in this design.

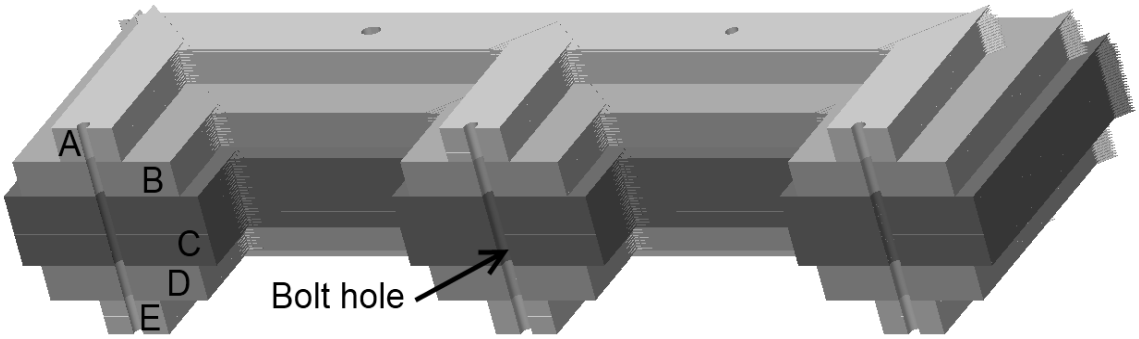

Figure 9.4 Cross-sectional view of the core with 5 stacks of laminations labelled A-E and bolt holes in each limb.

9.2 LAMINATIONS USED FOR THIN FILM SENSOR DEPOSITION

Thin film sensors produced on transformer laminations using PVD technique are presented in this section. A confirmation of the method was made on a 50 mm wide lamination with a layer of lacquer applied as base and insulation of the sensor from the steel. A sketch of the needle probe sensor measuring flux density across a 30 mm width is shown in Figure 9.5.

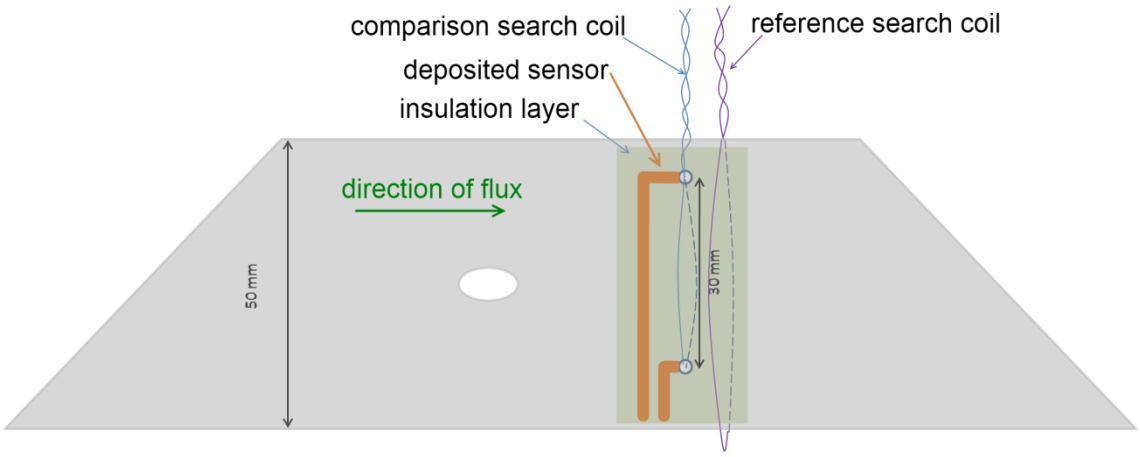

Figure 9.5 Thin film needle probe made using PVD on a 50 mm wide lamination. A transparent lacquer was used to insulate the steel from the deposited sensor. Deposited sensor is adjacent to a search coil measuring the same flux density. A reference search coil measured flux density of the whole lamination.

The method of thin film sensors produced on transformer laminations using PVD technique was validated on a 50 mm wide lamination with a layer of lacquer applied as base and insulation of the sensor from the steel. The results as shown in Figure 9.6 confirm that the two sensors give the same results with the difference reaching approximately 2.5% at 1.7 T.

The peak flux density measured using the needle probe sensor and the equivalent search coil for a range of flux densities is shown in Figure 9.7. The error between the two measurements is within 1 % for the range of flux densities 0.1 T – 1.6 T and rises to 5% for 1.8 T.

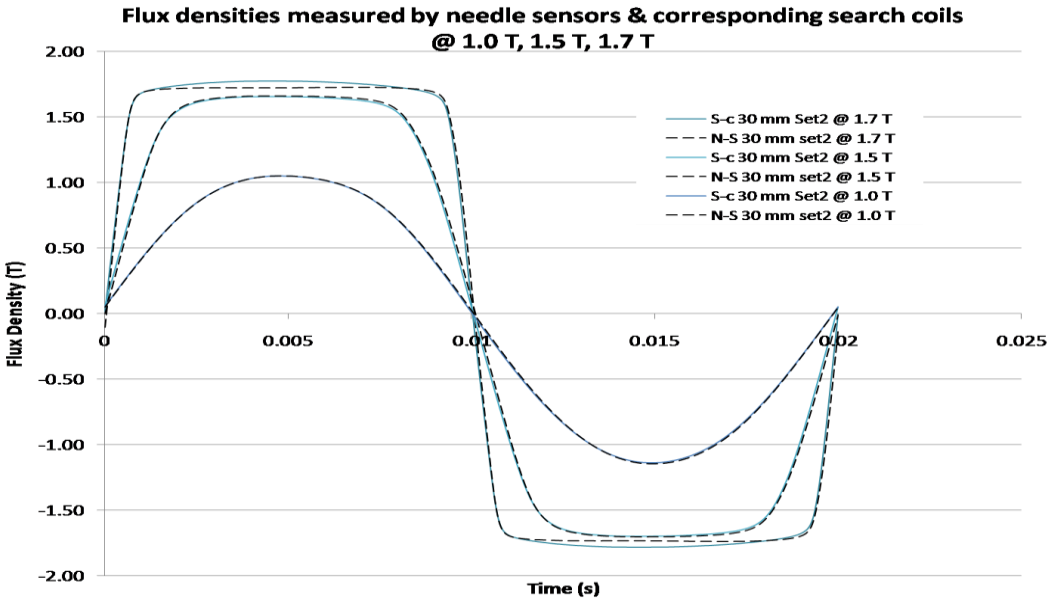

Figure 9.6 A comparison of flux density measured by a search coil and a needle probe flux density sensor. Both sensors measuring across 30 mm width of the sample as shown in Figure 9.5.

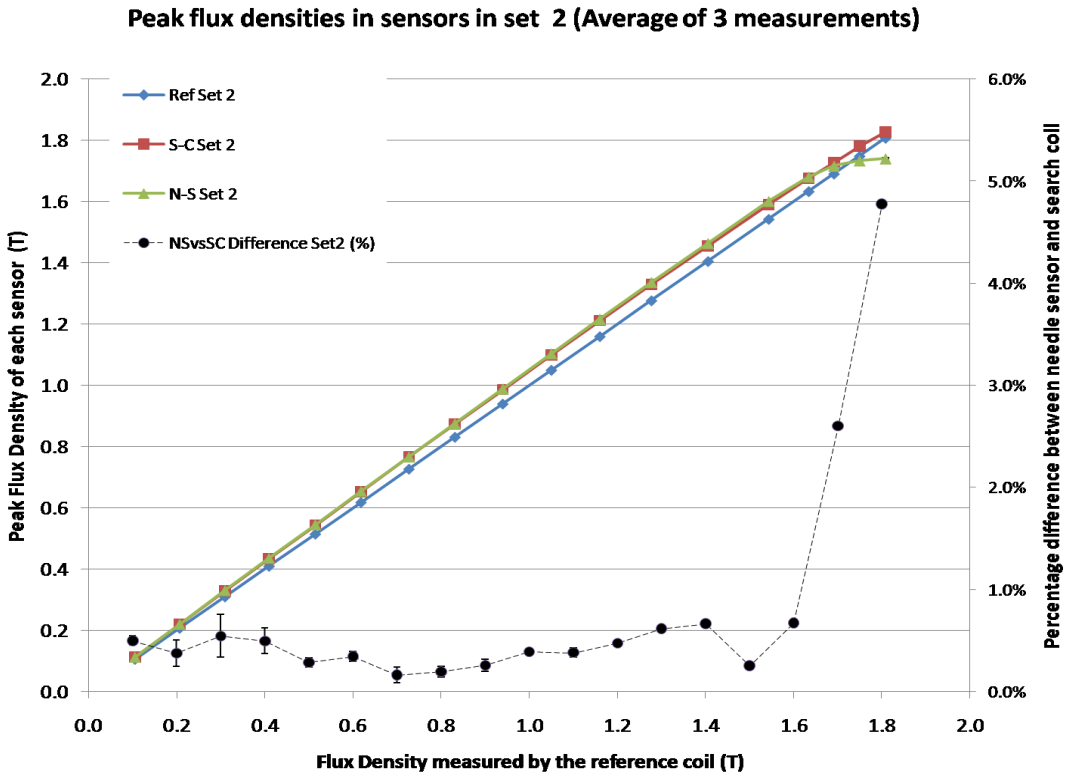

Figure 9.7 Peak flux density measured by the deposited needle sensor, comparison search coil and the reference search coil as shown in Figure 9.5.

The set of four thin film needle sensors shown previously in Figure 6.18 were placed within a stack of the experimental transformer core. The resulting setup is shown in Figure 9.8.

Figure 9.8 The lamination with thin film flux density needle probe sensors as shown in Figure 6.18 placed within a stack of the experimental core.

Figure 9.9 shows a set of thin film flux density needle probe sensors designed for measurement in rolling direction as well as in the transverse direction.

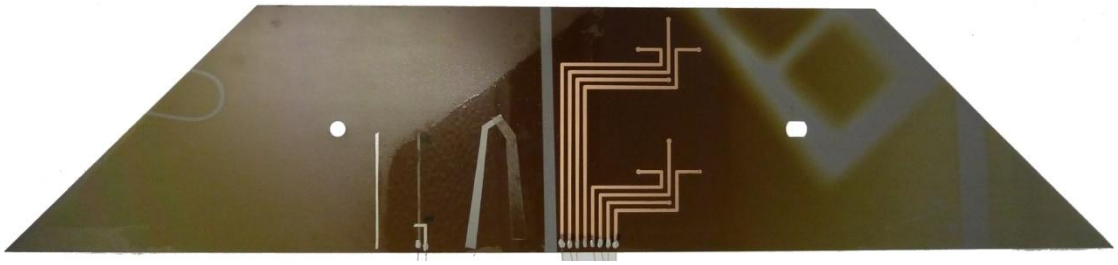

Figure 9.9 A set of thin film flux density needle probe sensors designed to measure flux density in rolling and transverse direction.

9.3 TOTAL CORE LOSS MEASUREMENT SETUP AND METHOD

The experimental transformer core was wound with 30 primary and 30 secondary turns of insulated copper wire connected in a star – star configuration as shown in Figure 9.10. The no-load core loss of the core was measured using a NORMA D6000 power analyser using primary currents I_1, I_2, I_3 and secondary induced voltages V_1, V_2 and V_3; A 415 V, three phase constant voltage transformer (CVT) designed to supply currents to unbalanced loads and equipped with three variable transformers to allow control of its output currents as shown in Figure 9.10, was used to magnetise the core. Using this setup, the flux density up to 1.8 T at 50 Hz could be applied symmetrically in

each limb to an accuracy of better than 0.3 %. If required, artificial burrs were applied to the core and the setup description input within the LabView program to be recorded in the result file.

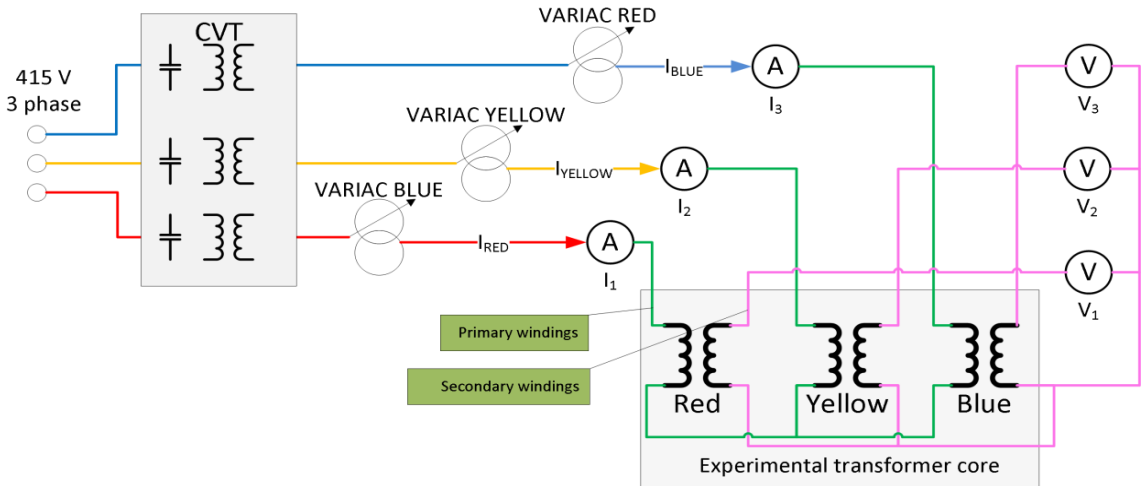

Figure 9.10 Schematic diagram of the experimental three phase transformer core measurement rig. The primary current and secondary voltage measurements are used for total power loss measurement using the NORMA D6000 in a three watt meter method mode.

A LabView program was developed to control the power analyser and collect the measurement values. A partial screenshot with all functionalities labelled is shown in Figure 9.11. The labelled areas contain functionalities responsible for

- creating a new result file
- writing a description of the experiment to be written in the result file
- setting core design and material parameters
  - core density
  - cross section area
  - stacking factor
  - number of turns of windings,
- resetting the NORMA D6000 display settings
- setting the flux density required
- displaying measured values of
  - induced voltages with percentage difference from expected value and corresponding flux densities
  - other real time measurement values.

Primary currents measured are highlighted in red and audible alarm is sound if the current exceeds the shunt limit.

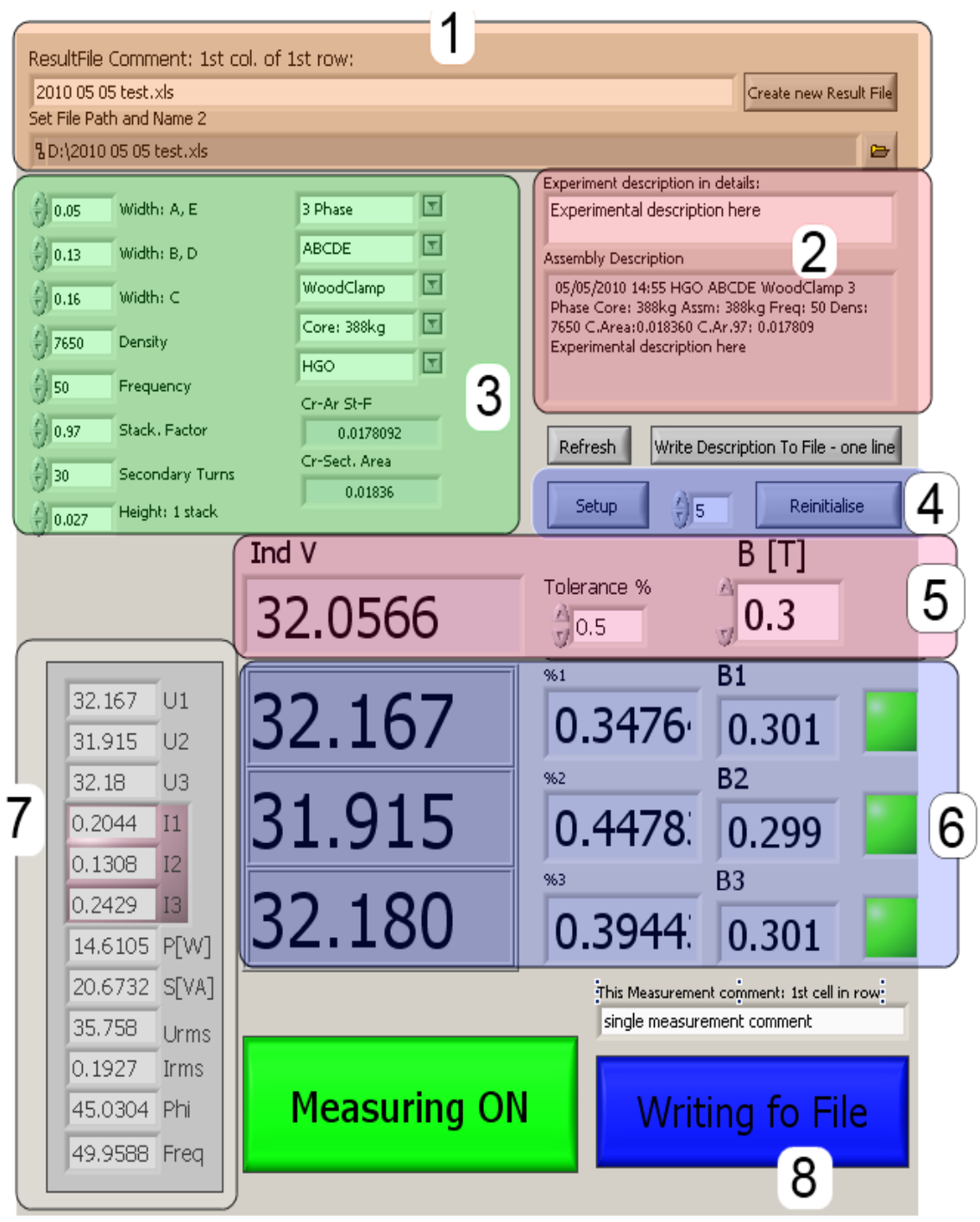

Figure 9.11 Screenshot of the LabView program to control NORMA D6000 power analyser. 1 – creating a new result file, 2 – adding experiment description to the result file, 3 – setting core design and material parameters, 4 – setting of NORMA D6000 configuration file, 5 – Setting flux density with its tolerance for the measured values and expected secondary induced voltage, 6 – measured values of induced voltages with percentage difference from expected value and corresponding flux density, 7 – NORMA D6000 measurement values in real time, 8 – writing to result file.

LabView program monitored the secondary voltages and indicated when they were within the desired accuracy and allowed to record all the measured values including date, time, desired flux density, percentage difference of desired flux density and measured flux density on each limb, measured rectified mean voltages on each limb, measured rectified mean square currents in each primary winding, power loss, apparent power, phase angle and frequency.

9.4 LOCAL LOSS MEASUREMENT

Magnetisation of the core was made as described in section 9.3. The local loss measurement was made based on the initial rate of rise of temperature method using type K wire thermocouples. The magnetisation variacs were preset to magnetise the core to the required flux density and the system was switched off to allow the core temperature to return to room temperature which was confirmed by comparing temperature measurements made in interval of 10 minutes. The system was then switched on and the change of temperature in the investigated locations was measured and recorded. The loss was deduced from the initial rate of rise of temperature applied to the obtained temperature traces. Uncertainty of the localized loss measurements was estimated at ± 6.2 % taking into account factors such as: acquisition card accuracy, accuracy of the integrated circuit board components, noise filters, selection of the linear part of the temperature rise and control of B_{max}. The details are presented in Table 9.1.

Table 9.1 Uncertainty of local loss measurement using initial rate of rise of temperature.

Source of uncertainty	Value	Probability	Divisor	U(xi)±%
Accuracy of PCI-6052E DAQ	0.05	Normal	2	0.025
CJC	0.5	Normal	2	0.25
Themocouple amplifier	0.5	Normal	2	0.25
Hot junction	0.5	Normal	2	0.25
Noise filter	1.0	Normal	2	0.50
Subjective decision on linear part	5.0	Rectangular	√3	2.89
Specific coeffieicnt	1.0	Rectangular	√3	0.58
Type A uncertainty (repeatability)	0.7	Normal	1	0.70
Sum of squares				9.595
Combined standard uncertainty				3.097
Expanded uncertainty U(B)				6.19
Declared uncertainty				6.2

9.5 FLUX DISTRIBUTION MEASUREMENT

Flux distribution within the core was measured by search coils looped around a required portion of laminations as well as by needle probe technique. Figure 9.12 shows a schematic diagram of a search coil wound around a portion of the core and a set of needle probes measuring flux density within one stack of laminations. Measurements using search coils require disassembly of the core in most cases while the measurement using needle probes can be made without any preparation on any location of the core magnetised as described in section 9.3. A Keithley 2001 multimeter was used for all needle probe measurements.

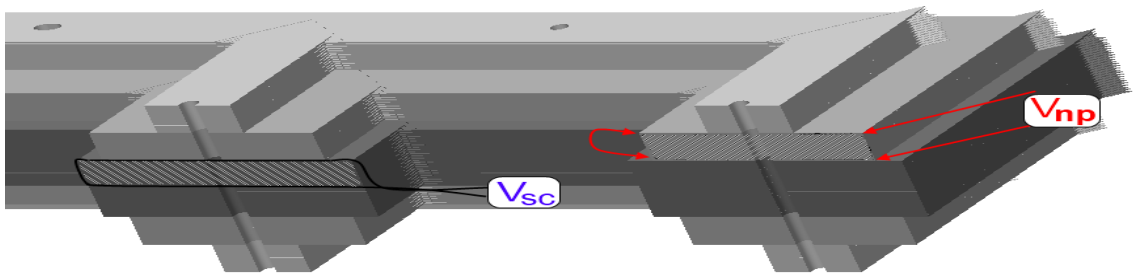

Figure 9.12 Schematic of flux density measurements made using wound search coils (V_{SC}) and a set of needle probes (V_{NP}).

9.6 TEMPERATURE MEASUREMENT

The temperature measurements in this project was made using PCI-6052E data acquisition card and a set of six integrated circuit thermocouple amplifiers with type K wire thermocouples. Thermocouples were positioned on the surface of the steel where the temperature measurement was desired. Thermocouple tips were isolated from the surrounding by insulating foam tape. The whole setup including the transformer core was kept within a semi adiabatic environment which was assured by bubble wrap insulation.

Chapter 10. **Results and discussion**

The results discussion begins with the proposed model of eddy current loss analysis followed by the investigation of effects of burrs on a toroidal core and the experimental transformer core with effects such as burr height, length and arrangement on total loss as well as flux density redistribution and local loss in the vicinity of the applied burrs. Finally the suitability of thin film needle probes for use within a commercial size transformer core is investigated.

10.1 DISCUSSION OF THE EDDY CURRENT LOSS MODEL

The eddy current loss model is discussed first because it is used as a comparison in later stages for some of the experimental results.

The eddy current loss models presented in Chapter 7 are an improvement over the classical methods as they do not neglect the eddy current component flowing in the direction perpendicular to the electrical steel sheet plane.

The simple model presented in 7.1.1 shows the idea of how to calculate eddy current losses in both directions for a symmetrical case while the expanded model presented in 7.1.2 introduces a way to calculate eddy current loss for cases where short circuits are not symmetrical on the two sides of the stack or are located within the stack rather than on the edge of it.

The third model adds consideration of non-uniform flux density within the stack of laminations and shows equations for flux density as a function of distance to the centre of the electrical steel sheet. However, the assumption of constant permeability

made in deriving (7.27) is oversimplified. The calculations cannot be performed analytically in a generalised way when permeability is taken as a function of flux density instead of (A.11.6). A more advisable approach is to model it as a function of x in deriving (7.27), however, in this case the calculations have to be performed numerically.

10.1.1 **Simple model discussed with result comparison**

The models presented in this thesis are based on an assumption that introduction of burrs does not change the hysteresis and excess losses which can be calculated for the experimental transformer core by subtracting the classical eddy current losses in a 0.3 mm thick sheet of electrical steel from the measured specific total core losses. This separation is shown in Figure 10.1.

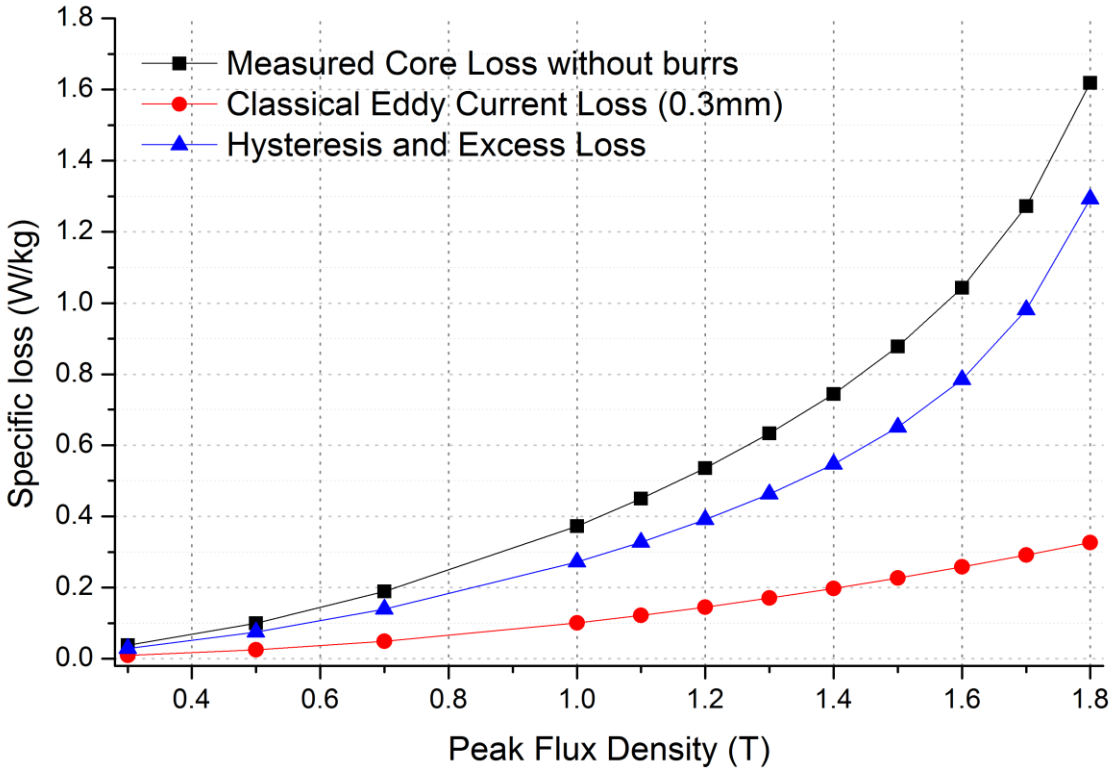

Figure 10.1 Variation of specific loss with the overall peak flux density of the experimental core in case of the core measurement, classical eddy current losses and hysteresis and excess losses.

Based on the above, the model was used to calculate the overall specific total core loss as a sum of the hysteresis and excess loss and a proportional sum of eddy current losses within unaffected region and within the region affected by the burr. Figure 10.2 shows that this model does not reflect the full character of the measured losses.

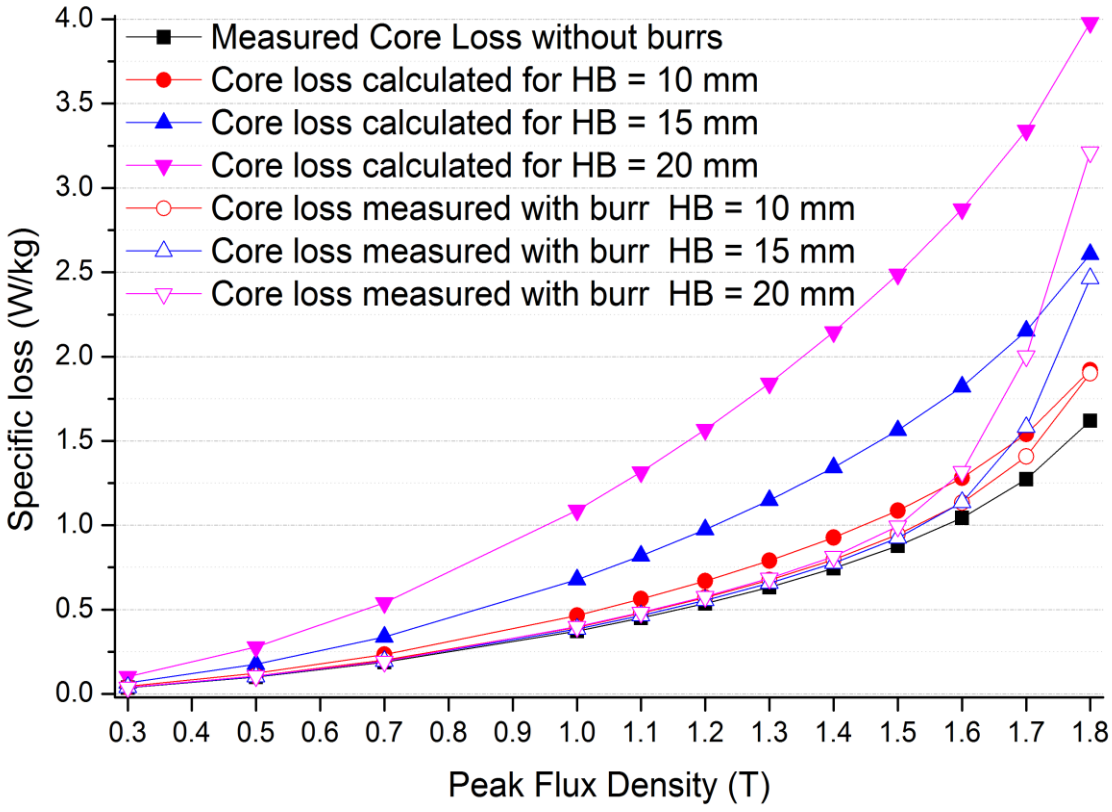

Figure 10.2 Variation of specific total loss of the core with peak flux density in case without burrs, with three size burrs and calculated core losses for the three burr sizes.

The problem here is the flux density redistribution within the affected region. This will be further discussed in the next section.

Measurement of flux density around the affected region brought the calculations closer to the measured core losses as shown in Figure 10.3. Therefore more attention needs to be paid to the flux redistribution within the region affected by burrs and within the stack of laminations the burrs are affecting.

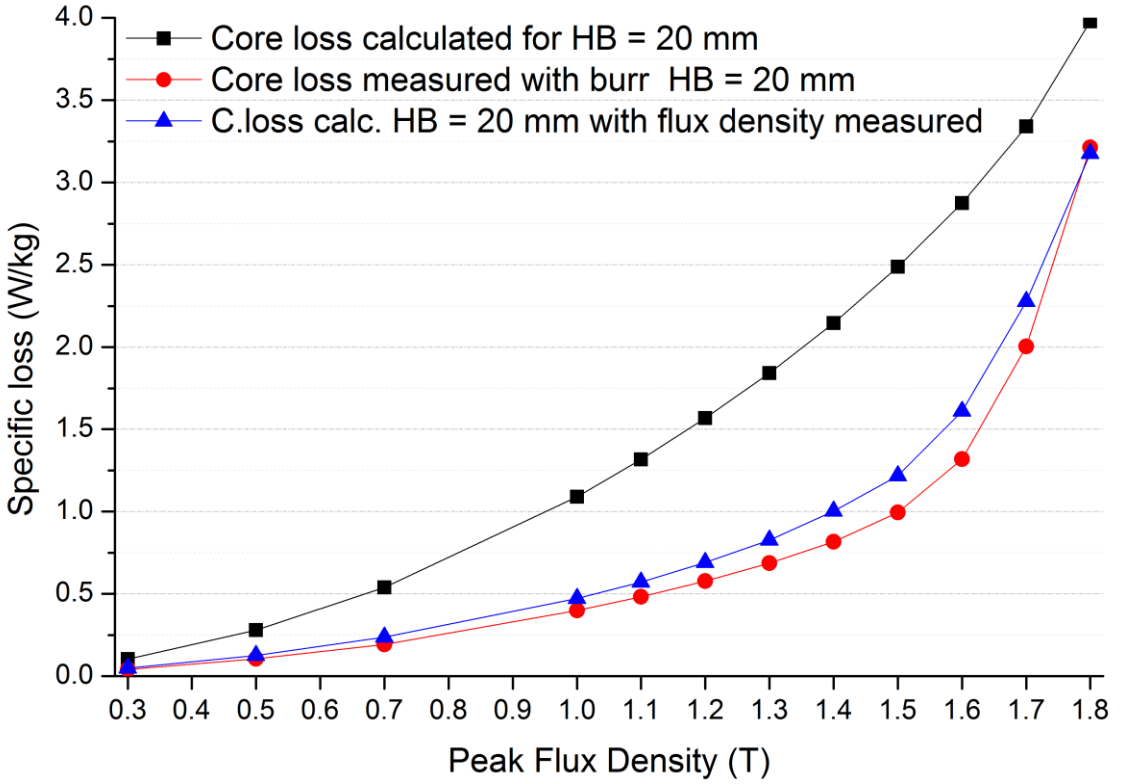

Figure 10.3 Variation of specific total loss of the core with peak flux density of the core. Comparison of measured loss, loss calculated using the overall peak flux densities and loss calculated using the measured flux density of the region affected by the burr of H_B = 20 mm.

10.1.2 **Flux density distribution model discussed**

Taking typical numbers of permeability, resistivity, frequency and height of artificial burrs applied to the core in this investigation, profiles of flux density within the material can be investigated.

Using (7.27) the relative profiles of peak flux density on the surface and within a sheet of electrical steel with resistivity of 48×10^{-8}, μ_r = 40 000 at 50 Hz for thicknesses H_B of 0.0003 m, 0.005 m, 0.01 m, 0.015 m, 0.02 m and 0.025 m were calculated as shown in Figure 10.4.

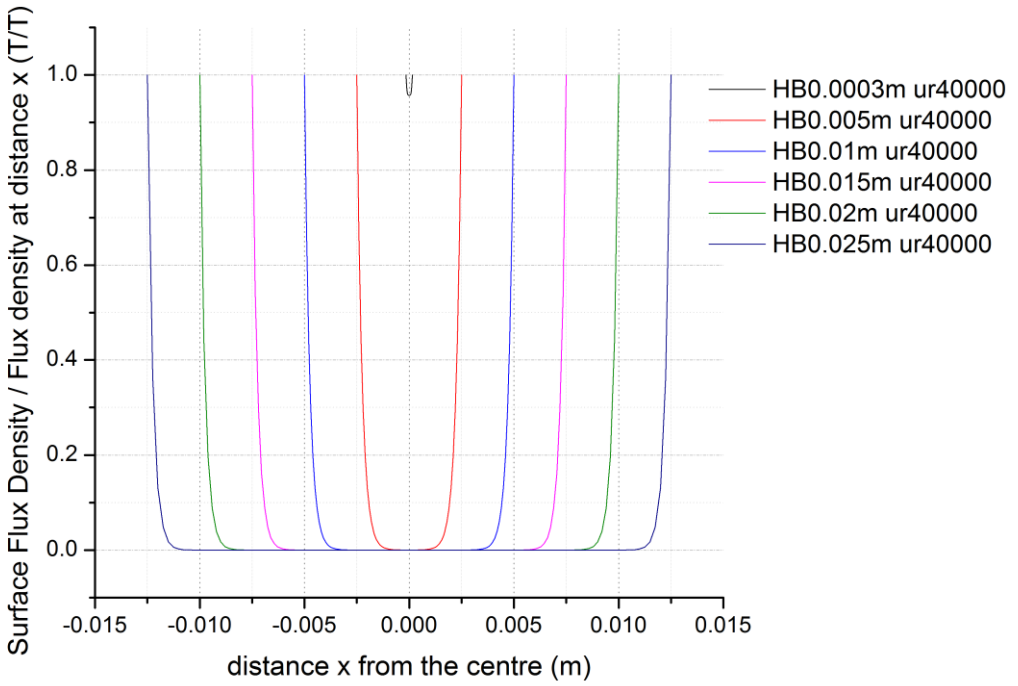

Figure 10.4 Relative flux density profiles on the surface and within electrical steel for thicknesses of 0.0003 m, 0.005 m, 0.01 m, 0.015 m, 0.02 m and 0.025 m, with μ_r = 40 000, $\rho=48\times10^{-8}$, at 50 Hz.

This illustrates that for electrical steel sheets of all thicknesses flux density is reduced in the middle part. For thickness of 5 mm, which is relevant to experimental work in this thesis, almost half of the material thickness is magnetically shielded and carries no flux while flux density in the remaining part of the sheet increases significantly above the overall flux density of the sheet assuming that the whole flux remains within the sheet.

A calculation of the flux density at the surface of the sheet, when the overall flux density of the sheet is known (ie. from measurement), is possible by comparing the integral of the constant value of the measured flux density with the integral of (7.27) which is illustrated in Figure 10.5. For a sheet of electrical steel of thickness 0.0003 m, $\rho = 48\times10^{8}\,\Omega$m, $\mu_r = 40000$, at 50 Hz which is magnetised to an overall flux density of 1.00 T, flux density at the surface of the sheet is 1.035 T and in the middle it reaches 0.991 T which gives a variation of 4.5 % in peak flux density within the sheet.

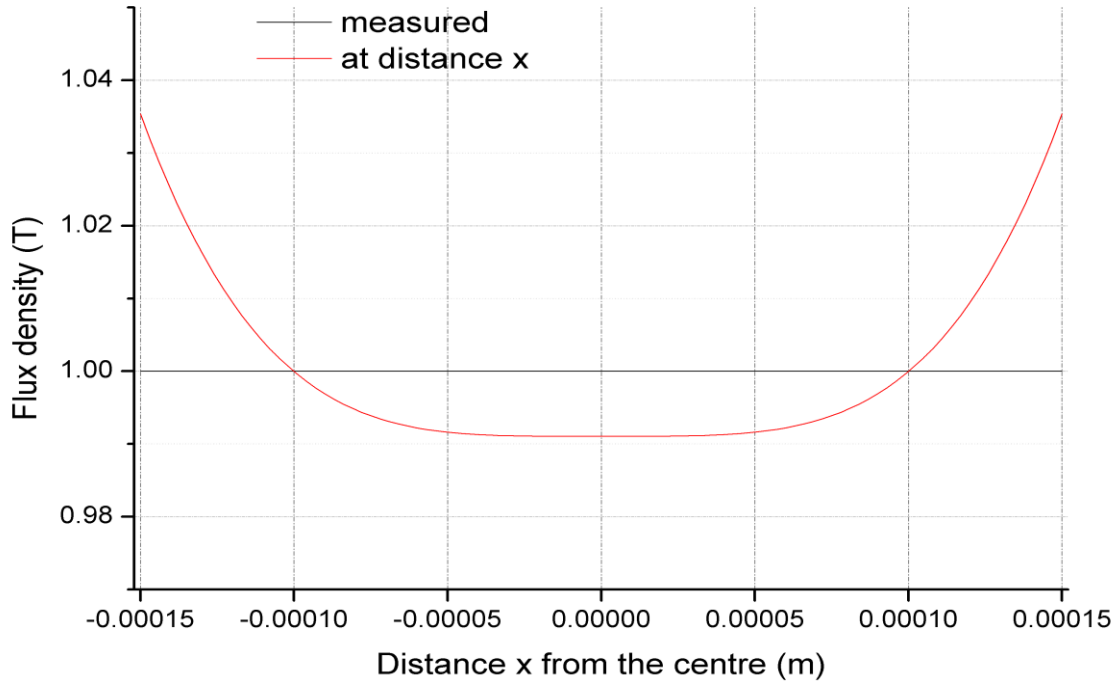

Figure 10.5 Peak flux density profile within a sheet of electrical steel with thickness 0.3 mm magnetised to 1.0 T at 50 Hz. Constant relative permeability μr = 40000 is assumed.

The effect of shielding the centre part of the sheet as shown in Figure 10.5 grows with the thickness of the sheet just as with the number of shortened laminations in a stack affected by burrs. Figure 10.6 shows this shielding effect for 5 mm thick sheet, where the ratio between the flux density measured and calculated using (7.27) reaches more than 10 which leads to incorrect values of flux density indicated by this model. This is a direct result of the assumption of constant permeability in the flux density profile model. It can be argued that for any value of the calculated flux density over 2.03 T permeability decreases to 1 (saturation) and therefore the flux density profile will look more like the yellow dotted line in Figure 10.6. The flux density marked by the stripped area is actually spread below the blue line across an area where permeability has not yet decreased to 1.

The relative profiles of flux density on the surface and within electrical steel sheet of 0.005 m thickness, resistivity of 48×10^{-8}, at 50 Hz for permeabilities μ_r = 1, 500, 1000, 4000 and 40 000 were calculated as shown in Figure 10.7. This result confirms

that for low permeability values, the flux density profile is closer to uniform while for high permeability, the shielding of the central part of the sheet is higher. This agrees with the variation of permeability against flux density and partially confirms the flat profile marked with a dotted yellow line in Figure 10.6.

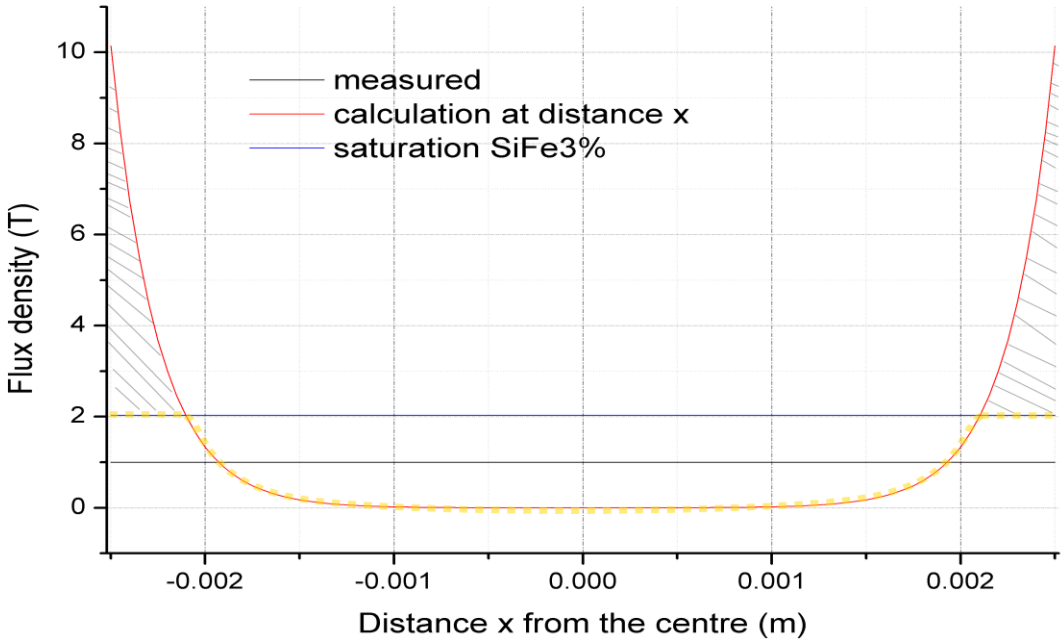

Figure 10.6 Peak flux density profile within a sheet of electrical steel with thickness 0.3 mm magnetised to 1.0 T at 50 Hz. Constant relative permeability μr = 40000 is assumed.

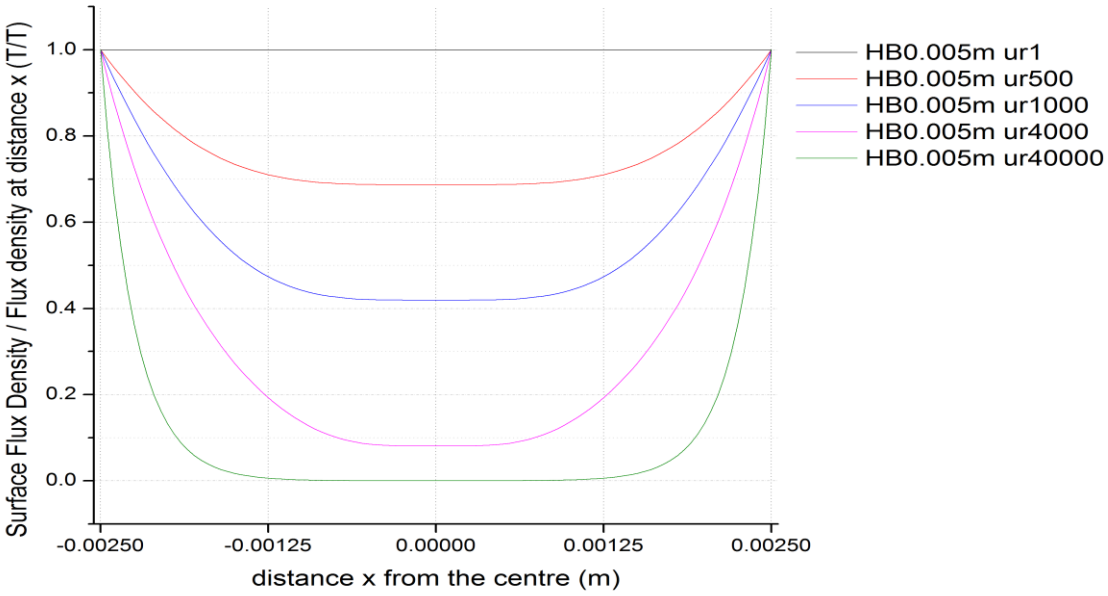

Figure 10.7 Relative profiles of flux density on the surface and within a sheet of electrical steel with thickness of 0.005 m, resistivity of 48×10^{-8}, at 50 Hz for permeabilities μ_r = 1, 500, 1000, 4000 and 40 000.

10.2 EFFECTS OF BURRS ON A TOROIDAL CORE

A wound toroidal core as shown in Figure 10.8 was used to undertake the initial experiments with burrs.

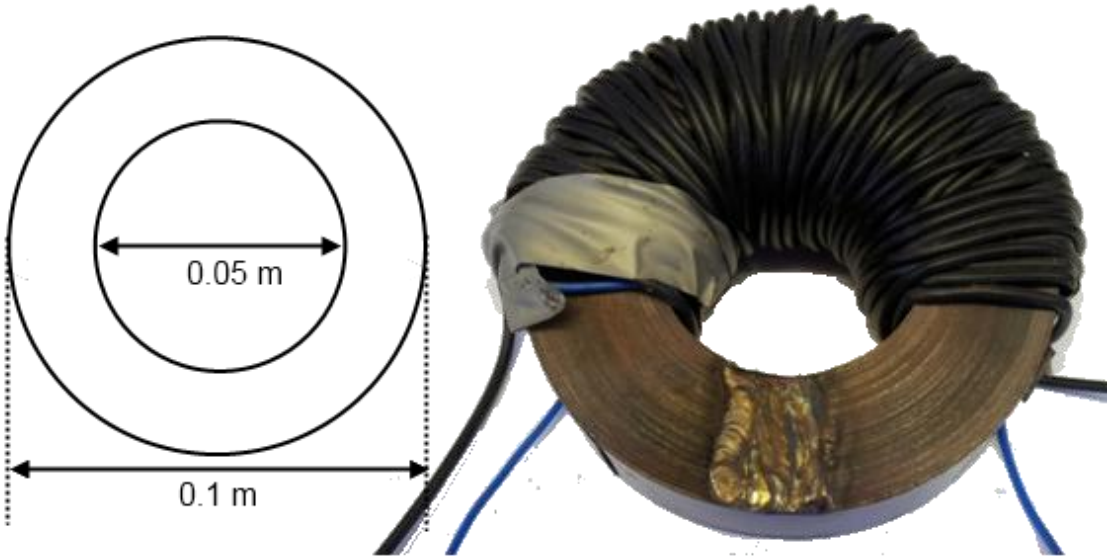

Figure 10.8 Toroidal core made of GO used for burrs application. Welding seen in the figure used as one of the burr application methods. Outer diameter 0.1 m, inner diameter 0.05 m, height 0.025 m, 100 primary windings (black), 10 secondary windings (blue).

The wound toroidal core weighing 1.09 kg with outer diameter of 0.1 m and inner diameter of 0.05 m and height of 0.025 m was threaded manually with 10 secondary turns and 100 primary turns as shown in the figure by blue and black wires respectively covering only half of the circumference of the core and leaving the rest of the core uncovered and accessible for application of artificial burrs.

Steel wool, copper wires pressed against the core and welding of the steel, as described in Chapter 8, were used to introduce short circuits in the core on one or both sides of the core.

10.2.1 **Burr location on the toroidal core**

Figure 10.9 presents results for burrs applied to the toroidal core on one and both sides with burr widths of 5, 10, 15 and 20 mm for welding, steel wool and aligned wires used as the shorting method. All burrs applied in this investigation short circuited the whole height of the stack as shown in red in Figure 10.10.

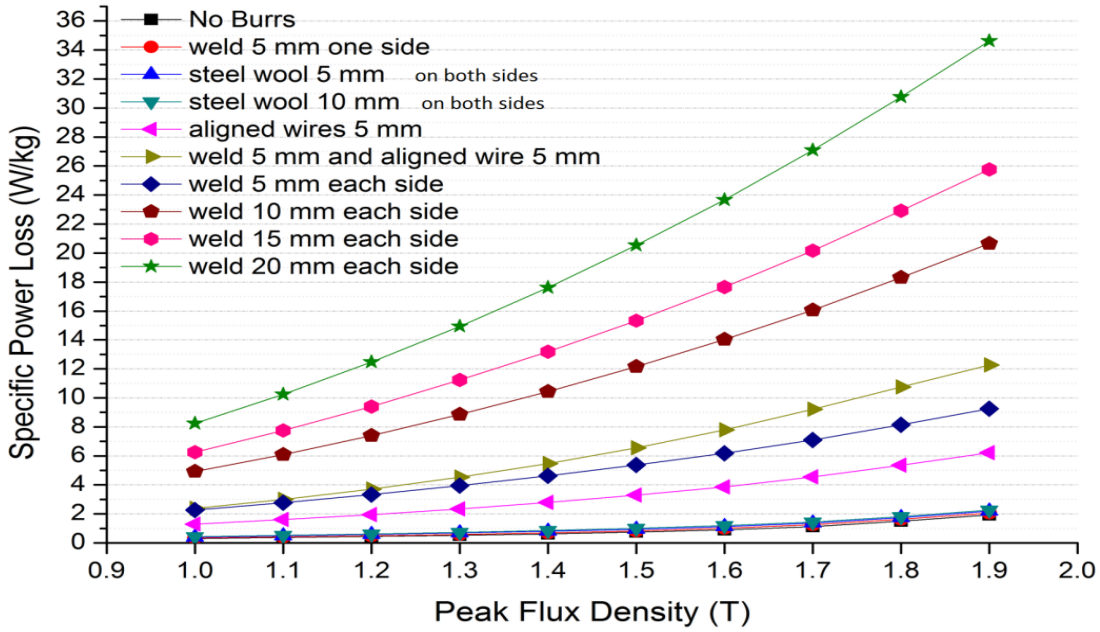

Figure 10.9 Variation of specific power loss with flux density with steel wool, copper wires and welding used as artificial burrs for a wound toroidal sample made of of GO @ 50 Hz.

As stated in section 5.3, the burrs have to be present on both sides of the stack such as to create a plane through which magnetic flux flows during magnetisation of the core. This is confirmed in the results shown in Figure 10.9 by the red trace with a circle marker for which only one side of the core is affected by the burr effect - a single weld. With a single weld on one side of the core the change in the loss observed is insignificant compared to losses caused by burrs affecting both sides of the core. What is more, this small increase in loss for a single weld is likely to be caused by the change in the material within the volume of the weld itself rather than by additional eddy currents circulating within the core. Only after the burrs are introduced on both sides, a

strong effect is visible as depicted by all traces marked with triangles, rhombus, pentagon, hexagon and a star. With increasing of the volume affected by burrs the losses increase. For a case with four weld strips on each side of the core, the losses increased 18 to 26 times throughout the range of flux densities measured. These measurements confirm the negative effect of burrs on wound toroidal cores as well as the necessity for more than one burr to be present for any effect to take place.

10.2.2 **Global and local power loss effect on the toroidal core**

The overall specific total power loss of the core, which is a proportional sum of losses within the regions affected and not affected by the burrs, increases in presence of burrs as shown in Figure 10.9.

To assess the specific total loss of the core in the regions affected and not affected by burrs a simplified calculation of the losses was made based on the model geometry shown in Figure 10.10 with an assumption that the volume affected by the burrs is equivalent to a rod instead of a cut out of a toroid. This assumption was made so that a classical eddy current loss equation (10.1) derived for cylindrical conductors could be used for loss estimation [18].

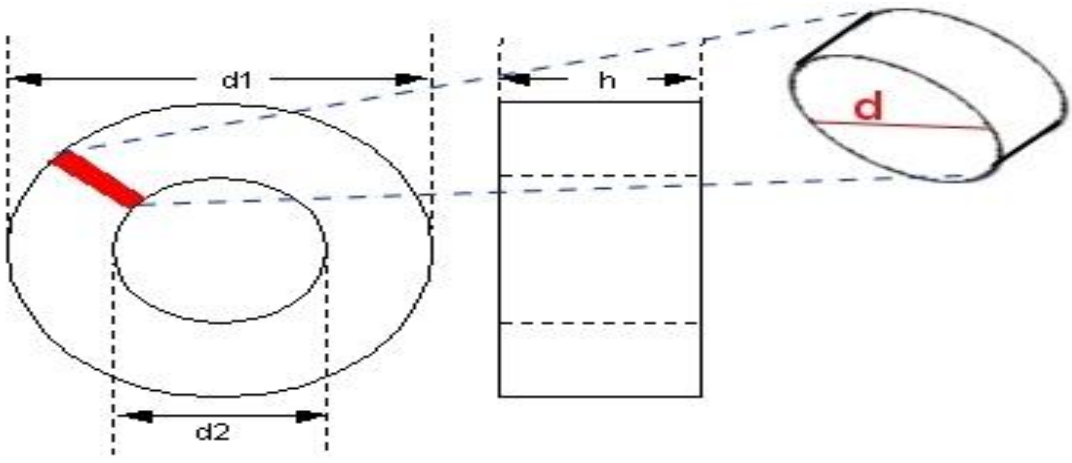

Figure 10.10 Schematic of a GO wound toroidal core used for burrs application with a burr affected volume marked in red and approximated as a cyllinder.

$$P_{eddy} = \frac{\left(\pi B_{pk} f d\right)^2}{\beta \rho D} \quad \textbf{(10.1)}$$

where β is the shape factor equal to 16 for cylindrical shape and 6 for thin sheet in which case the equation is identical to (2.30) described in section 2.7.

For example at 1.5 T peak magnetisation at 50 Hz, d = 0.025 m, β = 16, ρ = 48E-8 Ωm, D = 7650 kg/m^3 the eddy current component of loss within the volume affected by burrs is calculated as

$$P_{eddy.burred} = \frac{(3.14159 \times\ 1.5 \times 50 \times 0.025)^2}{16 \times 48 \times 10^{-8} \times 7650} = 590.58 \left[\frac{W}{kg}\right] \quad \textbf{(10.2)}$$

while in unaffected volume the eddy current loss is calculated as

$$P_{eddy.normal} = \frac{(3.14159 \times\ 1.5 \times 50 \times 0.0003)^2}{6 \times 48 \times 10^{-8} \times 7650} = 0.22678 \left[\frac{W}{kg}\right] \quad \textbf{(10.3)}$$

with d = 0.0003, β = 6 and the rest of the parameters remaining unchanged.

Taking into account the proportional volume affected by burrs, the increased eddy current loss $P_{eddy.burred}$ calculated in (10.2) relates only to approximately 0.025 m × 0.025 m × 0.005 m which constitutes 2.19% volume (mass) of the core and the remaining 97.81% remains at a normal level of $P_{eddy.normal}$ of 0.227 W/kg as calculated in (10.3). Adding these two up proportionally gives an overall eddy current loss in the whole core 13.17 W/kg. Measurement results for various cases of burrs applied to the core compared to calculated values are presented in Figure 10.11. The calculations exceed all measurements with a significant margin. However, overestimation of eddy current loss is often reported in scientific papers [83]. This is mainly due to the incorrect assumptions of uniform flux density distribution within the

material and constant permeability of the material. Flux density within conductive materials is subject to skin effect as described in section 2.7.2 which reduces the flux density within the material.

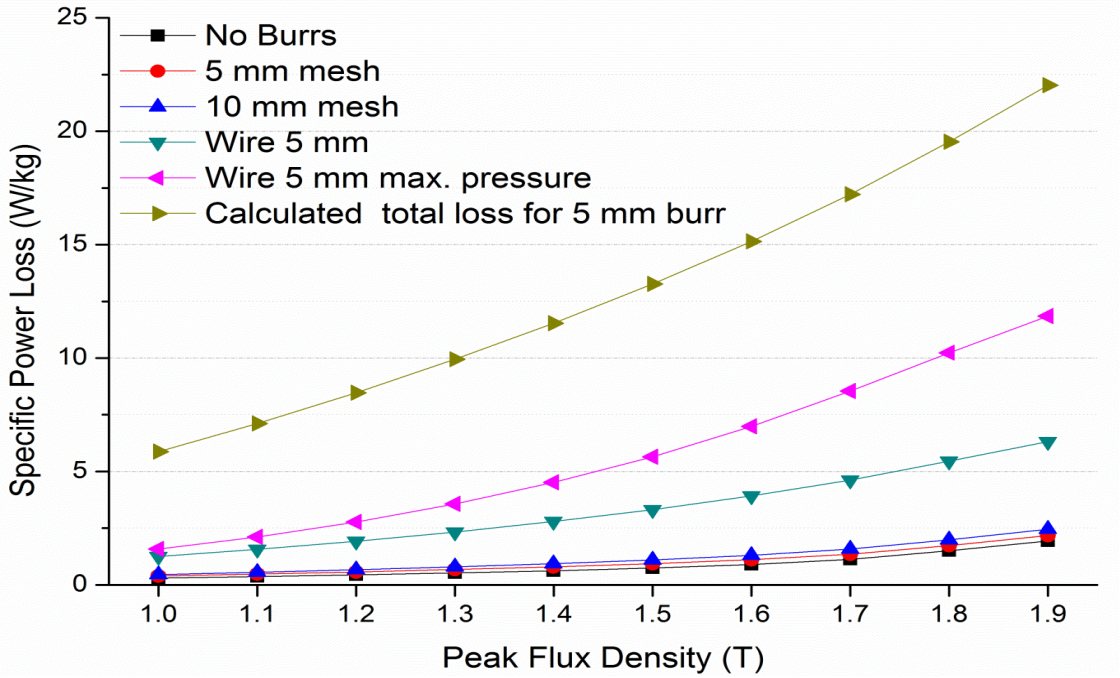

Figure 10.11 Variation of specific power loss with flux density for various methods of artificial burrs applied to a wound toroidal sample made of of GO @ 50 Hz.

Despite the high margin between the measurements and the eddy current loss estimation, the measurement results did show consistency in the effect of burrs on losses of a toroidal core. The discrepancy could be explained by the assumption of perfect connection between the short circuiting material and the stack of laminations, but also by the fact that the aligned wires do not have a full surface contact with the stack.

10.2.3 **Flux distribution effect on the toroidal core**

Calculations shown in Figure 10.11 are based on the overall flux density of the toroidal core measured on the secondary winding as shown in Figure 10.8. However, in presence of burrs shorting the whole height of the stack in the core, it is expected that

flux concentrates on the outside of the cross section of the core causing saturation magnetisation and reducing permeability in that region to 1 which makes it possible for leakage flux to flow through the air and omit the burred region. This in turn means that flux density within the burred region of the material would be lower than the one measured on the secondary windings and the eddy current loss estimations should be based on lower flux density reducing the difference between the measured and calculated values shown in Figure 10.11.

10.3 EFFECTS OF BURRS ON A THREE PHASE CORE

A three phase, 388 kg, 350 kVA transformer core as shown and described in section 9.1 was used throughout the investigation. Application of artificial burrs to this core was made using the clamping device as described in Chapter 8. The effect of burrs on total loss was measured using a NORMA D6000 power analyser in a setup as shown and described in Chapter 8.

10.3.1 Burr location on the three phase core

As described in section 5.3, burrs need to meet certain requirements to generate an effect on power loss of a transformer core. There needs to be an electrical short circuit created on two sides of the stack in such a way to create a loop through which there will be flux flowing during normal operating of the core. A comparison of total specific power loss of the transformer without any burrs and with burrs applied to one side of a limb, two different stacks and two different limbs is shown in Figure 10.12. There is no effect of a single side burr or a set of two burrs located on different limbs or two different stacks of the core on specific power loss of the core which confirms the theory presented in section 5.3.

Figure 10.13 shows a schematic of one artificial burr applied inside the pin guide hole of the experimental core using the device shown in Figure 8.13 and another applied on the outside of limb Blue using the clamping device shown in Figure 8.8.

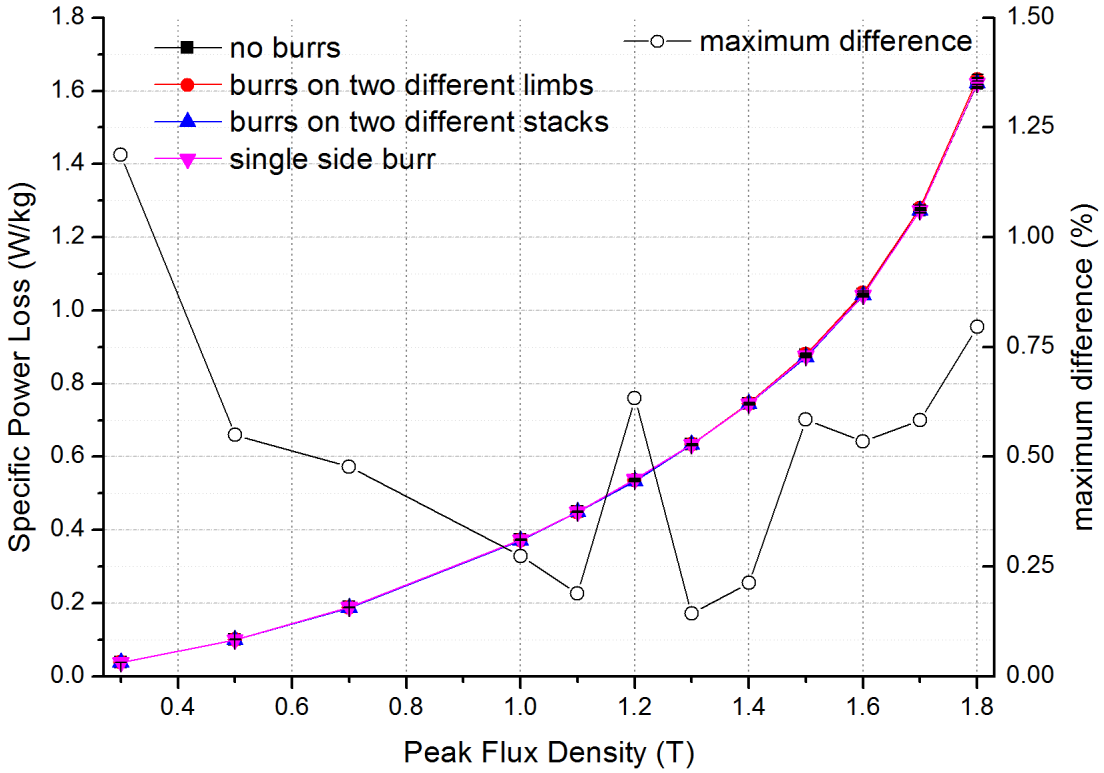

Figure 10.12 Specific total power loss of the three phase core with burrs on one side of a limb, two different limbs and two different stacks within one limb compared to the case without burrs applied to the core.

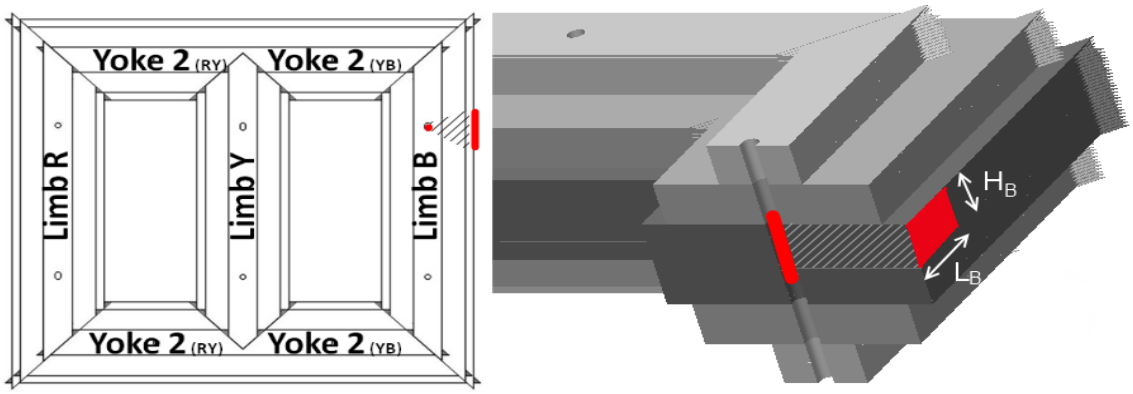

Figure 10.13 Schematic of placement of burrs inside the pin guide hole with burrs marked in red and approximate regions affected by burrs stripped.

The results shown in Figure 10.14 were not repeatable due to poor performance of the pin guide hole pressure device shown in Figure 8.13. However, they confirm that the effect of increased eddy current loss exists for burrs within pin guide holes and is not only relevant to edge burrs.

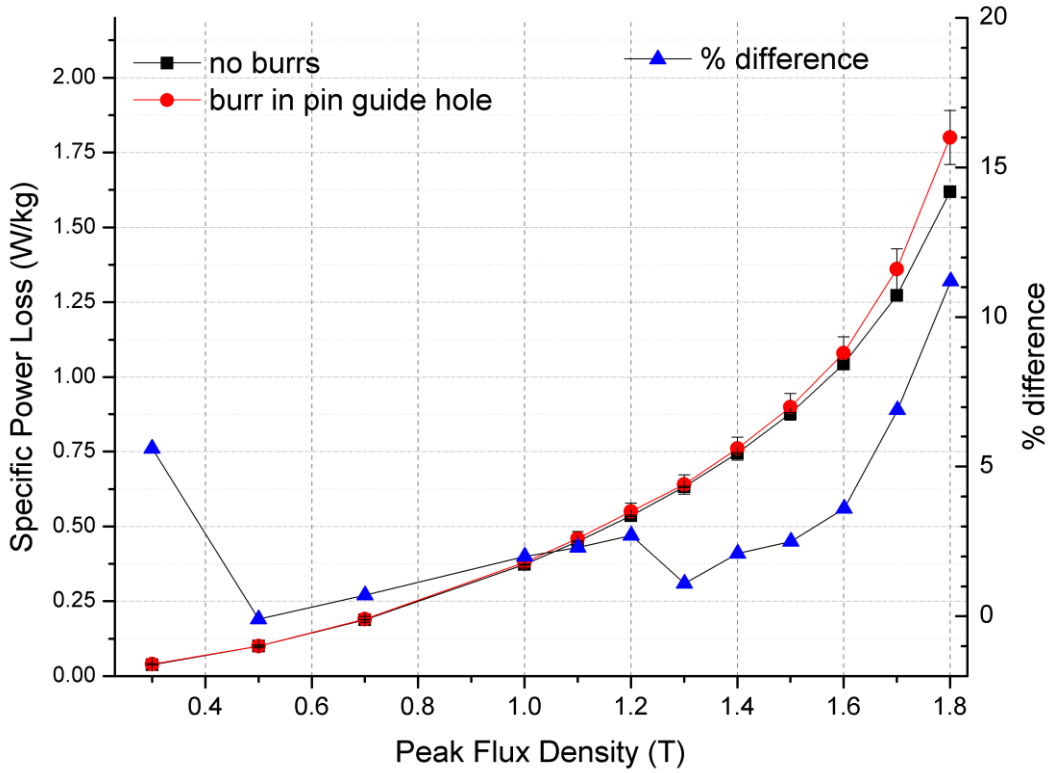

Figure 10.14 Variation of specific power loss of the experimental three phase core with peak flux density with one burr placed on stack C on the outside of limb Red and another one within the pin guide hole of limb Red.

10.3.2 Global power loss effect on the three phase core

An investigation of the effects of burr height, burr length and shifting of burrs on the total specific loss of the experimental core was undertaken and the results shown in this section were published in an IEEE journal paper [4].

10.3.2.a Burr height

Figure 10.15 shows a schematic of artificial burrs applied to stack C of the Blue limb of the experimental core in a symmetrical arrangement. Burr length L_B was set to 25 mm and kept constant throughout this experiment while burr height H_B was varied at 10 mm, 15 mm and 20 mm.

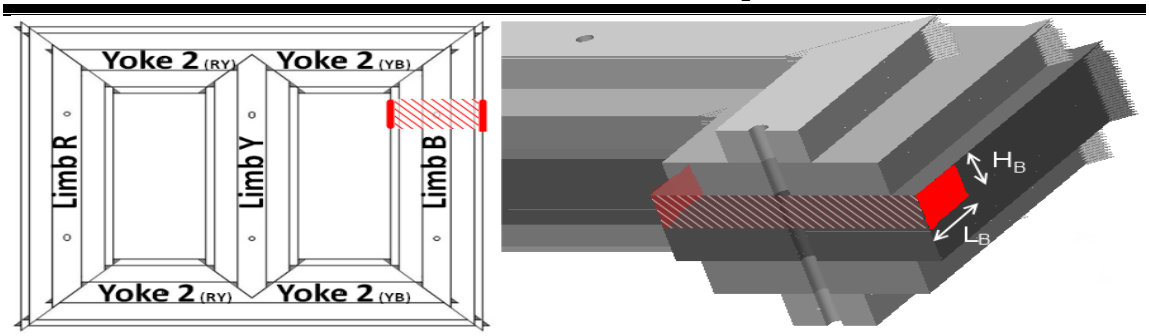

Figure 10.15 Schematic of placement of symmetrical burrs on limb Blue on stack C in opposite configuration with burrs marked in red and approximate regions affected by burrs stripped.

Figure 10.16 and Figure 10.17 show the variation of specific total loss of the core with the height of the burr applied to stack C of limb B of the core and with the peak flux density of the core respectively. The increase in the burr height significantly increases the power loss at high flux density but below 1.5 T the increase is not so significant since it is proportional to peak flux density squared. It will also be shown later in 10.3.4 that flux density within the burred region is significantly reduced as compared to the overall core flux density and the reduction is stronger below 1.5 T overall core flux density and reduces rapidly above that value.

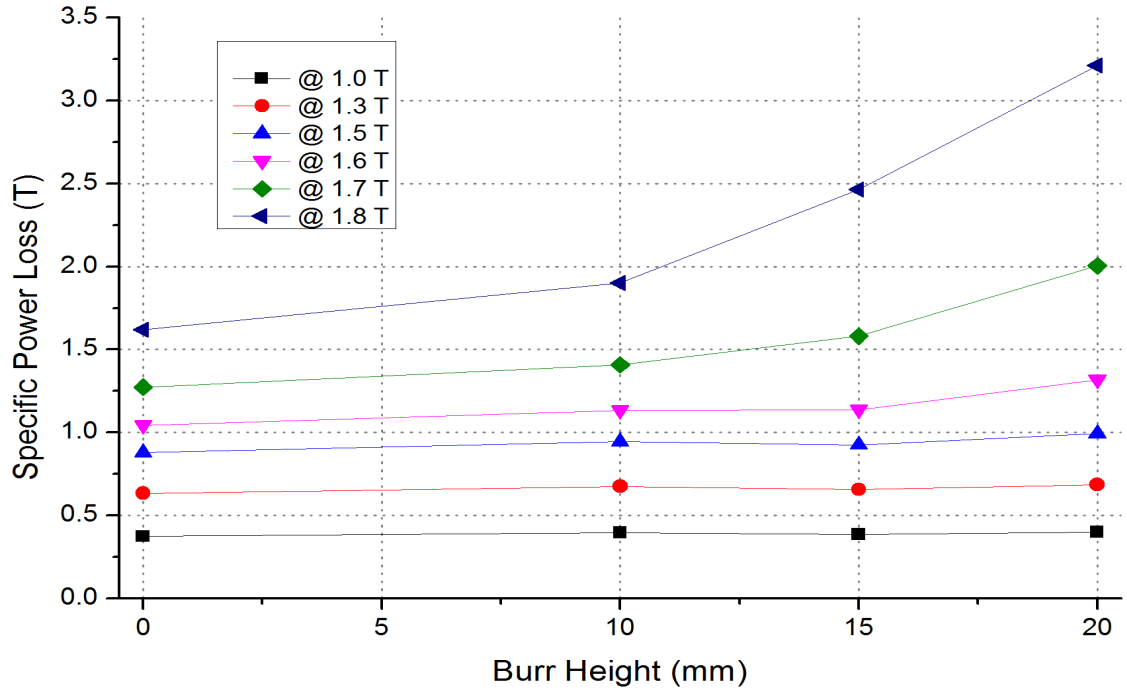

Figure 10.16 Variation of specific total power loss of the experimental core with the height of the burr applied to stack C of limb B of the core.

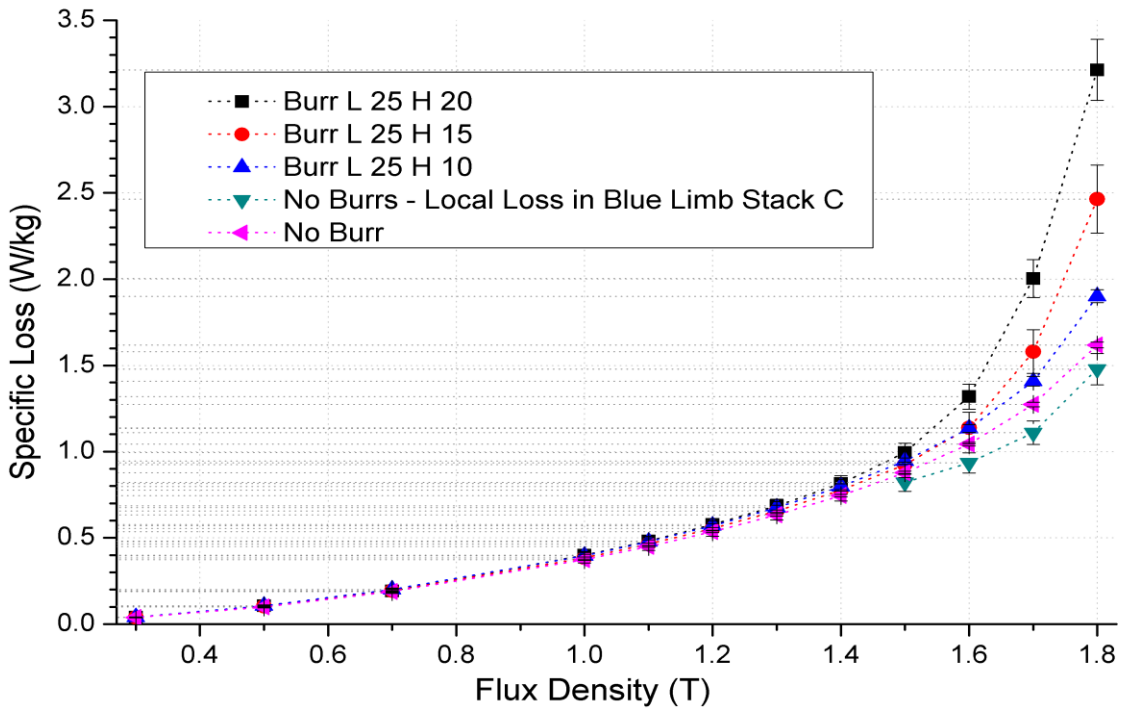

Figure 10.17 Variation of total specific power loss with peak flux density for three sizes of burrs in the experimental core. H refers to the number of laminations burred, L is the length of the burr.

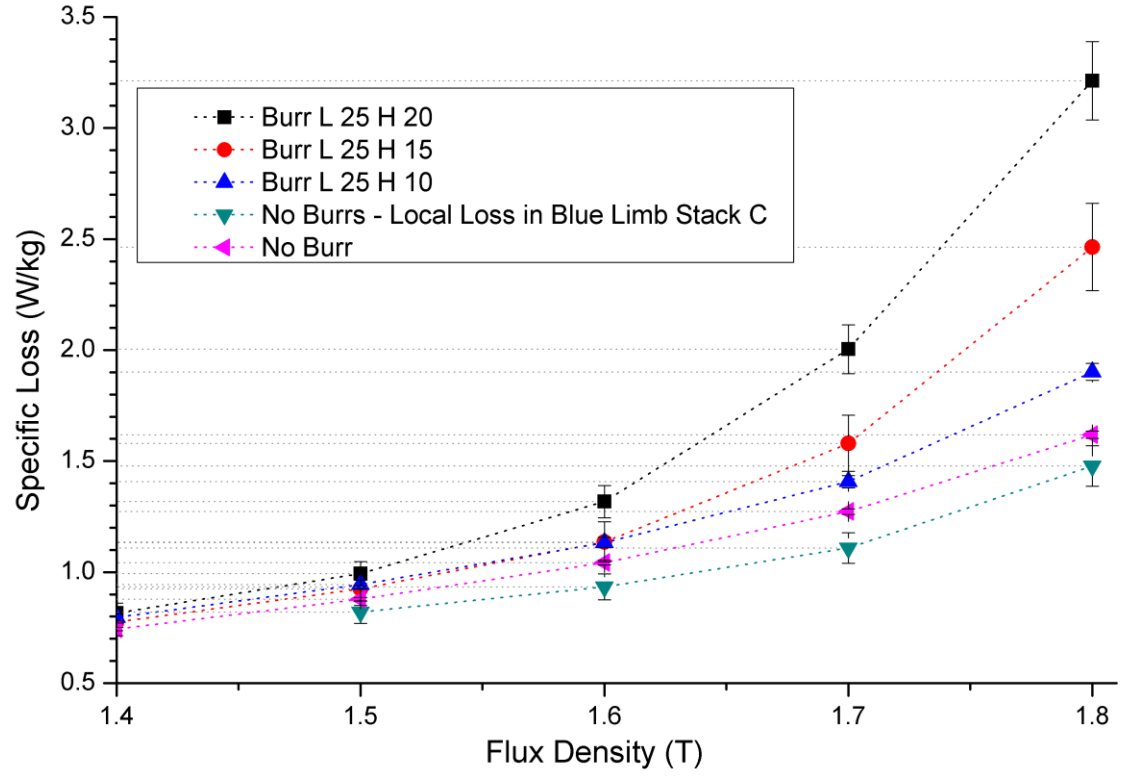

Figure 10.18 Rescaled graph of the variation of total specific power loss with peak flux density for three sizes of burrs in the experimental core. H refers to the number of laminations burred, L is the length of the burr.

10.3.2.b ***Burr Length***

The burr placement schematic is identical to the one shown in Figure 10.15. Burr height H_B was set to 10 mm and kept constant throughout this experiment while burr length L_B was varied at 10 mm, 15 mm, 20 mm and 25 mm.

The theoretical models presented in Chapter 7 suggest that the increase in length of burr does not change the value of the eddy current loss in any case but only increases the volume affected by the burr proportionally. Hence the resulting increase in loss should also grow proportionally. As anticipated from theoretical models, the influence of burr length on power loss is linear as can be seen in the measurement results shown in Figure 10.19.

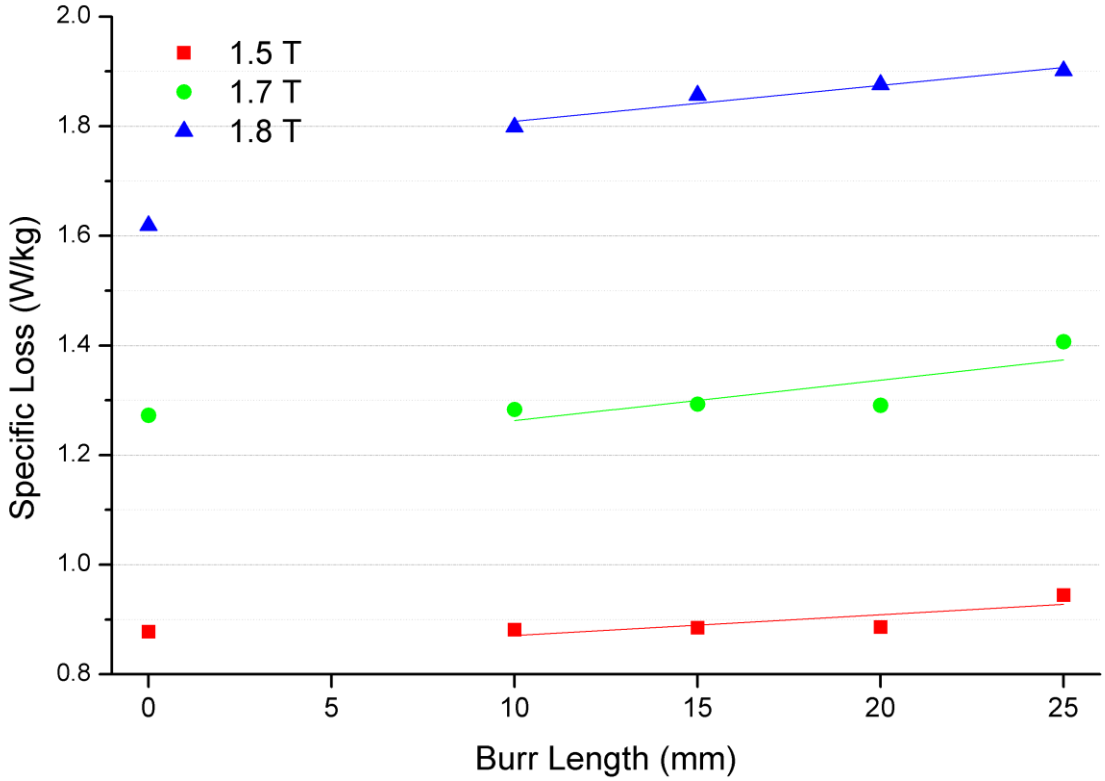

Figure 10.19 Variation of specific total power loss of the experimental core with the length of burr L_B = (10 mm, 15 mm, 20 mm, 25 mm) for a constant burr height H_B = 10 mm.

This supports the theory that the increase in loss is proportional to the burr length.

This linearity of this effect is subject to the burred region not affecting the full cross section of the core as it was the case in the investigation of the toroidal sample described in section 10.2.2. In case of the whole cross section being affected by the burr, flux is repressed from the inside of the limb to the outside increasing the flux density on the outside of the cross section to saturation values which in turn reduces permeability to a value close to μ_0 which results in some of the flux flowing as leakage flux through the air around the burred region.

10.3.2.c Burrs shifted

Figure 10.20 shows a schematic of artificial burrs applied to stack C of limb B of the experimental core. Burr length L_B was set to 25 mm and burr height H_B was set to 20 mm and kept constant throughout this experiment. The positioning of the burrs on either side of the limb was shifted by 150 mm, 200 mm, 250 mm and 300 mm.

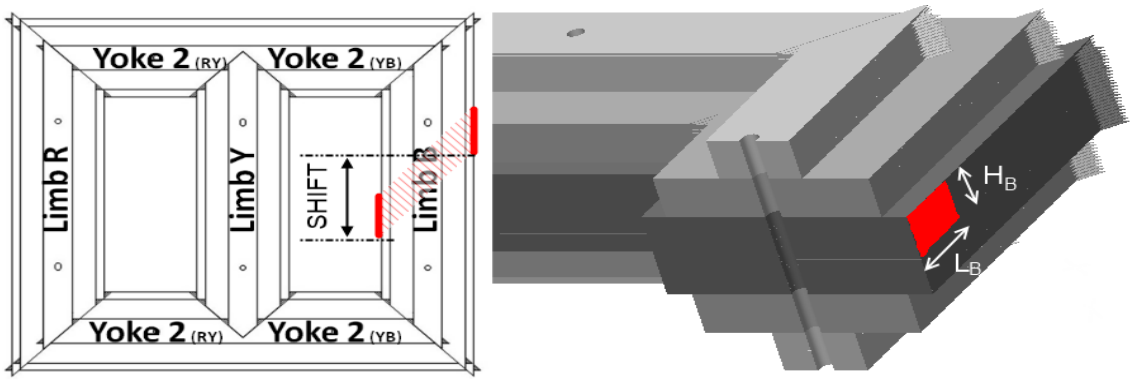

Figure 10.20 Schematic of placement of symmetrical burrs on limb Blue on stack C in shifted configuration with burrs of height H_B and length L_B marked in red and approximate regions affected by burrs stripped.

The results shown in Figure 10.21, Figure 10.22 and Figure 10.23 suggest that with increasing of the shift between the burrs on the two sides of the limb the effect of increase on the eddy currents weakens significantly for experiments and in some cases disappears completely. This can be explained by increasing of the resistance between the two short circuits with increasing the distance between them.

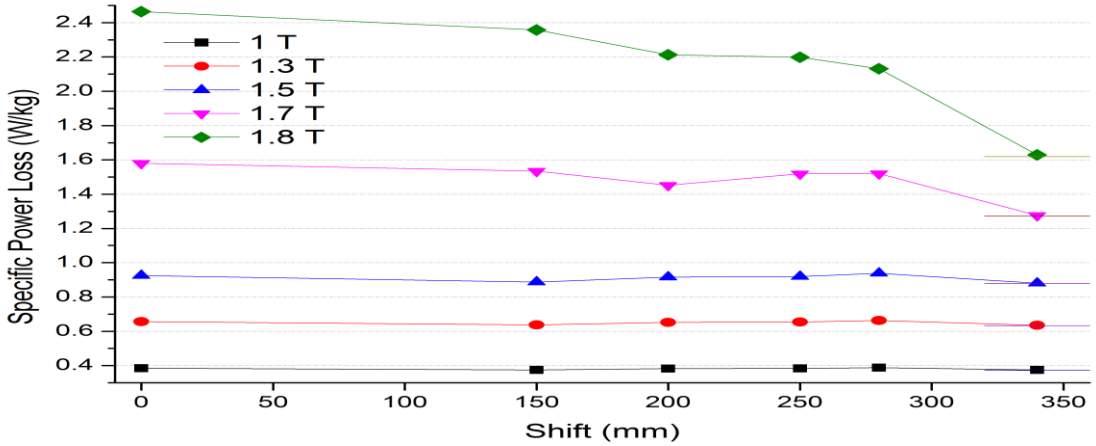

Figure 10.21 Variation of the increase in specific total power loss of the experimental core with shifting of the artificial burrs away from the opposite arrangement. Burrs applied on both sides of Limb Blue on stack C measured L_B=25 mm and H_B=15 mm. Horizontal lines indicate the specific power loss of the core without burrs.

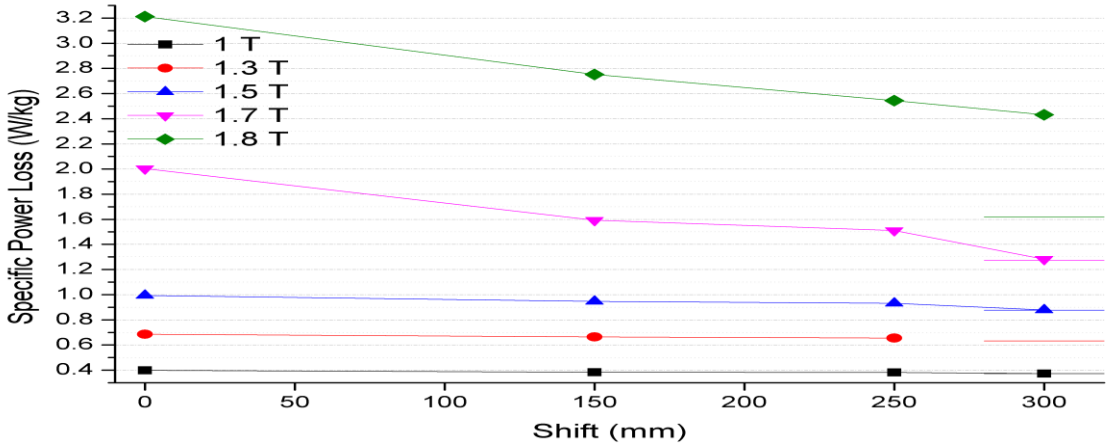

Figure 10.22 Variation of the increase in specific total power loss of the experimental core with shifting of the artificial burrs away from the opposite arrangement. Burrs applied on both sides of Limb Blue on stack C measured L_B=25 mm and H_B=20 mm. Horizontal lines indicate the specific power loss of the core without burrs.

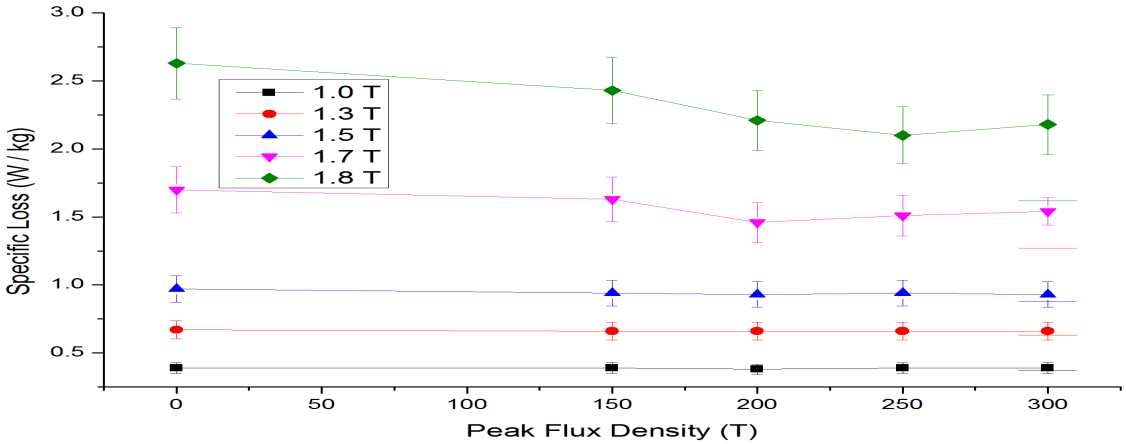

Figure 10.23 Variation of the increase in specific total power loss of the experimental core with shifting of the artificial burrs away from the opposite arrangement. Burrs applied on both sides of Limb Blue on stack B measured L_B=25 mm and H_B=20 mm. Horizontal lines indicate the specific power loss of the core without burrs.

10.3.3 **Local power loss effect on the three phase core**

An investigation of the effects of burrs on the local specific total loss of the experimental core in the vicinity of the applied burrs was undertaken and the results shown in this section were published in an IEEE journal paper [85].

Figure 10.24 shows the schematic of the experimental setup for localised loss measurements on the three phase core described in Chapter 8. The clamping device as described in Chapter 8 was used for applying artificial burrs of length LB and height HB on either side of stack C of limb B of the core. LB was fixed at 25 mm and HB was set to 10 mm, 15 mm and 20 mm shorting out approximately the top 33, 50 and 66 laminations of stack C which itself comprises 182 laminations, 160 mm width. The flux density in each packet was measured using needle probes at locations marked X in Figure 10.24. Conventional wound search coils were used to measure flux density in the region affected by the burrs. Type K thermocouples were fixed on the lamination at the top of stack C at the positions shown at set distances from the centre of the burr location to measure the initial rate of rise of temperature and hence localised losses with and without burrs. A six channel thermocouple amplifier circuit was connected to a National Instruments 6259 data acquisition card and the voltage signal was filtered and plotted to obtain the initial slope using the Excel curve fitting function. Uncertainty of the localised loss measurement was estimated at ±6.2% taking into account factors such as: acquicition card accuracy, accuracy of the integrated circuit board components, noise filters, selection of the linear part of the temperature rise and control of peak flux density of the core. Total loss was measured using a NORMA D6000 power analyser with uncertainty of ±5.5% taking into account the power analyser, core mass, control of peak flux density, current and voltage measurements.

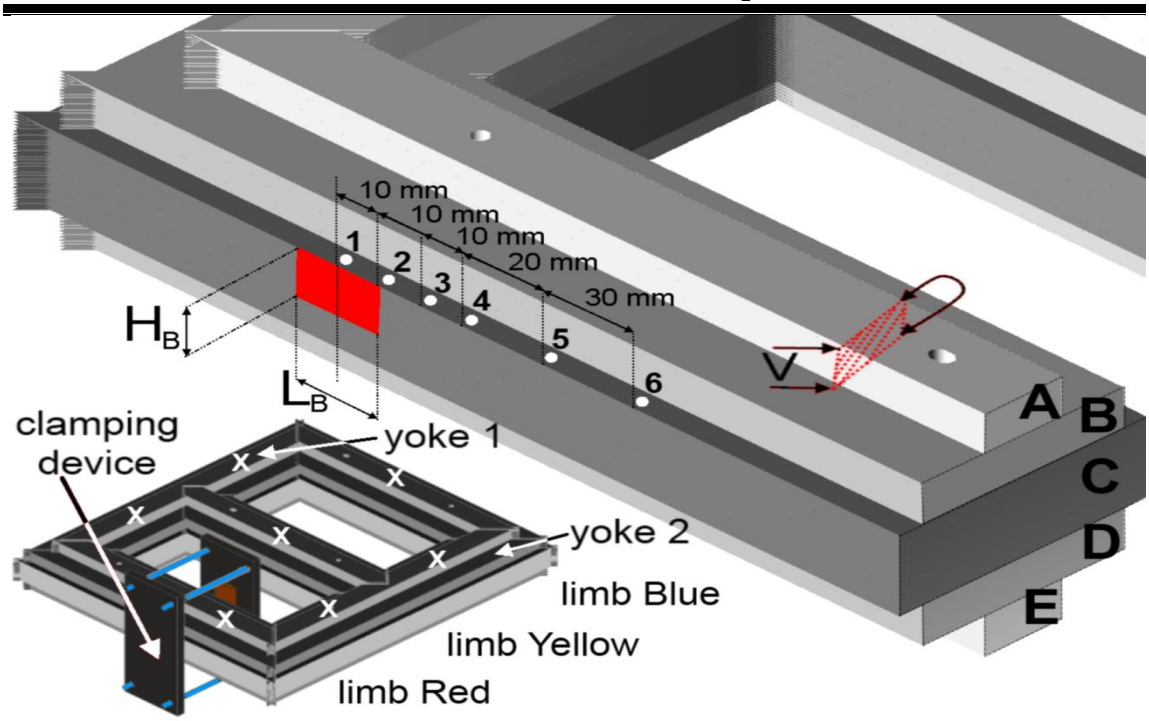

Figure 10.24 Experimental core showing clamping rig for applying artificial burrs and thermocouples and needle probe measurement positions.

A measurement of local specific total loss without any burrs applied to the core was taken for reference as shown in Figure 10.25. The local loss in the centre of the outer lamination of stack C in limb B of the non-burred core is lower than the total per unit core loss but higher than the Epstein loss due to the building factor of the core which in this case is around 1.25 at 1.7 T.

Figure 10.26 shows the effect of increasing the number of burred laminations on the local loss in the centre of the burred region at core flux densities from 1.5 T to 1.8 T. Between 1.5 T and 1.7 T a square relationship exists between the loss and the number of laminations but this breaks down at higher flux density.

Figure 10.27 shows the variation of local specific total loss with the distance from the centre of the burred region. The results show the region affected by the burrs extends as far as 80 mm from the centre of the burr. Further results presented in Table 10.1 confirm that the affected region is larger than 50 mm in all cases.

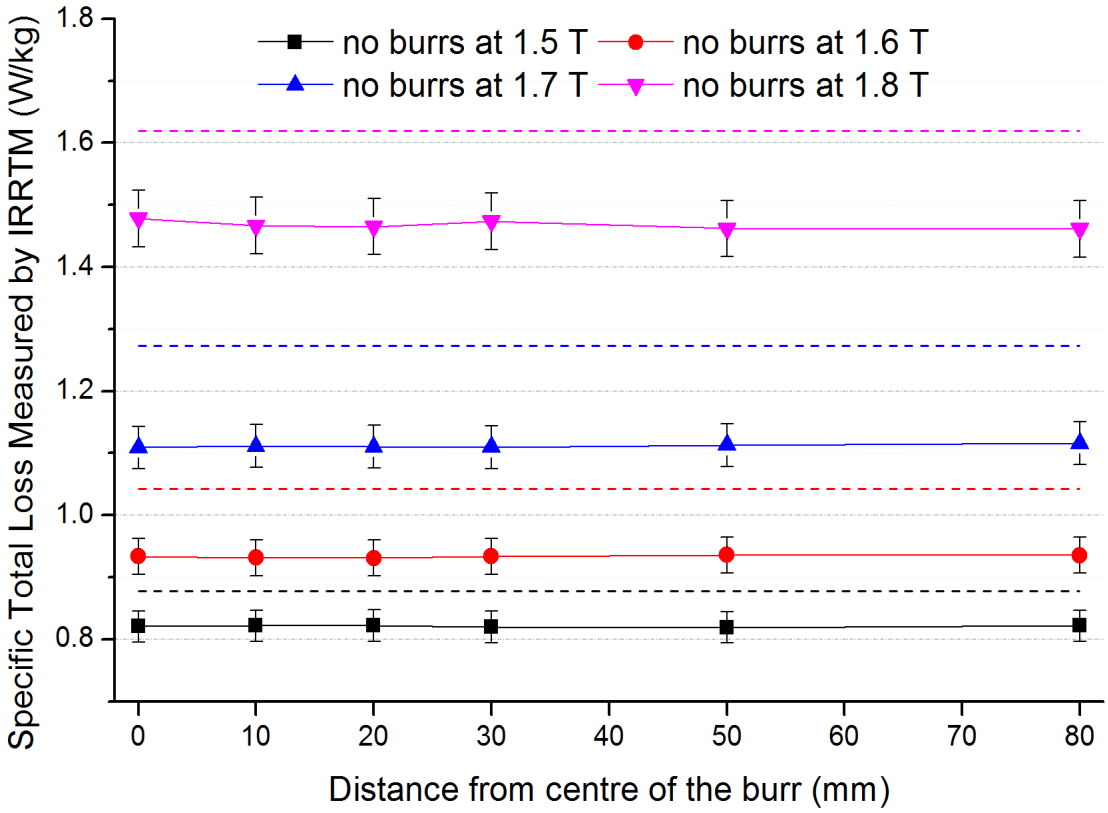

Figure 10.25 Variation of specific power loss with distance of measurement point to the centre of the artificial burr location.

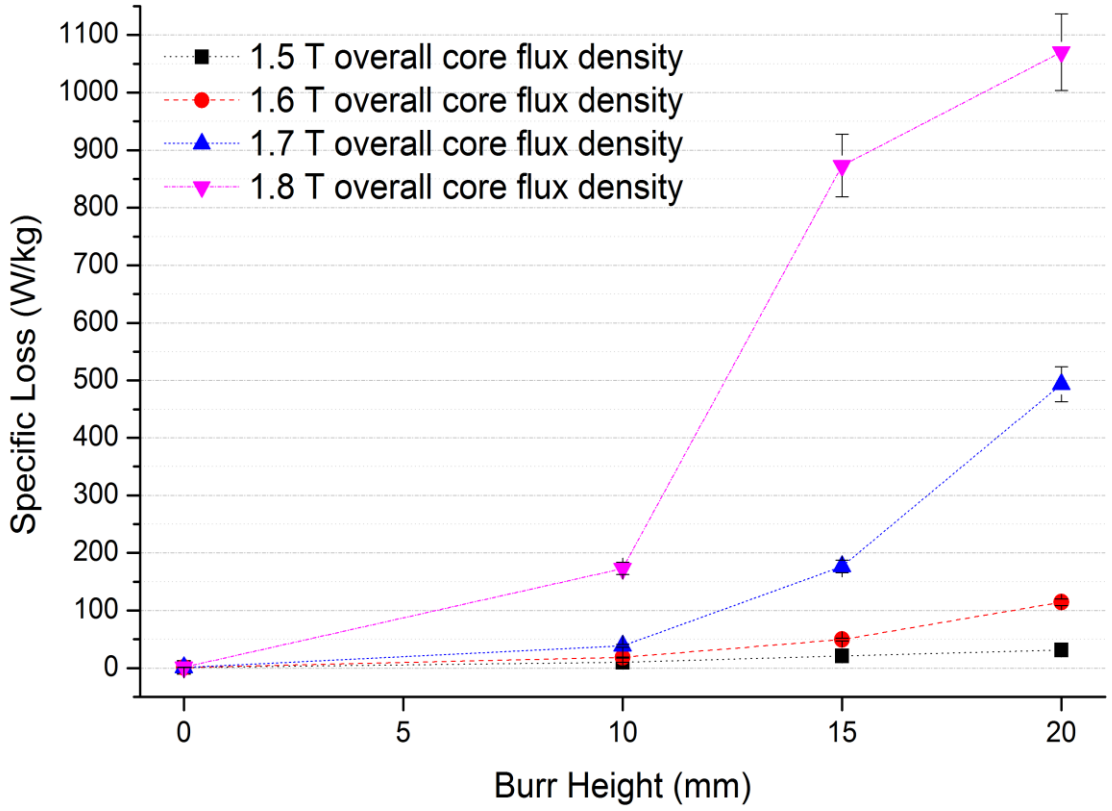

Figure 10.26 Variation of specific power loss at location 1 with burr height for 1.5 T, 1.6 T, 1.7 T and 1.8 T.

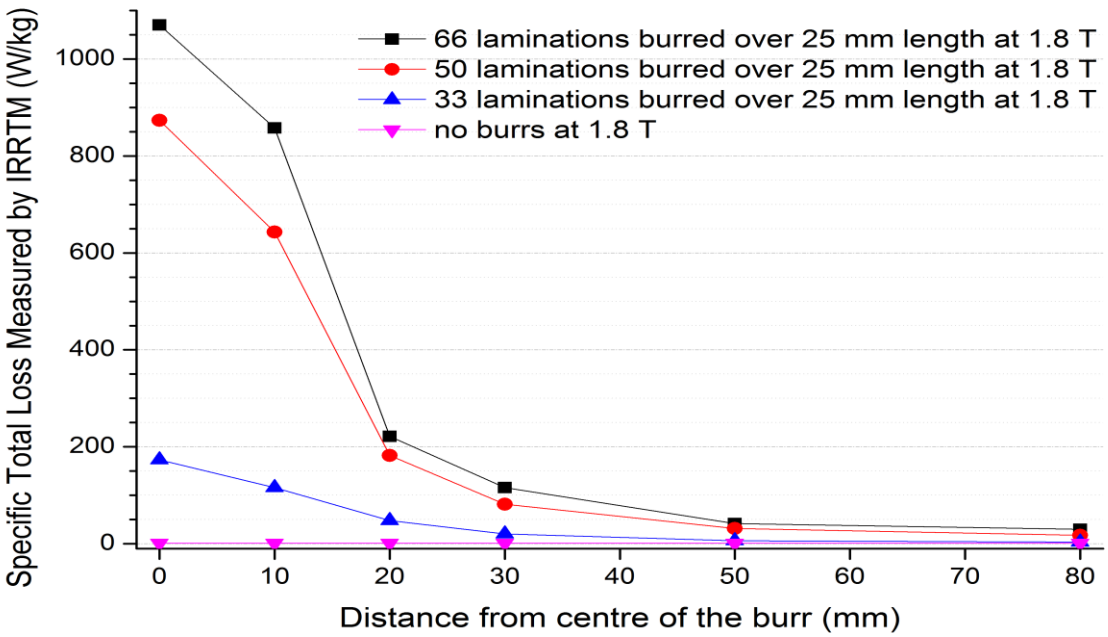

Figure 10.27 Variation of local specific total loss with distance to the centre of the artificial burr for burr height H_B = 10 mm, 15 mm and 20 mm.

Table 10.1 Local specific total loss measured using the initial rate of rise of temperature method at 6 locations described in Figure 10.24 for burr length L_B = 25 mm, burr heights H_B=10, 15 and 20 mm at 1.5 T, 1.6.T, 1.7 T and 1.8 T core peak flux density.

	0 mm	10 mm	20 mm	30 mm	50 mm	80 mm
noBurrs, 1.5 T	0.8	0.8	0.8	0.8	0.8	0.8
noBurrs, 1.6 T	0.9	0.9	0.9	0.9	0.9	0.9
noBurrs, 1.7 T	1.1	1.1	1.1	1.1	1.1	1.1
noBurrs, 1.8 T	1.5	1.5	1.5	1.5	1.5	1.5
H_B = 10, L_B = 25, 1.5 T	10.3	7.5	3.3	2.8	0.9	0.8
H_B = 10, L_B = 25, 1.6 T	18.6	13.4	5.6	2.8	1.0	0.9
H_B = 10, L_B = 25, 1.7 T	38.6	25.6	8.7	5.7	2.6	2.2
H_B = 10, L_B = 25, 1.8 T	173.2	115.7	47.8	20.4	6.2	3.5
H_B = 15, L_B = 25, 1.5 T	20.8	17.5	5.5	3.2	1.3	0.8
H_B = 15, L_B = 25, 1.6 T	49.6	37.1	12.1	6.4	2.5	1.6
H_B = 15, L_B = 25, 1.7 T	176.5	130.5	38.8	22.0	8.6	5.4
H_B = 15, L_B = 25, 1.8	873.4	643.1	182.3	81.3	31.3	17.6
H_B = 20, L_B = 25, 1.5	31.2	27.5	7.7	5.6	2.4	1.8
H_B = 20, L_B = 25, 1.6	114.5	99.4	23.5	16.8	6.2	4.7
H_B = 20, L_B = 25, 1.7	493.6	397.6	87.8	55.7	20.3	17.4
H_B = 20, L_B = 25, 1.8	1070.3	857.8	221.3	115.8	41.6	30.0

The comparison of the measurements made using the initial rate of rise of temperature method with the calculations made using the simple symmetrical model and measured flux density within the burred region is shown in Figure 10.28. The poor correlation over much of the peak flux density range is mainly due to the assumption that flux density is uniform throughout the whole volume affected by the burr. This problem can be tackled by using the more advanced model which utilises the decay of peak flux density within the material. However, the problem of measuring or recalculation of peak flux density at the surface of the material pointed out in section 10.1 remains unsolved.

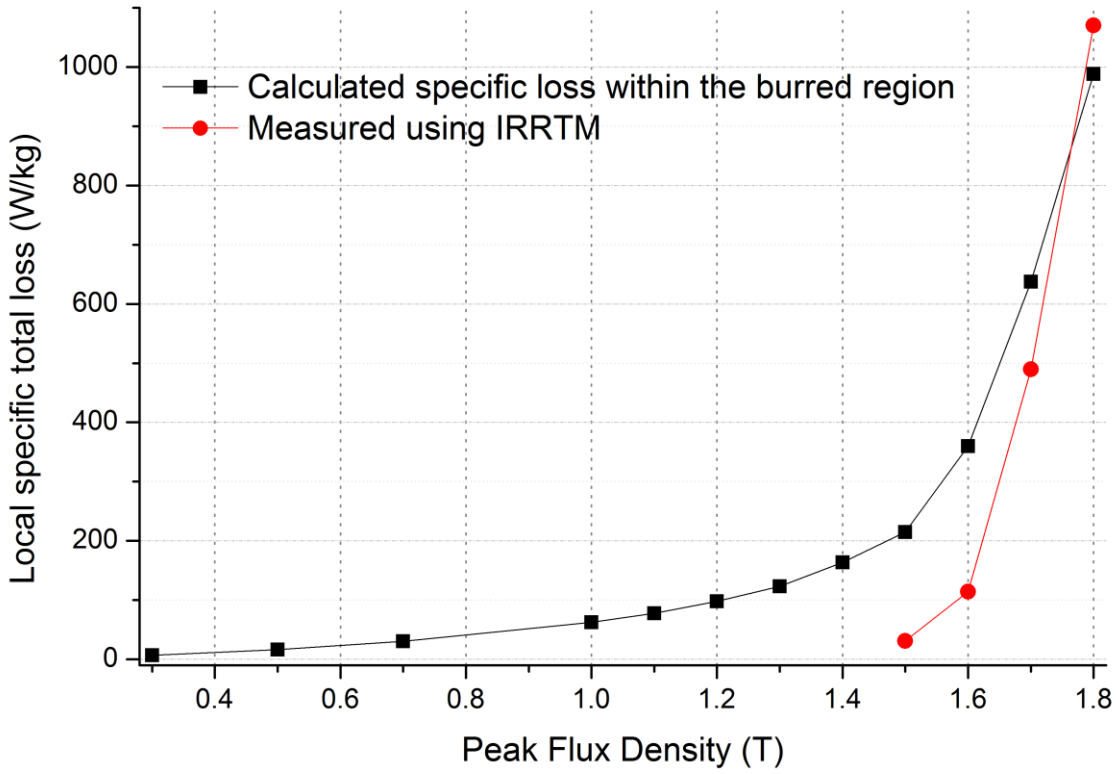

Figure 10.28 Variation of local specific total loss calculated using the simple symmetrical model and measured using the initial rate of rise of temperature method with overall peak flux density of the core.

10.3.4 **Flux distribution effect on the three phase core**

Figure 10.29 shows the layout of the experimental transformer core with seven locations on the core where flux density distribution between stacks A, B, C, D and E was measured for a case without any burrs and with burrs applied to the core.

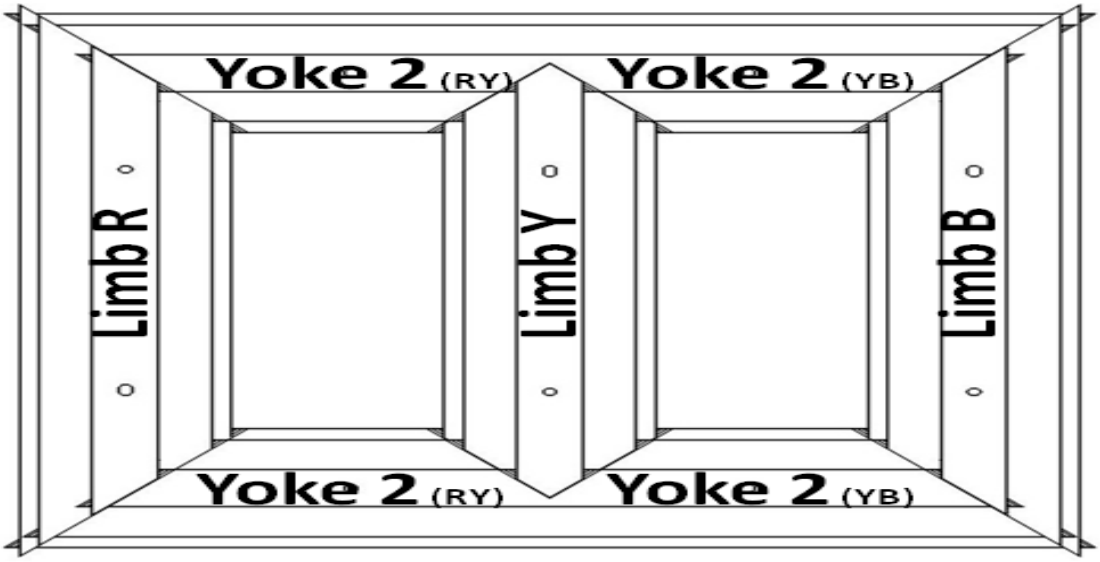

Figure 10.29 Layout of the experimental transformer core with seven locations labelled.

Figure 10.30, Figure 10.31 and Figure 10.32 show the flux density distribution in the cross section of the core at seven locations as pictured in Figure 10.29 without any burrs applied to the core which was magnetised at 1.0 T, 1.5 T and 1.7 T respectively. It can be seen that flux density varies from stack to stack as well as from location to location for all measurements but resulting in a 0.99 T, 1.50 T and 1.70 T average peak flux density respectively. Higher flux densities are measured in packs of laminations with higher ratio of pin guide hole diameter to lamination width which is consistent with reports from Balehosur [86]. The variation of peak flux density within the same packet at different locations in the cores layout is an interesting result here but can be explained by non-identical domain structure of the material in each location.

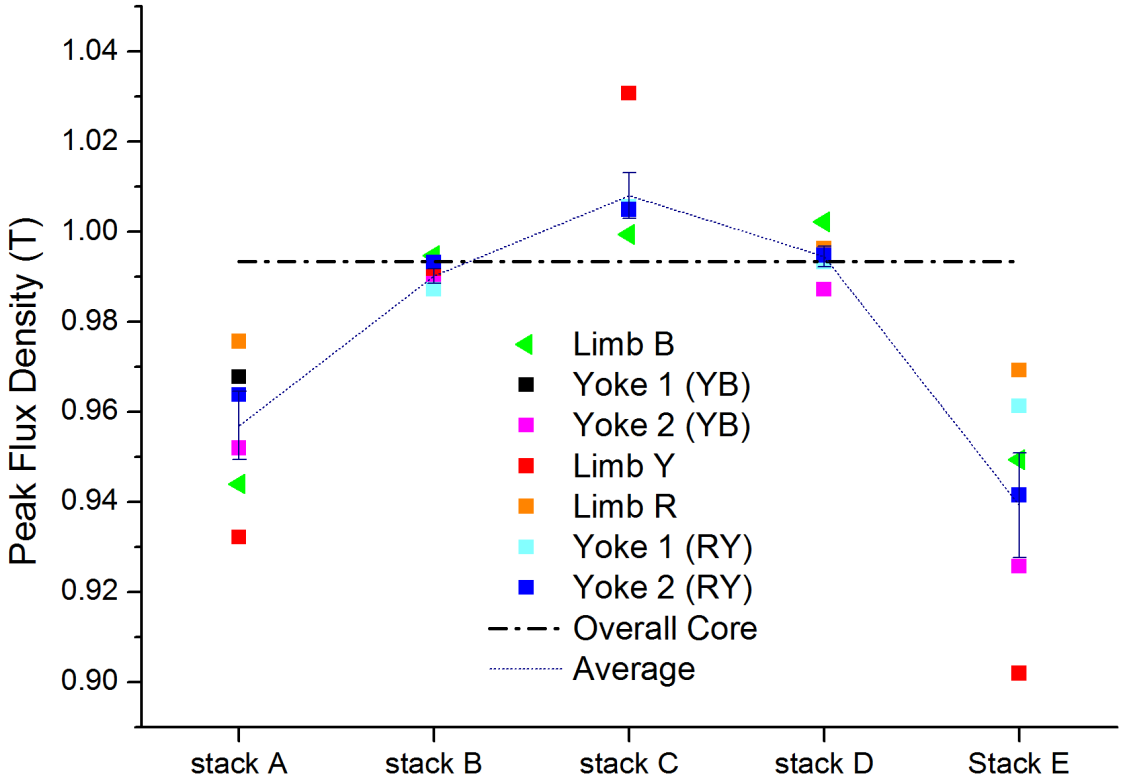

Figure 10.30 Flux density distribution within stacks of laminations of the experimental core, magnetised to 1.0 T, across several locations of the cores layout marked in Figure 10.29.

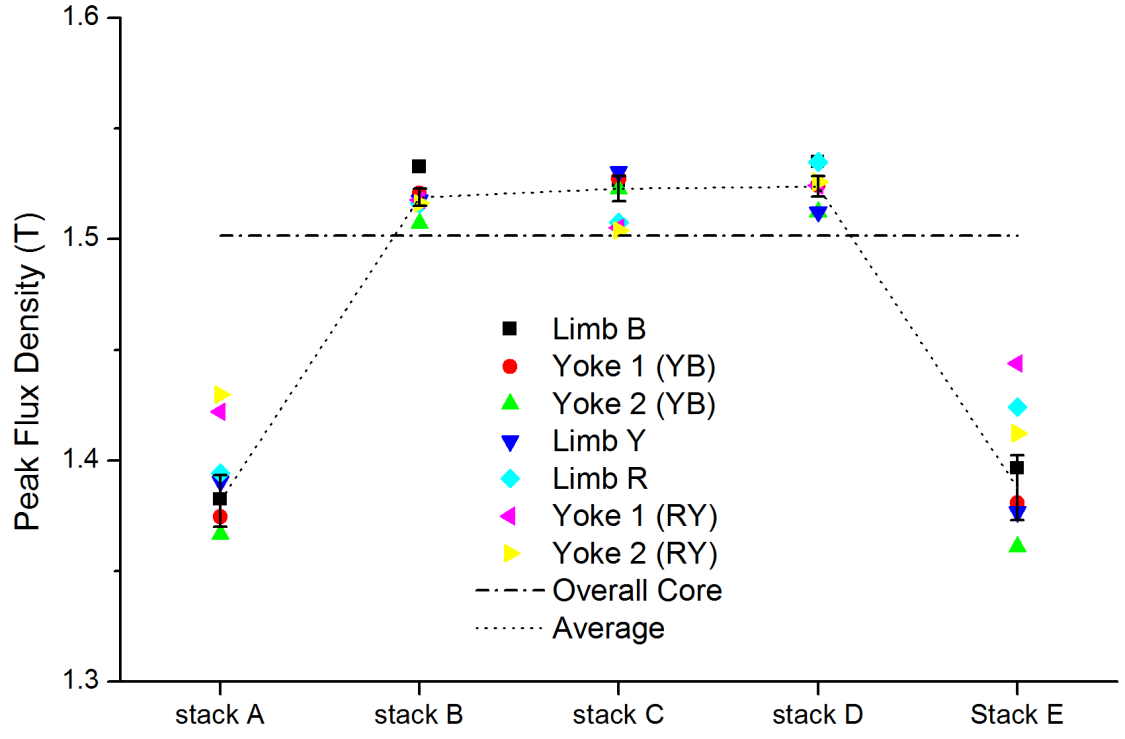

Figure 10.31 Flux density distribution within stacks of laminations of the experimental core, magnetised to 1.5 T, across several locations of the cores layout marked in Figure 10.29.

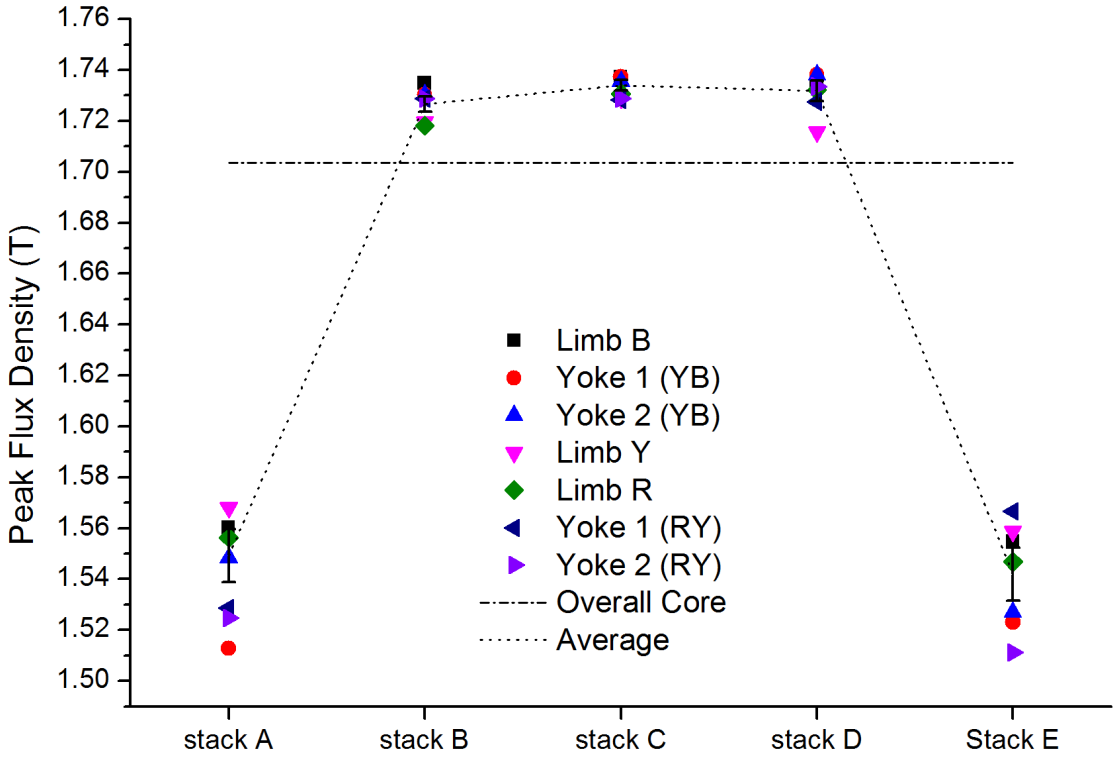

Figure 10.32 Flux density distribution within stacks of laminations of the experimental core, magnetised to 1.7 T, across several locations of the cores layout marked in Figure 10.29.

Figure 10.33, Figure 10.34 and Figure 10.35 show the overall flux density of the core at 1.0 T, 1.5 T and 1.7 T compared to the flux density distribution across the stacks of the core at locations shown in Figure 10.29 with and without burrs applied to stack C of limb B. With artificial burrs of height H_B=20 mm and length L_B=25 mm applied to stack C of limb B there was a change in the peak flux density distribution within the core cross sections at the same locations. Due to additional eddy currents induced within stack C by the presence of the artificial burr, flux density was repressed from stack C. Assuming no leakage flux, the amount of flux through any cross section of the experimental core is constant which implies that the portion of flux repressed from stack C crossed to the remaining stacks and increased flux density within them which is confirmed in the results.

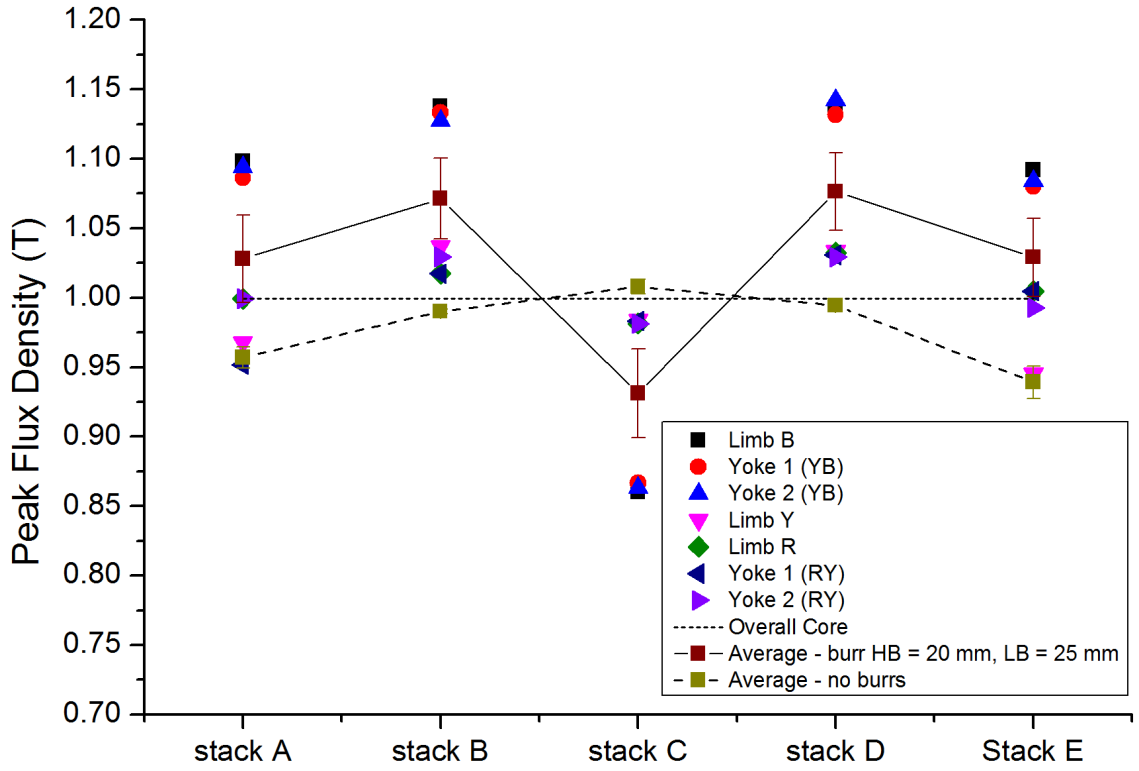

Figure 10.33 Comparison of flux density distribution within stacks of laminations of the experimental core magnetised to 1.0 T, across several locations, with artificial burrs applied to stack C of limb B and without any burrs.

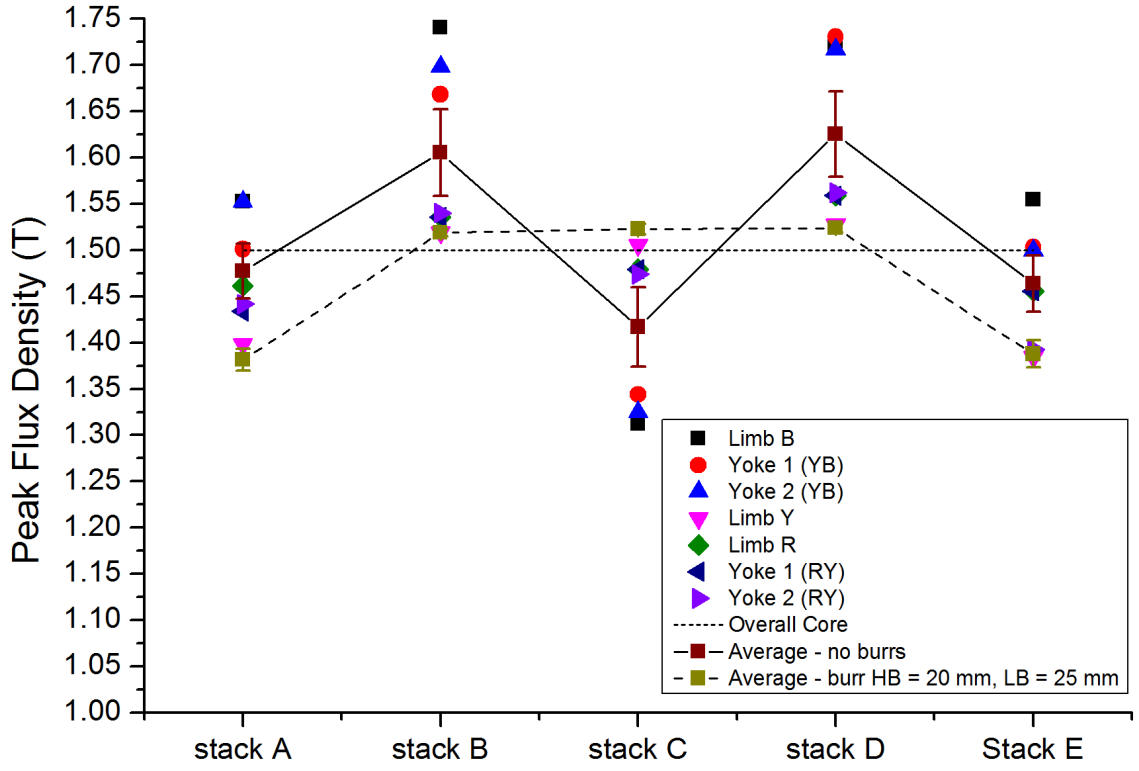

Figure 10.34 Comparison of flux density distribution within stacks of laminations of the experimental core magnetised to 1.5 T, across several locations, with artificial burrs applied to stack C of limb B and without any burrs.

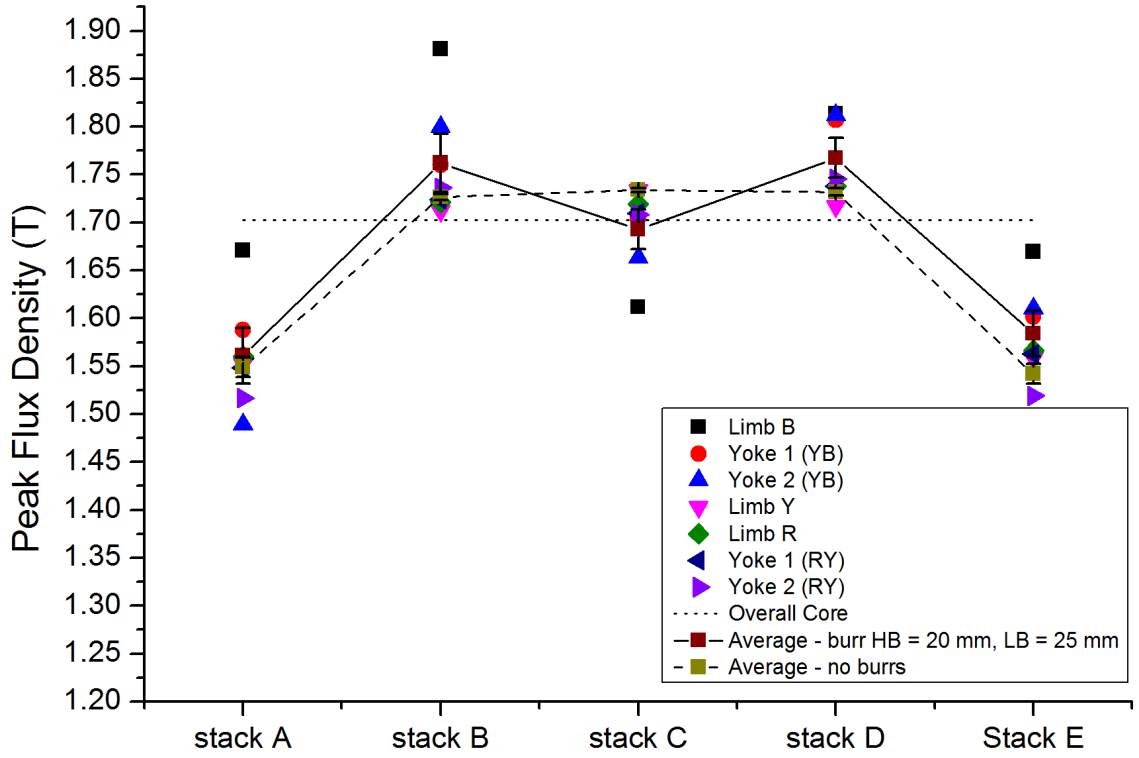

Figure 10.35 Comparison of flux density distribution within stacks of laminations of the experimental core magnetised to 1.7 T, across several locations, with artificial burrs applied to stack C of limb B and without any burrs.

The relationship between the overall flux density of the core and the peak flux density in the cross sectional area within stack C of limb B occupied by burr of H_B = 20 mm and L_B = 25 mm is shown in Figure 10.36. The values are similar at low and high flux density but between 1.0 T and 1.5 T the flux density in the burred region is significantly reduced by the eddy currents. At low core flux densities, the flux flows along the low reluctance path around the burred volume which results in a close to linear relationship between the applied field and effective flux density up to about 1.5 T. At average core flux densities approaching the knee of the magnetisation curve, the permeability drops in the regions not affected by the burrs and the reluctance becomes higher than within the burred volume hence the flux density within the burred volume increases more rapidly.

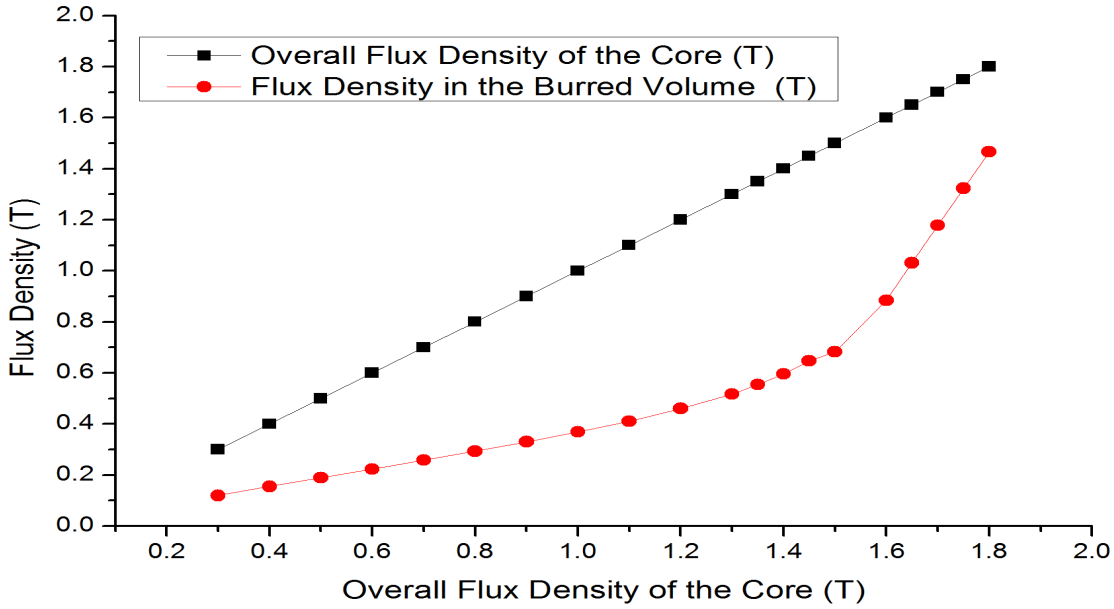

Figure 10.36 Flux density distribution within the region affected by a burr of HB=20 mm and LB=25 mm applied to stack C of limb Blue of the experimental core.

For a case where burrs of H_B=20 mm and L_B = 25 mm applied to stack B of limb B of the core the effect is analogous and the results of flux density distribution within the cross section of Limb B are shown in Figure 10.37 and Figure 10.38. The flux density within stack B is reduced across the full range of flux densities. The effect is strongest for overall peak flux densities of the core up to 1.5 T.

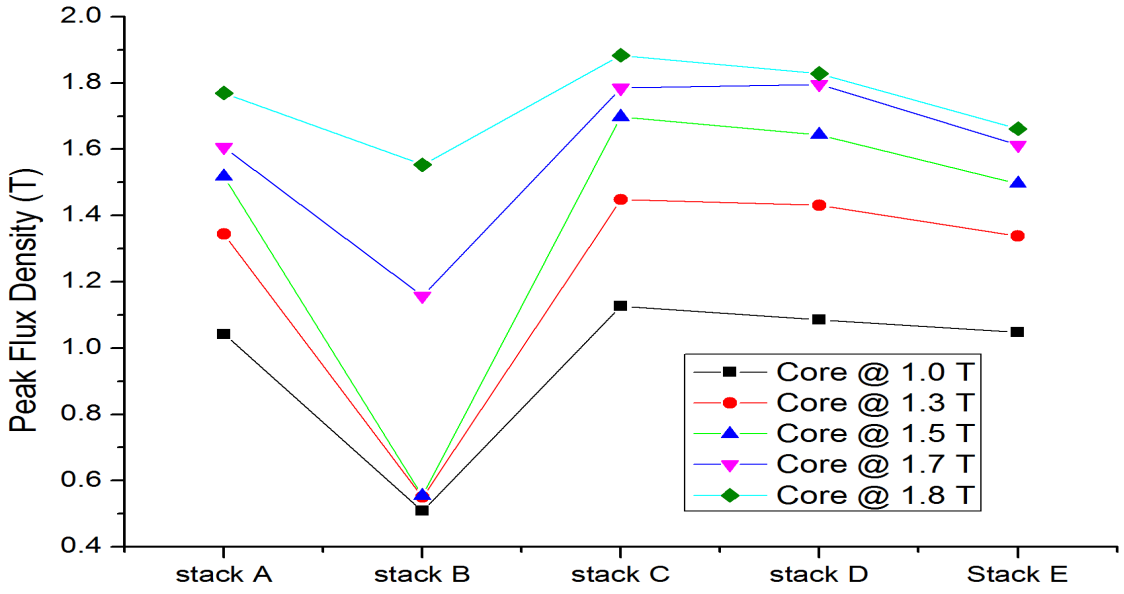

Figure 10.37 Flux density distribution within stacks of laminations of the experimental core magnetised to a range of flux densities with the burr of H_B = 20 mm and L_B=25 mm applied to stack B of limb B.

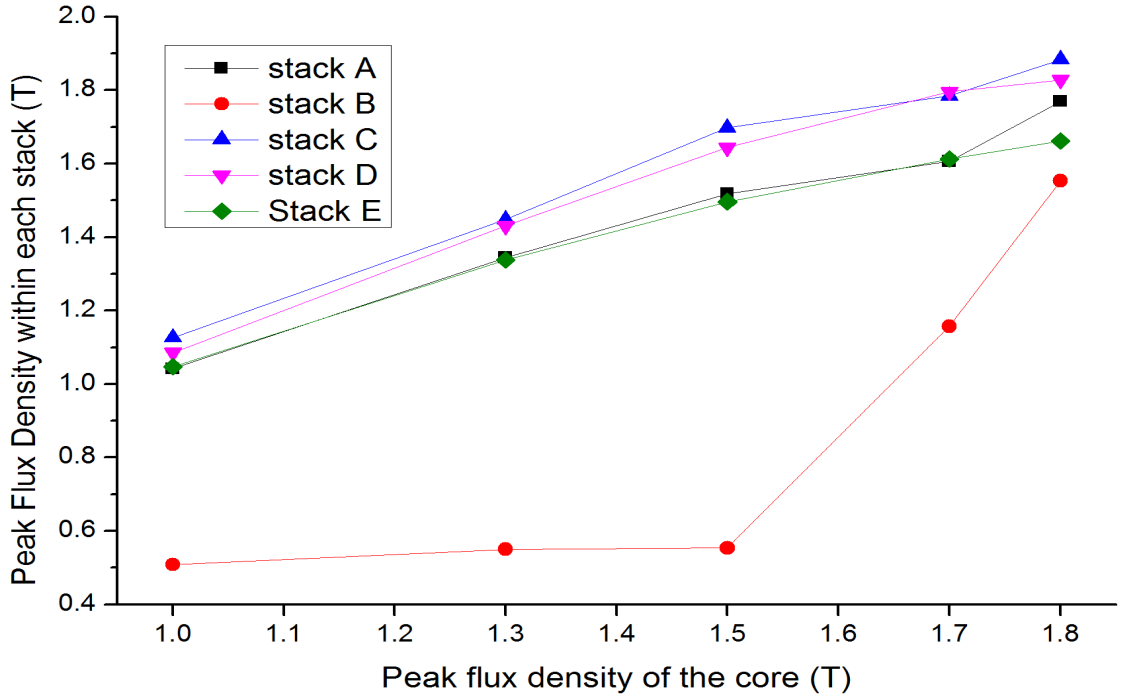

Figure 10.38 Variation of peak flux density distribution across the stacks of limb B of the experimental core with overall peak flux density of the core with a burr of HB =20 mm and LB =25 mm applied to stack B of limb B.

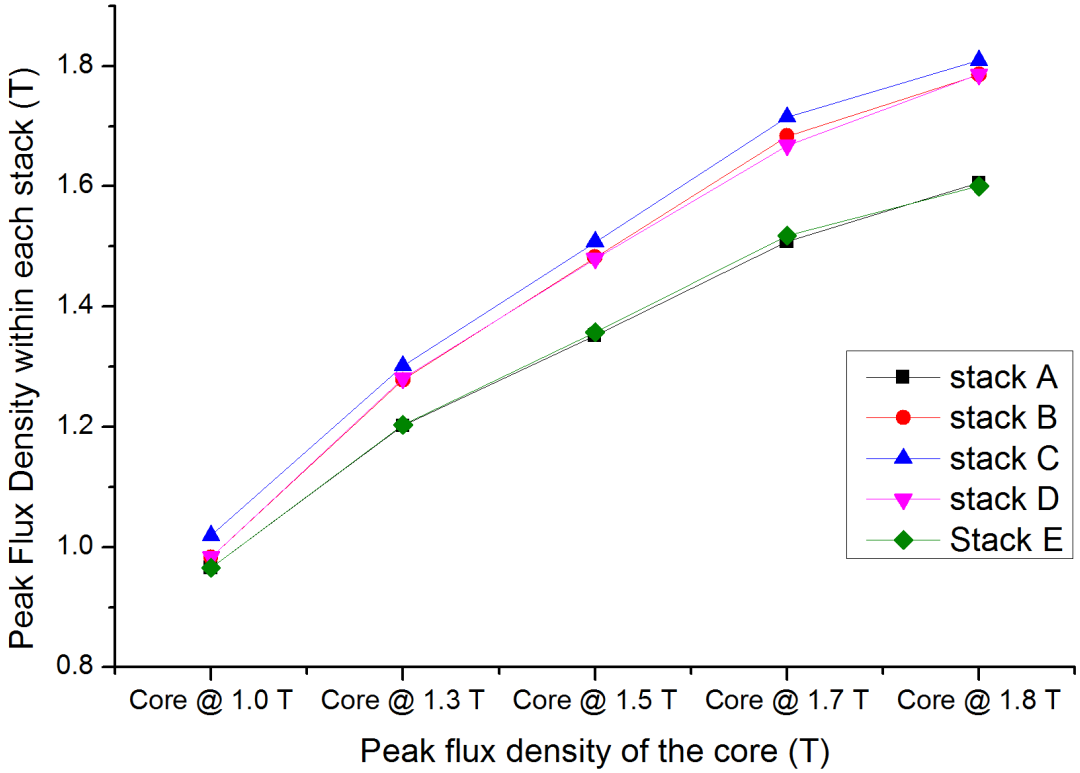

Figure 10.39 Flux density distribution within stacks of laminations of limb B of the experimental core without any burrs applied and magnetised to a range of flux densities.

10.4 THIN FILM SENSORS

An investigation of suitability of thin film sensors embedded on electrical steel laminations for use within a transformer core was undertaken. Results for flux density measurements within a transformer core shown in this section were accepted for publication in an IEEE Sensor Letters paper and are currently in print [87].

The investigation started by comparing the hand held needle probes with a search coil; then it progressed to modified needle probes eliminating holding the probes by hand and the large electrical loop created by the probes, leads and the sample; the next step was a comparison of a deposited needle sensor with a search coil measuring over the same cross section area the results of which were presented in section 9.2 but are repeated here to show a continuous investigation flow; next step is a comparison of a set of four thin film sensors with a set of four search coils arranged such as to cover the whole cross section area of a 160 mm wide lamination of the experimental core; the final step was to use the lamination with the four thin film needle probes inside a stack of the experimental core.

10.4.1 Flux density measurement within a solenoid

A schematic of the comparison of hand held needle probes and a search coil made on a 160 mm wide lamination is shown in Figure 10.40. The sample was magnetised within a solenoid using a LabView data acquisition card as a signal generator and for recording of the search coil and needle probe induced voltages. The resulting waveforms are shown in Figure 10.41 and the peak flux density values are shown in Figure 10.42. The difference between the two sensors which was more pronounced at high flux densities originated from the air flux enclosed by the large area formed by the

sample, needle probes and the leads. At low magnetisation field values flux flows entirely through the high permeable lamination, but at high field values, with induction values above the knee of magnetisation curve, permeability of the material drops and more flux flows through the air.

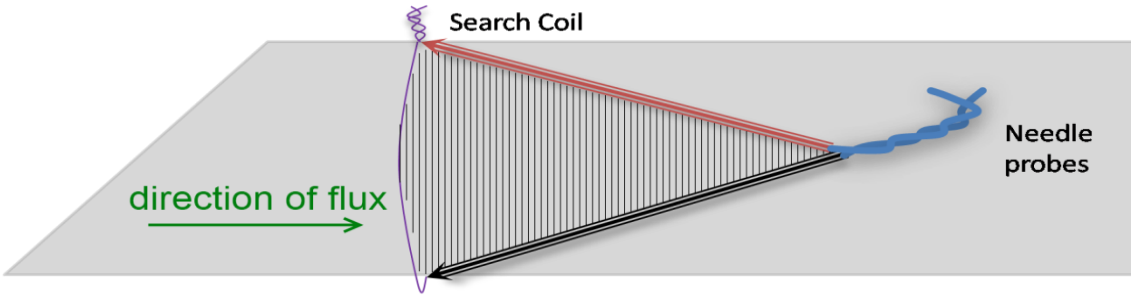

Figure 10.40 Schematic of a comparison measurement of flux density by using a search coil and needle probes.

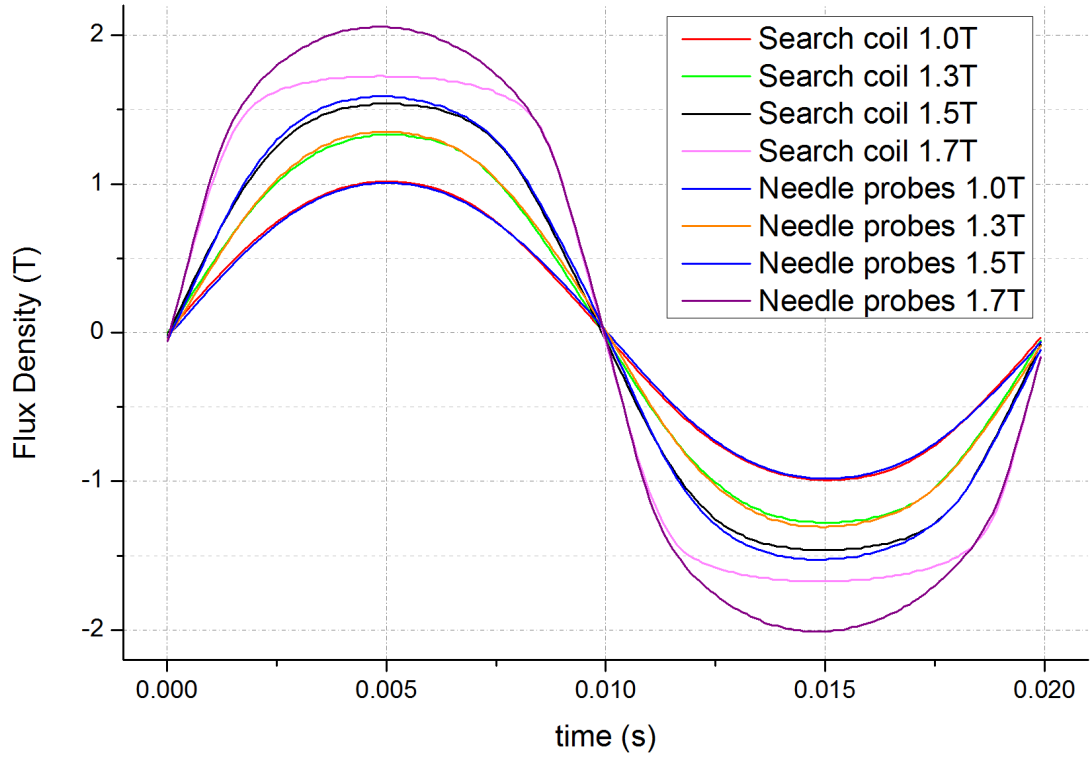

Figure 10.41 Comparison of measurements of flux density made by a search coil and by needle probes.

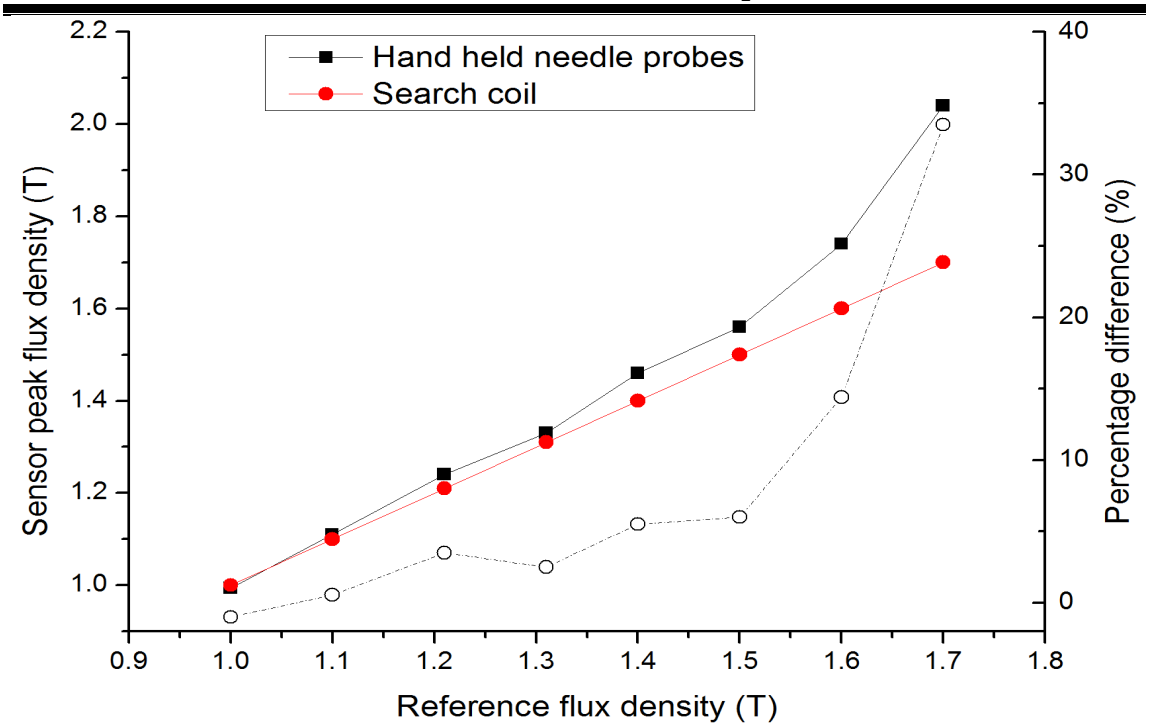

Figure 10.42 Variation of peak flux density measured by hand held needle probes and by a reference search coil with the overall flux density of the lamination measured by the reference search coil

A schematic of the comparison of a twisted wire needle probes and a search coil made on a 160 mm wide lamination is shown in Figure 10.43. The area enclosed by the needle probes and the sample in this case is minimised. Also, holding the probes by hand was eliminated by application of a wooden block to hold the needle probes in place during the measurements made in the same solenoid. The results obtained in this comparison present a significant improvement over the hand held needle probes. Both the waveforms shown in Figure 10.44 and the peak values of flux density agree within 4.5% throughout the range.

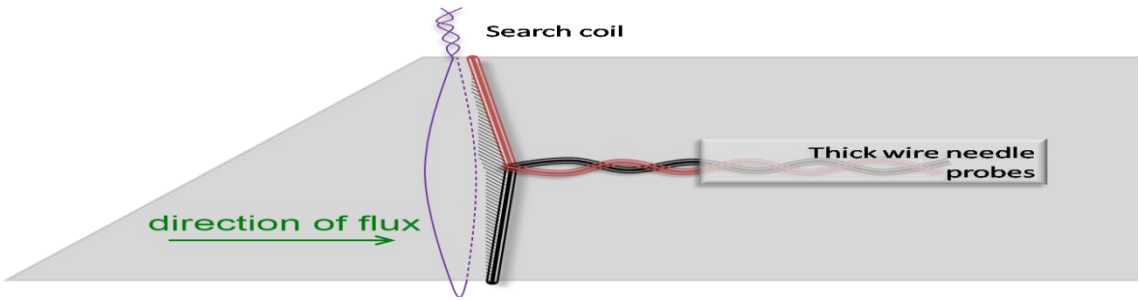

Figure 10.43 Schematic of a comparison measurement of flux density by using a search coil and needle probes.

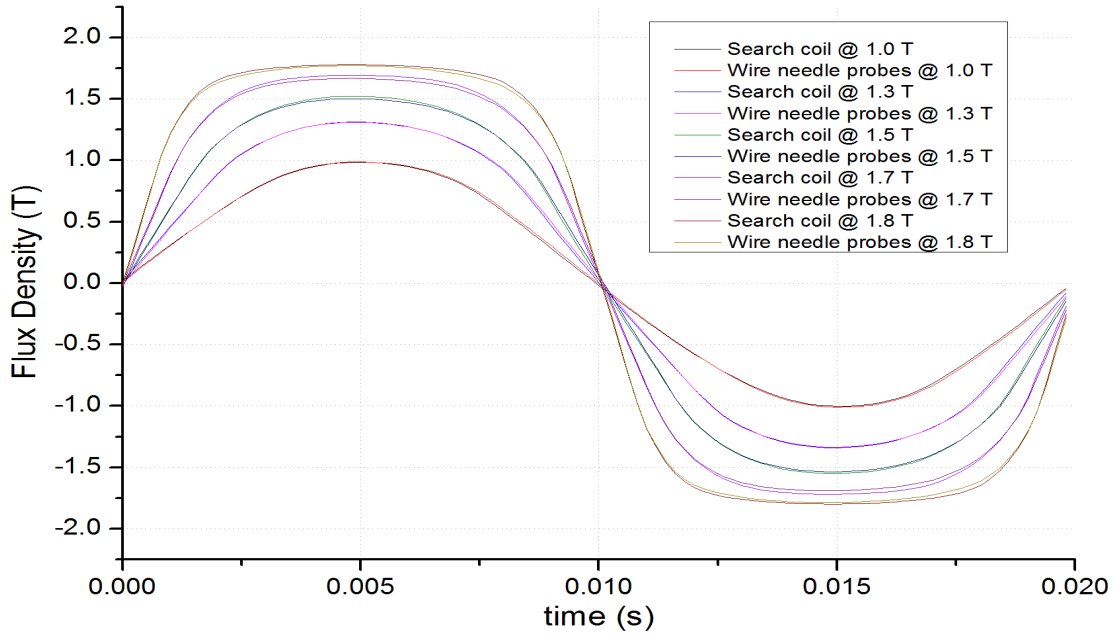

Figure 10.44 Comparison of measurements of flux density made by a search coil and by needle probes made of twisted wire of 2 mm diameter.

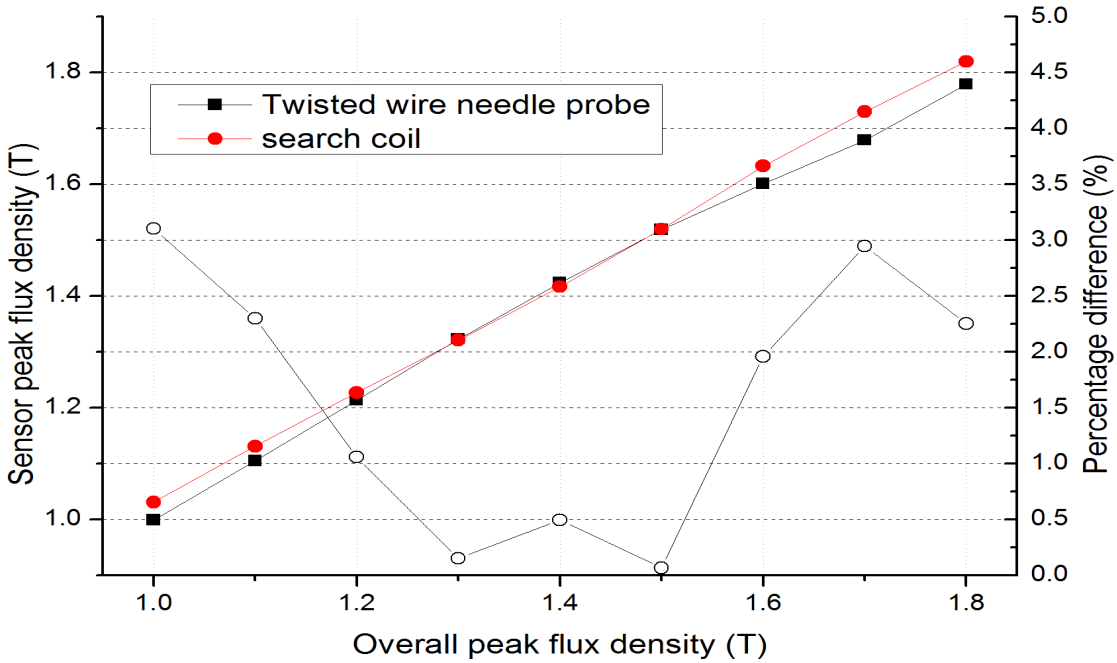

Figure 10.45 Variation of peak flux density measured by twisted wire needle probe and by a reference search coil with the overall flux density of the lamination measured by the reference search coil.

The comparison of a deposited needle sensor on a 50 mm wide lamination as shown in Figure 9.5 confirmed the trend throughout the range measured. The agreement between the thin film needle sensor and the search coil in both waveforms and the peak flux density values was consistent and did not exceed 1% in the whole range between

1.0 T and 1.7 T, raising however, to nearly 5% at 1.8 T. The results shown here have already been shown in section 9.2 and are shown here again to maintain the continuity of investigation.

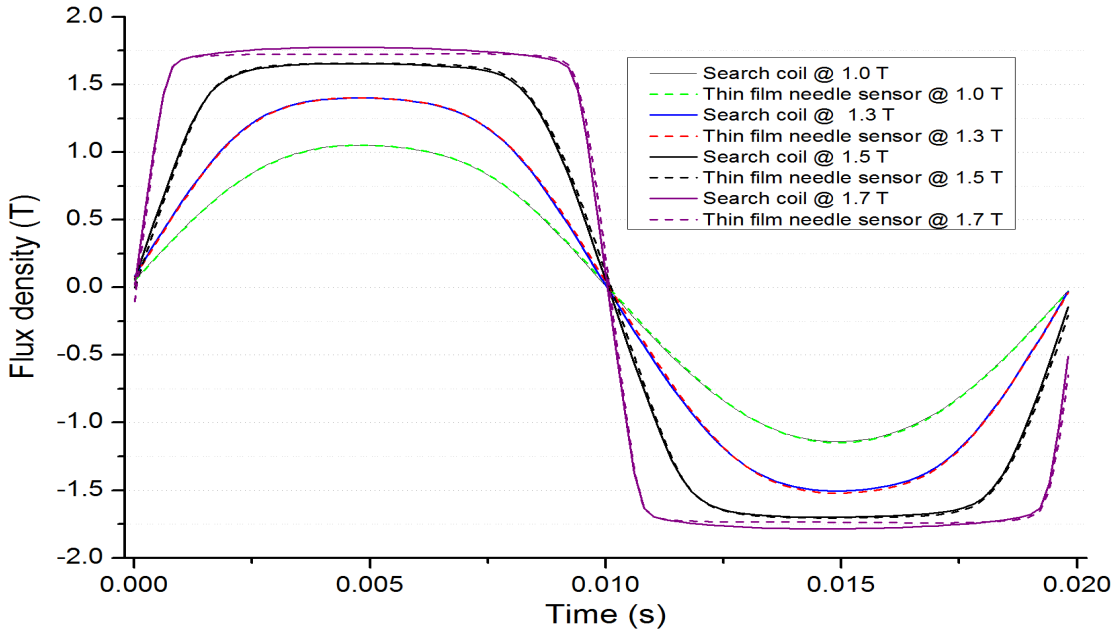

Figure 10.46 A comparison of flux density measured by a search coil and a needle probe flux density sensor. Both sensors measuring across 30 mm width of the sample as shown in Figure 9.5.

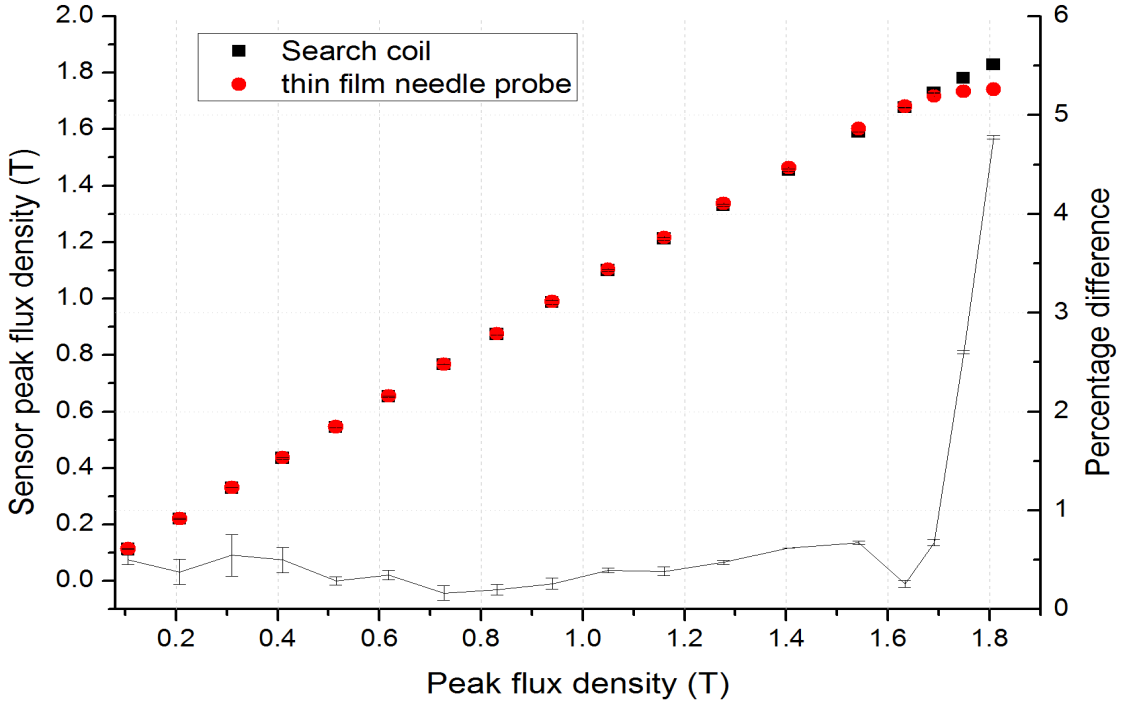

Figure 10.47 Variation of peak flux density of the 50 mm width lamination measured by deposited thin film needle sensor of 30 mm width and by a reference search coil of 30 mm width with the overall flux density of the lamination measured by the reference search coil.

A lamination taken out of Limb B of the core with four thin film needle sensors deposited onto it and four equivalent search coils threaded side by side as shown in Figure 10.48 was placed in a solenoid and magnetised to a range of peak flux densities from 0.1 T to 1.8 T. The results of the thin film needle probes and the search coils agreed within 2% throughout the range as shown in an example result for the sensor pair 3 in Figure 10.49.

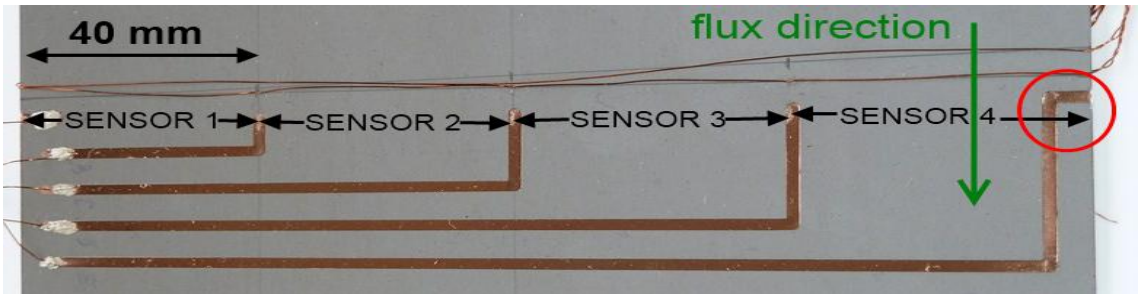

Figure 10.48 Four search coils side by side with four thin film needle sensors deposited on a 160 mm wide lamination taken out of limb B of the experimental core.

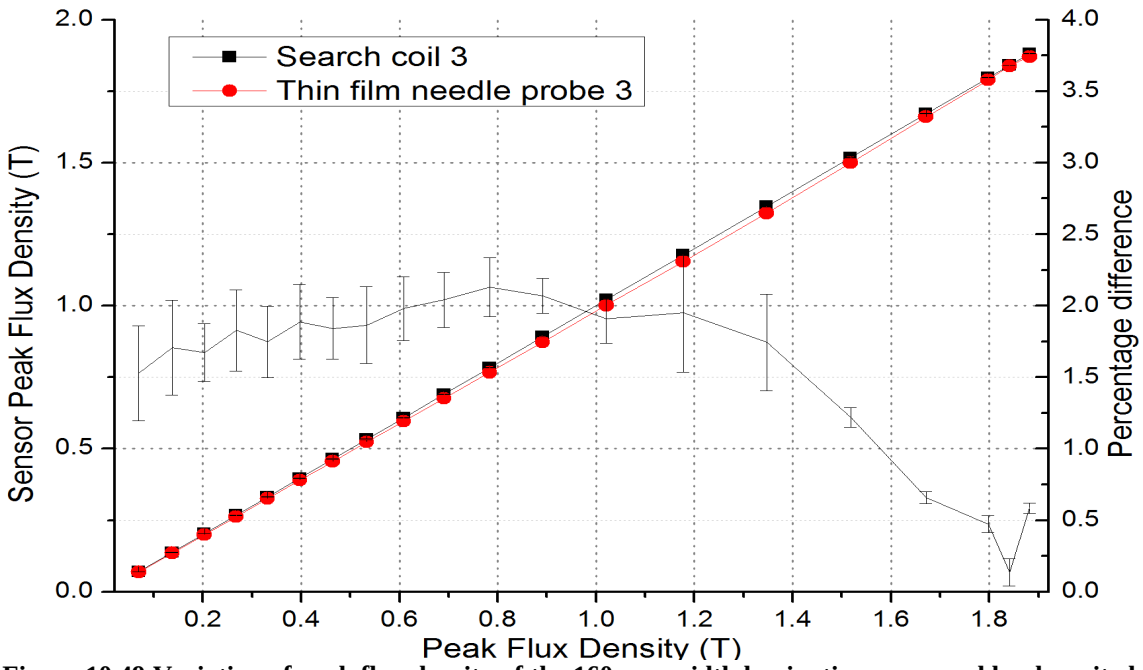

Figure 10.49 Variation of peak flux density of the 160 mm width lamination measured by deposited thin film needle sensor nr 3 of 40 mm width and by a reference search coil of 40 mm width with the overall flux density of the lamination measured by the reference search coil.

The thin film sensor technique developed here was later used for production of strain gauges on electrical steel laminations [88]. The work continues to refine this kind of sensors.

10.4.2 **Flux density measurement within a transformer**

The same lamination with four thin film needle sensors and four equivalent search coils as shown in Figure 10.48 was placed inside stack B of Limb B of the core as shown in Figure 9.8 and the core was magnetised to peak flux densities from 0.1 T up to 1.8 T. The results for each pair of thin film needle sensor and search coil are shown in Figure 10.50 and Figure 10.51. The agreement between thin film needle probes and equivalent search coils varies from less than 4% for sensor pair 2, through 5% and 7% for sensor pairs 3 and 1 respectively up to 20% for sensor pair number 4. However, for pair number 4 the result is much better up to 1.7 T with less than 8% difference and only for 1.8 T it presents a large discrepancy between the thin film sensor and the search coil. The difference between the overall flux density of the (X-axis) and all sensor readings can be caused by using a sensor lamination wider than the stack it was placed in or by already reported variations of flux densities between laminations within a stack.

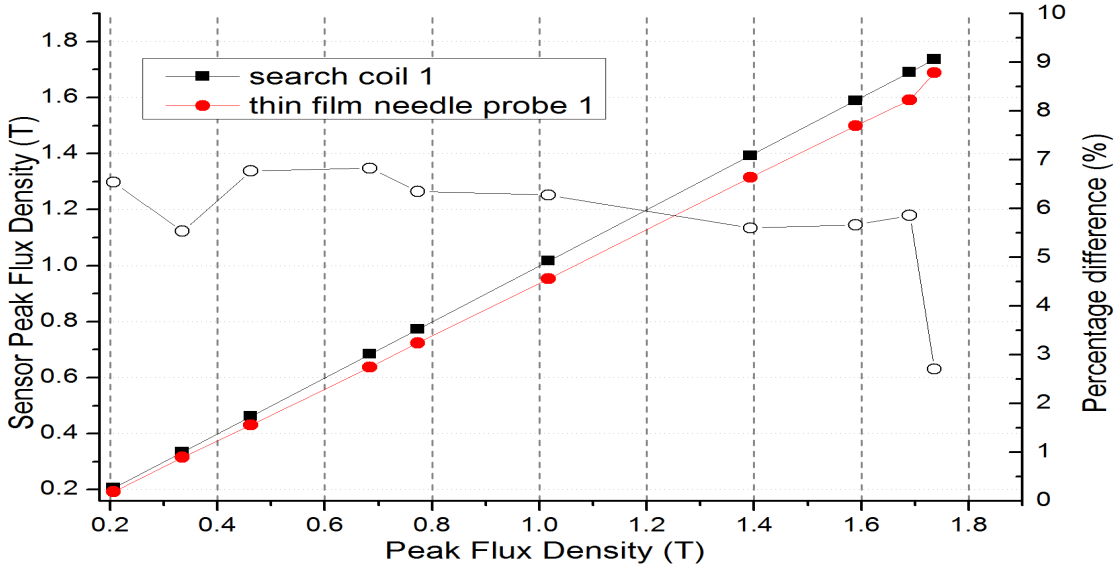

Figure 10.50 Variation of peak flux density of the 160 mm width lamination inserted into stack B of limb B of the experimental core measured by deposited thin film needle sensor nr 1 of 40 mm width and by a reference search coil of 40 mm width with the overall flux density of the lamination measured by the reference search coil.

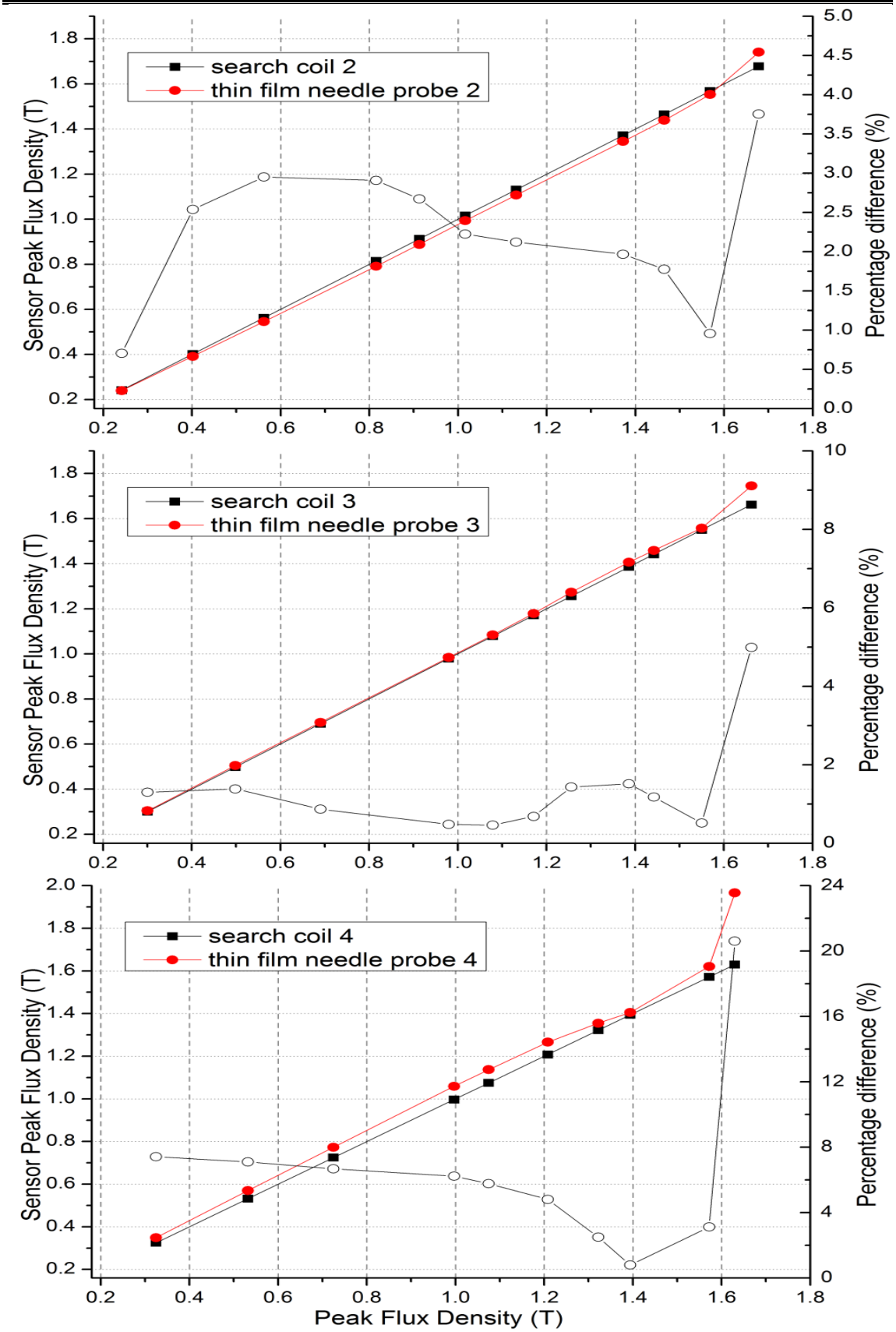

Figure 10.51 Variation of peak flux density of the 160 mm width lamination inserted into stack B of limb B of the experimental core measured by deposited thin film needle sensors nr 2, 3 and 4 of 40 mm width and by reference search coils of 40 mm width with the overall flux density of the lamination measured by the reference search coil. The X axis is common.

Chapter 11. **General conclusions and future work**

A novel technique for simulating burrs in transformer cores was developed allowing repeatable and completely reversible measurements with artificial burrs. The application of burrs is based on a clamping system which on its own does not affect the performance of the core. Out of several tested materials and solutions, copper foil has proven to be the most reliable material for simulating artificial burrs in a repeatable fashion. This method is better than previous techniques due to being completely reversible as well as to better control over the experimental conditions and flexibility in application in any desired configuration.

It was observed that the number of short circuited laminations is the most important factor increasing the core losses which results in a single effect being capable of causing changes reaching 20% - 80% increase in power loss at peak magnetisation levels of 1.5 T – 1.7 T at which transformers are used daily. The length of the short circuit presented a proportional effect on the increment in core loss while shifted arrangement of burrs on either side of the stack of laminations proved to decrease the effect with increasing shift.

The investigation has shown that for 12% layers of laminations burred the localised loss within the affected region was more than 600 times of the normal core loss value. Modelled results agreed very closely with these measurements. Local loss measurements have shown that the region affected by increased power loss is larger than a simple geometrical shape enclosed by the short circuit areas on the two sides of the limb. It reached as far as 80 mm away from the centre of the applied burrs. The reason for this may be that eddy currents circulating within the affected volume flow not

in straight lines between the short circuited sides but rather spread out away from the affected region. Also, because flux is repelled from within the affected region due to skin effect, it flows through the adjacent laminations along the lowest reluctance path and hence creates normal flux which in turn induces in-plane eddy currents contributing to the loss increase.

Burrs located on a limb or yoke of a transformer core significantly change the flux density distribution within that limb but importantly they also influence flux density distribution within the whole layout of the core.

It was confirmed that to affect the core performance, burrs short circuiting laminations have to be present in at least two locations on the core in an arrangement creating a closed loop through which there is flux flowing. The effect of increased total losses intensifies above 1.5 T for the model transformer core which is most likely caused by the skin effect and the flux density re-distribution within the cross-section of the core where the burrs are located.

Also, Prediction of eddy current loss strongly depends on flux distribution within the affected region. Higher accuracy of this calculation can be achieved by mapping flux distribution while core is affected by burrs.

A physical Vapour Deposition system was successfully developed for the production of thin film sensors on large electrical steel laminations which create significant opportunities for in depth investigation of electrical machines. Valid and accurate measurements were made using thin film flux density needle probes placed within a stack of a distribution transformer core which is again a significant milestone in developing this technique for use in commercial electrical machines. Use of such

sensors in commercial machines is desired for monitoring the efficiency and condition of machines which are in use continuously without the need of any down time.

Future work:

- Modelling permeability as a function of x for the flux density within the material model will improve the calculations of the flux density profile within the burred regions.
- Thin film thermocouples used for local loss measurement within a transformer core will allow monitoring the temperature within the core as well as take measurements of localised losses with minimised down time of the core.
- FE modelling of eddy current loss and distribution within cores affected by burrs will give more understanding of the phenomena occurring within the core affected by burrs and allow validating and improving the model.
- FE modelling of flux density distribution within a region affected by burrs will help validating the modelled flux density profiles and allow further validating of the power loss model.

REFERENCES

[1] E. PARLIAMENT, "On the promotion of the use of energy from renewable sources and amending and subsequently repealing Directives 2001/77/EC and 2003/30/EC," ed. Official JournaloftheEuropeanUnion, 2009.

[2] U. NATIONS, "KYOTO Protocol To The United Nations Framework Convention On Climate Change," ed. Kyoto: UNITED NATIONS, 1998.

[3] J. D. Ronnie Belmans, Hans De Keulenaer, Katsuaki Furuya, Mayur Karmarkar, Manuel Martinez, Mike McDermott, Ivo Pinkiewicz. (2005, 2011.11.11). The Potential for Global Energy Savings from High Effciency Distribution Transformers. 50. Available: http://www.leonardo-energy.org

[4] R. Mazurek, P. Marketos, A. Moses, and J. N. Vincent, "Effect of Artificial Burrs on the Total Power Loss of a Three-Phase Transformer Core," *Magnetics, IEEE Transactions on,* vol. 46, pp. 638-641, 2010.

[5] W. S. Jr., "Induction Coil " United States Patent No. 349,611, 1886

[6] D. Jiles, *Introduction to magnetism and magnetic materials*: Chapman and Hall, 1998.

[7] J. J. Winders, *Power transformers: principles and applications*: Marcel Dekker, 2002.

[8] P. Beckley, *Electrical steels: a handbook for producers and users*: European Electrical Steels, 2000.

[9] P. Beckley, *Electrical steels for rotating machines*: Institution of Electrical Engineers, 2002.

[10] W. Hayt and J. Buck, *Engineering Electromagnetics*: McGraw-Hill Companies,Incorporated, 2011.

[11] F. C. Campbell, *Elements of Metallurgy and Engineering Alloys*: Asm International, 2008.

[12] P. Marketos, S. Zurek, and A. J. Moses, "A Method for Defining the Mean Path Length of the Epstein Frame," *Magnetics, IEEE Transactions on,* vol. 43, pp. 2755-2757, 2007.

[13] M. A. Laughton and D. F. Warne, *Electrical Engineer's Reference Book*: Newnes, 2003.

[14] G. Bertotti, *Hysteresis in Magnetism: For Physicists, Materials Scientists, and Engineers*: Academic Press, 1998.

[15] T. E. S. GmbH, "PowerCore® Product Catalogue," T. E. S. GmbH, Ed., ed. http://www.tkes.com: ThyssenKrupp Electrical Steel GmbH, 2010.

[16] N. E. M. Association, *A chronological history of electrical development from 600 B.C*: National Electrical Manufacturers Association, 1946.

[17] B. D. Cullity, *Introduction to Magnetic Materials*, 1 ed. Reading: Addison-Wesley Publishing Company, Inc., 1972.

[18] E. W. Golding, *Electrical measurements and measuring instruments / by E.W. Golding and F.C. Widdis*. London :: I. Pitman, 1963.

[19] N. P. Goss, "Electrical sheet and method and apparatus for its manufacture and test," United States Patent 1965559, 1934.

[20] N. P. Goss, "New development in electrical strip steels characterized by fine grain structure approaching the properties of a single crystal," *Transactions of the American Society for Metals,* vol. 23, pp. 511-531, 1935.

[21] P. Klimczyk, "Novel Techniques for Characterisation and Control of Magnetostriction in G.O.S.S," Doctor of Philosophy, Cardiff School of Engineering, Cardiff University, 2012.

[22] S. Taguchi, T. Yamamoto, and A. Sakakura, "New grain-oriented silicon steel with high permeability "ORIENTCORE HI-B"," *Magnetics, IEEE Transactions on,* vol. 10, pp. 123-127, 1974.

[23] T. Yamamoto, S. Taguchi, A. Sakakura, and T. Nozawa, "Magnetic properties of grain-oriented silicon steel with high permeability Orientcore HI-B," *Magnetics, IEEE Transactions on,* vol. 8, pp. 677-681, 1972.

[24] T. Suzuki, H. Nakayama, T. Yamamoto, and S. Taguchi, "The transformer characteristics of "Orientcore HI-B"," *Magnetics, IEEE Transactions on,* vol. 8, pp. 321-323, 1972.

[25] S. Taguchi, A. Sakakura, and H. Takashima, "PROCESS FOR PRODUCING SINGLE-ORIENTED SILICON STEEL SHEETS HAVING A HIGH MAGNETIC INDUCTION," 1964.

[26] A. J. Moses, "Electrical steels: past, present and future developments," *IEE Proceedings,* vol. 137, pp. 233-245, 1990.

[27] P. L. Inc. (2012, 2012/10/10). *Silicon Steel (Electrical Steel)*. Available: http://www.protolam.com/page7.html

[28] R. M. Bozorth, *Ferromagnetism*: Wiley, 1993.

[29] K. Mousavi Takami, J. Mahmoudi, E. Dahlquist, and M. Lindenmo, "Study of magnetic aging in electrical steel and artificial neural network analyzing in real time mode : Modelling," presented at the International Energy Conference, Energitek : Modelling and industrial production, Stockholm, Sweden, 2009.

[30] T. B. S. Institution, "Magnetic materials Part 2: Methods of measurement of the magnetic properties of electrical steel strip and sheet by means of an Epstein frame," in *Methods of measurement of the magnetic properties of electrical steel strip and sheet by means of an Epstein frame* vol. EN 60404-2:1998+A1, ed. British Standards Online British Standards, 1998.

[31] N. E. M. Association, "Guide for Determining Energy Efficiency for Distribution Transformers," vol. TP 1-2002, ed. 1300 North 17th Street, Rosslyn, Virginia 22209: National Electrical Manufacturers Association, 2002.

[32] M. Jones, A. Moses, and J. Thompson, "Flux distribution and power loss in the mitered overlap joint in power transformer cores," *Magnetics, IEEE Transactions on,* vol. 9, pp. 114-122, 1973.

[33] T. Slawomir, "Induction coil sensors—a review," *Measurement Science and Technology,* vol. 18, p. R31, 2007.

[34] D. A. Ward and J. L. T. Exon, "Using Rogowski coils for transient current measurements," *Engineering Science and Education Journal,* vol. 2, pp. 105-113, 1993.

[35] A. Khanlou, A. J. Moses, T. Meydan, and P. Beckley, "A computerised on-line power loss testing system for the steel industry, based on the RCP compensation technique," *Magnetics, IEEE Transactions on,* vol. 31, pp. 3385-3387, 1995.

[36] A. Mohamed Abouelyazied Abdallh and L. Dupré, "A Rogowski-Chattock coil : sources of error," in *1&2 Dimensional Magnetic Measurement and Testing, 11th International workshop, Abstracts*, 2010.

[37] W. E, "Einrichtung zur Messung magnetischer Eigenschaften von Blechen bei Wechselstrommagnetisierung," Austrian patent no. 191015, 1957.

[38] G. Loisos and A. J. Moses, "Critical evaluation and limitations of localized flux density measurements in electrical steels," *Magnetics, IEEE Transactions on,* vol. 37, pp. 2755-2757, 2001.

[39] M. Nau, *Electrical Temperature Measurement: With Thermocouples and Resistance Thermometers*: Juchheim, 2002.

[40] P. Ripka and A. Tipek, *Modern Sensors Handbook*: John Wiley & Sons, 2010.

[41] T. B. S. Institution, "Thermocouples," in *Extension and compensating cables — Tolerances and identification system* vol. 60584-3, ed. https://bsol.bsigroup.com, 2008, p. 12.

[42] A. J. Gilbert, "A method of measuring loss distribution in electrical machines," *Proceedings of the IEE - Part A: Power Engineering,* vol. 108, pp. 239-244, 1961.

[43] A. Basak, D. M. Rowe, and F. J. Anayi, "Thin film senses magnetic flux and loss in rotary electric motors," *Magnetics, IEEE Transactions on,* vol. 33, pp. 3382-3384, 1997.

[44] F. J. Anayi, A. Basak, and D. M. Rowe, "Thin film sensors for flux and loss measurements," in *Condition Monitoring of Large Machines and Power Transformers (Digest No: 1997/086), IEE Colloquium on*, 1997, pp. 3/1-3/4.

[45] A. Basak, D. M. Rowe, and F. J. Anayi, "Thin film sensors for magnetic flux and loss measurements," *Journal of Magnetism and Magnetic Materials,* vol. 160, pp. 197-198, 1996.

[46] A. Basak, D. M. Rowe, and F. J. Anayi, "Magnetic flux and loss measurements using thin film sensors," *Magnetics, IEEE Transactions on,* vol. 31, pp. 3170-3172, 1995.

[47] C. Appino, F. Fiorillo, and C. Ragusa, "One-dimensional/two-dimensional loss measurements up to high inductions," *Journal of Applied Physics,* vol. 105, pp. 07E718-07E718-3, 2009.

[48] H. Pfutzner and E. Mulasalihovic, "Thin-film technique for interior magnetic analysis of laminated machine cores," *Przeglad Elektrotechniczny,* vol. 85, pp. 39-42, 2009.

[49] A. Basak, D. M. Rowe, and F. Anayi, "Thin film senses flux and loss in machines," in *UK Magnetics Society Seminar*, 1994, p. 12.

[50] A. J. Moses, N. Derebasi, G. Loisos, and A. Schoppa, "Aspects of the cut-edge effect stress on the power loss and flux density distribution in electrical steel sheets," *Journal of Magnetism and Magnetic Materials,* vol. 215-216, pp. 690-692, 2000.

[51] E. P. DeGarmo, J. T. Black, and R. A. Kohser, *Degarmo's Materials and Processes in Manufacturing*: John Wiley & Sons, 2011.

[52] P. K. Klimczyk, P. Anderson, A. Moses, and M. Davies, "Influence of Cutting Techniques on Magnetostriction Under Stress of Grain Oriented Electrical Steel," *Magnetics, IEEE Transactions on,* vol. 48, pp. 1417-1420, 2012.

[53] E. C. Jameson, *Electrical Discharge Machining*: Society of Manufacturing Engineers, 2001.

[54] T. B. S. Institution, "Magnetic materials - Methods of determination of the geometrical characteristics of electrical steel sheet and strip," vol. BS EN 10251:1997, ed: The British Standards Institution, 1997.

[55] T. B. S. Institution, "Grain-oriented electrical steel sheet and strip delivered in the fully processed state," in *Technical requirements* vol. EN 10107:2005 (E), ed, 2005.

[56] T. Belgrand, "client requirements regarding burr height in electrical steel," ed. email, 2012.

[57] D. Snell and A. Coombs, "Novel coating technology for non-oriented electrical steels," *Journal of Magnetism and Magnetic Materials,* vol. 215–216, pp. 133-135, 2000.

[58] M. Lindenmo, A. Coombs, and D. Snell, "Advantages, properties and types of coatings on non-oriented electrical steels," *Journal of Magnetism and Magnetic Materials,* vol. 215-216, pp. 79-82, 2000.

[59] T. Nakata, M. Nakano, and K. Kawahara, "Effects of Stress Due to Cutting on Magnetic Characteristics of Silicon Steel," *Magnetics in Japan, IEEE Translation Journal on,* vol. 7, pp. 453-457, 1992.

[60] M. Emura, F. J. G. Landgraf, W. Ross, and J. R. Barreta, "The influence of cutting technique on the magnetic properties of electrical steels," *Journal of Magnetism and Magnetic Materials,* vol. 254–255, pp. 358-360, 2003.

[61] A. STEEL, "Selection of Electrical Steels for Magnetic Cores," A. S. Corporation, Ed., ed. http://www.aksteel.com: AK Steel Corporation, 2007.

[62] K. H. Schmidt, "Influence of punching on the magnetic properties of electric steel with 1% silicon," *Journal of Magnetism and Magnetic Materials,* vol. 2, pp. 136-150, 1975.

[63] A. Moses, "Transformer Fault Analysis Report," Wolfson Centre for Magnetics Technology.

[64] S. Bin Lee, G. B. Kliman, M. R. Shah, W. T. Mall, N. K. Nair, and R. M. Lusted, "An advanced technique for detecting inter-laminar stator core faults in large electric machines," *Ieee Transactions on Industry Applications,* vol. 41, pp. 1185-1193, Sep-Oct 2005.

[65] D. R. Bertenshaw, J. F. Lau, and D. J. Conley, "Evaluation of EL CID indications not associated with stator core interlaminar insulation faults," in *Electrical Insulation Conference (EIC), 2011*, 2011, pp. 254-260.

[66] K. C. Lin and H. Jong-Sen, "Selection of silicon steel for transformer cores," in *Electrical Electronics Insulation Conference, 1995, and Electrical Manufacturing & Coil Winding Conference. Proceedings*, 1995, pp. 147-152.

[67] G. Klempner and I. Kerszenbaum, *Handbook of Large Turbo-Generator Operation and Maintenance*: John Wiley & Sons, 2011.

[68] C. Rickson, "Electrical machine core imperfection detection," *Electric Power Applications, IEE Proceedings B,* vol. 133, pp. 190-195, 1986.

[69] I. Power, "EL CID Evolution(TM) - The next generation in EL CID technology for detecting stator core problems," in *Internet*, I. Power, Ed., 2 ed. Internet: http://www.megavar.com.au, 2009, p. 4.

[70] G. K. Ridley, "EL CID test evaluation, 1984-96," *Power Engineering Journal,* vol. 11, pp. 21-26, 1997.

[71] J. Sutton, "EL Cid: an easier way to test stator cores," *Electrical Review,* vol. 207, pp. 33-37, 1980.

[72] J. Sutton, "Method and apparatus for testing laminated cores of electrical machines," United States Patent, 2005.

[73] D. B. Paley, "Current low power core testing using EL CID," in *Understanding your Condition Monitoring (Ref. No. 1999/117), IEE Colloquium on*, 1999, pp. 7/1-7/4.

[74] D. B. Paley, "Low power stator core fault testing using EL CID," in *Power System Technology, 1998. Proceedings. POWERCON '98. 1998 International Conference on*, 1998, pp. 1010-1014 vol.2.

[75] C. A. Schulz, S. Duchesne, D. Roger, and J.-N. Vincent, "Capacitive short circuit detection in transformer core laminations," *Journal of Magnetism and Magnetic Materials,* vol. 320, pp. e911-e914, 2008.

[76] G. B. Kliman, S. Bin Lee, M. R. Shah, R. M. Lusted, and N. K. Nair, "A new method for synchronous generator core quality evaluation," *Ieee Transactions on Energy Conversion,* vol. 19, pp. 576-582, Sep 2004.

[77] A. J. Moses and M. Aimoniotis, "Effects of artificial edge burrs on the properties of a model transformer core," *Physica Scripta,* vol. 39, pp. 391-393, 1989.

[78] D. Edwards, "Influence Of Virtual Leaks On The Pressure In High And Ultrahigh-Vacuum Systems," *Vacuum,* vol. 29, pp. 169-172, 1979.

[79] I. Meyer Tool & Manufacturing. (2012, 12/06/2012). *Guide to custom manufactured vacuum (and other) equipment* [html]. Available: http://www.mtm-inc.com/reduce_project_risk/

[80] D. M. Mattox, *Handbook of Physical Vapor Deposition (PVD) Processing*: William Andrew, 2010.

[81] I. C. E. CORPORATION. Changing Wafer Size and the Move to 300mm. Available: http://smithsonianchips.si.edu/ice/cd/CEICM/SECTION7.pdf

[82] A. Russell, *A treatise on the theory of alternating currents*: University Press, 1916.

[83] T. Shimazu and M. Shiozaki, "Effects of grain size and frequency on eddy current loss in Si-Fe sheets," *Magnetics, IEEE Transactions on,* vol. 26, pp. 1972-1974, 1990.

[84] H. Hamzehbahmani, P. I. Anderson, J. Hall, and D. Fox, "Eddy Current Power Loss Estimation in a Wide Range of Magnetising Frequency Based on Equivalent Electrical Circuit of Magnetic Laminations " unpublished|.

[85] R. Mazurek, H. Hamzehbahmani, A. J. Moses, P. I. Anderson, F. J. Anayi, and T. Belgrand, "Effect of Artificial Burrs on Local Power Loss in a Three-Phase Transformer Core," *Magnetics, IEEE Transactions on,* vol. 48, pp. 1653-1656, 2012.

[86] M. B. Balehosur, P. Marketos, A. J. Moses, and J. N. Vincent, "Packet-to-Packet Variation of Flux Density in a Three-Phase, Three-Limb Power Transformer Core," *Magnetics, IEEE Transactions on,* vol. 46, pp. 642-645, 2010.

[87] R. Mazurek, F. Marketos, A. J. Moses, and T. Belgrand, "Development of Sensors for Measurement of Localised Flux Density in Transformer Cores," Sensor Letters, vol 11, pp 56-58, 2013.

[88] J. Harcourt, J. Loktionov, E. Thoni, and R. Townsend, "Investigating techniques for modelling and measuring internal strain in transformer cores," MEng MEng, Cardiff University, 2012.

APPENDIX I. Derivation of flux density within a sheet of material

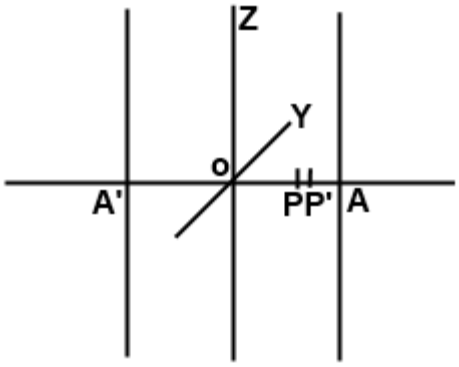

Taking thickness of the material AA', from Ohms law, the emf in PP'P_y'P_y is calculated in

$$emf_{OHM} = \rho\left(i + \frac{\partial i}{\partial x}\partial x\right)L - \rho iL \tag{A.11.1}$$

Where PP' = dx and P'P_y = L

From Faradays Law the same emf is calculated as in

$$emf = -\frac{\partial}{\partial t}B\partial xL \tag{A.11.2}$$

Hence (A.11.1) and (A.11.2) together give

$$\left(\rho\left(i + \frac{\partial i}{\partial x}\partial x\right) - \rho i\right)L = -\frac{\partial}{\partial t}B\partial xL$$

$$\rho\frac{\partial i}{\partial x} = -\frac{\partial B}{\partial t} \tag{A.11.3}$$

From Ampers circuital law for PP'P_z'P_z we get

$$i\partial xL = \left(H - \left(H + \frac{\partial H}{\partial x}\partial x\right)\right)L$$

$$i = -\frac{\partial H}{\partial x} \tag{A.11.4}$$

Substituting (A.11.4) into(A.11.3) we get

$$\rho\frac{\partial^2 H}{\partial x^2} = \frac{\partial B}{\partial t} \tag{A.11.5}$$

Neglecting the hysteresis effect and assuming μ(t, x) = const. we can write

$$B = \mu_0 \mu_r H \tag{A.11.6}$$

And substitute(A.11.6) to(A.11.5) gives

$$\rho \frac{\partial^2 H}{\partial x^2} = \mu_0 \mu_r \frac{\partial H}{\partial t} \tag{A.11.7}$$

The solution of (A.11.7)has a form of

$$H(x,t) = h \cos \omega t + k \sin \omega t \tag{A.11.8}$$

Where h and k are functions of x, therefore

$$\omega(-h \sin \omega t + k \cos \omega t) = \frac{1}{\sigma \mu_0 \mu_r}\left(\frac{\partial^2 h}{\partial x^2} \cos \omega t + \frac{\partial^2 k}{\partial x^2} \sin \omega t\right) \tag{A.11.9}$$

Expression (A.11.9) must be valid for all values of t and so

$$h = -\frac{1}{\sigma \mu_0 \mu_r \omega} \frac{\partial^2 k}{\partial x^2}\ ; \quad k = \frac{1}{\sigma \mu_0 \mu_r \omega} \frac{\partial^2 h}{\partial x^2} \tag{A.11.10}$$

And substituting k into the equation for h we get

$$h = -\left(\frac{1}{\sigma \mu_0 \mu_r \omega}\right)^2 \frac{\partial^4 h}{\partial x^4} \tag{A.11.11}$$

Substituting

$$\left(\frac{1}{\sigma \mu_0 \mu_r \omega}\right)^2 = \frac{1}{4p^4} \tag{A.11.12}$$

The value of p is always positive as $\sigma, \mu_0, \mu_r \ and \ \omega$ are always positive, hence:

$$p^2 = \frac{1}{2} \sigma \mu_0 \mu_r \omega$$
$$p = \sqrt{\pi f \sigma \mu_0 \mu_r} \tag{A.11.13}$$

From and we can write

$$h = -\frac{1}{4p^4} \frac{\partial^4 h}{\partial x^4} \tag{A.11.14}$$

A standard way of solving is in the form of

$$h = Ae^{nx} \tag{A.11.15}$$

Therefore we get

$$Ae^{nx} = -\frac{1}{4p^4} \frac{\partial^4 Ae^{nx}}{\partial x^4}$$
$$n^4 = -4p^4 \tag{A.11.16}$$

Equation has 4 roots therefore substituting $m = n^2$ we get two solutions $m_1 = 2p^2 i\ ;\ m_2 = -2p^2 i$

Reversing m to n this gives four solutions:

$$\begin{aligned} n_1 &= \sqrt{2p^2\sqrt{-1}} = p(1+i) \\ n_2 &= -\sqrt{2p^2\sqrt{-1}} = -p(1+i) \\ n_3 &= \sqrt{-2p^2\sqrt{-1}} = p(1-i) \\ n_4 &= -\sqrt{-2p^2\sqrt{-1}} = -p(1-i) \end{aligned} \tag{A.11.17}$$

Recalling that $e^{i\alpha} = \cos\alpha + i\sin\alpha$ we get a solution with four terms one for each root, hence

$$\begin{aligned} &h = A_1 e^{n_1 x} + A_2 e^{n_2 x} + A_3 e^{n_3 x} + A_4 e^{n_4 x} = \\ &= A_1 e^{px}(\cos(px) + i\sin(px)) + A_3 e^{px}(\cos(-px) + i\sin(-px)) + \\ &+ A_2 e^{-px}(\cos(px) + i\sin(-px)) + A_4 e^{-px}(\cos(px) + i\sin(px)) \\ &= (A_1 + A_3)e^{px}\cos(px) + \ (iA_1 + iA_3)e^{px}\sin(px) + \\ &+ (A_2 + A_4)e^{-px}\cos(px) + \ (-iA_2 + iA_4)e^{-px}\sin(px) = \\ &= Ae^{px}\cos(px) + \ Be^{px}\sin(px) + Ce^{-px}\cos(px) + De^{-px}\sin(px) \end{aligned} \tag{A.11.18}$$

The final solution for h is

$$h = Ae^{px}\cos(px) + \ Be^{px}\sin(px) + Ce^{-px}\cos(px) + De^{-px}\sin(px) \tag{A.11.19}$$

Where A, B, C and D are constants. Calculation of k requires second order derivation of h as follows:

$$k = \frac{1}{\sigma\mu_0\mu_r\omega}\frac{\partial^2(Ae^{px}\cos(px) + \ Be^{px}\sin(px) + Ce^{-px}\cos(px) + De^{-px}\sin(px}{\partial x^2}$$

$$k = \frac{1}{2p^2}\frac{\partial}{\partial x}\left(\frac{\partial}{\partial x}(Ae^{px}\cos(px) + \ Be^{px}\sin(px) + Ce^{-px}\cos(px) + De^{-px}\sin(px))\right) \tag{A.11.20}$$

$$\begin{aligned} k = \frac{1}{2p^2}\frac{\partial}{\partial x}\big(&Ape^{px}\cos px - Ae^{px}p\sin px + Bpe^{px}\sin px + Bpe^{px}\cos px \\ &+ (-Cpe^{-px}\cos px - Cpe^{-px}\sin px) \\ &+ (-Dpe^{-px}\sin px + Dpe^{-px}\cos px)\big) \end{aligned}$$

$$k = \frac{1}{2p^2}(Ap^2e^{px}\cos px - Ap^2e^{px}\sin px - Ap^2e^{px}\sin px - Ap^2e^{px}\cos px + Bp^2e^{px}\sin px + Bp^2e^{px}\cos px + Bp^2e^{px}\cos px - Bp^2e^{px}\sin px + Cp^2e^{-px}\cos px + Cp^2e^{-px}\sin px + Cp^2e^{-px}\sin px - Cp^2e^{-px}\cos px + Dp^2e^{-px}\sin px - Dp^2e^{-px}\cos px - Dp^2e^{-px}\cos px - Dp^2e^{-px}\sin px)$$

$$k = \frac{1}{2p^2}(-2Ap^2e^{px}\sin px + 2Bp^2e^{px}\cos px + 2Cp^2e^{-px}\sin px - 2Dp^2e^{-px}\cos px)$$

$$k = \frac{1}{2p^2}\left(2p^2(-Ae^{px}\sin px + Be^{px}\cos px + Ce^{-px}\sin px - De^{-px}\cos px)\right)$$

Which results in

$$k = -Ae^{px}\sin px + Be^{px}\cos px + Ce^{-px}\sin px - De^{-px}\cos px \quad \text{(A.11.21)}$$

And again $H = h\cos\omega t + k\sin\omega t$; we can use the symmetry H(t, x) = H(t, -x) and write the equation for H (wt=0, x) and H(wt=0, -x).

$$\begin{aligned} H(\omega\, t = 0, x) &= Ae^{px}\cos(px) + \ Be^{px}\sin(px) + Ce^{-px}\cos(px) \\ &\quad + De^{-px}\sin(px) \\ H(\omega t = 0, -x) &= Ae^{-px}\cos(px) + \ Be^{-px}\sin(-px) + Ce^{px}\cos(px) \\ &\quad + De^{px}\sin(-px) \end{aligned} \quad \text{(A.11.22)}$$

And a case for wt=pi/2

$$\begin{aligned} H\left(\omega t = \frac{\pi}{2}, x\right) &= -Ae^{px}\sin px + Be^{px}\cos px + Ce^{-px}\sin px \\ &\quad - De^{-px}\cos px \\ &\quad H\left(\omega t = \frac{\pi}{2}, -x\right) \\ &= Ae^{-px}\sin px + Be^{-px}\cos px - Ce^{px}\sin px \\ &\quad - De^{px}\cos px \end{aligned} \quad \text{(A.11.23)}$$

The two symmetrical cases have to be equal at all times, hence

$$\begin{cases} Ae^{px}\cos(px) + Be^{px}\sin(px) + Ce^{-px}\cos(px) + De^{-px}\sin(px) = Ae^{-px}\cos(px) - Be^{-px}\sin(px) + Ce^{px}\cos(px) - De^{px}\sin(px) \\ -Ae^{px}\sin(px) + Be^{px}\cos(px) + Ce^{-px}\sin(px) - De^{-px}\cos(px) = Ae^{-px}\sin(px) + Be^{-px}\cos(px) - Ce^{px}\sin(px) - De^{px}\cos(px) \end{cases} \quad \text{(A.11.24)}$$

The relation B = - D can be shown as follows

$$\begin{cases} A - C = (-B - D)\dfrac{\sin px\,(e^{px} + e^{-px})}{\cos px\,(e^{px} - e^{-px})} \\ -A + C = (-B - D)\dfrac{\cos px\,(e^{px} + e^{-px})}{\sin px\,(e^{px} - e^{-px})} \end{cases} \quad \text{(A.11.25)}$$

$$0 = (-B - D)\frac{\cos px\,(e^{px} + e^{-px})}{\sin px\,(e^{px} - e^{-px})} - (-B - D)\,\frac{\sin px\,(e^{px} + e^{-px})}{\cos px\,(e^{px} - e^{-px})}$$

$$0 = (-B - D)\left(\frac{\cos px\,(e^{px} + e^{-px})}{\sin px\,(e^{px} - e^{-px})} + \frac{\sin px\,(e^{px} + e^{-px})}{\cos px\,(e^{px} - e^{-px})}\right)$$

$$B = -D$$

And relation A=C can be shown

$$A - C = (D - D)\frac{\sin px\,(e^{px} + e^{-px})}{\cos px\,(e^{px} - e^{-px})} \qquad (A.11.26)$$

$$A = C$$

Hence h takes the form of (A.11.27)

$$h = Ae^{px}\cos(px) + \ Be^{px}\sin(px) + Ae^{-px}\cos(px) - Be^{-px}\sin(px)$$
$$h = A(e^{px}e^{-px})\cos(px) + B(e^{px} - e^{-px})\sin(px) \qquad (A.11.27)$$

Using $\cosh\alpha = \frac{e^{\alpha}+e^{-\alpha}}{2}$; $\sinh\alpha = \frac{e^{\alpha}-e^{-\alpha}}{2}$ we get

$$h = 2A\cosh px\cos px + 2B\sinh px\sin px \qquad (A.11.28)$$

And k is equal to

$$k = -2A\sinh px\sin px + 2B\cosh px\cos px \qquad (A.11.29)$$

We use the boundary conditions at the surface where x=+-a and H = H_0cos(wt)

$$H_0\cos\omega t = \cos(\omega t)\,(2A\cosh pa\cos pa + 2B\sinh pa\sin pa)$$
$$+ \sin(\omega t)\,(-2A\sinh pa\sin pa + 2B\cosh pa\cos pa) \qquad (A.11.30)$$

For (wt)=0

$$H_0 = 2A\cosh pa\cos pa + 2B\sinh pa\sin pa \qquad (A.11.31)$$

and for (wt)=pi/2

$$0 = -2A\sinh pa\sin pa + 2B\cosh pa\cos pa \qquad (A.11.32)$$

From (A.11.31) and (A.11.32)

$$A = \frac{2B\cosh pa\cos pa}{\sinh pa\sin pa}$$
$$B = \frac{H_0 - 2A\cosh pa\cos pa}{2\cosh pa\cos pa} \qquad (A.11.33)$$

Further (Using the rule)

$$\cosh^2\alpha\cos^2\alpha+\sinh^2\alpha\sin^2\alpha=\frac{\cosh 2\alpha+\cos 2\alpha}{2} \tag{A.11.34}$$

We obtain A and B as in (A.11.35)

$$B=\frac{H_0\sinh pa\sin pa}{\cosh 2pa+\cos 2pa}$$
$$A=\frac{H_0\cosh pa\cos pa}{\cosh 2pa+\cos 2pa} \tag{A.11.35}$$

And so from (A.11.28)and (A.11.35)we get (A.11.36)

$$\frac{h}{H_0}=\frac{\cosh pa\cos pa}{\cosh 2pa+\cos 2pa}2\cosh px\cos px$$
$$+\frac{\sinh pa\sin pa}{\cosh 2pa+\cos 2pa}2\sinh px\sin px \tag{A.11.36}$$

And from (A.11.29) and (A.11.35) we get (A.11.37)

$$\frac{k}{H_0}=-2\frac{\cosh pa\cos pa}{\cosh 2pa+\cos 2pa}\sinh px\sin px$$
$$+2\frac{\sinh pa\sin pa}{\cosh 2pa+\cos 2pa}\cosh px\cos px \tag{A.11.37}$$

Again, the basic form of the solution is $H=h\cos\omega t+k\sin\omega t$ and so

$$H=h\cos\omega t+k\sin\omega t=\sqrt{h^2+k^2}\left(\frac{h}{\sqrt{h^2+k^2}}\cos\omega t+\frac{k}{\sqrt{h^2+k^2}}\sin\omega t\right)$$
$$=\sqrt{h^2+k^2}(\cos\omega t\cos\gamma+\sin\omega t\sin\gamma) \tag{A.11.38}$$
$$=\sqrt{h^2+k^2}\cos(\omega t-\gamma)$$

$$H=h\cos\omega t+k\sin\omega t=\sqrt{h^2+k^2}\left(\frac{h}{\sqrt{h^2+k^2}}\cos\omega t+\frac{k}{\sqrt{h^2+k^2}}\sin\omega t\right)$$
$$=\sqrt{h^2+k^2}(\cos\omega t\cos\gamma+\sin\omega t\sin\gamma) \tag{A.11.39}$$
$$=\sqrt{h^2+k^2}\cos(\omega t-\gamma)$$

Finally we get

$$H=H_0\sqrt{\frac{\cosh 2px+\cos 2px}{\cosh 2pa+\cos 2pa}}\cos(\omega t-\gamma) \tag{A.11.40}$$

Where γ is the phase difference between the surface and

$$\gamma=\arctan\left(\frac{k}{h}\right)=\arctan\frac{-2A\sinh px\sin px+2B\cosh px\cos px}{2A\cosh px\cos px+2B\sinh px\sin px} \tag{A.11.41}$$

Hence, from (A.11.13)

$$H = H_0 \sqrt{\frac{\cosh 2x\sqrt{\pi f\sigma\mu_0\mu_r} + \cos 2x\sqrt{\pi f\sigma\mu_0\mu_r}}{\cosh 2a\sqrt{\pi f\sigma\mu_0\mu_r} + \cos 2a\sqrt{\pi f\sigma\mu_0\mu_r}}} \cos(\omega t - \gamma) \qquad \text{(A.11.42)}$$

And for H_B thickness of the sheet $a = \frac{H_B}{2}$ therefore

$$H = H_0 \sqrt{\frac{\cosh 2x\sqrt{\pi f\sigma\mu_0\mu_r} + \cos 2x\sqrt{\pi f\sigma\mu_0\mu_r}}{\cosh H_B\sqrt{\pi f\sigma\mu_0\mu_r} + \cos H_B\sqrt{\pi f\sigma\mu_0\mu_r}}} \cos(\omega t - \gamma) \qquad \text{(A.11.43)}$$

Since μ is constant we can use (A.11.6) to write

$$B = B_0 \sqrt{\frac{\cosh 2x\sqrt{\pi f\sigma\mu_0\mu_r} + \cos 2x\sqrt{\pi f\sigma\mu_0\mu_r}}{\cosh H_B\sqrt{\pi f\sigma\mu_0\mu_r} + \cos H_B\sqrt{\pi f\sigma\mu_0\mu_r}}} \cos(\omega t - \gamma) \qquad \text{(A.11.44)}$$

APPENDIX II. List of publications

Journal publications

1 Mazurek, R.; Marketos, P.; Moses, A.; Vincent, J.-N.; "Effect of Artificial Burrs on the Total Power Loss of a Three-Phase Transformer Core", *IEEE Transactions on Magnetics*, vol.46, no.2, pp.638-641, Feb. 2010

2 Mazurek, R.; Marketos, P.; Moses, A.; Belgrand, T.; "Development of sensors for measurement of localised flux density in transformer cores", Sensor Letters, vol 11, pp 56-58, 2013

3 Mazurek, R.; Anderson, P.; Moses, A.; Belgrand, T.; Hamzehbahmani, H.; "Effect of Artificial Burrs on Local Power Loss of a Transformer Core", *IEEE Transactions on Magnetics*, vol.48, no.4, pp.1653-1656, Apr 2012

Conference publications and presentations

1 R Mazurek, Dr P Marketos, Prof. A J Moses and J N Vincent "Effect of Artificial Burrs on the Total Power Loss of a Three Phase Transformer Core" 19th Soft Magnetic Materials Conference, Torino, Italy, 6-9 September, 2009 –Book of abstracts (H2-20) – Poster Presentation

2 Mazurek, R.; "Novel embedded sensors for evaluating the effect oflamination burrs on the efficiency of power transformers" **Energy in a Carbon Constrained World – Launch of New Initiatives in Energy at Cardiff University**, Cardiff, United Kingdom, 4 June, 2009 – Poster Presentation

3 Mazurek, R.; "Novel embedded sensors for evaluating the effect of lamination burrs on the efficiency of power transformers" **IEEE Magnetics Society UKRI Chapter Postgraduate Conference 2009**, Cardiff, United Kingdom, 9 July, 2009 – Poster Presentation

4 Mazurek, R.; Marketos, P.; Moses, A.; Belgrand, T.; "Development of sensors for measurement of localised flux density in transformer cores" **8th European Conference on magnetic sensors and actuators,** Bodrum, Turkey, 4-7 July 2010 – Poster Presentation

5 Mazurek, R.; Marketos, P.; Moses, A.; Belgrand, T.; "Development of sensors for measurement of localised flux density in transformer cores" **Cardiff University, Institute of Energy Seminar** 24 November 2010 – Poster Presentation

6 Mazurek, R.; Anderson, P.; Moses, A.; Belgrand, T.; Hamzehbahmani, H.; "Effect of Artificial Burrs on Local Power Loss of a Transformer Core", SMM20, KOS, Greece, 18-22 September 2011 – Poster Presentation